



**HAL**  
open science

# Nanomateriaux hybrides poreux à base de silice et de dioxyde de titane : de la synthèse aux applications

Pengkun Chen

► **To cite this version:**

Pengkun Chen. Nanomateriaux hybrides poreux à base de silice et de dioxyde de titane : de la synthèse aux applications. Other. Université de Strasbourg, 2017. English. NNT : 2017STRAF010 . tel-01635731

**HAL Id: tel-01635731**

**<https://theses.hal.science/tel-01635731>**

Submitted on 15 Nov 2017

**HAL** is a multi-disciplinary open access archive for the deposit and dissemination of scientific research documents, whether they are published or not. The documents may come from teaching and research institutions in France or abroad, or from public or private research centers.

L'archive ouverte pluridisciplinaire **HAL**, est destinée au dépôt et à la diffusion de documents scientifiques de niveau recherche, publiés ou non, émanant des établissements d'enseignement et de recherche français ou étrangers, des laboratoires publics ou privés.

**ÉCOLE DOCTORALE DES SCIENCES CHIMIQUES**  
**Institut de Science et d'Ingénierie Supramoléculaires (ISIS)**

**THÈSE** présentée par :

**Pengkun CHEN**

soutenue le : **10 février 2017**

pour obtenir le grade de : **Docteur de l'université de Strasbourg**

Discipline/ Spécialité : **CHIMIE**

**Titania and silica based hybrid porous  
nanomaterials: from synthesis to  
applications**

**THÈSE dirigée par :**

**Mme DE COLA Luisa**

Professeur, Université de Strasbourg

**RAPPORTEURS :**

**Mme GIORDANO Cristina**

**M. MAGGINI Michele**

Professeur, Queen Mary University of London

Professeur, Università degli Studi di Padova

---

**AUTRES MEMBRES DU JURY :**

**M. RABU Pierre**

Docteur, Université de Strasbourg



# Table of contents

<b>Résumé .....</b>	<b>1</b>
<b>Chapter 1 Introduction.....</b>	<b>21</b>
1.1 Nanotechnology .....	22
1.2 Mesoporous and microporous materials .....	24
1.2.1 <i>Microporous materials</i> .....	24
1.2.2 <i>Mesoporous materials</i> .....	25
1.3 Porosity characterization.....	26
1.3.1 <i>BET theory</i> .....	27
1.3.2 <i>Thickness equation</i> .....	28
1.3.3 <i>BJH method</i> .....	29
1.3.4 <i>t-plot method</i> .....	30
1.3.5 <i>Molecular simulation methods</i> .....	31
1.3.6 <i>DFT method</i> .....	32
1.4 Surface characterization.....	33
1.4.1 <i>Basic principles</i> .....	34
1.4.2 <i>Quantification</i> .....	38
1.4.3 <i>Unwanted features</i> .....	39
1.4.4 <i>Chemical state information</i> .....	40
1.4.5 <i>Adventitious carbon</i> .....	41
1.5 Scope of the thesis .....	42
1.6 References .....	44
<b>Chapter 2 Synthesis and characterization of the silica and titania based porous materials .....</b>	<b>50</b>
2.1 Introduction.....	51
2.2 Zeolite LTL.....	55
2.2.1 <i>Synthesis and morphology control of zeolite LTL</i> .....	55

2.2.2 Disc shaped zeolite LTL .....	57
2.2.3 Barrel shaped zeolite LTL .....	59
2.2.4 Hexagonal shaped zeolite LTL .....	62
2.3 Mesoporous silica material .....	64
2.3.1 Synthesis method and theory of mesoporous silica .....	64
2.3.2 MCM-41 type mesoporous silica .....	66
2.3.3 SBA-15 type mesoporous silica .....	68
2.4 Mesoporous titania .....	71
2.4.1 Mesoporous titania particles.....	71
2.4.2 Mesoporous titania film .....	74
2.5 Mesoporous silica/titania hybrid film .....	76
2.6 Conclusion and perspectives .....	78
2.7 Experimental section .....	79
2.8 References .....	81

**Chapter 3 Functionalized mesoporous silica for the adsorption of organic dye pollutant**  
..... **84**

3.1 Introduction.....	85
3.2 Dye adsorption study over bulk powder of mesoporous silica .....	87
3.2.1 Effect of the functionalization .....	87
3.2.2 Effect of the material dosage and dye concentration .....	90
3.2.3 Effect of pH .....	93
3.2.4 Effect of the dye.....	96
3.2.4 Effect of the porosity of mesoporous silica.....	97
3.3 Dye adsorption over stationary phase of mesoporous silica materials .....	100
3.4 Dye adsorption over stationary powder of mesoporous silica materials with enhanced performance .....	103
3.5 Conclusion and perspectives .....	106
3.6 Experimental section .....	107
3.7 References .....	110

<b>Chapter 4 Highly selective artificial neurotransmitter receptors from zeolite based nanoporous materials .....</b>	<b>112</b>
4.1 Introduction.....	113
4.2 Proof of concept.....	114
4.3 Detection limit.....	120
4.4 Molecule selectivity.....	125
4.5 Sensing applications .....	128
4.5.1 <i>Ratiometric sensing</i> .....	128
4.5.2 <i>Release indicator for label-free drugs</i> .....	129
4.6 Conclusion and perspectives .....	130
4.7 Experimental section .....	131
4.8 References .....	139
<b>Chapter 5 X-Ray induced luminescent Cu(0) clusters inside porous materials .....</b>	<b>141</b>
5.1 Introduction.....	142
5.2 General approach for the synthesis of Cu(0) cluster inside porous materials .....	143
5.3 Luminescence Cu(0) clusters from Cu <sup>2+</sup> .....	146
5.4 Luminescence Cu(0) clusters from CuI .....	151
5.4 Conclusion and perspectives .....	160
5.5 Experimental section .....	162
5.6 References .....	165
<b>Chapter 6 Multi-functionalized mesoporous titania for bio-application.....</b>	<b>167</b>
6.1 Introduction.....	168
6.2 Functionalization and characterization .....	169
6.3 In vitro bio-application .....	172
6.3.1 <i>Drug delivery</i> .....	172
6.3.2 <i>ROS release under UV irradiation</i> .....	175
6.4 Conclusion and perspectives .....	179
6.5 Experimental section .....	180
6.6 References .....	182

<b>Chapter 7 Organotitania material for photocatalytic application(s)</b> .....	<b>184</b>
7.1 Introduction.....	185
7.2 Synthesis and characterization.....	188
7.2.1 <i>Ti-Ben</i> .....	188
7.2.2 <i>Ti-Thio</i> .....	194
7.3 Photocatalysis.....	199
7.3.1 <i>Photophysics properties</i> .....	199
7.3.2 <i>Photocatalysis under UV</i> .....	202
7.3.3 <i>Photocatalysis under visible light</i> .....	204
7.3.4 <i>Discussion of photocatalysis reaction</i> .....	205
7.4 Conclusion and perspectives .....	208
7.5 Experimental section .....	209
7.6 References .....	213
<b>Chapter 8 Instruments</b> .....	<b>216</b>
8.1 UV-Vis spectroscopy .....	217
8.2 Steady-state emission spectroscopy .....	218
8.3 Scanning electron microscopy (SEM) .....	219
8.4 Transmission electron microscopy (TEM) .....	220
8.5 Laser scanning confocal microscope .....	221
8.6 Dynamic light scattering (DLS).....	222
8.7 Zeta-potential .....	223
8.8 Thermogravimetric analysis (TGA) .....	224
8.9 Powder X-ray diffraction (PXRD) .....	225
8.10 References .....	227
<b>Summary</b> .....	<b>228</b>
<b>Acknowledgements</b> .....	<b>246</b>
<b>Curriculum Vitae</b> .....	<b>248</b>

# Résumé

## Introduction

En 1992, l'entreprise pétrolière Mobil a découvert une nouvelle classe de matériaux poreux composés de silice et ayant des pores uniformes, nommé M41S.<sup>1</sup> Depuis, les nanomatériaux poreux ont attiré l'intérêt de beaucoup de chercheurs en raison de leur capacité à encapsuler des molécules, leur grande surface ainsi que leur facilité de fonctionnalisation.<sup>2</sup> De nombreux autres matériaux poreux ont été développés depuis,<sup>3</sup> et certains d'entre eux, comme les zéolites, ont été utilisés dans des applications autres que la catalyse.<sup>4</sup> De nos jours, ces matériaux poreux trouvent des applications en photovoltaïque, pour des capteurs, en bio-imagerie, ou encore en libération de médicament.<sup>5,6</sup>

Dans notre groupe, des chercheurs ont développé des nanoparticules mésoporeuses de silice pour la libération de médicaments,<sup>7</sup> ainsi que des zéolites de type LTU, fonctionnalisées de différentes manières afin de transporter des médicaments et pour la thérapie génique.<sup>8</sup> De plus, de tels systèmes ont été utilisés comme des substrats pour l'adhésion de cellules.<sup>9</sup> En me basant sur les résultats précédents, le but de ma thèse est de **développer de nouveaux matériaux poreux hybrides à base de silice (SiO<sub>2</sub>) et de dioxyde de titane (TiO<sub>2</sub>), ainsi que de contrôler leur taille et leur porosité afin de les utiliser pour diverses applications.**

## Résultats et Discussions

### *Synthèse de matériaux poreux*

Un effort conséquent a été dévoué au contrôle de la morphologie et des propriétés de matériaux poreux. Ces systèmes sont décrits dans le tableau 1.



**Tableau 1** Liste des synthèses de matériaux poreux et leurs propriétés.

Matériau	Description	Taille de Pore
Zéolite LTL	Forme de disque, 1 $\mu\text{m}$ de diamètre, 200 nm d'épaisseur ou moins	0.7 nm
Zéolite LTL	Forme de tonneau, 800 nm de diamètre, 400 nm d'épaisseur	0.7 nm
Zéolite LTL	Forme Hexagonale, 2 $\mu\text{m}$ de diamètre, 5 $\mu\text{m}$ de long	0.7 nm
MCM-41	Sphère, 100 nm de diamètre	3 nm
SBA-15	Forme Hexagonale	12 nm
Particules $\text{TiO}_2$	Sphère, 400 nm de diamètre	11 nm
P123- $\text{TiO}_2$	Film	7 nm
P123- $\text{TiO}_2$ -silice	Film	8 nm

Dépendamment du matériau, chaque série de matériaux poreux a été synthétisée via différentes approches. Pour les matériaux microporeux tels que les zéolites, la cristallisation de gel dans des conditions hydrothermales a été utilisée.<sup>10</sup> Tout comme pour les matériaux mésoporeux, nous avons employé des méthodes de synthèse sol-gel ainsi que l'auto-assemblage induit par évaporation.<sup>11-13</sup> Dans tous ces cas, la modification et l'optimisation de synthèse ont été effectuées. La caractérisation de ces matériaux a été effectuée à l'aide de microscopie électronique à transmission (TEM) et à balayage (SEM). Les pores ont été étudiés avec le TEM mais également par diffusion aux rayons-X à petit angles (SAXS) et par mesure de sorption d'azote. La structure cristalline a été obtenue par diffraction aux rayons X de poudre. Un exemple de caractérisation de matériau poreux est donné en Fig. 1.

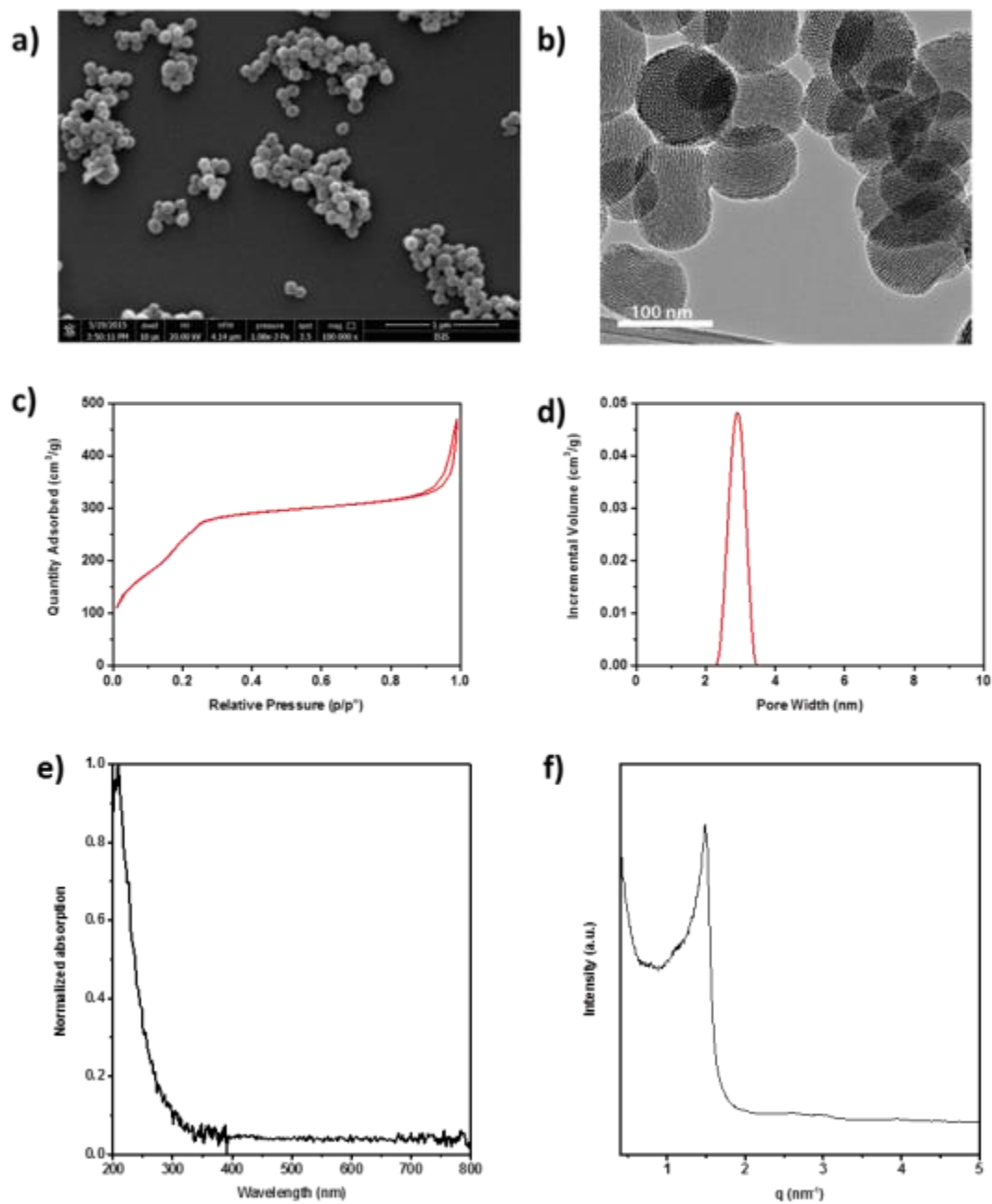


**Fig. 1** Caractérisation de matériaux poreux. a) image SEM de CTAB-silice; b) image TEM de MCM-41; c) courbe de sorption d'azote isothermale de MCM-41; d) distribution des pores de MCM-41; e) spectre UV-visible à l'état solide de MCM-41; f) diffractogramme SAXS de MCM-41.

### *Adsorption de colorants par des matériaux de silice fonctionnalisés*

Depuis des décennies, le problème lié à l'introduction des déchets dans l'environnement est mis en évidence comme une alarme à l'échelle mondiale. La nature de ces déchets s'étend des produits inorganiques aux produits organiques qui ont été utilisés pour plusieurs applications.<sup>14</sup> Parmi les polluants, les colorants représentent une classe importante de composés dangereux. Il n'est pas surprenant que le rejet d'eaux usées contenant des colorants dans les cours d'eau provenant des industries du textile, du papier, des tapis, du cuir, de la distillerie et de l'impression induise des problèmes pour la santé humaine tels que la dermatite allergique, l'irritation cutanée, le cancer et la mutation. Il en est de même pour les organismes aquatiques, ayant pour conséquence des problèmes relatifs à la nature esthétique de l'environnement.<sup>15</sup> Les déchets rejetés contenant des colorants induisent la formation de sous-produits dangereux provenant de l'oxydation, de l'hydrolyse ou d'autres réactions chimiques dans les eaux usées.<sup>16</sup> Il est important de mentionner que, comme l'indiquent Singh et al., Les eaux usées des industries textiles sont considérées comme les plus polluées parmi tous les secteurs industriels.<sup>17</sup> En effet, les industries textiles emploient un volume important d'eau et de produits chimiques pour le traitement de leurs produits. L'indice de couleur énumère plus de 8 000 produits chimiques associés au processus de teinture, y compris plusieurs variétés de colorants.<sup>14</sup> Dans la plupart des cas, l'utilisation de différentes méthodes de traitement est nécessaire pour éliminer tous les contaminants présents dans les eaux usées. Parmi ces méthodes, l'adsorption physique est l'une des méthodes les plus efficaces pour éliminer la couleur de l'eau.<sup>18</sup> Récemment, les matériaux à base de silice mésoporeuse ont fait l'objet d'une attention considérable en raison de leur structure hautement ordonnée, de pores de taille nanométrique et de leur surface importante.<sup>19, 20</sup> Lors de ces travaux, l'adsorption de colorants avec un groupe sulfonique par des silices fonctionnalisées a été étudiée (Fig. 2a, b). Les méthodes de sonication et d'agitation ayant leurs propres limites et ne pouvant pas être appliquées pour le traitement de l'eau avec une grande quantité un dispositif a été développé en utilisant une méthode de filtrage (Fig. 2c). Alors que ce dispositif puisse traiter une grande quantité d'eau, une diminution des performances a été observée en raison du temps de contact entre l'adsorbant et la solution de colorant inférieur. Pour résoudre ce problème, un système de polymère réticulé a été développé pour ajouter plus

de groupements de type amine, efficaces pour l'adsorption de colorant. En comparaison avec le filtrage simple, la capacité d'adsorption a été augmentée. Les préoccupations en matière de santé et d'environnement ayant augmentées ces dernières années,<sup>21</sup> la création de ce réseau de particules réticulé pourrait empêcher les particules de s'échapper du dispositif et de diffuser dans un environnement susceptible de créer des problèmes environnementaux.

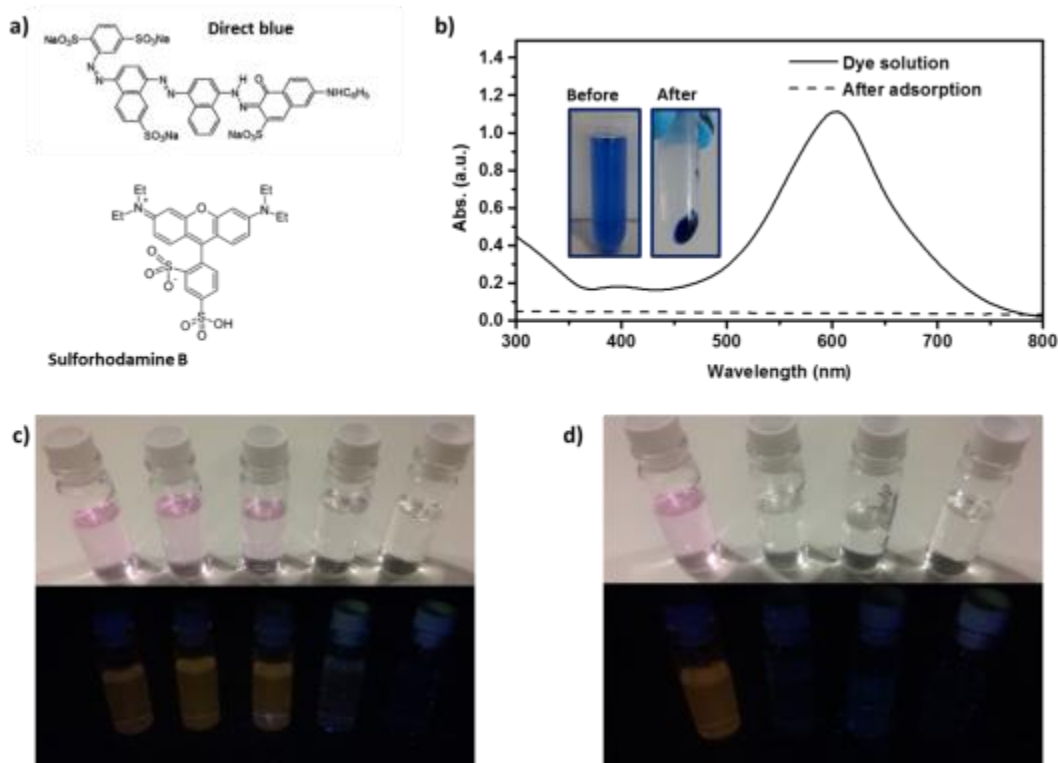


**Fig. 2** a) structures chimiques des colorants “direct blue” et “sulforhodamine” b) comparaison entre le spectre d’absorption UV-visible et les images obtenues d’une solution aqueuse de “direct blue” à  $5 \cdot 10^{-5}$  M (2 mL) en présence de MCM-41 non fonctionnalisés et fonctionnalisés par des groupements amines (12 mg) après 5 minutes de contact; c) images de solutions de “sulforhodamine B” sous lumière ambiante et lumière UV, de gauche à droite: solution initiale ( $5 \cdot 10^{-7}$  M), solution filtrée par du gel de silice 60, solution filtrée par du gel de silice 60 fonctionnalisé, solution filtrée avec des particules de SBA-15 fonctionnalisés, eau sans colorant ; d) images de solutions de “sulforhodamine B” sous lumière ambiante et lumière UV, de gauche à droite : solution initiale ( $5 \cdot 10^{-7}$  M), solution filtrée par du gel de silice 60 fonctionnalisé et réticulé,

solution filtrée par des particules de SBA-15 fonctionnalisées et réticulées, eau sans colorant.

*Matériaux nanoporeux à base de zéolites pour une détection très hautement sélective de petites biomolécules*

Malgré des décennies d'efforts concentrés, les récepteurs artificiels restent inférieurs comparés à leurs homologues naturels en ce qui concerne l'affinité et la sélectivité. Les récepteurs candidats dont la conception était destinée à optimiser les interactions récepteur-ligand (modèle dit de serrure-clé d'Emil Fischer)<sup>22</sup> permettaient, à l'exception notable des systèmes multivalents,<sup>23</sup> des affinités de liaison modérées dans l'eau, n'atteignant en aucun cas celle des récepteurs protéiques.<sup>24</sup> La découverte récente de l'importance de l'effet hydrophobe non classique dans les poches de liaison des protéines, bien protégées, et dans les cavités de l'hôte offre une autre stratégie de conception de récepteurs biomimétiques.<sup>25-28</sup> Dans ce chapitre, nous suivons cette voie et signalons plusieurs effets extrêmement sélectifs de récepteurs artificiels pour les neurotransmetteurs d'amines aromatiques, par exemple la sérotonine, la dopamine, la (nor)épinéphrine et l'histamine (Fig. 3).

Le concept (illustré sur Fig. 3a) est basé sur le piégeage de colorants chargés positivement à l'intérieur de zéolithes chargés négativement, et l'interaction avec les neurotransmetteurs, possédant également une structure chargée positivement (l'amine protonée), résultant ainsi en une extinction de l'émission du colorant. Il est important de noter que les récepteurs sont fonctionnels dans des tampons et des milieux biologiques (par exemple le sérum sanguin) et peuvent être utilisés pour étudier la dégradation des neurotransmetteurs ou leur délivrance dans des cellules vivantes en temps réel. Il est connu que les matériaux zéolitiques peuvent être chargés avec des colorants fluorescents, ce qui est étendu ici à des colorants sensibles à l'analyte indiquant ainsi la présence d'un neurotransmetteur de type amine aromatique. Nous remarquons que nos matériaux récepteurs peuvent atteindre des facteurs de sélectivité d'environ 10 000, alors qu'une différence de sélectivité supérieure à 100 est rarement observée pour la complexation de

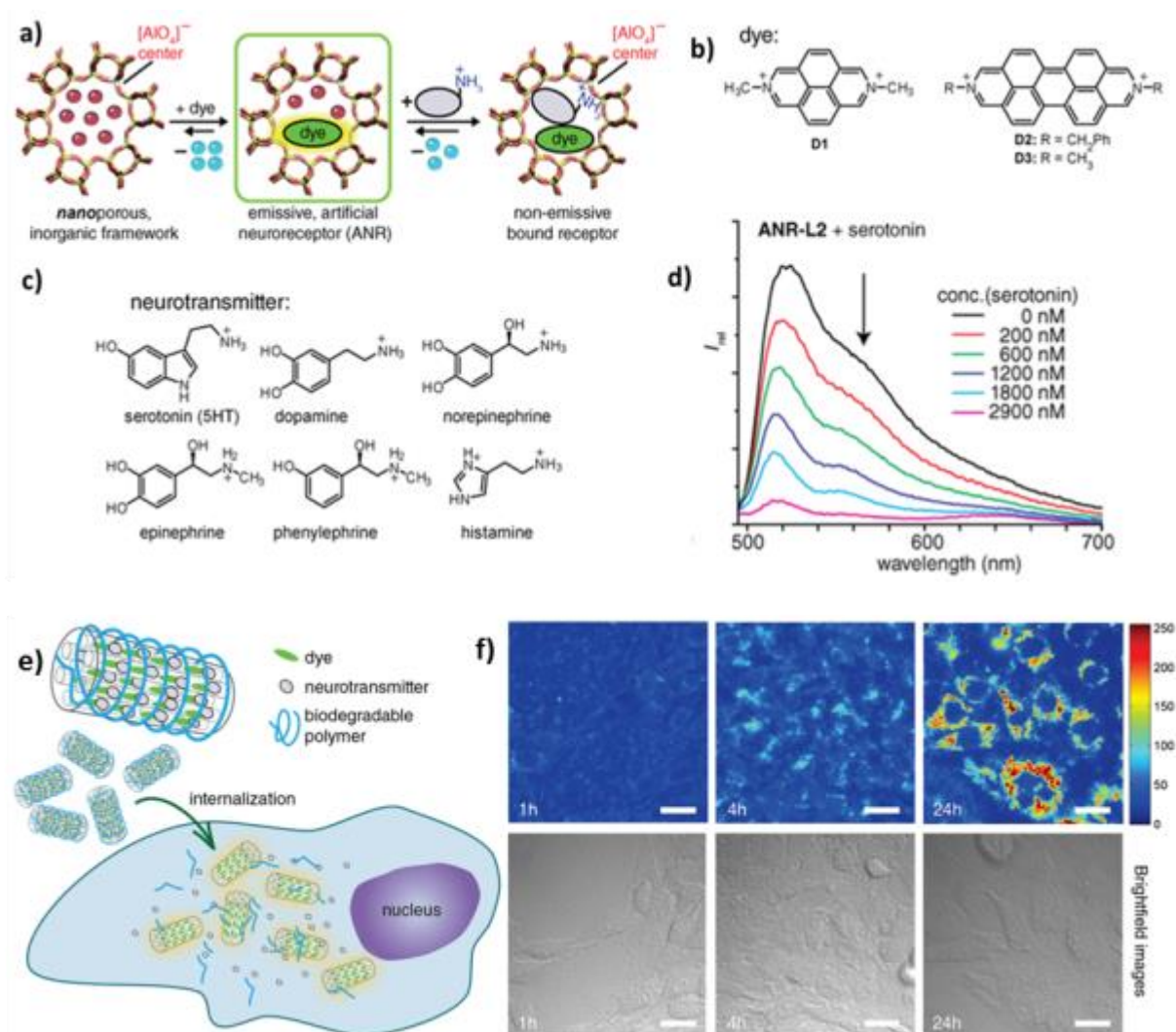


**Fig. 3** a) représentation schématique du concept pour les détecteurs de neurotransmetteurs. La fluorescence d'un colorant encapsulé dans les canaux d'une zéolite peut être éteinte après l'encapsulation d'une biomolécule. b)-c) structures chimiques de neurotransmetteurs/hormones contenant des amines aromatiques et pouvant être détectés par les ANRs, et de colorants; d) spectres d'émissions de ANR-L2 (25 µg/mL) après addition de sérotonine e) prise cellulaire des ANRs chargés par des médicaments et couverts à la surface, résultant après relargage du médicament d'une augmentation de l'intensité d'émission de l'ANR. f) Micrographes confocales à intensité codée montrant une prise cellulaire de l'ARN chargé par la sérotonine et couverts à la surface par des polylysines à différents temps d'incubation : 1h (gauche), 4h (centre) et 24h (droite), et leurs images à champ clair correspondantes.  $\lambda_{exc} = 405 \text{ nm}$ , échelle= 20 µm.

molécules organiques par d'autres hôtes artificiels dans l'eau.<sup>29, 30</sup>

Plusieurs applications ont été développées sur cette base de neurotransmetteurs artificiels. Des matériaux poreux capables de stocker des gaz<sup>31</sup> ou de relarguer des médicaments<sup>32</sup> ont trouvé de larges gammes d'applications industrielles et médicales, mais l'émergence de stratégies de suivi pour des processus de chargement et déchargement de cargaison est relativement récente.<sup>33, 34</sup> Souvent, des analogues de médicament marqués par un fluorophore<sup>35</sup> ont été employés pour étudier la cinétique de relargage du dit médicament. Cependant, les médicaments marqués présentent inévitablement un profil biologique modifié par rapport au médicament parent. L'utilisation de matériaux poreux avec un transducteur intégré émettant un signal fluorescent, est une donc alternative prometteuse, permettant de surveiller le chargement et le relargage de produits sans marquage. Nous avons chargé de l'ANR-L1 (« Artificial neurotransmitter receptor » avec des zéolites L et le colorant 1) avec de la sérotonine (non émissive) et recouvert d'une couche de polylysine attirant les cellules (Fig. 3e). Ce transporteur de médicament a été facilement pris en charge par des cellules vivantes de gliome C6 de *Rattus norvegicus*. Ensuite, la libération intracellulaire de la sérotonine s'est déroulée au cours de 24 heures, comme on peut le déduire du rétablissement progressif de l'émission de l'ANR (Fig. 3f).

#### *Formation de clusters luminescents de Cu (0) dans des matériaux poreux induits par irradiation aux rayons X*

En tirant profit de la différente taille de pores, les clusters de Cu (0) ont été synthétisés avec succès sous exposition de rayons X. Les clusters métalliques sont largement utilisés dans des applications en catalyse, bio-imagerie, et optique.<sup>36, 37</sup> En comparaison avec les clusters de métaux nobles, bien étudiés, le cuivre pourrait être une bonne alternative dans différentes applications, car il n'est pas onéreux et est relativement écologique. Au cours des dernières années, seuls quelques articles ont rapporté la synthèse réussie de clusters luminescents de Cu (0).<sup>38, 39</sup> Le principal problème est que comparé à l'or ou l'argent, le cuivre est relativement facile à oxyder, entraînant la perte de ses propriétés optiques. C'est pourquoi la plupart de la synthèse rapportée a été réalisée en solution et les clusters

ont dû être protégés par des surfactants ou des ligands.<sup>38, 40</sup> Comparé à la réduction par d'autres agents réducteurs, la réduction photo-assistée présente l'avantage d'avoir un certain contrôle de la position de réduction et de purification, ce qui est très approprié pour la formation de clusters dans un espace confiné. A. Katrib a découvert dans les années 1980 que, par exposition aux rayons X, le Pt (IV) peut être réduit en Pt (II).<sup>41</sup> Depuis, plusieurs recherches ont montré la possibilité de réduction du platine, de l'or ou de l'argent sous irradiation aux rayons X.<sup>42</sup> En 2014, le groupe de recherche de J. Hofkens a développé la méthode de formation de clusters d'argent à l'intérieur de zéolites par cette méthode.<sup>43</sup> L'avantage de l'utilisation des rayons X est que la réduction peut être contrôlée *in situ*, ce qui n'est pas possible en utilisant l'hydrogène ou un autre agent réducteur chimique. En modulant la taille et la forme de la source de rayons X, différents motifs de l'espèce réduite peuvent être créés. Dans notre cas, nous utilisons la méthode de réduction induite par les photons (rayons X) pour réduire les espèces de Cu (I) chargées en clusters de Cu (0) à l'intérieur de nos matériaux poreux (zéolite et silice) (Fig. 4a).

Les clusters ont été protégés par leur encapsulation et restent stables dans l'air pendant plusieurs mois. Les échantillons ont été caractérisés en tant que matériaux et pour leurs propriétés spectroscopiques. Par microscope à fluorescence, on observe que les parties ayant été exposées aux rayons X sont émissives, ce qui n'est pas le cas des parties non exposées (Fig. 4b). Selon des analyses en XPS, le cuivre obtenu est de type Cu (0). La très courte durée de vie (nano secondes) de l'état excité suggère que le cuivre a une forme de cluster. L'émission du cluster de Cu (0) en fonction de la taille des pores a été étudiée. Il est clair qu'avec une plus grande taille des pores, l'émission de longueur d'onde supérieure à 400 nm augmente (Fig. 4c). Nous avons donc développé avec succès une méthode pour former des clusters de Cu (0) *in situ* en utilisant les rayons X. Les applications potentielles telles que la catalyse ou la création d'un dispositif optique pourrait être possible via nos clusters de Cu (0).



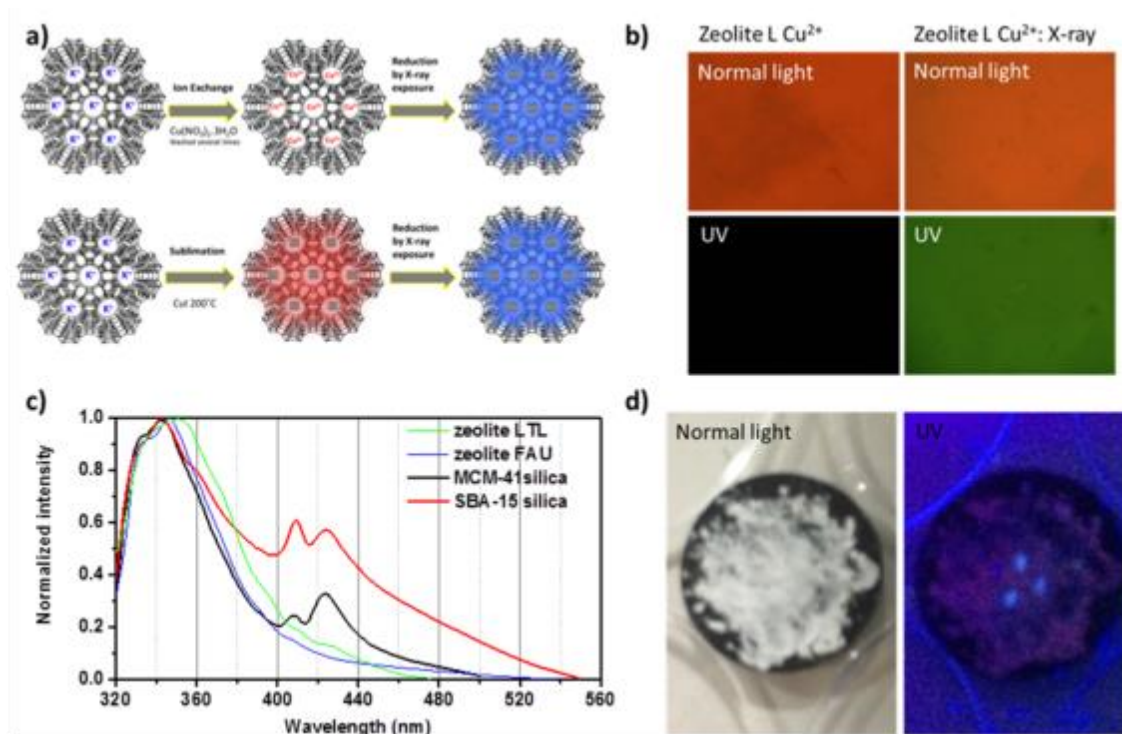


**Fig. 4** a) Approche synthétique des clusters de Cu (0) par échange ionique et insertion de CuI; b) images au microscope à fluorescence d'échantillons avant et après exposition aux rayons X; c) spectres d'émission (excitation: 270 nm) de clusters de Cu (0) dans différents matériaux poreux; d) clusters de Cu (0) obtenus par exposition aux rayons X à partir de CuI à l'intérieur des zéolites sous lumière ambiante et sous irradiation UV (bleu brillant: clusters de Cu (0); rouge: clusters de CuI non réduits).

#### *Titane mésoporeux pour des applications biologiques.*

Il est connu que la silice a été utilisée comme agent de libération de drogue.<sup>44</sup> Néanmoins, l'utilisation de TiO<sub>2</sub> dans de telles applications est largement moins étudiée. Par exemple, les matériaux hybrides poreux à base de TiO<sub>2</sub> ont été testés pour la libération de médicaments. En raison de sa biocompatibilité, sa facilité à être fonctionnalisé et ses propriétés photo-actives, le TiO<sub>2</sub> pourrait être un candidat idéal pour des applications biologiques.<sup>45, 46</sup> Les nanoparticules de TiO<sub>2</sub> n'étant pas émissives, la fluorescence sera encapsulée dans les pores afin de servir comme marqueur optique mais aussi pour mimer l'encapsulation de médicaments que l'on pourra suivre à la trace. Afin de parvenir à cela,

des nanoparticules mésoporeuses de  $\text{TiO}_2$  de 400 nm de diamètre, avec des pores de 11 nm ainsi qu'une surface fonctionnalisée ont été utilisés.

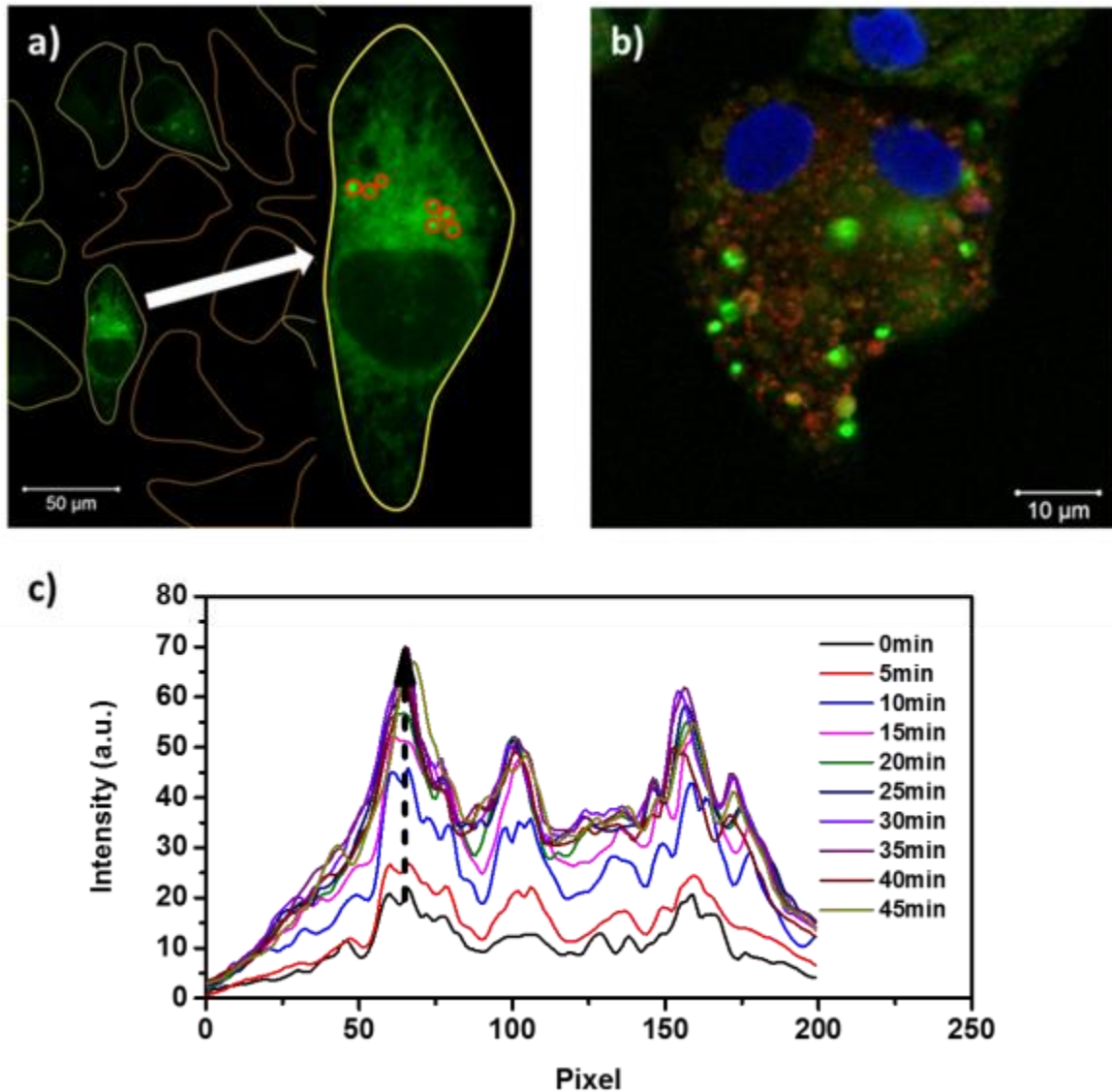


**Fig. 5** Expérience *in vitro* de nanoparticules mésoporeuses de  $\text{TiO}_2$  a) internalisation dans les cellules et libération de fluorescence ; b) les cellules contenant les nanoparticules de  $\text{TiO}_2$  sont tuées après irradiation UV (vert : fluorescence, bleu : DAPI, rouge : cell-ROX) ; c) intensité de fluorescence du luminophore cell-ROX sous irradiation UV, indiquant la cinétique de libération des molécules.

Nous avons fonctionnalisé la surface des nanoparticules à l'aide d'acides aminés afin d'avoir une meilleure biocompatibilité. Les nanoparticules mésoporeuses de  $\text{TiO}_2$  ont été décorées avec de l'alanine, en attachant des groupements  $-\text{COOH}$  à la surface des particules, et en couplant ces derniers avec des groupements libres  $-\text{NH}_2$  de l'alanine de la fluorescéine isocyanate. Enfin, nous avons couvert le tout avec de la polylysine afin de protéger le matériau et d'augmenter la charge positive de la surface pour faciliter l'internalisation des particules dans la cellule. À l'aide d'expériences *in vitro*, nous avons confirmé l'internalisation des nanoparticules mésoporeuses de  $\text{TiO}_2$  dans les cellules en observant l'émission de la fluorescéine attachée covalentement aux particules. Parmi toutes les cellules, la fluorescéine n'a été trouvée que dans les cellules qui contenaient des nanoparticules (Fig. 5a), cela suggérant que la libération de fluorescéine a été effectuée après l'internalisation des particules. Des études de microscopie confocale par co-localisation ont montré que ces particules n'ont pas d'affinité particulière pour un organe spécifique.

Les nanoparticules mésoporeuses de  $\text{TiO}_2$  sont connues pour leurs propriétés de libération d'espèces réactives oxydantes (ROS) par irradiation UV.<sup>47</sup> La particule elle-même possède donc la capacité d'agir comme un agent pathogène. Afin d'étudier la cinétique de relargage de ROS sous lumière UV, un pigment couramment utilisé appelé cell-ROX, a été employé. Le cell-ROX n'est pas émissif en temps normal mais une émission dans la région du rouge peut être détectée après oxydation. Les détails cinétiques du relargage de ROS par l'étude de l'intensité d'émission du cell-ROX sont montrés dans la Fig. 5c.

#### *Matériaux de type organotitane pour des applications en photocatalyse*

Un grand défi dans la modification du dioxyde de titane est la possibilité de modifier la bande interdite (band gap) en introduisant des groupements chimiques dans la structure du  $\text{TiO}_2$ . En raison de la réactivité différente du  $\text{TiO}_2$  par rapport à la silice, la procédure normale décrite pour la silice hybride ne peut pas être appliquée pour le  $\text{TiO}_2$ . Par conséquent, nous avons développé une stratégie pour la synthèse d'un complexe organotitane ayant une liaison Ti-C covalente en utilisant des molécules organiques

comme agents de liaison (linkers). En tant que matériaux très prometteur, le dioxyde de titane est principalement utilisé pour des applications photochimiques telles que les cellules solaires à colorants photosensibles et comme un photocatalyseur, en raison de son excellente fonctionnalité, sa stabilité à long terme, et sa non-toxicité<sup>48, 49</sup> Afin d'améliorer la photoactivité du TiO<sub>2</sub> et d'étendre sa limite d'absorption dans la région de la lumière visible, le dopage par divers cations métalliques de transition a été intensivement étudié<sup>50, 51</sup> Toutefois, en raison de l'instabilité thermique du matériau dopé la photoactivité du TiO<sub>2</sub> à dopage cationique se trouve diminuée, même dans la région UV.<sup>52</sup> C'est pourquoi les nanomatériaux organotitane hybrides sont censés être plus efficaces en raison de la combinaison des parties organiques-inorganiques par des liaisons covalentes.

En utilisant des organolithiens réactifs synthésés des matériaux à base de liaisons Ti-C ont été synthésés. Les agents de liaison utilisés étaient le benzène et le thiophène (Fig. 6a). Les produits ont été caractérisés par différentes méthodes. Grâce à la spectroscopie de photoélectrons induite par rayons X, XPS, nous pouvons voir clairement la différence entre le TiO<sub>2</sub> et l'organotitane. En effet, concernant l'élément titane, nous remarquons une différence d'énergie de liaison de Ti-C, comparée à Ti-O (Fig. 6c). De plus, l'élément carbone de la liaison C-Ti aromatique a été identifié (Fig. 6b). Par spectroscopie UV-Visible, nous pouvons transformer les spectres en courbe de Tauc,<sup>53</sup> et la bande interdite a été déterminée. Le Ti-benzène et le Ti-thiophène ont une bande interdite respectivement de 2.43 et 2.05 eV, ce qui est plus faible que le TiO<sub>2</sub> pur qui est de 3,03 eV (Fig. 6d). De plus, le monomère de l'organotitane que nous avons obtenu peut-être polymérisé et un réseau à base de dioxyde de titane hybride avec des agents de liaison de type benzène ou thiophène peut être formé

Les propriétés photocatalytiques de des matériaux Ti-benzène et Ti-thiophène ont été étudiés, et des mélanges matériaux hybrides (masse fixée et constante) /rhodamine B en solution (concentration fixée et constante) ont été exposés à de la lumière UV ou visible. Comme attendu, sous irradiation UV, le matériau de dioxyde de titane non-hybride a montré les meilleures performances photocatalytiques. (Fig. 6e). Mais sous irradiation à

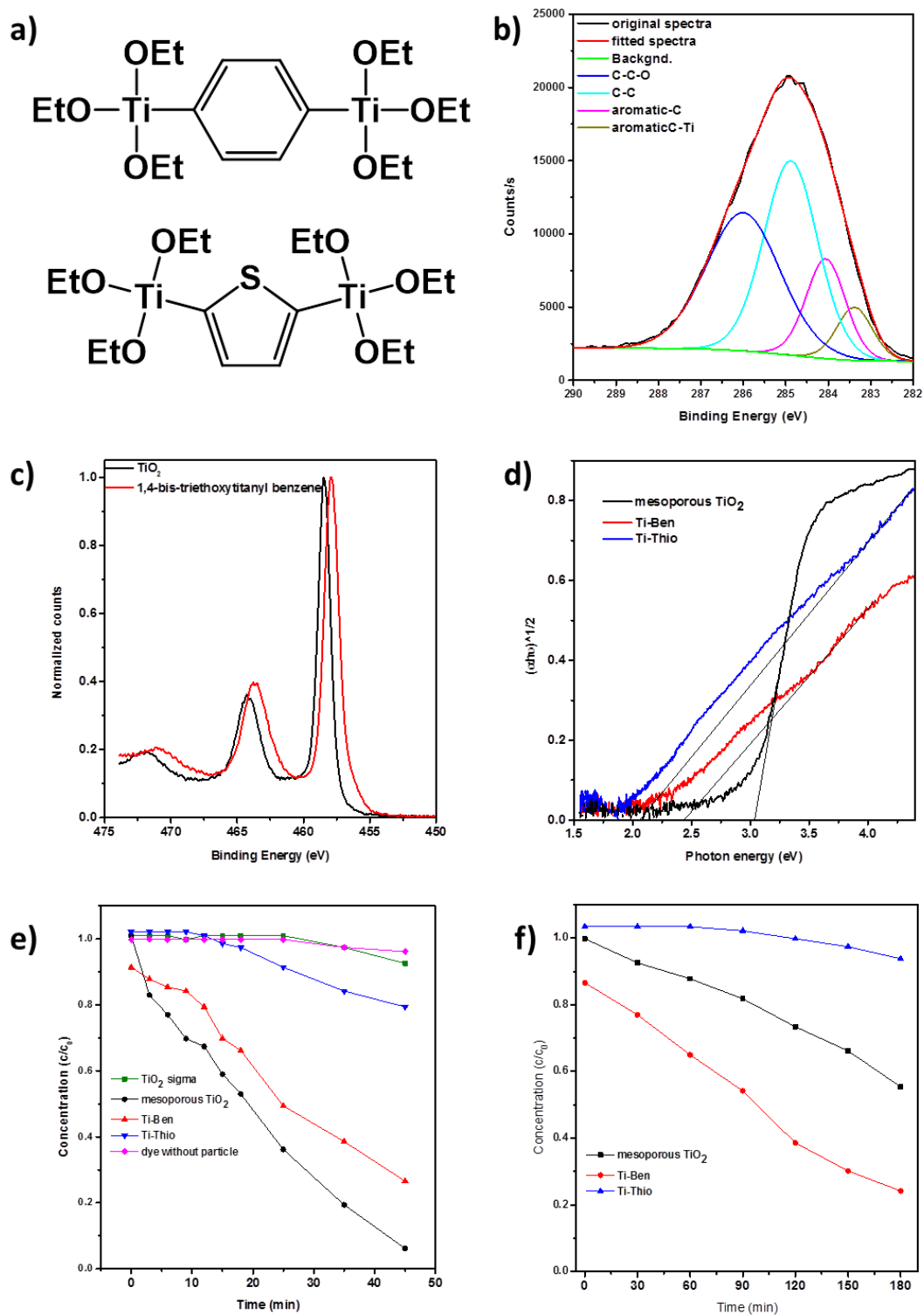


**Fig. 6** a) Structure de 1,4-bis-triethoxytitanyl benzene and 2,5-bis-triethoxytitanyl thiophene; b) déconvolution du spectre de l'élément de carbone de Ti-thiophène; c)

spectre XPS de l'élément Ti; d) spectre UV-Vis du pure TiO<sub>2</sub> et des organotitane. e) réaction photocatalytique de la dégradation de la rhodamine B par les matériaux de dioxyde de titane sous irradiation UV ; f) réaction photocatalytique de la dégradation de la rhodamine B par les matériaux de dioxyde de titane sous irradiation à lumière visible.

lumière visible, notre Ti-benzène a montré la meilleure performance photocatalytique en raison de sa bande interdite inférieure par rapport au matériau de titane inorganique (Fig. 6f). D'autres applications basées sur la photoactivité sous lumière visible pourraient être développées en se basant notre découverte.

## **Conclusion**

Pour conclure, mon doctorat se focalise sur la synthèse, la caractérisation et les applications de matériaux poreux à base de silice, dioxyde de titane et zéolite.

La silice poreuse, le dioxyde de titane et les zéolites ont été synthétisés en utilisant des méthodologies différentes. Des matériaux de silice fonctionnalisés ont été utilisés pour des applications en adsorption de colorant, ce qui est utile pour le traitement de l'eau. Un nouveau système réticulé et un nouveau dispositif ont été créés pour améliorer la capacité d'adsorption et pour le traitement d'une grande quantité d'eau. En tirant parti des pores, une nouvelle méthode de formation de clusters de Cu (0) a été établie. Les propriétés photophysiques ont été étudiées, en utilisant plusieurs sources de cuivre et différents matériaux poreux. L'utilisation du confinement pour la détection de petites molécules biologiques tels que les neurotransmetteurs a été démontrée. Plusieurs applications ont été développées sur la base de ces récepteurs de neurotransmetteurs artificiels. Un matériau de titane mésoporeux multifonctionnel a été utilisé pour les applications en biologie. En comparaison avec la silice, plus couramment utilisée, sa photoactivité pourrait apporter des avantages supplémentaires. Finalement, de nouveaux types de matériaux de type organotitane hybrides ont été développés, et leurs propriétés photo-

catalytiques ont été démontrées. Durant cette période, de profondes connaissances et compétences sur les instruments de caractérisation ont également été acquis.

## References

1. C. T. Kresge, M. E. Leonowicz, W. J. Roth, J. C. Vartuli and J. S. Beck, *Nature*, 1992, **359**, 710-712.
2. C. T. Kresge and W. J. Roth, *Chem. Soc. Rev.*, 2013, **42**, 3663-3670.
3. L. Han and S. Che, *Chem. Soc. Rev.*, 2013, **42**, 3740-3752.
4. I. I. Ivanova and E. E. Knyazeva, *Chem. Soc. Rev.*, 2013, **42**, 3671-3688.
5. R. Zhang, A. A. Elzatahry, S. S. Al-Deyab and D. Zhao, *Nano Today*, 2012, **7**, 344-366.
6. P. Innocenzi and L. Malfatti, *Chem. Soc. Rev.*, 2013, **42**, 4198-4216.
7. A. Bertucci, E. A. Prasetyanto, D. Septiadi, A. Manicardi, E. Brognara, R. Gambari, R. Corradini and L. De Cola, *Small*, 2015, **11**, 5687-5695.
8. H. Lülfi, A. Bertucci, D. Septiadi, R. Corradini and L. De Cola, *Chem. Eur. J.*, 2014, **20**, 10900-10904.
9. N. S. Kehr, B. Ergün, H. Lülfi and L. De Cola, *Adv. Mater.*, 2014, **26**, 3248-3252.
10. Z. A. Ruiz, D. Brühwiler, T. Ban and G. Calzaferri, *Monatsh. Chem.*, 2005, **136**, 77-89.
11. Q. Cai, Z.-S. Luo, W.-Q. Pang, Y.-W. Fan, X.-H. Chen and F.-Z. Cui, *Chem. Mater.*, 2001, **13**, 258-263.
12. W. Dong, Y. Sun, C. W. Lee, W. Hua, X. Lu, Y. Shi, S. Zhang, J. Chen and D. Zhao, *J. Am. Chem. Soc.*, 2007, **129**, 13894-13904.
13. D. Chen, L. Cao, F. Huang, P. Imperia, Y.-B. Cheng and R. A. Caruso, *J. Am. Chem. Soc.*, 2010, **132**, 4438-4444.
14. S. P. Buthelezi, A. O. Olaniran and B. Pillay, *Molecules*, 2012, **17**, 14260-14274.
15. M. Anbia and S. Salehi, *Dyes Pigm.*, 2012, **94**, 1-9.
16. C.-H. Huang, K.-P. Chang, H.-D. Ou, Y.-C. Chiang and C.-F. Wang, *Microporous Mesoporous Mater.*, 2011, **141**, 102-109.
17. K. P. Singh, D. Mohan, S. Sinha, G. Tondon and D. Gosh, *Ind. Eng. Chem. Res.*, 2003, **42**, 1965-1976.
18. S. Sivamani and B. Leena Grace, *IJBST*, 2009, **2**, 47-51.
19. A. R. Nesic, M. J. Kokunesoski, T. D. Volkov-Husovic and S. J. Velickovic, *Environ. Monit. Assess.*, 2016, **188**, 1-12.
20. K. Y. Ho, G. McKay and K. L. Yeung, *Langmuir*, 2003, **19**, 3019-3024.



21. M. Hassellöv, J. W. Readman, J. F. Ranville and K. Tiede, *Ecotoxicology*, 2008, **17**, 344-361.
22. E. Fischer, *Berichte der deutschen chemischen Gesellschaft*, 1894, **27**, 2985-2993.
23. J. Rao, J. Lahiri, L. Isaacs, R. M. Weis and G. M. Whitesides, *Science*, 1998, **280**, 708-711.
24. H.-J. Schneider, P. Agrawal and A. K. Yatsimirsky, *Chem. Soc. Rev.*, 2013, **42**, 6777-6800.
25. P. Snyder, M. Lockett, D. Moustakas and G. Whitesides, *Eur. Phys. J. Spec. Top.*, 2014, **223**, 853-891.
26. E. Persch, O. Dumele and F. Diederich, *Angew. Chem. Int. Ed.*, 2015, **54**, 3290-3327.
27. D. Chandler, *Nature*, 2005, **437**, 640-647.
28. F. Biedermann, W. M. Nau and H.-J. Schneider, *Angew. Chem. Int. Ed.*, 2014, **53**, 11158-11171.
29. H.-J. Schneider, *Angew. Chem. Int. Ed.*, 2009, **48**, 3924-3977.
30. D. A. Dougherty, *Acc. Chem. Res.*, 2012, **46**, 885-893.
31. R. E. Morris and P. S. Wheatley, *Angew. Chem. Int. Ed.*, 2008, **47**, 4966-4981.
32. M. Vallet-Regí, F. Balas and D. Arcos, *Angew. Chem. Int. Ed.*, 2007, **46**, 7548-7558.
33. J. Kärger, T. Binder, C. Chmelik, F. Hibbe, H. Krautscheid, R. Krishna and J. Weitkamp, *Nat Mater*, 2014, **13**, 333-343.
34. N. Yanai, K. Kitayama, Y. Hijikata, H. Sato, R. Matsuda, Y. Kubota, M. Takata, M. Mizuno, T. Uemura and S. Kitagawa, *Nat Mater*, 2011, **10**, 787-793.
35. N. G. Gubernator, H. Zhang, R. G. W. Staal, E. V. Mosharov, D. B. Pereira, M. Yue, V. Balsanek, P. A. Vadola, B. Mukherjee, R. H. Edwards, D. Sulzer and D. Sames, *Science*, 2009, **324**, 1441-1444.
36. E. C. Tyo and S. Vajda, *Nat Nano*, 2015, **10**, 577-588.
37. Y. Lu and W. Chen, *Chem. Soc. Rev.*, 2012, **41**, 3594-3623.
38. W. Wei, Y. Lu, W. Chen and S. Chen, *J. Am. Chem. Soc.*, 2011, **133**, 2060-2063.
39. C. Vázquez-Vázquez, M. Bañobre-López, A. Mitra, M. A. López-Quintela and J. Rivas, *Langmuir*, 2009, **25**, 8208-8216.
40. C. Wang, Y. Yao and Q. Song, *Colloids Surf., B*, 2016, **140**, 373-381.
41. A. Katrib, *J. Electron. Spectrosc. Relat. Phenom.*, 1980, **18**, 275-278.
42. M. Fujiwara, H. Fujii, K. Tainaka, T. Matsushita and S. Ikeda, *Analytical Sciences/Supplements*, 2002, **17icas**, i1065-i1067.

43. E. Coutino-Gonzalez, D. Grandjean, M. Roeffaers, K. Kvashnina, E. Fron, B. Dieu, G. De Cremer, P. Lievens, B. Sels and J. Hofkens, *Chem. Commun.*, 2014, **50**, 1350-1352.
44. I. I. Slowing, B. G. Trewyn, S. Giri and V. S. Y. Lin, *Adv. Funct. Mater.*, 2007, **17**, 1225-1236.
45. K. C. W. Wu, Y. Yamauchi, C.-Y. Hong, Y.-H. Yang, Y.-H. Liang, T. Funatsu and M. Tsunoda, *Chem. Commun.*, 2011, **47**, 5232-5234.
46. Z. Fei Yin, L. Wu, H. Gui Yang and Y. Hua Su, *PCCP*, 2013, **15**, 4844-4858.
47. R. Konaka, E. Kasahara, W. C. Dunlap, Y. Yamamoto, K. C. Chien and M. Inoue, *Free Radical Biol. Med.*, 1999, **27**, 294-300.
48. A. Fujishima, T. N. Rao and D. A. Tryk, *J. Photochem. Photobiol. C.*, 2000, **1**, 1-21.
49. A. Hagfeldt and M. Graetzel, *Chem. Rev.*, 1995, **95**, 49-68.
50. H. Yamashita, Y. Ichihashi, M. Takeuchi, S. Kishiguchi and M. Anpo, *J. Synchrotron Radiat.*, 1999, **6**, 451-452.
51. J.-M. Herrmann, J. Disdier and P. Pichat, *Chem. Phys. Lett.*, 1984, **108**, 618-622.
52. T. Umebayashi, T. Yamaki, H. Itoh and K. Asai, *Appl. Phys. Lett.*, 2002, **81**, 454-456.
53. J. Tauc, *Mater. Res. Bull.*, 1968, **3**, 37-46.



# **Chapter 1**

## **Introduction**

### *Abstract*

As stated in the title, in my thesis I will discuss from the synthesis to application of the titania and silica based hybrid porous nanomaterials. In this first chapter of my thesis, I would like to first introduce briefly about the nanoscience and nanotechnology. Then series of porous materials will be introduced. The porosity and surface characterization which are critical for porous materials will be introduced. And finally there will be the scope of this thesis.

## 1.1 Nanotechnology

Nanotechnology which means the technology to manipulate nanometer sized (normally less than 100 nm) objects was firstly described as a concept in the year 1970s.<sup>1</sup> Since then, it has become one of the fastest developed technologies which applied into physics, chemistry and biology field.<sup>2-7</sup> Nanomaterials are the materials which have the size in the same division. Due to the small size, nanomaterials have its exceptional electrical, optical, magnetic, mechanical etc. properties.<sup>8-10</sup>

A lot of nanostructures already exist in nature. Just list few of them: the hydrophobic lotus leaf, the "spatulae" on the bottom of gecko feet and some butterfly wing scales. These nanostructures give the unique property such as the self-cleaning ability of the lotus leaf. For the artificial nanomaterials, in fact, human beings have used nanomaterials without noticing in ancient time. A famous example would be the Lycurgus cup from 4<sup>th</sup> century which made from glass contains gold and silver nanoparticles (Fig. 1.1a). The boost of nanotechnology started in the 1980s with the invention of scanning tunneling microscope (STM).<sup>11</sup> It provides the essential technique to do researches in the nanoscale. Later on, the discovery of fullerenes (Fig. 1.1b) and carbon nanotubes brought the promising applications in the field of nanoelectronics.<sup>2, 12</sup> In the meanwhile, due to their unique optical and electrical properties, nanoparticles also attracted a lot of research interest in the field such as catalysis, biomedical application and optical devices.<sup>13-16</sup> According to Scifinder, there were more than 200000 papers which contain the concept of nanotechnology published in the year 2015. Without any doubt, nanotechnology is a promising field.

To create nanomaterials, there are two general fabrication approaches: bottom up and top down. From the bottom up approach, small components are used to build bigger complex systems. More precisely, several different techniques have been used in this approach. The first technique we can easily think about is the traditional organic and inorganic synthesis. In fact, the Nobel Prize in chemistry 2016 has been awarded to Jean-Pierre Sauvage, Sir J. Fraser Stoddart and Bernard L. Feringa "for the design and synthesis of

molecular machines".<sup>17</sup> They have developed several molecular machines via organic synthesis.<sup>18-20</sup> Self-assembly of molecules is another widely used technique in the bottom up approach.<sup>21-23</sup> The driving forces for the molecular self-assembly are typically weak interactions such as van der Waals force,  $\pi$ - $\pi$  interaction, hydrogen bonds etc. which differs from the covalent or ionic bonds.<sup>24-26</sup> Another well-known technique for bottom up approach would be using the microscopic method to manipulate single molecules.<sup>27</sup> From the top down approach, large objects are used to fabricate smaller structures. The most common technique is lithography which is widely used in the semiconductor industry.<sup>28, 29</sup> Without this, we will never have powerful smart phones in our everyday life.

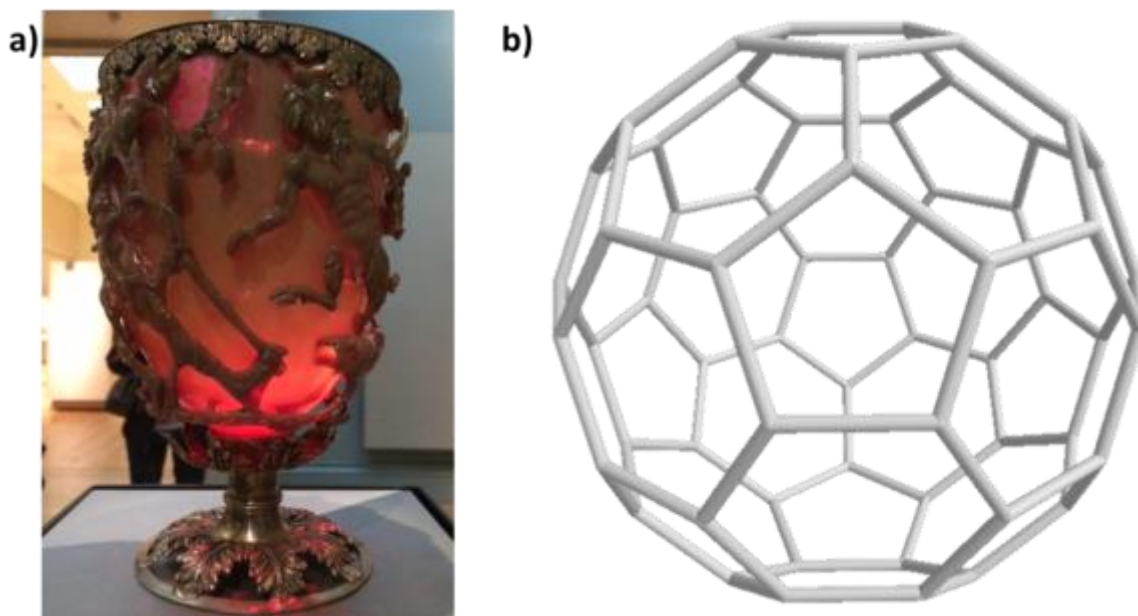


**Fig. 1.1** a) Lycurgus cup; b) structure of C<sub>60</sub>.

Due to the small size, it is more complicated to characterize nanomaterials and nanostructures. In the beginning of the nanotechnology development, STM and atomic force microscope (AFM) was invented in the 1980s.<sup>3, 11</sup> In fact, earlier techniques such as scanning electron microscope (SEM) and transmission electron microscope (TEM) can also be used for the characterization.<sup>30, 31</sup> For the characterization of electrical and optical properties, techniques such as optical spectroscopy and fluorometer can be used. Molecular characterization method such as nuclear magnetic resonance spectroscopy and

mass spectroscopy which widely used in the organic chemistry field can be also used for nanoscale objects such as structures and quantum dots.<sup>32, 33</sup>

However, since the beginning of the 21<sup>st</sup> century, there are more and more concerns about the nanotechnology, especially for the toxicity and the impact to the environment.<sup>34-36</sup> In vivo study on mice showed that the exposure of carbon nanotubes could result in pathogenic behavior.<sup>37</sup> The transformation of the nanomaterials in both environmental and biological systems has been studied.<sup>38</sup> All these studies remind us that even through this is a promising field, certain concerns and regulations should still be applied during the research.

## **1.2 Mesoporous and microporous materials**

Porous material is the material that contains pores. As we are discussing in the nanoscale, mesoporous materials and microporous materials are the main candidates in our research. According to the international union of pure and applied chemistry (IUPAC), the pore size of mesoporous material is between 2-50 nm and the pore size of the microporous material is between 0.2-2 nm.<sup>39</sup> Herein, we are going to introduce both of these two categories of porous materials.

### *1.2.1 Microporous materials*

Three major types of microporous materials have been intensively investigated through the years: microporous carbon, zeolites and metal-organic frameworks (MOFs).<sup>40, 41</sup>

With its microporosity, high surface area and high degree of surface reactivity, activated carbon has been widely used for adsorption of dyes, heavy metal ions, toxic gas etc.<sup>42-44</sup> The surface area of activated carbon could reach as high as 3000 m<sup>2</sup>/g.<sup>45</sup> Although the adsorption property of activated carbon was well-investigated and we have already used it widely in our daily life (such as the smell adsorption material in the refrigerator),<sup>42</sup> people are still trying to find new applications for this material. Pure and metal doped

activated carbon can be used in catalysis applications.<sup>46, 47</sup> In recent years, as global warming has become a problem around the world, researcher have explored the possibility of carbon dioxide capture using activated carbon.<sup>48</sup> Also, application such as the hydrogen storage by activated carbon has been investigated.<sup>49</sup> Graphite, carbon black and carbon nanotubes are another type of microporous carbon which their pore is more slit-like.<sup>40, 50, 51</sup> Single and multilayer graphene which have unique electrical properties attracted the research interests in the past decade.<sup>52</sup> A more recent example, modular graphene-based 3D covalent networks with slit micropores in between layers of graphene sheets have been developed for energy applications such as supercapacitors.<sup>53</sup>

Zeolites are aluminosilicate minerals with microporosity. They exist in nature and have been discovered by people in the 18<sup>th</sup> century.<sup>54</sup> Up to now, more than 200 different types of zeolite framework have been identified, and the porosity of zeolites is due to the unique arrangement of the crystal structures.<sup>41</sup> Thus, zeolites are widely used as adsorbents such as molecular sieves we use in almost every chemistry lab, and catalysts that widely used in oil industry.<sup>55-57</sup> Artificial zeolite synthesis was first attempted in the 1960s.<sup>58</sup> Afterwards, a lot of artificial zeolites have been synthesized and used based on different needs.<sup>59, 60</sup> More recently, researchers are trying to synthesize special designed zeolite framework for certain catalysis applications.<sup>61</sup>

MOFs are another typical microporous material which is relatively new if compared with carbons and zeolites. It was first reported by Yaghi et al.<sup>62</sup> Since then, a lot of research has been applied on MOFs.<sup>63, 64</sup> The straightforward synthesis, nanoscale process ability, predictable structures, network geometry, possibility of post-synthetic modification, and relatively tunable porosity makes it interesting for many fields of researches.<sup>65</sup> The applications of MOFs are including the fields such as catalysis,<sup>66</sup> sensing,<sup>67</sup> gas storage,<sup>68</sup> medicine<sup>69</sup> and optics.<sup>70</sup>

### *1.2.2 Mesoporous materials*

Several patents of mesoporous silica have been recorded around 1970,<sup>71, 72</sup> based on the Stöber process developed from 1968.<sup>73</sup> The commonly used mesoporous silica synthesis



based on surfactant formed liquid crystal template was reported in 1992.<sup>74</sup> Since then, more types of mesoporous silica materials have been developed using the same principle.<sup>75,76</sup> This synthetic method is not only applicable to mesoporous silica synthesis, but also to other oxides such as titanium oxide,<sup>77</sup> tin oxide<sup>78</sup> and zirconium oxide.<sup>79</sup> Due to the unique properties of each oxide, these mesoporous materials have been used in catalysis, photovoltaics, biomedical application etc.<sup>80-82</sup> It is worthy to mention here that since the residual of nanoparticles remains in the cells after drug-delivery could bring potential health problems, breakable mesoporous silica which is bio-degradable was recently developed in Prof. De Cola's group.<sup>83</sup> As discussed from the risks of the nanotechnology and the toxicity of nanomaterials, this type of research would be helpful to solve the problem.

### **1.3 Porosity characterization**

Since we synthesize porous materials and use them for various applications, the pore characterization is a critical point in our research. According to IUPAC, the pores are classified into three categories based on their size. Pores with pore width less than 2 nm are defined as micropore. Pores with pore width between 2 nm to 50 nm are defined as mesopore. And macropores are the pores with pore width bigger than 50 nm.<sup>39</sup> With the size difference, different techniques have been used to investigate the pores. The pore characterization methods can be categorized into the direct methods and the simulation/calculation methods. Among the direct methods, microscopy methods such as scanning tunneling electron microscope (STEM) or transmission electron microscope (TEM) can give us the image of pores directly, but it's not statistical data since only a small part of sample is observed. Also, worm-like complicated pore structures are difficult to characterize with microscopes. X-ray scattering/diffraction methods such as X-ray diffraction (XRD) and small angle X-ray scattering (SAXS) would give statistical information of the ordered pores, but the pore size measured is the distance between atom cores which is bigger than the effective pore diameter. They also have difficulties to characterize the irregular pores. Traditionally, the theoretical calculation method was

attempted to describe the experimental data by fitting isothermal data with ideal isothermal equation which contains limited parameters, such as the K constant in the Langmuir adsorption model and the C constant in the Brunauer–Emmett–Teller (BET) theory adsorption model.<sup>84-86</sup> In some equations, additional parameters which make the calculation more complicated are added into account to optimize the model.<sup>85, 87, 88</sup>

### 1.3.1 BET theory

In 1916, I. Langmuir presented the Langmuir equation which explains the monolayer adsorption on a solid surface.<sup>84</sup> It is the first adsorption theory proposed but with limitations such as multilayer adsorption is not applicable. BET theory was developed from Langmuir theory. With the development, it can explain the physical adsorption of multilayer gas molecules on solid surface other than monolayer.<sup>85</sup> There are three assumptions to create the BET model: a, gas molecules adsorb infinitely on solid surface in layers; b, layers don't influence each other and c, Langmuir theory can be applied on each layer. The linear form of BET equation can be expressed as following:

$$\frac{p}{v(p_0-p)} = \frac{1}{v_m c} + \frac{c-1}{v_m c} \frac{p}{p_0} \quad (1)$$

where p and p<sub>0</sub> is the equilibrium and saturation pressure of the gas adsorbed at the measurement temperature, v and v<sub>m</sub> are the total and monolayer adsorbed quantity, c is the BET constant. By experimental data, it is confirmed that between the relative pressure p/p<sub>0</sub> 0.05 and 0.3, linear relationship have been found between p/[v(p<sub>0</sub>-p)] and p/p<sub>0</sub> (Fig. 1.2).<sup>85</sup> Thus we can obtain the value of v<sub>m</sub> and c by knowing the p, p<sub>0</sub> and v value from the measurement. Since the monolayer quantity v<sub>m</sub> is known, by knowing the size of the gas molecules, the surface area of the sample can be calculated.

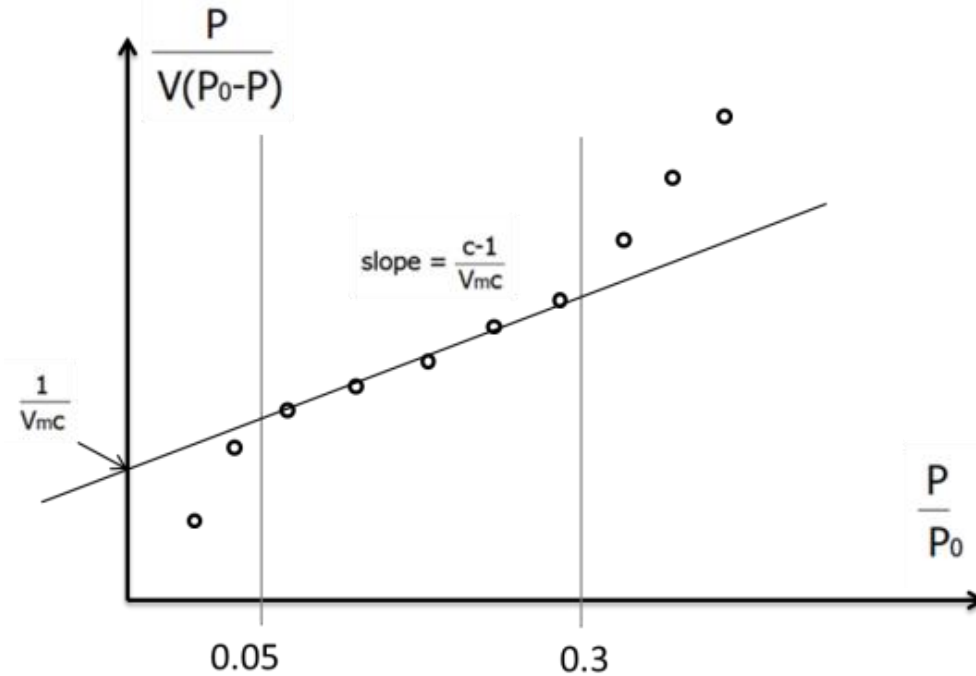


**Fig. 1.2** Scheme of using linear form BET equation to determine the volume of adsorbed monolayer. Based on adsorbed gas molecule, BET surface area can be calculated.

### 1.3.2 Thickness equation

Based on the BET multilayer adsorption theory, thickness equations were developed in the 1940s and 1950s. It describes the relationship between the pressure and the thickness of gas layer. W.D. Harkins and G. Jura developed the Harkins-Jura equation in 1944.<sup>89</sup> They obtained the thickness curve data from the non-porous alumina material. Later, from J. Frenkel in 1946, G. Halsey in 1948 and T.L. Hill in 1952, Frenkel-Halsey-Hill equation was developed by these scientists independently.<sup>90-92</sup> This equation can be applied into various non-uniform surfaces. The equation is given as following:

$$t = a \left( \frac{1}{\ln p_r} \right)^{\frac{1}{m}} \quad (2)$$

where  $t$  is the thickness,  $p_r$  is the relative pressure,  $a$  and  $m$  are empirical constants which related gas molecule and the surface. In the situation we use nitrogen adsorption at under the liquid nitrogen environment (at 77K), the constant  $a$  equals to 6.0533 and  $m$  equals to 3.

### 1.3.3 BJH method

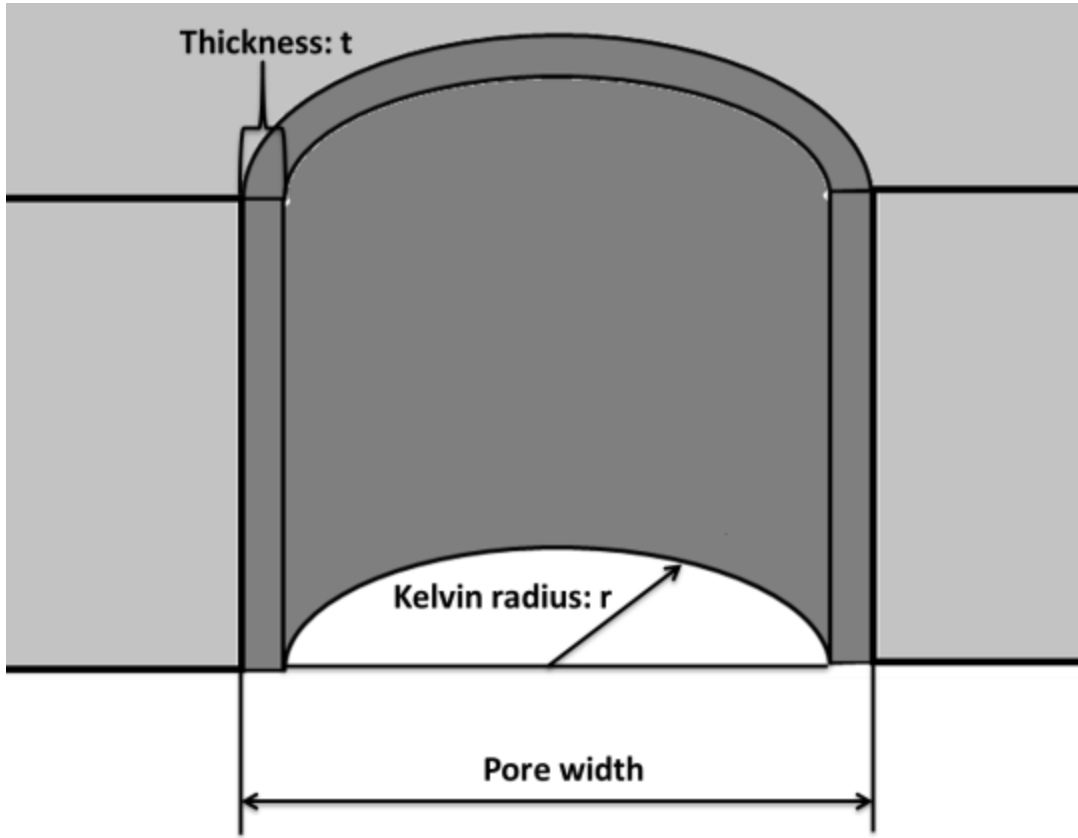


**Fig. 1.3** Scheme of cross section of a pore. Using BJH method, at the pressure  $p$  when capillary condensation happens, pore width equals to the combination of Kelvin radius  $r$  and the thickness of gas adsorbed  $t$ .

Thickness equations are not suitable for the determination of mesopores because of the capillary condensation. In this case, BJH method was developed in the 1950s to determine of pore volume and area distributions in porous substances through nitrogen adsorption isotherms, especially for mesopore and macropore.<sup>88</sup> The theory is based on the following assumptions: a, the pores are cylindrical shaped; b, the diameter of the pore is the sum-up of the Kelvin radius of the capillary and the thickness of the gas adsorbed on the wall of the pore. The Kelvin radius is the radius of a capillary which the condensation of the gas happens at a given pressure and temperature. It's given as following:

$$\ln \frac{P_v}{P_{sat}} = \frac{2H\gamma V_l}{RT} \quad (3)$$

where  $P_v$  is the equilibrium vapor pressure,  $P_{sat}$  is the saturation vapor pressure,  $H$  is mean curvature of meniscus,  $\gamma$  is the liquid/vapor surface tension,  $V_l$  is the liquid molar volume,  $R$  is the ideal gas constant and  $T$  is the temperature. For cylindrical pores,  $H=1/2r$  which  $r$  is the Kelvin radius. By combine the Kelvin equation and thickness equation at different pressure, the volume, diameter and surface area distribution of pores can be calculated based on the experimental isothermal curve (Fig. 1.3).

#### 1.3.4 *t*-plot method

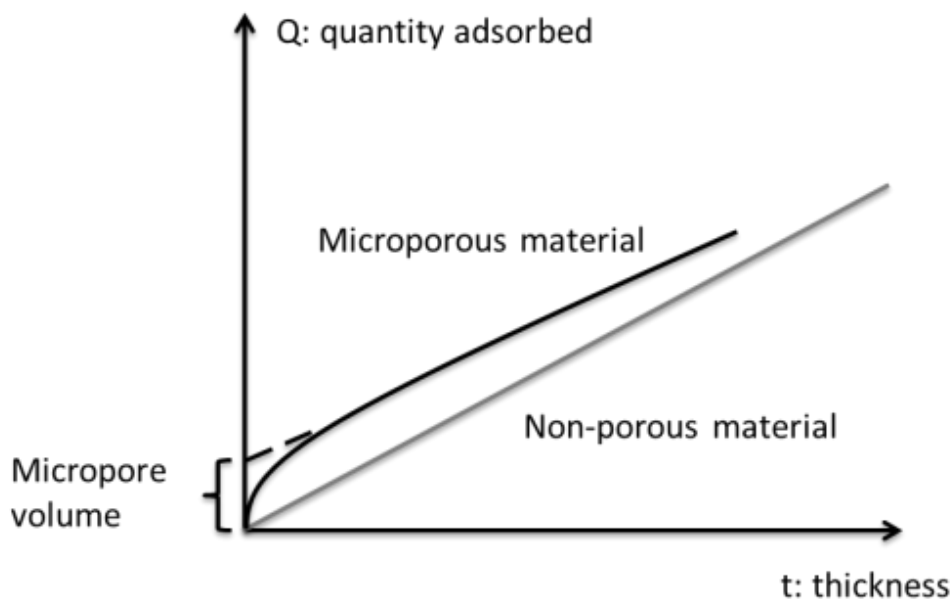


**Fig. 1.4** Scheme of the Q/t curve to determine the micropore volume.

Due to the fact that Kelvin equation is explaining the macroscopic phenomenon of capillary condensation, while in micropores, there are strong interaction in-between gas molecules and between the gas molecules and the surrounding walls, BJH method can only applicable with meso or macroporous material where condensed gas can be considered as liquid as the macroscopic phenomenon.<sup>88</sup> It seems to be not possible to quantify the micropores in a direct way. In the year 1966, J.H. de Boer proposed the *t*-plot method based on the thickness equation which can calculate the volume of micropore.<sup>93</sup> It is assumed that from the microporous material, the external surface without the pores have same adsorption behavior of gas compare to the non-porous

material. For the non-porous material, quantity of adsorbed gas and thickness of gas layer have a proportional linear relationship ( $Q/t$  curve) which starts from zero. For microporous material, external surface behaves the same for the gas adsorption which makes the  $Q/t$  curve still linear at higher thickness. But in the region of very low thickness, there are gas condensed inside the micropores which cause a rise of the  $Q/t$  curve thus a positive value of intercept (Fig. 1.4). By the obtained  $Q/t$  curve, we can calculate that the intercept of  $Q$  from the microporous material is the pore volume of micropores and the slope of the higher thickness region is the external surface area.

### *1.3.5 Molecular simulation methods*

As we know, there are limitations of assumption and simplification of the adsorption phenomenon. In this case, traditional models can give an approximate evaluation of the surface and the pores but not really accurate. According to literatures and our experiences, these methods are more accurate to characterize big pores which the phenomenon is more similar with macro scale. For small mesopores such as MCM41 mesoporous silica, error could be up to 30% by applying the traditional methods.<sup>94, 95</sup> In order to obtain accurate data, reference measurements such as TEM or XRD have to be done for adjusting some parameters of the traditional model.<sup>96</sup> Instead of the classic kinetic or phenomenological approach, models using molecular-based statistical thermodynamic theory can also be applied. In this method, the adsorption isotherm can be correlated to the microscopic properties of the system, such as the fluid-fluid and fluid-solid interaction energy parameters, the pore size, the pore geometry, and the temperature. The equilibrium distribution of the gas molecules then can be calculated through the fundamental thermodynamic law which adopts a configuration of minimum energy at the equilibrium state. The interaction energy between different atoms are also needed here, which commonly given by Lennard-Jones potential.<sup>97</sup> Molecular dynamics method and Monte Carlo method are the most common methods to determine the distribution of gas molecules in a system in equilibrium which are widely applied into physics, chemistry and biology field.<sup>98-101</sup> The disadvantage of these simulations is that if the system contains hundreds or thousands of particles, calculation ability of super computer is needed which is not accessible by many researchers.

### 1.3.6 DFT method

In this case, density functional theory (DFT) gives an alternative for the molecular simulation methods. DFT was developed in the 1960s based on the Thomas-Fermi model to describe a system with many electrons.<sup>102</sup> Such density function can be also applied to the gas adsorption model. Slit pores of carbon were explored through DFT model in the early research.<sup>103</sup> In 1995, J.P. Oliver developed a DFT model that can describe the physical adsorption of gas on both porous and non-porous materials.<sup>104</sup> Later in the year 2000 this model have been modified and applied in the determination of MCM41 mesoporous silica material with a significant improvement of accuracy compare to the traditional method.<sup>105</sup> The model describes the density of certain adsorbed gas as a function of distance from the solid surface at each temperature and relative pressure. For the cylindrical shaped pore gas adsorption model, temperature is fixed but the pore is a confined space. In this case, each density function of gas molecules adsorbed is related to the pressure and pore diameter. By experimental isothermal curve, the quantity of gas adsorbed and the pressure are measured. The following equation can be expressed:

$$Q(p) = \int dH q(p, H)f(H) \quad (4)$$

where  $Q(p)$  is the quantity adsorbed at  $p$ ,  $q(p, H)$  is the quantity adsorbed per unit of  $H$  sized pore at  $p$  which can be calculated from the density function of  $p$  and  $H$ , and  $f(H)$  is the total area of  $H$  sized pores. To simplify the model, limited numbers of  $p$  and  $H$  was selected. The equation can be rewrite as:

$$Q(p) = \sum_i q(p, H_i)f(H_i) \quad (5)$$

Through the fitting of equation 5, information such as pore diameter, surface area and volume can be obtained. Compare to the molecular dynamic method, a large amount of calculation is reduced. But still, the calculation of the density function for gas adsorption is still quite complicated. Generally speaking, four key parameters are considered: chemical potential of the gas molecules, repulsion between gas molecules, attraction force between the gas molecules and the wall potential from the surface. At infinite far away from the pore, the wall potential is not applicable so there are only three parameters and the pressure is equal to the equilibrium pressure. For porous materials such as mesoporous silica, cylindrical pore models are applied. The capillary condensation

moment is defined as at the certain pressure in a pore with a certain diameter, two different density functions can both be the solution for the system. And by combining a matrix of density functions for each pore diameter at different pressure, pore distributions can be calculate through fitting the density function with each point of the experimental isothermal curve (Fig. 1.5). Among our materials, the pores are either formed from surfactant or crystal structure which are all cylindrical, the DFT model of cylinder on oxidized surface were used for all our materials.<sup>105</sup>

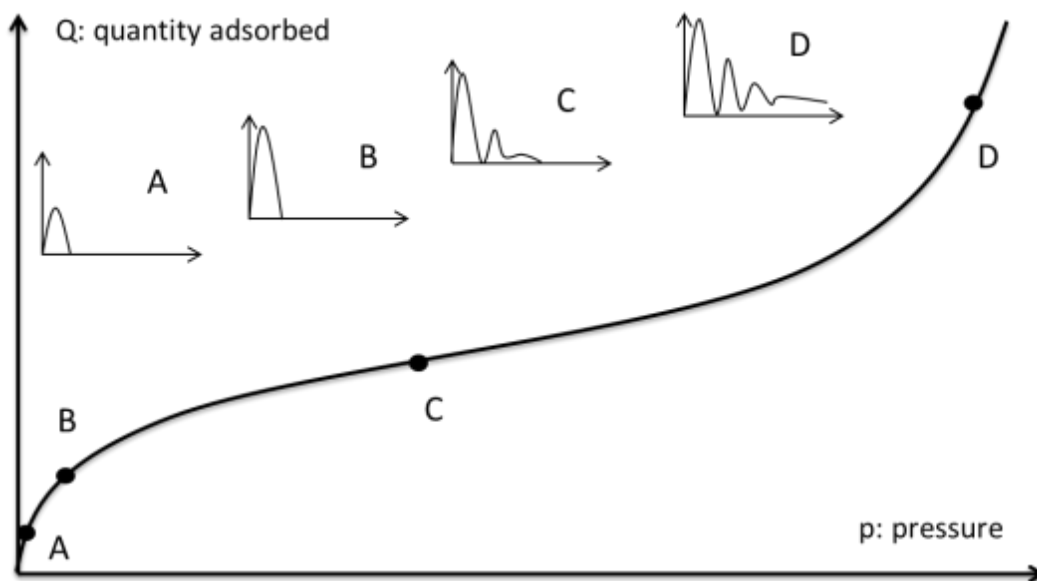


**Fig. 1.5** Scheme of the DFT method. Quantity adsorbed volume was calculated from the density function of each pressure, and fitted with the experimental isothermal curve.

#### 1.4 Surface characterization

A material with just porosity would limit its application. Surface functionalization could make it possible for various applications. In this case, the characterization of functionalized surface is also a critical point in our research. Many surface characterization methods have been developed through the years. There are two major categories of these techniques: mass based techniques such as secondary ion mass spectroscopy (SIMS) and energy based techniques such as X-ray photoelectron



spectroscopy (XPS). For our purpose, Energy based XPS is the best technique for us because it's nondestructive (compare with all the mass based techniques), quantitative (compare with SIMS), detective for both elemental and chemical information (compare with energy-dispersive X-ray spectroscopy: EDX) and suitable for both inorganic and organic characterization (compare with electron energy loss spectroscopy: EELS).<sup>106</sup>

#### 1.4.1 Basic principles

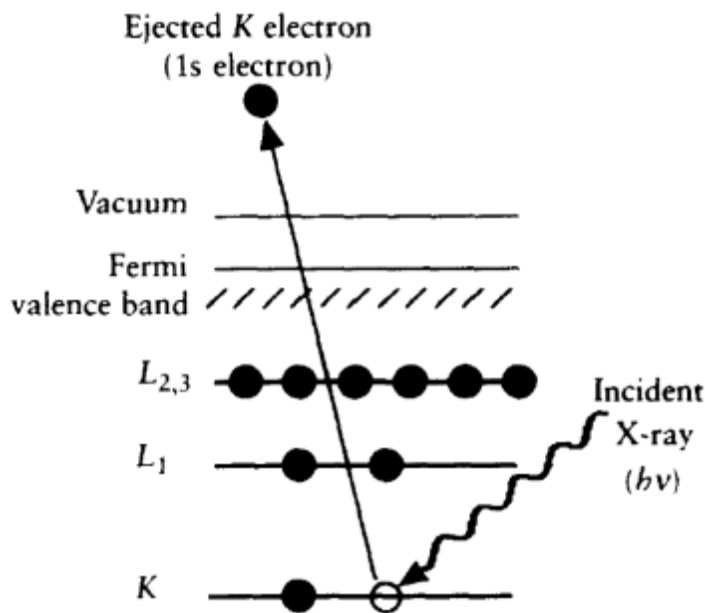


**Fig. 1.6** Schematic diagram of the XPS process of a 1s electron. Adapt from J. F. Watts and J. Wolstenholme, *An Introduction to Surface Analysis by XPS and AES*, John Wiley & Sons Ltd, 2003, with permission from John Wiley & Sons.

XPS is a surface sensitive and quantitative spectroscopic technique. In the 1950s, Kai Siegbahn and his research group first developed the knowledge of XPS as an analysis tool,<sup>107</sup> and few years after, the first commercial XPS instrument was produced by HP.

The principle of XPS is shown in Fig.1.6. A 1s electron was ejected due to the absorption of the energy from X-ray. The ejected electron has a certain kinetic energy. The relationship of the binding energy, kinetic energy and the initial X-ray photon energy is expressed as following:

$$E_B = h\nu - E_k - W \quad (6)$$

where  $E_B$  is the binding energy of the electron before ejected,  $h\nu$  is the photon energy of the X-ray,  $E_k$  is the kinetic energy of the electron after ejection and  $W$  is the work function of the instrument. In this way, a photoelectric spectrum will accurately represent the electron structure (of the electrons which their binding energy is less than  $h\nu - W$ ) of an element. Fig. 1.7 shows the contribution of different electrons to a certain spectrum. Ejected electrons without any energy loss contribute to the characteristic peaks of the spectrum. The ejected electrons which have inelastic scattering and other energy loss contribute to the background of the spectrum. And of course, the characteristic electrons with less binding energy will have more kinetic energy.

**Table 1.1** The relationship between quantum numbers, spectroscopists' notation and X-ray notation.

Quantum numbers				Spectroscopists' notation	X-ray notation
n	l	s	j		
1	0	$\pm 1/2$	$1/2$	$1s_{1/2}$	K
2	0	$\pm 1/2$	$1/2$	$2s_{1/2}$	$L_1$
2	1	$1/2$	$1/2$	$2p_{1/2}$	$L_2$
2	1	$-1/2$	$3/2$	$2p_{3/2}$	$L_3$
3	0	$\pm 1/2$	$1/2$	$3s_{1/2}$	$M_1$
3	1	$1/2$	$1/2$	$3p_{1/2}$	$M_2$
3	1	$-1/2$	$3/2$	$3p_{3/2}$	$M_3$
3	2	$1/2$	$3/2$	$3d_{3/2}$	$M_4$
3	2	$-1/2$	$5/2$	$3d_{5/2}$	$M_5$

Peak split is a common feature for electrons which their orbital angular momentum quantum number ( $l$ ) is not 0. This is because that the electron angular momentum is the result of the interaction between its spin and its orbital angular momentum. Table 1.1 shows the relationship between quantum numbers, spectroscopists' notation and X-ray notation. Each electron has a spin angular momentum which can be either  $1/2$  or  $-1/2$ . The orbital angular momentum and the spin angular momentum adding together vectorially to produce the quantity of the electron angular momentum  $j=|l+s|$ . Thus, the electrons from the p orbital typically have j numbers of  $1/2$  and  $3/2$ . Similarly, electrons from d orbital would have j numbers of  $3/2$  and  $5/2$ , and for f orbitals,  $5/2$  and  $7/2$ .

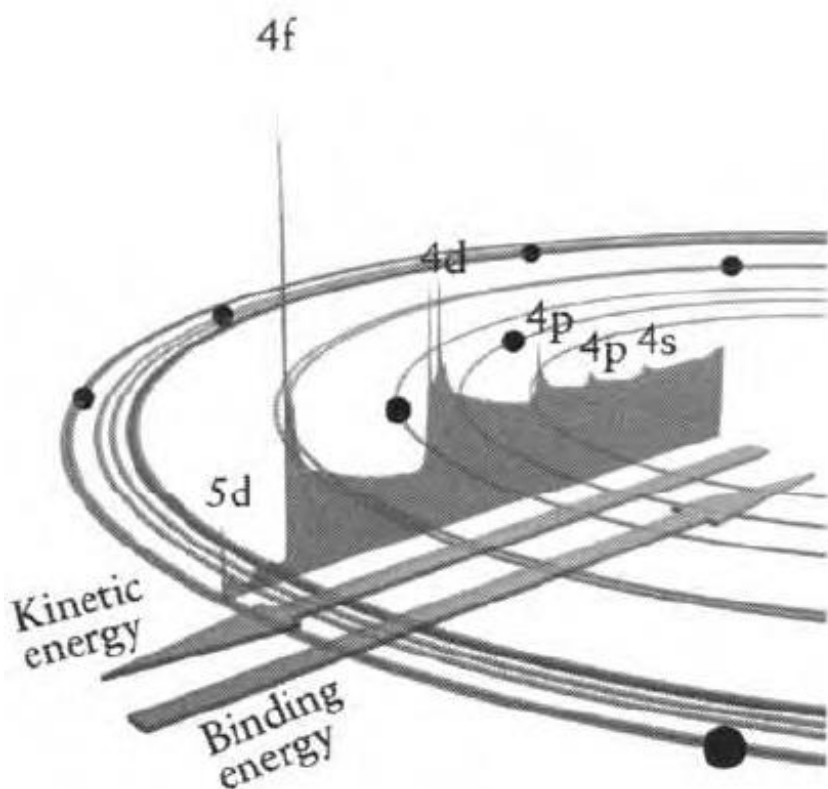


**Fig. 1.7** Photoelectron spectrum of lead showing the manner in which electrons escaping from the solid can contribute to discrete peaks or suffer energy loss and contribute to the background; the spectrum is superimposed on a schematic of the electronic structure of lead to illustrate how each orbital gives rise to photoelectron lines. Adapt from J. F. Watts and J. Wolstenholme, *An Introduction to Surface Analysis by XPS and AES*, John Wiley & Sons Ltd, 2003, with permission from John Wiley & Sons.

After one electron has been ejected, there has to be another electron to fill this whole. This could be achieved by emission of a photon from a relaxed electron which called X-ray fluorescence.<sup>108</sup> But there's also another possibility that an electron absorbed this energy and get ejected. This ejected electron is called Auger electron and can contribute to characterized peak in the final spectrum. Fig. 1.8 shows a the process of a  $KL_{2,3}L_{2,3}$  Auger electron ejection. Due to the fact that Auger electrons are usually from the outer orbitals, they contain more chemical state information than the core electrons.

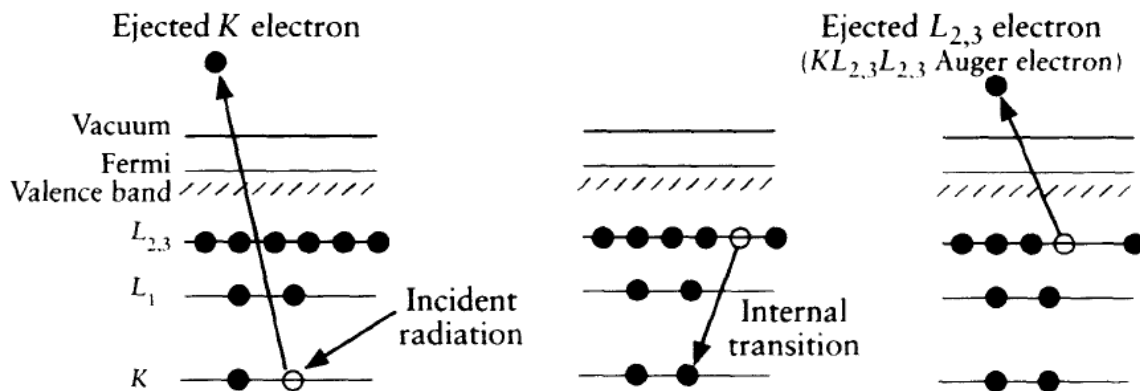


**Fig. 1.8** Example of an Auger electron emission: relaxation of the ionized atom by the emission of a  $KL_{2,3}L_{2,3}$  Auger electron. Adapt from J. F. Watts and J. Wolstenholme, *An Introduction to Surface Analysis by XPS and AES*, John Wiley & Sons Ltd, 2003, with permission from John Wiley & Sons.

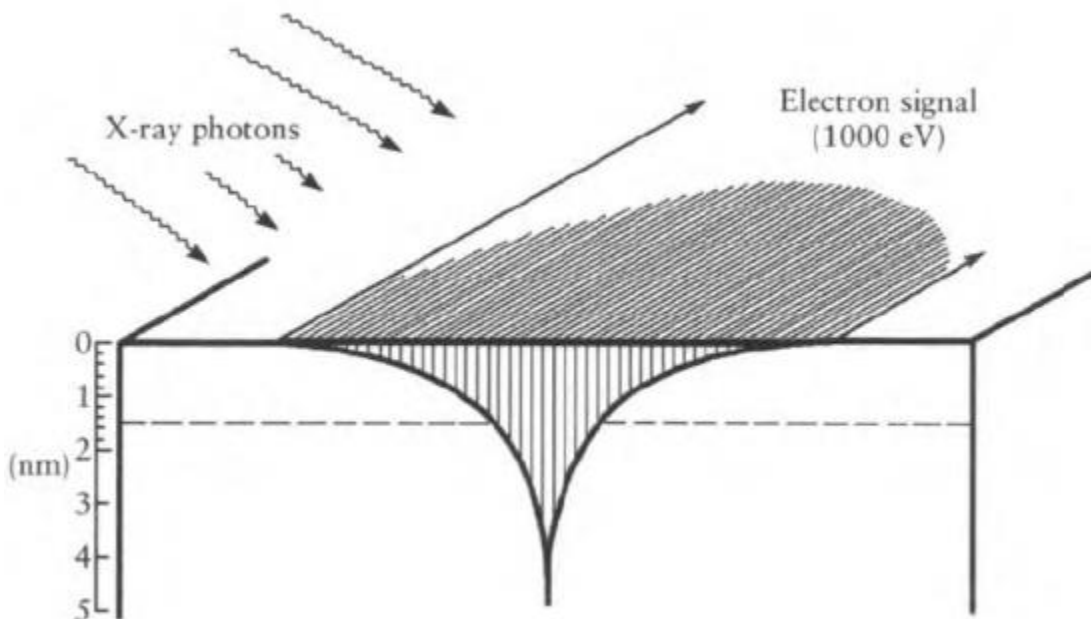


**Fig. 1.9** Representation of electron intensity as a function of depth. Adapt from J. F. Watts and J. Wolstenholme, *An Introduction to Surface Analysis by XPS and AES*, John Wiley & Sons Ltd, 2003, with permission from John Wiley & Sons.

For a surface characterization technique, it is essential to know the depth limit of the detection. Beer-Lambert law describes how far for photon with certain energy can travel through a material. It was discovered in the 1700s and with development since.<sup>109, 110</sup> The

intensity of electrons (I) that emitted deeper than a thickness (d) can be explained by the following equation:

$$I = I_0 \exp\left(-\frac{d}{\lambda}\right) \quad (7)$$

where  $I_0$  is the intensity of an infinite uniformed material and  $\lambda$  is the wavelength of the X-ray. For example, an aluminum X-ray source has a  $K_{\alpha 1}$  emission of 1486.6 eV. We can know that the detection depth for an infinite uniformed surface is 4-5 nm.

#### 1.4.2 Quantification

Quantification is also an important feature for XPS analysis. Two major aspects could influence the quantification: from the instrument and from the material. For instrument related factors, there are mainly three. The first one is the transmission function of the spectrometer. This gives the proportion of the electrons that transmitted through the spectrometer against the kinetic energy. This function mainly depends on how the lenses are arranged and usually measured by the manufacturers. The second one is the efficiency of the detector which means how many electrons of all the electrons hit the detector can be detected. The third factor is the stray magnetic field. These magnetic fields would affect more for the electrons with low kinetic energy than with high kinetic energy. Thus, this factor also has to be considered for the quantification. From the material point of view, there are two factors that influence the quantification. The first one is the cross-section of the emission electrons. This means how many electrons can emit upon the initial X-ray irradiation. It depends on various factors such as the property of targeted element, property of the certain electron orbital and energy of the excitation radiation. Second factor is the distance of depth that the electrons can get escaped which introduced before.

Finally, to quantify an element from a material, the following simplified equation is used:

$$I = J\rho\sigma K\lambda \quad (8)$$

where I is the intensity of the photoelectron peak, J is the photo flux,  $\rho$  is the concentration of the atom or ion in the detection area,  $\sigma$  is the cross-section of the

photoelectron production,  $K$  is the instrument factor that consist of all the factors described above and  $\lambda$  is the wavelength of the X-ray.

### 1.4.3 Unwanted features

X-ray satellite is one of the unwanted features in the XPS spectrum. The reason for this is that the X-ray source always has several emissions other than the  $K_{\alpha 1}$  emission. Table 1.2 shows the emission peaks of aluminum and magnesium X-ray source.

**Table 1.2** X-ray satellite emission peaks.<sup>111</sup>

Peak	$\alpha_{1,2}$	$\alpha_3$	$\alpha_4$
Mg emission (eV)	1253.6	1262.0	1263.9
Relative height	100	8.0	4.1
Al emission (eV)	1486.7	1496.5	1498.5
Relative height	100	6.4	3.2

From equation (6) we can know that if the energy of the excitation photon is higher, the detected kinetic energy would be higher. Thus small satellite peaks with lower binding energy could appear on the spectrum. These features are called X-ray satellites.

The second unwanted feature is called shake-up satellite which we can see from the Cu 2p spectrum from CuO in Fig. 1.10. The shake-up satellite appears when an outgoing electron interacts with valence band electron and excites it to higher energy level (shake-up). This interaction would cause the loss of kinetic energy of the outgoing electron. From equation (6) it's clear that the binding energy calculated would be higher. These electrons contribute to the final spectrum as shake-up satellites. Shake-up satellites are observed in transition metal complexes and aromatic compounds which has the  $\pi-\pi^*$  transition. All these unwanted features would make the quantification more complicated and should always be aware from.

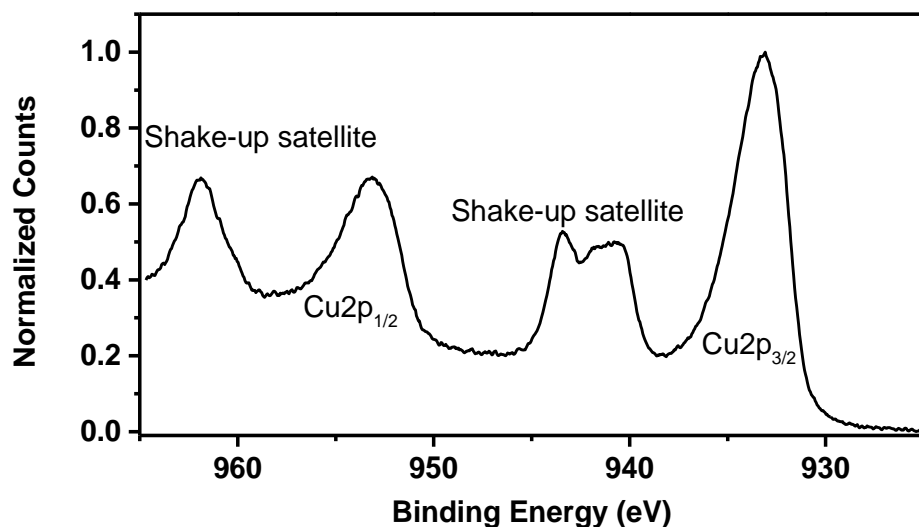


**Fig. 1.10** XPS Cu 2p spectrum for CuO.

#### 1.4.4 Chemical state information

Apart from the quantification of elements, the other important information XPS provides is the chemical state information. The chemical state information is obtained by analyzing the XPS chemical shift of the binding energy from the spectrum. The chemical shift can be up to several eVs which can be seen from the XPS spectrum. The shift of the binding energy can be caused by initial state and final state effects. For initial state effect, the initial charge on the target atom before the photoemission process plays the major role on the magnitude of chemical shift. For example, the nitrogen 1s binding energy for amine group is around 399 eV but for protonated amine is around 402 eV.<sup>111</sup> In essence, for the targeted atom, the more bonds formed by electronegative atoms, the more chemical shift there would be. An example is that for the C 1s electron, the binding energy of C-C is 284.8 eV, C-O is 286 eV, C=O is 288 eV, C-F is around 289 eV and CF<sub>3</sub> is 293 eV.<sup>111</sup> Thus, it is possible to deconvolute the XPS spectrum and get the composition of each chemical state. Compare with the initial state effects, the final state effects are less common. Final state effects happen following the photoelectron process. In this case, the chemical shift is contributed by effect such as core hole screening, relaxation of electron orbitals and the polarization of surrounding ions.<sup>106</sup>

#### *1.4.5 Adventitious carbon*

Adventitious carbon is a thin layer of carbonaceous material that usually found on the surface of most samples which have been exposed with air even for a very short time. Research suggested that the composition of adventitious carbon is variety of polymeric hydrocarbon species (short chain) and not graphitic units.<sup>112</sup> For the chemical bond point of view, it is mostly C-C  $sp^3$ , with 10%-30% C-O. The source of these carbons is possibly due to the CO and CO<sub>2</sub> species.<sup>113</sup> Adventitious carbon is considered as contamination and could influence the quantitative analysis. But on the other hand, as most of the carbon component from adventitious carbon is the C-C  $sp^3$ , it can be used as a reference for the calibration of the system shift of XPS instrument.<sup>112</sup>



## 1.5 Scope of the thesis

The unique properties of porous material could bring a lot of applications in many promising fields. In this thesis, the complete procedure from synthesis to application of titania and silica based porous materials have been presented. Applications have been applied in different fields including biomedical, photocatalysis, sensing and polluted water treatment. As there are various applications presented in this thesis, the introduction chapter is quite general. The introduction of each chapter describes the related research progress in the specific field.

Chapter 2 describes the synthesis of a series of materials (zeolite, silica and titania) having porosity from micro to nanometer. Key factors in the synthesis and characterization have been discussed in detail. The materials synthesized in this chapter will be further used in the next chapters.

Chapter 3 presents a dye removal application based on functionalized mesoporous silica. A device based on this system has been built for large quantity of water treatment. Furthermore, to avoid the diffusion of the silica as a potential pollutant into the environment, polymer based “glue” has been developed to hold the silica materials together.

In chapter 4, artificial neurotransmitter receptors based on microporous zeolite material have been developed. For specific neurotransmitter, the highest sensitivity among all the artificial neurotransmitter receptors has been achieved. Several applications are also presented by using this system.

In chapter 5, a novel way of luminescent Cu(0) cluster synthesis is presented. In situ formation of Cu(0) clusters by X-ray irradiation inside porous materials has been described. According to the cavities of different porous materials, the synthesized clusters have different photophysical properties.

In chapter 6, multi-functionalized mesoporous titania particle has been used in biomedical application. More specifically, a drug delivery system using the multi-functionalized mesoporous titania particle as cargo has been developed. Moreover, due to the photoactive property of titania, the release reactive oxygen species (ROS) under UV irradiation in vitro has been studied.

Chapter 7 describes the development of a new type of organotitania material with Ti-C bond. The band gap is reduced compared to the inorganic titania material. This means that the photoactivity of this organotitania can be extended to the region of visible light. In particular, photocatalysis is discussed in this chapter.

In chapter 8, the principles of some commonly used techniques in this thesis are described.

## 1.6 References

1. N. Taniguchi, *On the basic concept of nanotechnology*, 1974.
2. H. W. Kroto, J. R. Heath, S. C. O'Brien, R. F. Curl and R. E. Smalley, *Nature*, 1985, **318**, 162-163.
3. G. Binnig, C. F. Quate and C. Gerber, *Phys. Rev. Lett.*, 1986, **56**, 930.
4. G. Binnig and H. Rohrer, *Rev. Mod. Phys.*, 1987, **59**, 615.
5. J. Lehn, *Science*, 1993, **260**, 1762-1763.
6. L. E. Euliss, J. A. DuPont, S. Gratton and J. DeSimone, *Chem. Soc. Rev.*, 2006, **35**, 1095-1104.
7. P. Kerativitayanan, J. K. Carrow and A. K. Gaharwar, *Advanced Healthcare Materials*, 2015, **4**, 1600-1627.
8. E. C. Dreaden, A. M. Alkilany, X. Huang, C. J. Murphy and M. A. El-Sayed, *Chem. Soc. Rev.*, 2012, **41**, 2740-2779.
9. L. Sun, Y. A. Diaz-Fernandez, T. A. Gschneidner, F. Westerlund, S. Lara-Avila and K. Moth-Poulsen, *Chem. Soc. Rev.*, 2014, **43**, 7378-7411.
10. R. R. Arvizo, S. Bhattacharyya, R. A. Kudgus, K. Giri, R. Bhattacharya and P. Mukherjee, *Chem. Soc. Rev.*, 2012, **41**, 2943-2970.
11. G. Binnig and H. Rohrer, *Surf. Sci.*, 1983, **126**, 236-244.
12. S. Iijima and T. Ichihashi, 1993.
13. C.-H. Lai, J. Hütter, C.-W. Hsu, H. Tanaka, S. Varela-Aramburu, L. De Cola, B. Lependies and P. H. Seeberger, *Nano Lett.*, 2016, **16**, 807-811.
14. X. Michalet, F. Pinaud, L. Bentolila, J. Tsay, S. Doose, J. Li, G. Sundaresan, A. Wu, S. Gambhir and S. Weiss, *Science*, 2005, **307**, 538-544.
15. V. I. Klimov, A. Mikhailovsky, S. Xu, A. Malko, J. Hollingsworth, C. Leatherdale, H.-J. Eisler and M. Bawendi, *Science*, 2000, **290**, 314-317.
16. M.-C. Daniel and D. Astruc, *Chem. Rev.*, 2004, **104**, 293-346.
17. Nobelprize.org, [http://www.nobelprize.org/nobel\\_prizes/chemistry/laureates/2016](http://www.nobelprize.org/nobel_prizes/chemistry/laureates/2016).
18. C. O. Dietrich-Buchecker, J. Sauvage and J. Kintzinger, *Tetrahedron Lett.*, 1983, **24**, 5095-5098.
19. P. L. Anelli, N. Spencer and J. F. Stoddart, *J. Am. Chem. Soc.*, 1991, **113**, 5131-5133.

20. N. Koumura, R. W. Zijlstra, R. A. van Delden, N. Harada and B. L. Feringa, *Nature*, 1999, **401**, 152-155.
21. G. M. Whitesides, J. P. Mathias and C. T. Seto, *Molecular self-assembly and nanochemistry: a chemical strategy for the synthesis of nanostructures*, DTIC Document, 1991.
22. S. Zhang, *Nat. Biotechnol.*, 2003, **21**, 1171-1178.
23. J. N. Israelachvili, D. J. Mitchell and B. W. Ninham, *J. Chem. Soc. Faraday Trans. 2.*, 1976, **72**, 1525-1568.
24. E. Winfree, F. Liu, L. A. Wenzler and N. C. Seeman, *Nature*, 1998, **394**, 539-544.
25. D. Chandler, *Nature*, 2005, **437**, 640-647.
26. M. Li, H. Schnablegger and S. Mann, *Nature*, 1999, **402**, 393-395.
27. R. D. Piner, J. Zhu, F. Xu, S. Hong and C. A. Mirkin, *Science*, 1999, **283**, 661-663.
28. S. Y. Chou, P. R. Krauss and P. J. Renstrom, *Science*, 1996, **272**, 85.
29. S. Y. Chou, P. R. Krauss, W. Zhang, L. Guo and L. Zhuang, *Journal of Vacuum Science & Technology B*, 1997, **15**, 2897-2904.
30. C. Oatley, W. Nixon and R. Pease, *Advances in Electronics and Electron Physics*, 1966, **21**, 181-247.
31. D. B. Williams and C. B. Carter, in *Transmission electron microscopy*, Springer, 1996, pp. 3-17.
32. B. Hasenknopf, J. M. Lehn, B. O. Kneisel, G. Baum and D. Fenske, *Angew. Chem. Int. Ed. Engl.*, 1996, **35**, 1838-1840.
33. J. Zheng, P. R. Nicovich and R. M. Dickson, *Annu. Rev. Phys. Chem.*, 2007, **58**, 409.
34. S. J. Klaine, P. J. Alvarez, G. E. Batley, T. F. Fernandes, R. D. Handy, D. Y. Lyon, S. Mahendra, M. J. McLaughlin and J. R. Lead, *Environ. Toxicol. Chem.*, 2008, **27**, 1825-1851.
35. C. Marambio-Jones and E. M. Hoek, *J. Nanopart. Res.*, 2010, **12**, 1531-1551.
36. K. L. Aillon, Y. Xie, N. El-Gendy, C. J. Berkland and M. L. Forrest, *Adv. Drug Deliv. Rev.*, 2009, **61**, 457-466.
37. C. A. Poland, R. Duffin, I. Kinloch, A. Maynard, W. A. Wallace, A. Seaton, V. Stone, S. Brown, W. MacNee and K. Donaldson, *Nat. Nanotechnol.*, 2008, **3**, 423-428.
38. G. V. Lowry, K. B. Gregory, S. C. Apte and J. R. Lead, *Environmental science & technology*, 2012, **46**, 6893-6899.

39. A. D. McNaught and A. Wilkinson, *IUPAC. Compendium of Chemical Terminology*, Blackwell Scientific Publications, Oxford, 2nd edn., 1997.
40. J. De Boer, B. Linsen, T. Van der Plas and G. Zondervan, *J. Catal.*, 1965, **4**, 649-653.
41. C. Baerlocher, L. B. McCusker and D. H. Olson, *Atlas of Zeolite Framework Types*, Elsevier, The Netherlands, 2007.
42. R. C. Bansal and M. Goyal, *Activated carbon adsorption*, CRC press, 2005.
43. B. Hameed, A. M. Din and A. Ahmad, *J. Hazard. Mater.*, 2007, **141**, 819-825.
44. C.-P. Huang and F. Ostovic, *Journal of the Environmental Engineering Division*, 1978, **104**, 863-878.
45. T. Otowa, Y. Nojima and T. Miyazaki, *Carbon*, 1997, **35**, 1315-1319.
46. K. Köhler, R. G. Heidenreich, J. G. Krauter and J. Pietsch, *Chem. Eur. J.*, 2002, **8**, 622-631.
47. U. Jans and J. Hoigné, 1998.
48. H. Mahmood, M. H. A. bin Ahmad Sayukhi, M. Moniruzzaman and S. Yusup, 2016.
49. G. Sethia and A. Sayari, *Carbon*, 2016, **99**, 289-294.
50. Q. Wang and J. K. Johnson, *The Journal of chemical physics*, 1999, **110**, 577-586.
51. C. Lastoskie, K. E. Gubbins and N. Quirke, *Langmuir*, 1993, **9**, 2693-2702.
52. A. K. Geim and K. S. Novoselov, *Nat. Mater.*, 2007, **6**, 183-191.
53. X. Zhang, A. Ciesielski, F. Richard, P. Chen, E. A. Prasetyanto, L. De Cola and P. Samorì, *Small*, 2016, **12**, 1044-1052.
54. A. F. Cronstedt, J. L. Schlenker and G. Kuhl, *K. vet. akad. handl.*, 1756, **18**, 120-123.
55. A. Tiselius, *J. Phys. Chem.*, 1936, **40**, 223-232.
56. C. D. Chang and A. J. Silvestri, *J. Catal.*, 1977, **47**, 249-259.
57. A. Corma, *J. Catal.*, 2003, **216**, 298-312.
58. *US Pat.*, 909264, 1962.
59. D. W. Breck, *Zeolite molecular sieves: structure, chemistry, and use*, John Wiley & Sons, New York, 1974.
60. S. Megelski and G. Calzaferri, *Adv. Funct. Mater.*, 2001, **11**, 277-286.
61. R. Martinez-Franco, C. Paris, M. E. Martinez-Armero, C. Martinez, M. Moliner and A. Corma, *Chem. Sci.*, 2016, **7**, 102-108.
62. O. Yaghi and H. Li, *J. Am. Chem. Soc.*, 1995, **117**, 10401-10402.
63. H. Li, M. Eddaoudi, M. O'Keeffe and O. M. Yaghi, *Nature*, 1999, **402**, 276-279.
64. B. Chen, M. Eddaoudi, S. Hyde, M. O'keeffe and O. Yaghi, *Science*, 2001, **291**, 1021-1023.

65. J. L. Rowsell and O. M. Yaghi, *Microporous Mesoporous Mater.*, 2004, **73**, 3-14.
66. J. Lee, O. K. Farha, J. Roberts, K. A. Scheidt, S. T. Nguyen and J. T. Hupp, *Chem. Soc. Rev.*, 2009, **38**, 1450-1459.
67. L. E. Kreno, K. Leong, O. K. Farha, M. Allendorf, R. P. Van Duyne and J. T. Hupp, *Chem. Rev.*, 2011, **112**, 1105-1125.
68. B. Chen, N. W. Ockwig, A. R. Millward, D. S. Contreras and O. M. Yaghi, *Angew. Chem.*, 2005, **117**, 4823-4827.
69. P. Horcajada, T. Chalati, C. Serre, B. Gillet, C. Sebrie, T. Baati, J. F. Eubank, D. Heurtaux, P. Clayette and C. Kreuz, *Nat. Mater.*, 2010, **9**, 172-178.
70. M. Allendorf, C. Bauer, R. Bhakta and R. Houk, *Chem. Soc. Rev.*, 2009, **38**, 1330-1352.
71. *US Pat.*, 3556725, 1971.
72. *US Pat.*, 3493341, 1970.
73. W. Stöber, A. Fink and E. Bohn, *J. Colloid Interface Sci.*, 1968, **26**, 62-69.
74. J. S. Beck, J. C. Vartuli, W. J. Roth, M. E. Leonowicz, C. T. Kresge, K. D. Schmitt, C. T. W. Chu, D. H. Olson, E. W. Sheppard, S. B. McCullen, J. B. Higgins and J. L. Schlenker, *J. Am. Chem. Soc.*, 1992, **114**, 10834-10843.
75. A. B. D. Nandiyanto, S.-G. Kim, F. Iskandar and K. Okuyama, *Microporous Mesoporous Mater.*, 2009, **120**, 447-453.
76. D. Zhao, J. Feng, Q. Huo, N. Melosh, G. H. Fredrickson, B. F. Chmelka and G. D. Stucky, *Science*, 1998, **279**, 548-552.
77. D. M. Antonelli and J. Y. Ying, *Angew. Chem. Int. Ed. Engl.*, 1995, **34**, 2014-2017.
78. L. Qi, J. Ma, H. Cheng and Z. Zhao, *Langmuir*, 1998, **14**, 2579-2581.
79. P. Yang, D. Zhao, D. I. Margolese, B. F. Chmelka and G. D. Stucky, *Nature*, 1998, **396**, 152-155.
80. I. I. Slowing, B. G. Trewyn, S. Giri and V. S. Y. Lin, *Adv. Funct. Mater.*, 2007, **17**, 1225-1236.
81. N. Yantara, D. Sabba, F. Yanan, J. M. Kadro, T. Moehl, P. P. Boix, S. Mhaisalkar, M. Gratzel and C. Gratzel, *Chem. Commun.*, 2015, **51**, 4603-4606.
82. A. Fujishima, T. N. Rao and D. A. Tryk, *J. Photochem. Photobiol. C.*, 2000, **1**, 1-21.
83. L. Maggini, I. Cabrera, A. Ruiz-Carretero, E. A. Prasetyanto, E. Robinet and L. De Cola, *Nanoscale*, 2016, **8**, 7240-7247.
84. I. Langmuir, *J. Am. Chem. Soc.*, 1916, **38**, 2221-2295.

85. S. Brunauer, P. H. Emmett and E. Teller, *J. Am. Chem. Soc.*, 1938, **60**, 309-319.
86. I. Langmuir, *J. Am. Chem. Soc.*, 1918, **40**, 1361-1403.
87. K. S. W. Sing, *Adv. Colloid Interface Sci.*, 1998, **76-77**, 3-11.
88. E. P. Barrett, L. G. Joyner and P. P. Halenda, *J. Am. Chem. Soc.*, 1951, **73**, 373-380.
89. W. D. Harkins and G. Jura, *J. Am. Chem. Soc.*, 1944, **66**, 1366-1373.
90. J. Frenkel, *Kinetic Theory of Liquids*, Clarendon Press, Oxford, 1946.
91. G. Halsey, *The Journal of Chemical Physics*, 1948, **16**, 931-937.
92. T. L. Hill, in *Advances in Catalysis*, eds. V. I. K. W.G. Frankenburg and E. K. Rideal, Academic Press, 1952, vol. 4, pp. 211-258.
93. J. H. de Boer, B. C. Lippens, B. G. Linsen, J. C. P. Broekhoff, A. van den Heuvel and T. J. Osinga, *J. Colloid Interface Sci.*, 1966, **21**, 405-414.
94. M. Luisa Ojeda, J. Marcos Esparza, A. Campero, S. Cordero, I. Kornhauser and F. Rojas, *PCCP*, 2003, **5**, 1859-1866.
95. M. Kruk, M. Jaroniec and A. Sayari, *J. Phys. Chem. B*, 1997, **101**, 583-589.
96. M. Kruk, M. Jaroniec and A. Sayari, *Langmuir*, 1997, **13**, 6267-6273.
97. J. E. Jones, *Proceedings of the Royal Society of London. Series A*, 1924, **106**, 463-477.
98. B. J. Alder and T. E. Wainwright, *J. Chem. Phys.*, 1959, **31**, 459-466.
99. N. Metropolis, A. W. Rosenbluth, M. N. Rosenbluth, A. H. Teller and E. Teller, *J. Chem. Phys.*, 1953, **21**, 1087-1092.
100. Y. Sugita and Y. Okamoto, *Chem. Phys. Lett.*, 1999, **314**, 141-151.
101. J. Tersoff, *Phys. Rev. B.*, 1989, **39**, 5566-5568.
102. P. Hohenberg and W. Kohn, *Phys. Rev.*, 1964, **136**, B864-B871.
103. C. Lastoskie, K. E. Gubbins and N. Quirke, *J. Phys. Chem.*, 1993, **97**, 4786-4796.
104. J. P. Olivier, *J. Porous Mater.*, 1995, **2**, 9-17.
105. M. Jaroniec, M. Kruk, J. P. Olivier and S. Koch, in *Stud. Surf. Sci. Catal.*, eds. K. K. Unger, G. Kreysa and J. P. Baselt, Elsevier, 2000, vol. 128, pp. 71-80.
106. J. F. Watts and J. Wolstenholme, *An Introduction to Surface Analysis by XPS and AES*, John Wiley & Sons Ltd, 2003.
107. K. Siegbahn and K. Edvarson, *Nucl. Phys.*, 1956, **1**, 137-159.
108. W. Bambynek, B. Crasemann, R. Fink, H.-U. Freund, H. Mark, C. Swift, R. Price and P. V. Rao, *Rev. Mod. Phys.*, 1972, **44**, 716.
109. P. Bouguer, *Essai d'optique sur la gradation de la lumière*, Jombert, 1729.

110. A. Beer, *Ann. Phys. Chem*, 1852, **86**, 78-88.
111. J. Chastain, R. C. King and J. Moulder, *Handbook of X-ray photoelectron spectroscopy: a reference book of standard spectra for identification and interpretation of XPS data*, Physical Electronics Eden Prairie, MN, 1995.
112. T. L. Barr and S. Seal, *J. Vac. Sci. Technol., A*, 1995, **13**, 1239-1246.
113. D. Miller, M. Biesinger and N. McIntyre, *Surf. Interface Anal.*, 2002, **33**, 299-305.



## **Chapter 2:**

# **Synthesis and characterization of the silica and titania based porous materials**

### **Abstract**

A series of materials possessing different sizes and shapes and having porosity from micro to nano meter have been synthesized. Most of the effort has been devoted to control the morphology and properties of these silica/(alumina) and titania based materials. Key factors to control the synthesis and characterization are discussed. The materials made in this chapter have also been functionalized and used for different purposes in the next chapters of this thesis.

## 2.1 Introduction

Nowadays porous materials are widely applied to many fields such as catalysis, photovoltaics, sensing, bio imaging and drug delivery.<sup>1, 2</sup> In 1992, the Mobil Oil Corporation discovered a new class of mesoporous materials which were based on silica and has uniform pores, named as the M41S family.<sup>3</sup> Since then, porous nanomaterials have attracted lots of research interests due to their ability to entrap molecules, large surface area, rather easy functionalization and other unique properties.<sup>4</sup> Different kinds of mesoporous materials have been developed during these years.<sup>5, 6</sup> In the last few decades, microporous materials such as zeolite have also attracted a lot of research interests especially in the catalysis field.<sup>7, 8</sup>

Natural zeolite was found and used as early as 18<sup>th</sup> century.<sup>9</sup> Following that, the composition of zeolite which contains silica, alumina and counter ion such as sodium has been discovered.<sup>10</sup> Since then, more and more types of natural zeolites have been discovered and numerous artificial zeolites have been synthesized.<sup>11</sup> According to the different crystal structures, zeolite can be categorized into around 200 different types.<sup>12, 13</sup> Zeolite LTL is one of them, processing a hexagonal symmetry. As for all the zeolites, it shows an anionic framework completed by charge-compensating counter ions. The crystals consist of so-called cancrinite cages ( $\epsilon$  cages), which are piled up and interconnected to form a one-dimensional channel system running parallel to the cylinder c-axis for the whole length. The smallest channel diameter is 0.71 nm, while the largest channel diameter is 1.26 nm. The unit cell length is 0.75 nm. The channels are oriented in a hexagonal manner and the center-to-center distance of two adjacent channels is 1.8 nm (Fig. 2.1).<sup>14</sup> Due to the presence of aluminum atoms in the zeolite framework (atomic ratio Al:Si = 1:3), a net negative charge is presented and needs to be compensated by counter ions, which are commonly observed such as sodium or potassium. Recent years, scientists are still trying to produce new type of zeolites with different pores especially for catalytic applications.<sup>15, 16</sup> As for zeolite LTL, because of its unique parallel pore structures, the organization of molecules packed inside the channels have been

investigated.<sup>17</sup> Very recently has been demonstrated that zeolite can be used as template to build three-dimensional porous grapheme-like structures.<sup>18</sup>

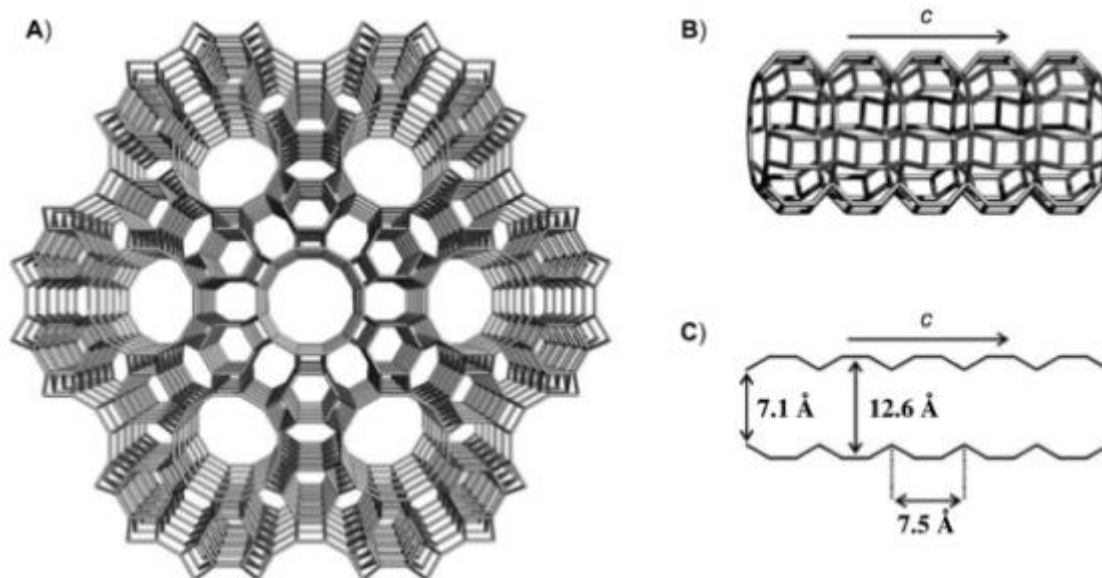


**Fig. 2.1** Zeolite LTL framework A) projected along the c-axis; B) side view of the main channel; C) its dimensions. Adapted from Ruiz, A., Brühwiler, D., Ban, T. et al. *Monatshefte für Chemie* (2005) 136: 77, with permission from Springer Link.

After the discovery of M41S mesoporous silica, more and more sol-gel synthesis based on self-assembly around the micelles have been developed, which result in mesoporous silica families such as MCM, SBA and HMM.<sup>4, 19-21</sup> These silica materials have different morphologies and pore size and shape. According to US food and drug administration - FDA (21CFR172.480), silica is considered, since few years, to be relatively safe and biocompatible and indeed in the last decades has been used for bio-medical applications. For example mesoporous silica has been widely investigated for drug delivery application.<sup>22</sup> The interest in these types of materials is clearly evidenced in the literature. Since the year 2010, more than 1500 papers have been published which are related with mesoporous silica each year. Just to cite few of the newest uses in different fields, mesoporous silica have been used as host of dyes for long term bio-imaging in vivo.<sup>23</sup> Hallowed mesoporous silica particles have been developed for drug delivery application.<sup>24, 25</sup> Palladium nanoparticles loaded mesoporous silica are applied as

catalysts in hydrogenation reactions.<sup>26</sup> Other catalyst application such as hydrocarbon oxidation by iron-porphyrin immobilized on SBA-15 has been developed.<sup>27</sup> Mesoporous silica has also been used in sensing applications such as surface-enhanced Raman scattering, by coating it on gold nanorods.<sup>28</sup>

Other mesoporous material can be also synthesized in a similar way compare to mesoporous silica. Titanium dioxide which is also called titania, due to its semiconductive nature and photocatalytic ability, has attracted a lot of research interests.<sup>29, 30</sup> Combining the unique property of titania and the advantage of porous material together, this material can be applied to many promising applications. Shortly after the announcement of mesoporous silica in 1994, synthesis of porous tungsten oxide and titania contained mesoporous silica have been reported.<sup>31, 32</sup> Finally, thermally stable mesoporous titania synthesis was first reported by D.M. Antonelli and J.Y. Ying in 1995.<sup>33</sup> In the synthesis procedure, titanium isopropoxide and tridecylphosphite have been used as titanium source and surfactant respectively. After that, more synthesis methods have been developed and mesoporous titania has been used for a wide range of applications such as photocatalysis, photovoltaics, lithium battery and sensors.<sup>1, 2, 34-36</sup> According to FDA (21CFR73.575), titania is also considered to be safe, thus, it can also be used in bio applications.<sup>37</sup> In recent years, new type of mesoporous titania material such as the one with inter-connected pores have been developed.<sup>38</sup> Also, some new development has been made in the solar cell field by combining mesoporous titania with perovskite.<sup>39, 40</sup> Hybrid hydrophobic mesoporous titania has been developed for photocatalytic application.<sup>41</sup>

In the group of Prof. De Cola, previous researchers have developed functionalized mesoporous silica particles for drug delivery,<sup>42</sup> and also, zeolites LTL functionalized in different ways have been used in as carriers systems for imaging agents and for gene therapy.<sup>43</sup> In addition such materials have been used to create patterned substrates for cell adhesion in bio-application.<sup>44</sup> The group is interested in developing new porous materials based on hybrid silica and titania with the control of the morphology and the pore, which can be used in bio- or electronic applications.

The synthesis and characterization of the porous materials are described as following (Table 2.1). It can be seen that depending on the materials, each series of porous materials have been synthesized via a different approach. For microporous materials such as zeolite, since the pore size is based on the crystal structure itself, gel crystallization under hydrothermal condition has been used for the synthesis.<sup>14</sup> Instead of tailoring the pore size, we will describe how we manage to obtain zeolite crystals of different morphology. The mixing and aging time, as well as the crystallization condition, is critical to get perfect crystal structure. As for mesoporous materials such as silica and titania, we have employed surfactant template based sol-gel synthesis, and to certain extend evaporation induced self-assembly (EISA) method.<sup>45-47</sup> In all cases, modification and optimization of described conditions have been applied to each synthesis route. The morphology of the materials was characterized by scanning electron microscope (SEM) and transmission electron microscope (TEM). The pores (size and shape) were characterized by TEM, small angle X-ray scattering (SAXS) and nitrogen adsorption measurements. The crystal structures were obtained by powder X-ray diffraction (PXRD).

**Table 2.1** List of the synthesized porous materials and their properties.

Material	Description	Pore size
Zeolite LTL	Disc shaped, 1 $\mu\text{m}$ diameter, 200 nm or less thickness	0.7 nm
Zeolite LTL	Barrel shaped, 800 nm diameter, 400 nm thickness	0.7 nm
Zeolite LTL	Hexagonal shaped, 2 $\mu\text{m}$ diameter, 5 $\mu\text{m}$ length	0.7 nm
MCM-41	Sphere, 100 nm diameter	3 nm
SBA-15	Hexagonal interconnected	12 nm
Titania particle	Sphere, 400 nm diameter	11 nm
P123-titania	Film	7 nm
P123-silica/titania	Film	8 nm

*In this chapter, big effort has been devoted to synthesize and to control the morphology and properties of porous materials based on silica, titania and to a less extent on zeolites.*

## 2.2 Zeolite LTL

### 2.2.1 Synthesis and morphology control of zeolite LTL

The procedure of zeolite LTL synthesis is shown in Fig. 2.2. Zeolite LTL crystals are synthesized using a hydrothermal condition from gels containing aluminum source, silicon source, the necessary counter ions and alkalinity environment. Upon mixing of the two solutions, the crystallization is carried out at relatively high pressure and temperature in either static or dynamic conditions by using sealed vessels and an oven equipped with a rotating unit. After that, the obtained crystals are washed with water to remove the base in order to stop the crystal growth. Finally, the sample is changed with other counter ions based on certain needs. Typically, the obtained zeolite LTL material was suspended into certain amount (10 mL/g) of saturated water solution of the target ion ( $K^+$  from  $KNO_3$  for example) for 5h at  $50^\circ C$ . The exchanged zeolite LTL was washed by water several times and dried at  $80^\circ C$  for 16h.

As we have seen from the previous synthesis, the gel composition and the crystallization condition play an important role on the final morphology of zeolite LTL. Even though the first report of zeolite LTL synthesis was in the 1960s,<sup>48</sup> the detailed mechanism of the crystal growth is still unclear. Through years, people were trying to find out the parameters that can affect the final morphology.<sup>49-51</sup>

S. Megelski and G. Calzaferri investigated the influence of the gel composition and the crystallization conditions.<sup>49</sup> It was found that within a certain range, more water content in the starting gel results in bigger crystals. Increasing the alkalinity would result in shorter crystals with an almost constant diameter, but more intergrowth at the crystal ends. The addition of  $Na^+$  instead of  $K^+$  (up to 50%) would give increasingly larger and better crystal quality with decreasing inter growths. By using dynamic condition for crystallization, larger crystals with smoother surfaces can be obtained. Higher crystallization temperature would shorten the crystallization time.

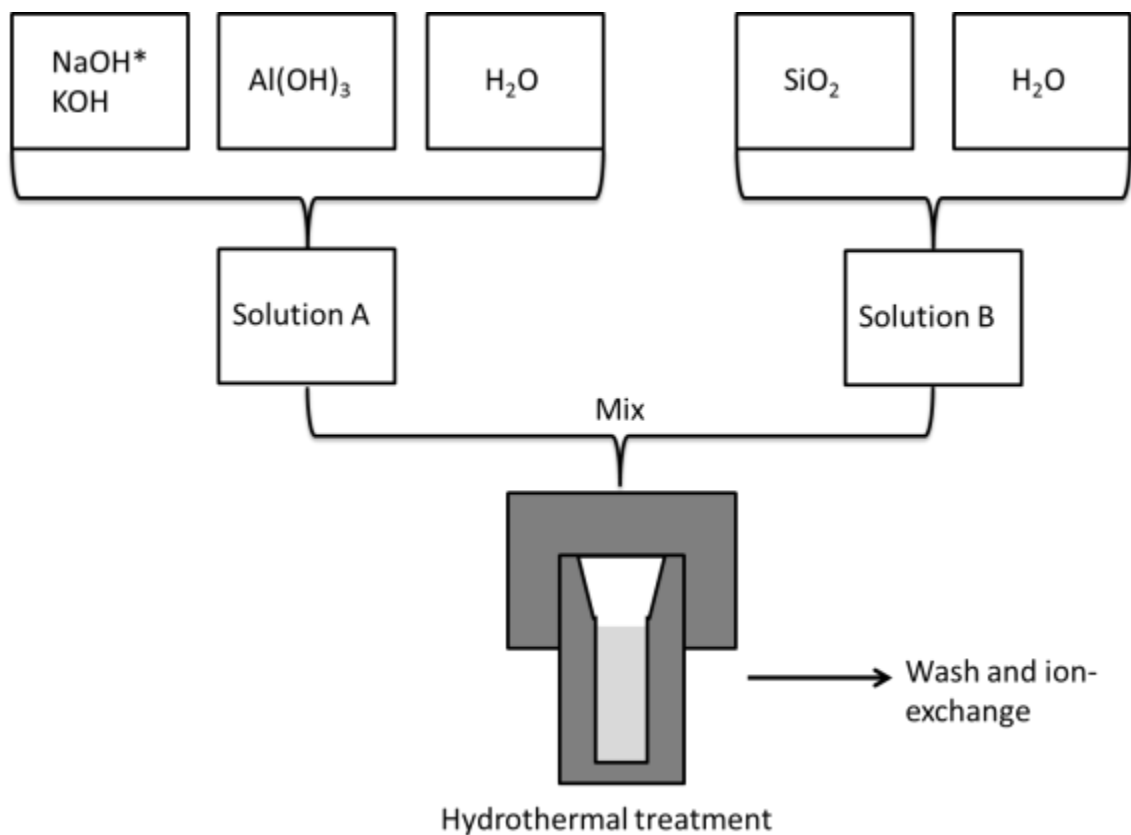


**Fig. 2.2** Schematic procedure of the zeolite LTL synthesis.

The effects of both the chemical and the physical parameters on the crystal size and morphology of zeolite L synthesis were studied by O. Larlus and V.P. Valtchev.<sup>50</sup> They conclude that the water content and the concentration of the K<sub>2</sub>O in the initial gel showed the most pronounced effects. Higher water content leads to longer crystals and higher alkalinity leads to smaller crystals. Introduction of Ba<sup>2+</sup> in the starting gel would give smaller crystals. Within one week, longer aging time leads to smaller crystals, while for 2-4 weeks, aging gives more uniform crystals but the size doesn't decrease anymore. Higher crystallization temperature would result in longer crystals.

The group of K.B. Yoon investigated the influence of the composition of the starting gel.<sup>51</sup> It is shown that higher SiO<sub>2</sub> content gives bigger crystals and a shape change from cylinder to hexagon but with more structures with non-specific morphology. Higher K<sub>2</sub>O content leads to smaller crystals and a change of crystals from hexagonal prism shape to

the cylindrical shape. Higher water content results in bigger crystals with flatter surface. By using  $\text{Al}_2(\text{SO}_4)_3$  as Al source, longer crystals with constant diameter are obtained with higher Al content. If the Al source is changed to  $\text{Al}(\text{OH})_3$ , longer crystals with decreasing diameter are obtained with higher Al content. Higher water content would give longer but thinner crystals. Different additive ions ( $\text{Na}^+$ ,  $\text{Li}^+$ ,  $\text{Mg}^{2+}$ ,  $\text{Ca}^{2+}$ ) gives different effects on the final morphology. Specifically for NaOH, the increase of its content would result in shorter crystals.

### 2.2.2 Disc shaped zeolite LTL

To obtain disc shaped zeolite L, solution A was made using 9.32 g KOH and 5.87 g NaOH with 59.5 g MilliQ water, then 2.1 g  $\text{Al}(\text{OH})_3$  was added and refluxed for 3 h to make it full dissolve. The solution was cooled down to room temperature and the lost volume of water during refluxing was re-added. Solution B was made of 58.9 g Ludox HS-40 (silica suspension in water) with 4.8 g EtOH. The solution was kept under sonication for 30 min. After these two solutions were ready, solution A was poured quickly into solution B with vigorous stirring. The stirring was kept for 10 min. The result milky steady liquid was split into 2 pressure vessels, put into a rotating oven at  $160^\circ\text{C}$  for 72 h with a rotating speed of 20 rpm. Afterwards, the vessels were cooled down in ice bath for 1 h. The final product was neutralized by washing with MilliQ water using centrifugation several times at 3100 rpm for 15 min until pH is 7.

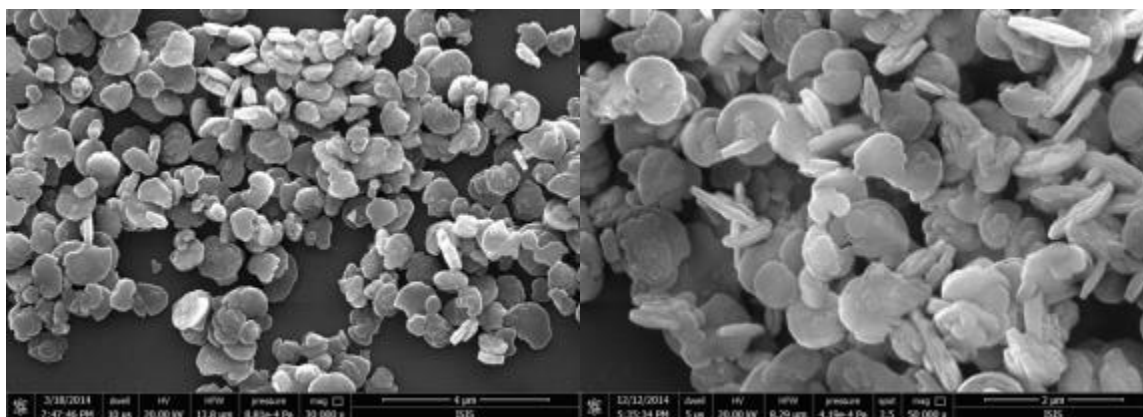


**Fig. 2.3** SEM images of the disc shaped zeolite LTL. Crystallization time 72h (left) and 48h (right).



SEM was used for characterization of the morphology of our material. We can see that the disc has a diameter of 1  $\mu\text{m}$  and a thickness around 200 nm (Fig. 2.3 left). If we shorten the crystallization time to 48 h other than 72 h, the diameter of the disc did not change but the thickness was thinner (Fig. 2.3 right). This indicates that during the crystallization, the disc shape itself on the diameter direction was formed relatively fast.

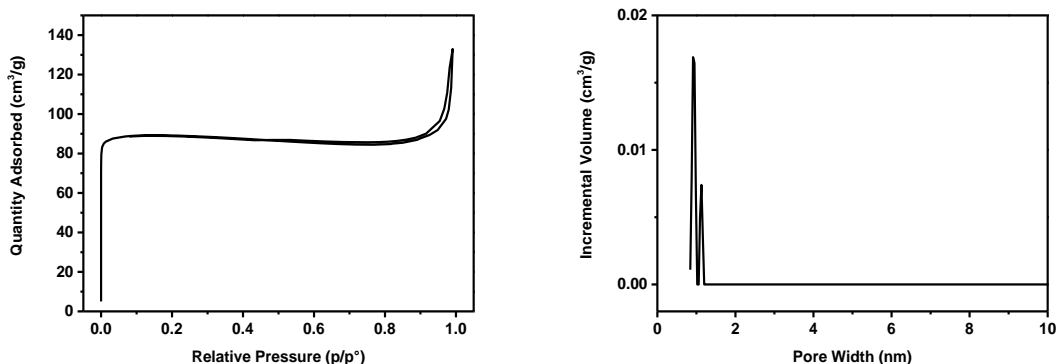


**Fig. 2.4** Nitrogen adsorption isothermal curve and pore distribution of disc shaped zeolite LTL.

From the nitrogen adsorption measurement we can see that the adsorption and desorption gave us a very obvious type I isothermal curve (Fig. 2.4). The characteristic of this curve is that the capacity condensation of the gas molecules inside the pores is overlapped with the monolayer Langmuir adsorption. It is suggested that we have micro-pores in our material which is exactly what zeolite LTL has. By DFT model the pore distribution was calculated. We have obtained the typical pore size for zeolite LTL which is 0.71 nm. Since the pores of the zeolite LTL was formed by the unique arrangement of the crystal, another pore size around 1 nm has also been observed which represents the bigger part of the crystal structure (see the crystal structure of zeolite LTL in Fig. 2.1). Due to the unique shape of the zeolite (disc), large spaces ( $>50\text{nm}$ ) in between the particles were observed at high relative pressure in the right part of the isothermal curve. As we introduced before in chapter 1, for microporous material, t-plot method have been developed for the micropore analysis.<sup>52</sup> The disc shaped zeolite LTL we synthesized is pure microporous material without any presence of mesoporosity. This suits well with the

t-plot method. All the pores are made from crystal structure so they have homogeneous cylindrical shape. The DFT cylindrical mode is thus suitable for the calculation. According to our analysis, by applying t-plot method and DFT method,  $0.138 \text{ cm}^3/\text{g}$  and  $0.135 \text{ cm}^3/\text{g}$  of pore volume has been obtained respectively which show very small difference.

The crystal structure of the disc shaped zeolite LTL has been obtained by PXRD (Fig. 2.5). The pattern was compared with the existing zeolite LTL PXRD pattern in the zeolite database.<sup>53</sup> It is confirmed that we have obtained the zeolite LTL crystals.

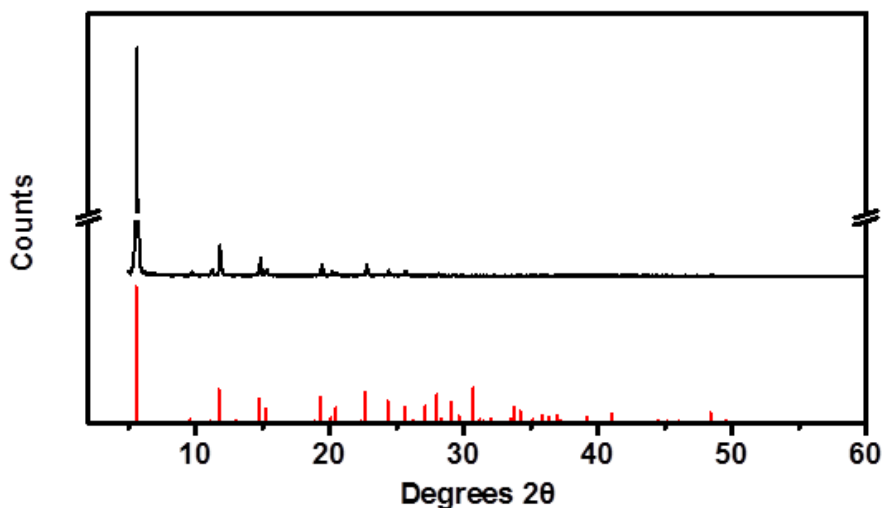


**Fig. 2.5** PXRD pattern of disc shaped zeolite LTL (up); simulated XRD pattern of zeolite LTL.

### 2.2.3 Barrel shaped zeolite LTL

Solution A: Solution A: 8.1 g KOH was dissolved into 25.4 g milliQ water, then 3.5 g  $\text{Al}(\text{OH})_3$  was added into the solution. The final solution was refluxed for 16 h, then cool down to room temperature. The water loss during the reflux has been re-added.

Solution B: 12.9 g Aerosil OX-50 (silica) was suspended into 30.2 g milliQ water. The solution was kept static for 1 h, then mixed again with stirring.

Solution A was poured into solution B with vigorous stirring. The mixture was stirred for 3 min, then transferred into pressure vessels, and kept at 160°C for 42h at 20rpm of rotation. The vessel was taken out and cooled in ice bath for 1 h. The final product was washed with milliQ water until the pH is 7.

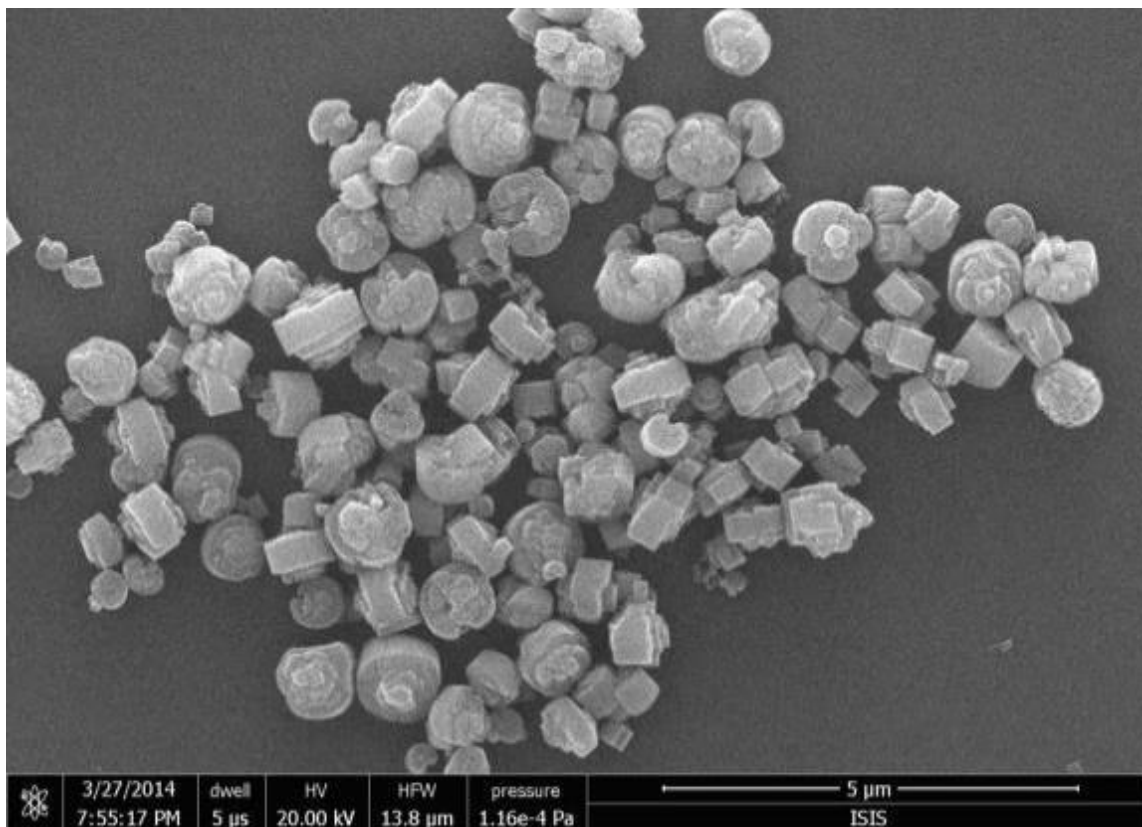


**Fig. 2.6** SEM image of the barrel shaped zeolite LTL.

SEM image shows that we have synthesized zeolite LTL crystal of around 800 nm in diameter and 400 nm in thickness (Fig. 2.6). The crystals are big and not inter-connected which shows clearly the orientation of the crystal.

From the nitrogen adsorption measurement we can see that the adsorption and desorption gave us a similar curve with the disc shaped zeolite LTL introduced before (Fig. 2.7). It is also a type I curve since the crystal structure is the same. The difference we observe with the disc shaped zeolite LTL is that we didn't see a significant large space in between the particles due to the morphology difference of these two zeolites. The pore volume from t-

plot and DFT is  $0.138 \text{ cm}^3/\text{g}$  and  $0.140 \text{ cm}^3/\text{g}$  respectively. Since the barrel shaped zeolite LTL is pure microporous material, it suits both t-plot and DFT model. Also, compare to disc shaped zeolite LTL, they have the same pore volume because they have the same crystal structure.

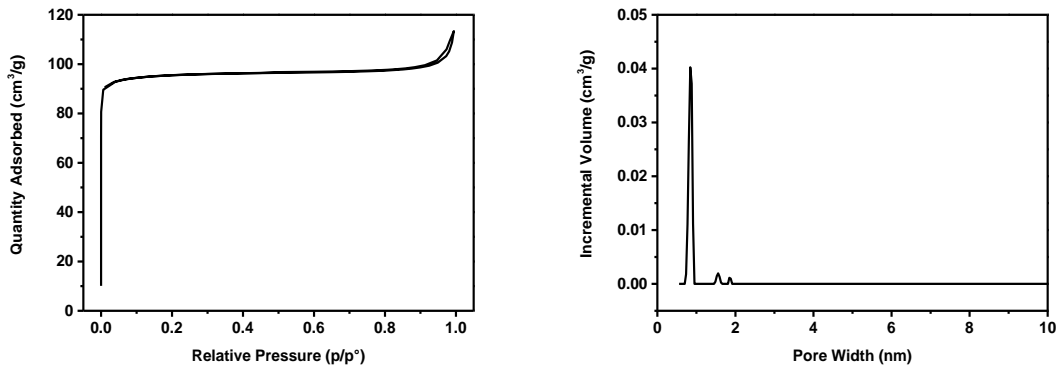


**Fig. 2.7** Nitrogen adsorption isothermal curve and pore distribution of barrel shaped zeolite LTL.

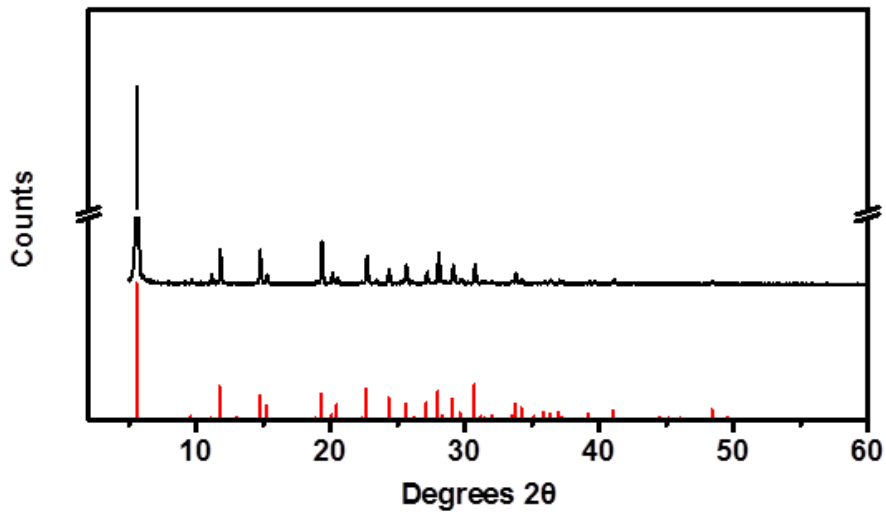


**Fig. 2.8** PXRD pattern of barrel shaped zeolite LTL (up); simulated XRD pattern of zeolite LTL.

The crystal structure of the barrel shaped zeolite LTL have been characterized by PXRD (Fig. 2.8) and compared with the existing zeolite LTL PXRD pattern in the zeolite database.<sup>53</sup> It is confirmed that we have obtained the zeolite LTL crystals.

#### *2.2.4 Hexagonal shaped zeolite LTL*

3.11 g KOH was dissolved into 22 g milliQ water and under stirring at 0°C for 5 min. 0.58 g Al powder was added into the previous solution in nitrogen atmosphere and stirred at 0°C for 15 min, then at room temperature for 1.5 h. The solution was then taken out from the nitrogen atmosphere and filtered with filter paper to make it clear (get rid of the other X(OH) from the impurity from the Al powder). The filtered solution was stirred for another 5-10 min, then 14.34g Ludox HS-40 was added under vigorous stirring. The solution was continued stir for 5 more min. The result solution was transfer into pressure vessel and put at 175°C for 72 h at static condition. The vessel was then taken out and cooled in ice bath for 1 h. The product was washed by water using centrifugation several times at 4000 rpm for 8 min until the pH is neutral.

SEM image shows us the morphology of this zeolite. Large hexagonal crystals with around 5 µm in length and 2 µm in diameter were successfully synthesized (Fig. 2.9). The orientation of the crystals was also clearly seen by SEM.

From the nitrogen adsorption measurement we can see that the adsorption and desorption also gave us a similar curve with the previous two zeolite LTL (Fig. 2.10). It is also a type I curve since the crystal structure is the same. Since the crystal of this zeolite is relatively very big, the space in between the particles also becomes very big and cannot be considered as pores anymore. In this case the increase of the quantity adsorbed at high relative pressure in the right part of the isothermal curve was not observed. The pore volume from t-plot method and DFT calculation is 0.126 cm<sup>3</sup>/g and 0.130 cm<sup>3</sup>/g respectively, which are comparable with the previous zeolites.

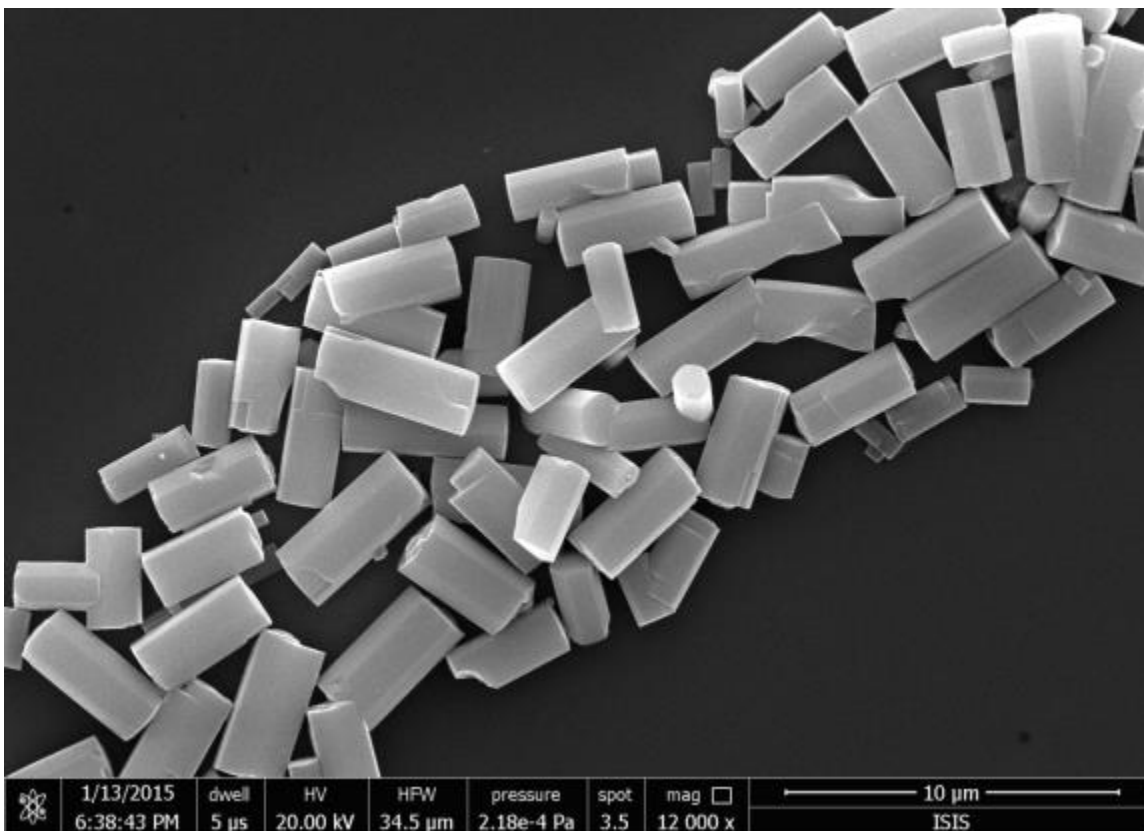


**Fig. 2.9** SEM image of the big hexagonal shaped zeolite LTL.

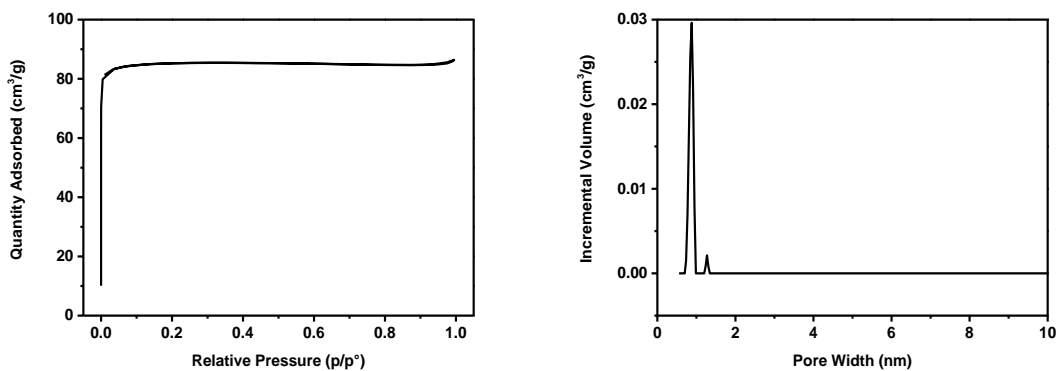


**Fig. 2.10** Nitrogen adsorption isothermal curve and pore distribution of big hexagonal shaped zeolite LTL.

The crystal structure of the disc shaped zeolite LTL have been characterized by PXRD (Fig. 2.11) and compared with the existing zeolite LTL PXRD pattern in the zeolite database.<sup>53</sup> The zeolite LTL crystal was confirmed.

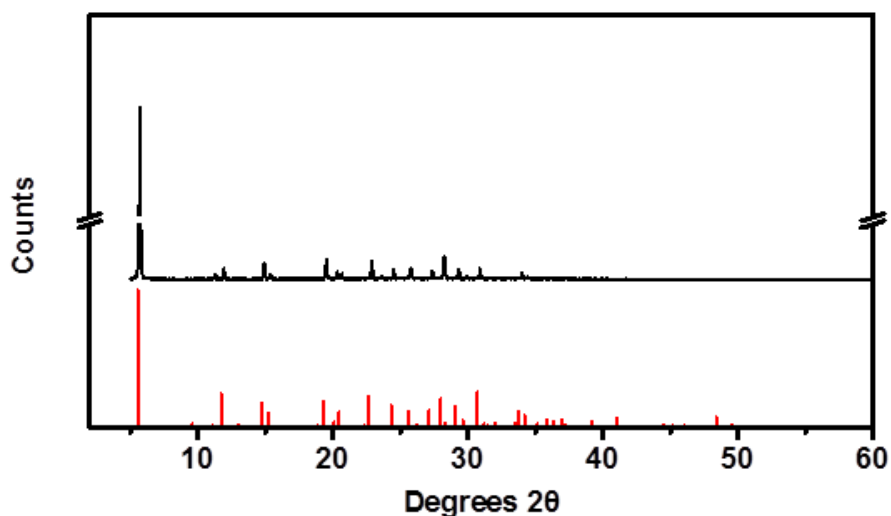


**Fig. 2.11** PXRD pattern of big hexagonal shaped zeolite LTL (up); simulated XRD pattern of zeolite LTL.

Generally speaking, without the additives, the most important factors for gel composition are the alkalinity and the Al content. From disc shaped to barrel shaped until hexagonal shaped zeolite LTL, bigger and longer crystals were synthesized. Zeolite LTL crystallites become larger when increasing the  $\text{SiO}_2/\text{Al}_2\text{O}_3$  or the  $\text{H}_2\text{O}/\text{Al}_2\text{O}_3$  ratio within a range of the starting gel. More  $\text{K}_2\text{O}$  (also higher alkalinity) in the starting gel would result in smaller zeolite L crystals.

## 2.3 Mesoporous silica material

### 2.3.1 Synthesis method and theory of mesoporous silica

Scheme of mesoporous silica/titania synthesis can be found in Fig. 2.12. The basic principle is that the self-assembly of surfactants form micelles in solution first, and then the silica/titania precursor such as tetraethyl orthosilicate and titanium isopropoxide polymerize outside the micelle template. The polymerized sample is then calcined in order to remove the organic surfactant. Mesoporous material is thus obtained.

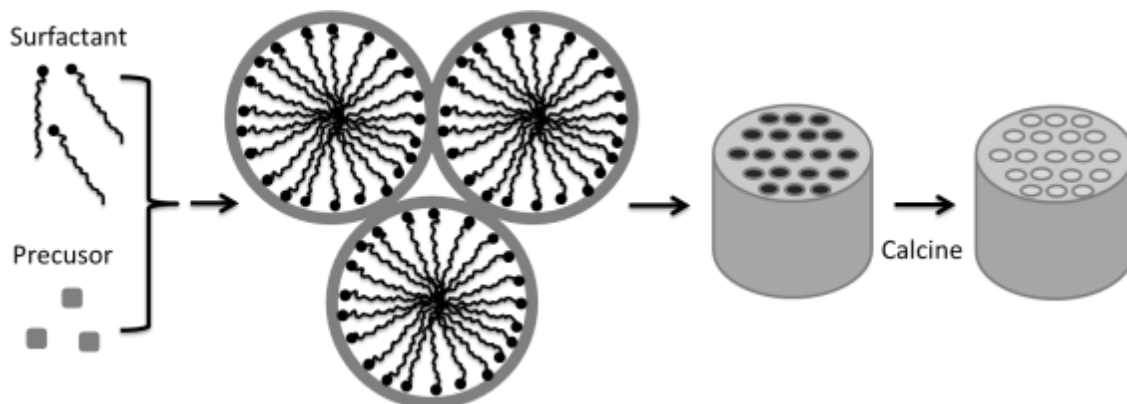


**Fig. 2.12** Schematic illustration of silica/titania sol-gel synthesis procedure.

As mentioned above in the synthesis of silica/titania material, the common principle is that in solution, the self-assembly of amphiphilic molecules forming micelles, and the silica/titania precursor polymerize outside the micelles to build the framework. It is essential to know the self-assembly behavior of these molecules in solution. Thus, the self-assembly of ionic surfactants have been studied by different groups in the 1970s.<sup>54,55</sup> For hexadecyltrimethylammonium bromide (CTAB), the self-assembly micelles formation below and above critical micelle concentration (CMC) have been investigated. Under certain temperature in solution, the self-assembly of CTAB molecule could be formed as monolayer, sphere, rod, cylinder or bilayer structures. By using the self-assembly structure of CTAB in solution as template, different materials could be synthesized. The self-assembly of amphiphilic polymers in solution was studied in the 1990s.<sup>56</sup> In this study, the detailed phase diagrams of several polymers have been shown. The morphology varies from isotropic, cubic, hexagonal, lamellar and multi-phase which depends on the concentration and the temperature of different polymer solutions. As we can see, after the self-assembly of surfactant was studied, further investigation about the interaction between the surfactant template and the material should be done. Indeed, the molecular and mesoscopic organization in silicate-surfactant system in basic aqueous solution has been studied.<sup>57</sup> It is suggested that the governing interactions between the silicate and the micelles are attractive inter-aggregate forces, which leads to the separation of the silicate-surfactant system and aqueous system. Thus, the polymerization of the silicate can be done surrounding the micelle template. All these theories and



experimental discoveries give us the details of how we can use the self-assembly of different micelle formation and sol-gel methods to synthesize mesoporous materials.

### 2.3.2 MCM-41 type mesoporous silica

CTAB 0.5 g was dissolved in a mixture of distilled water (240 mL) and 2M concentration solution of sodium hydroxide (1.75 mL). The solution was heated to 80°C and stirred vigorously. In another flask, tetraethyl orthosilicate (TEOS, 2.5 mL) was dissolved in ethanol (3 mL) and 3-Aminopropyl triethoxysilane (APTES, 100 µL) was added. Once the temperature of the CTAB solution had stabilized, the ethanol solution containing TEOS and APTES was added with vigorous stirring. After 2 h, the solution was cooled to room temperature and the particles were centrifuged and washed with methanol several times, dried in vacuum and calcined at 550°C for 6 h to remove the remaining surfactant.

The morphology and the pore orientation of the particles were characterized by SEM (Fig. 2.13 left) and HR-TEM (Fig. 2.13 right). From analysis of both the images we can see that the homogeneous particles are sphere shaped and with a diameter of around 100 nm. The pores are clearly seen under TEM. The pores are arranged parallel with each other without any inter-connection in between. This means that all pores are accessible. The pore arrangement in MCM-41 type mesoporous silica particles is similar with zeolite LTL even though the pores are larger here.

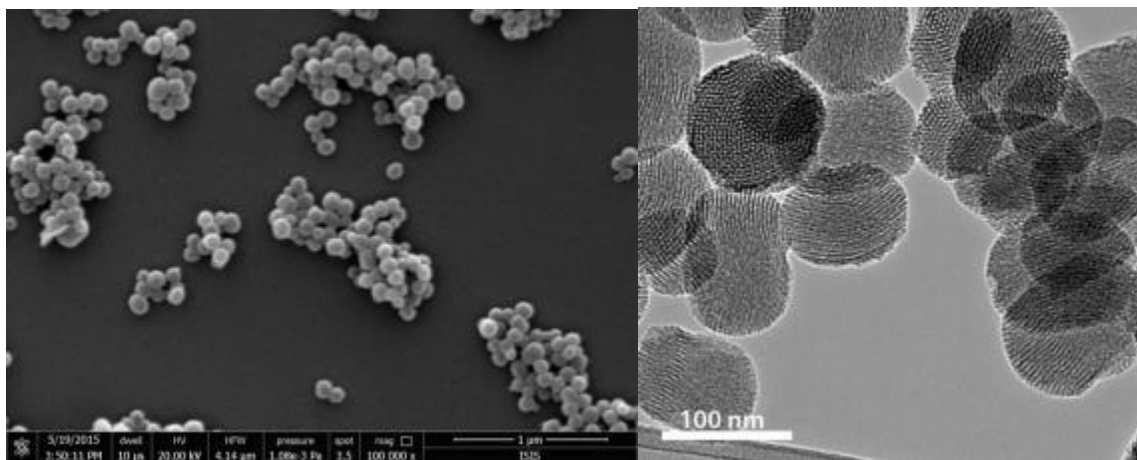


**Fig. 2.13** SEM and TEM images of the MCM-41 type mesoporous silica particles.

From the nitrogen adsorption measurement we can see that the adsorption and desorption gave us a not very typical IV isothermal curve (Fig. 2.14). The capacity condensation of the nitrogen gas molecules in small mesopores during the adsorption process is overlapped with the region of the multiple-layer adsorption. It is suggested that we have mesoporosity in MCM-41 type mesoporous silica. In the condensation process, no adsorption hysteresis was observed suggest that the pore diameter is constant without variation. By DFT model the pore distribution was calculated. The pores are mono-dispersed and the diameter of the pore is 3.4 nm. Since the diameter of the particles is only 100 nm, the aggregation of particles formed large spaces (>50nm) in between the particles at high relative pressure in the right part of the isothermal curve. As it is shown is chapter 1, traditionally BJH method has been applied for measuring the mesopororous structure.<sup>58</sup> By BJH and DFT method, the obtained pore diameter is 2.1 nm and 3.4 nm respectively, the error of around 30% is comparable with the earlier discovery of some researchers.<sup>59</sup> This would be another proof that for small sized mesopores, DFT method should be used for the determination of pore size.

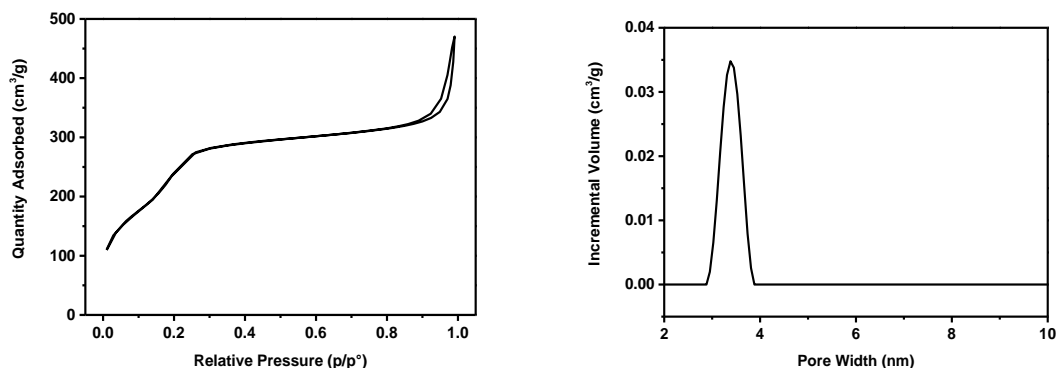


**Fig. 2.14** Nitrogen adsorption isothermal curve and pore distribution of MCM-41 type mesoporous silica.

Solid-state UV-Vis spectrum (Fig. 2.15 left) suggested that there is no absorption for MCM-41 type mesoporous silica in the visible and the near UV region which would result in no photo reactivity under sun light. SAXS pattern (Fig. 2.18 right) shows typical Bragg peaks of hexagonally arranged pores. Using Bragg's law, the distance ( $d$ ) is

calculated as 4.2 nm. This is the distance between the phases of the pores. For a hexagonal packed pores, a unit cell factor of  $2/\sqrt{3}$  is applied. The distance between the pore centers next to each other is thus 4.9 nm. The hexagonal lattice parameter is made up of the pore diameter and the thickness of the adjoin silica wall. From TEM image we can deduce a value for the silica wall thickness, namely about 1.4 nm. Subtracting this from the lattice parameter determined by SAXS we obtain a pore size of around 3.5 nm. Compare the result with nitrogen adsorption (3.4 nm), they show very small difference.

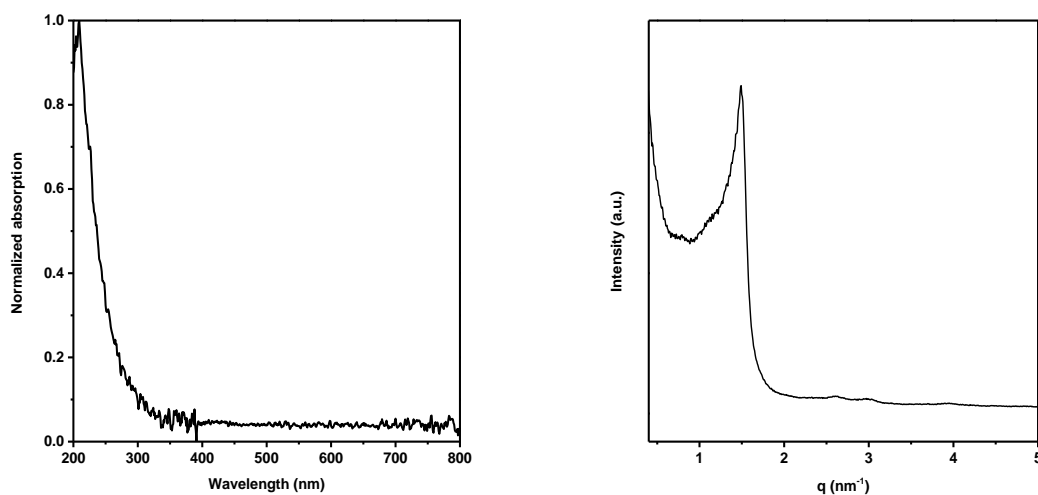


**Fig. 2.15** Solid state UV-Vis spectrum and SAXS pattern of MCM-41 type mesoporous silica.

### 2.3.3 SBA-15 type mesoporous silica

1.5 g [Poly(ethylene glycol)-block-poly(propylene glycol)-block-poly(ethylene glycol)] (Pluronic® P123) was dissolved into 42 mL water, then 4.36 g  $\text{Na}_2\text{SiO}_3 \cdot 9\text{H}_2\text{O}$  and 0.292 mL APTES was added. The solution was then heated up to  $40^\circ\text{C}$  with vigorous stirring. After the temperature was stable, 10.92 mL 37% HCl was added and the stirring was kept at  $40^\circ\text{C}$  for 1 h. The solution was transferred into a sealed glass bottle and kept at  $100^\circ\text{C}$  for 24 h. The final product was centrifuged and washed by water 3 times, then dried in vacuum, and calcined at  $550^\circ\text{C}$  for 6h to remove the remaining surfactant.

The SEM image shows us that the SBA-15 type mesoporous silica does not have certain clear morphology but likely to be hexagonal (Fig. 2.16 left). The size of the bulk is in the scale of micrometer. From the TEM image we see that the pores are packed together in a hexagonal order and parallel with each other (Fig. 2.16 right). The pore diameter is around 10 nm.

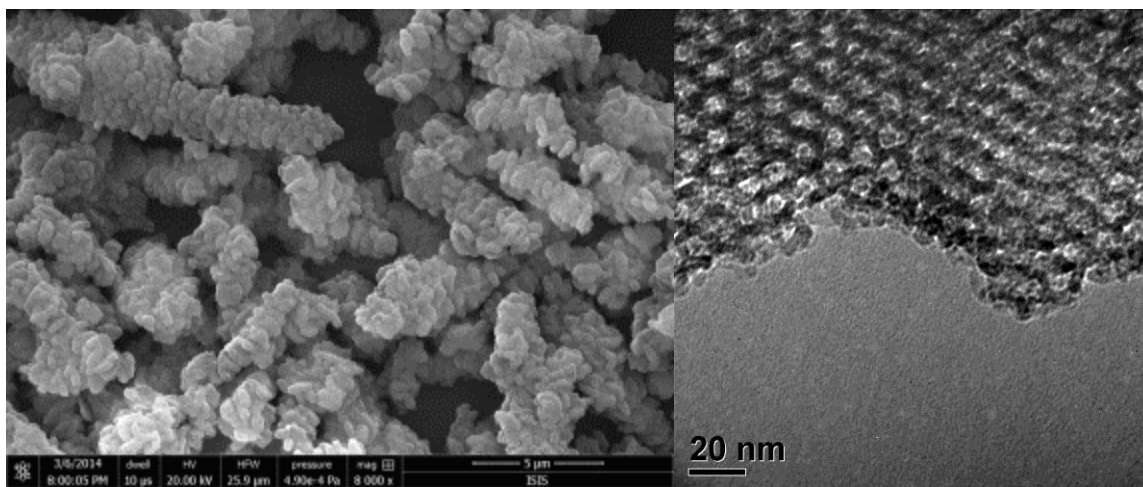


**Fig. 2.16** SEM and TEM images of the SBA-15 type mesoporous silica.

From the nitrogen adsorption measurement, we can see that the adsorption and desorption process gave us a typical IV isothermal curve (Fig. 2.17). Compare to the MCM-41 type mesoporous silica, the capacity condensation of the nitrogen gas molecules in big mesopores during the adsorption process is not overlapped with the region of the multiple-layer adsorption. We see the clear type IV curve with the steps of monolayer adsorption, multi-layer adsorption and capacity condensation in order. It is suggested that we have big mesopores in SBA-15 type mesoporous silica. During the pore condensation, adsorption hysteresis is observed. This indicates that for each pore, the pore size is not constant. By DFT model the pore distribution was calculated. The pores are mono-dispersed but with a little bit of variation which is typical for co-block polymer based surfactant and corresponded to the hysteresis we found in the isothermal curve. The diameter of the pore is 12 nm. Since the structure of the SBA-15 type mesoporous silica is quite big, only few large spaces (>50nm) in between the silica have been observed at high relative pressure in the right part of the isothermal curve. For the pore determination

methods, BJH method gave a pore size of 9.5 nm while for DFT method it was 12 nm. The error here is 20% which is smaller than the MCM-41 silica but still considerably big. As we see the hysteresis from the isothermal curve, we know the pore diameter is not constant in each pore. Thus, the pore condensation would happen when the condition of the condensation for the smallest diameter is fulfilled. In this case, DFT method provides more reliable data.

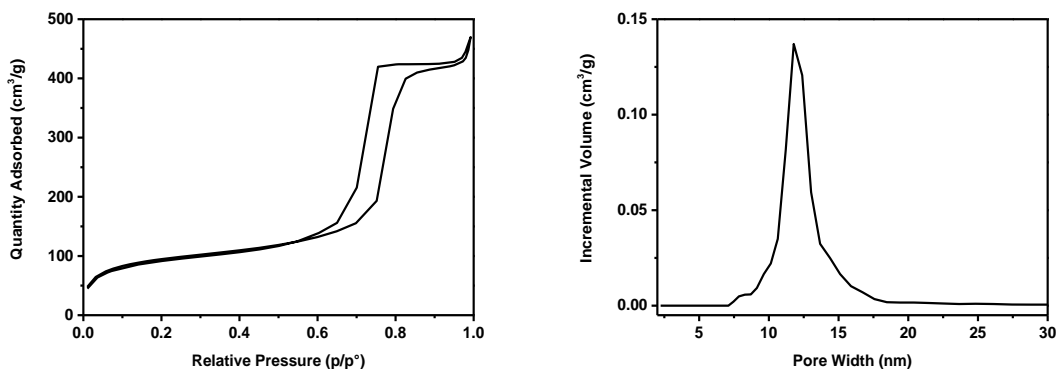


**Fig. 2.17** Nitrogen adsorption isothermal curve and pore distribution of SBA-15 type mesoporous silica.

Similar to MCM-41 type mesoporous silica, solid-state UV-Vis spectrum (Fig. 2.18 left) suggested that there's no absorption for SBA-15 type mesoporous silica in the visible and the near UV region. By SAXS pattern (Fig. 2.18 right), typical Bragg peaks of hexagonally arranged pores are shown. Using Bragg's law, the distance ( $d$ ) is calculated as 11 nm. This is the distance between the phases of the pores. For a hexagonal packed pores, a unit cell factor of  $2/\sqrt{3}$  is applied. The distance between the pore centers next to each other is thus 12.8 nm. The hexagonal lattice parameter is made up of the pore diameter and the thickness of the adjoint silica wall. From TEM image we can deduce a value for the silica wall thickness, namely about 1.6 nm. Subtracting this from the lattice parameter determined by SAXS we obtain a pore size of around 11.2 nm. Compare the result with nitrogen adsorption (12 nm), the value from SAXS is smaller. The reason is that as we mentioned before, the pore diameter in SBA-15 silica is not constant which leads to error to determine the wall thickness by TEM.

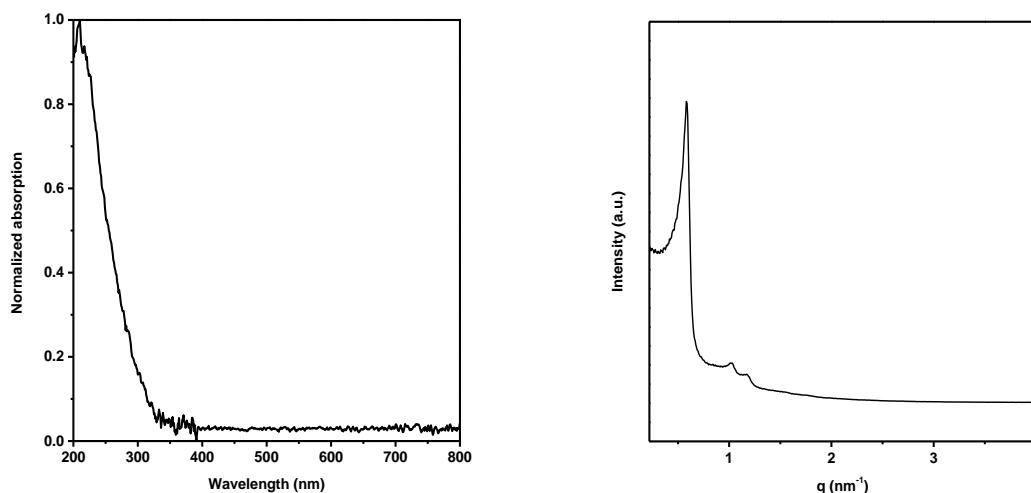


**Fig. 2.18** Solid state UV-Vis spectrum and SAXS pattern of SBA-15 type mesoporous silica.

## 2.4 Mesoporous titania

### 2.4.1 Mesoporous titania particles

1.21 g hexadecylamine was dissolved into 69 mL EtOH. MilliQ water was added into 27.5  $\mu$ L of KCl 1.0 M solution until 0.63mL. This solution was added into the first EtOH solution. Then 1.52 mL titanium isopropoxide (TIPO) was added with vigorous stirring. After the suspension was formed, it was kept static for 18 h at room temperature. The precipitate was washed by centrifugation 3 times using EtOH. The obtained powder was suspended into a mixture of 20 mL EtOH and 10 mL milliQ water. The suspension was transferred into a pressure vessel and kept at 160°C for 16h. The particles were then washed by EtOH and suspended into 28% ammonia solution (10 mL ammonia per 0.1g titania). The mixture was refluxed for 1 day to obtain the anatase phase.<sup>60</sup> The final product have been washed by EtOH several times and calcined at 350°C for 6 h.

Under the electron microscopes we see our particles are homogeneous and have a perfect sphere shape. The diameter of the particle is around 400 nm confirmed by both SEM (Fig.

2.19 left) and TEM (Fig. 2.19 right). The arrangement of the pore is random and worm like. The accessibility and the diameter of the pore cannot be determined by the electron microscope pictures.

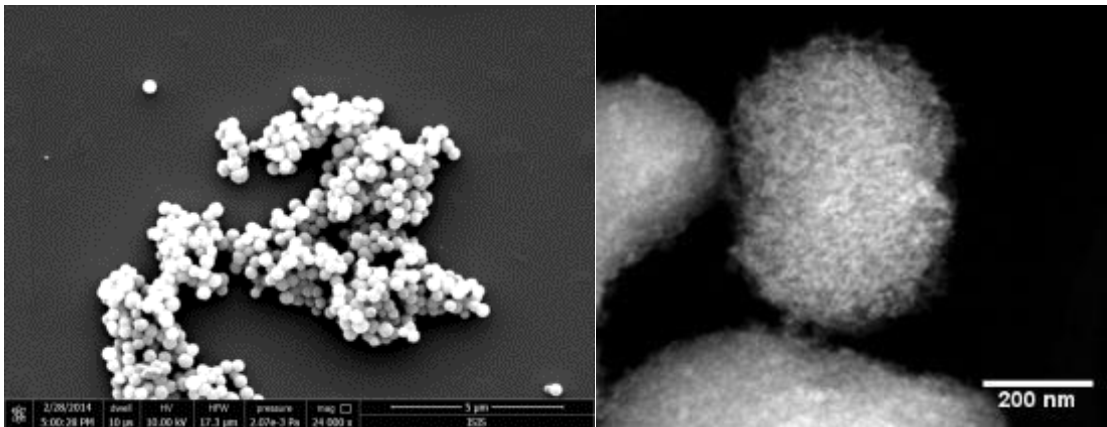


**Fig. 2.19** SEM and TEM image of the mesoporous titania particles.

The nitrogen adsorption measurement also gave us a type IV curve (Fig. 2.20). During the adsorption process, the three steps of monolayer adsorption, multi-layer adsorption and capacity condensation are clearly seen. Adsorption hysteresis suggested the variation of pore diameter for each pore. This also means that the pores of the particle are accessible from the environment outside. Due to the spherical shape, aggregation caused large space in between the particles was also observed. From the calculated pore distribution we see that the major pore size is around 11 nm but the distribution is quite broad which also corresponded to the hysteresis we found in the isothermal curve. The most possible reason is that crystalline titania is not thermally stable. During heat treatment or hydrothermal treatment, there is a possibility of having the rearrangement or the change of the crystal structure. This results in the change of the surrounding wall of the pores, leading to a loss in the regular shape and size.

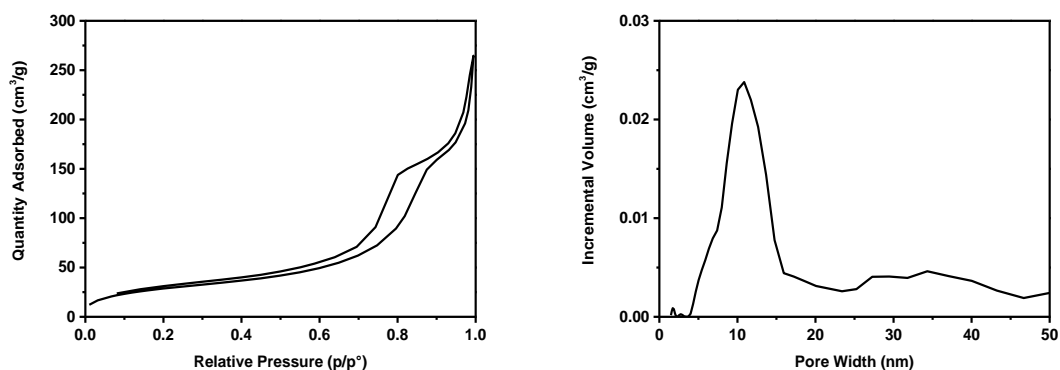


**Fig. 2.20** Nitrogen adsorption isothermal curve and pore distribution of mesoporous titania particle.

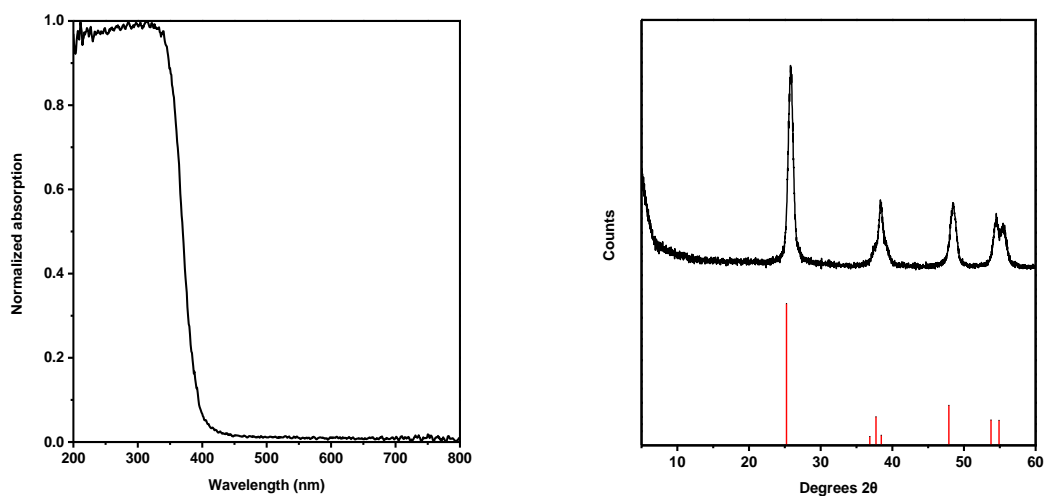


**Fig. 2.21** Solid state UV-Vis spectrum and PXRD pattern of mesoporous titania particle.

Solid-state UV-Vis spectrum (Fig. 2.21 left) showed a very typical absorption of titania which starts around 400nm. It is essential to know the starting point of absorption in order to estimate the band gap energy information. This discussion will be continued in the organotitania chapter (Chapter 7). PXRD pattern (Fig.2.21 right) showed that the crystal type of this material is anatase.



#### 2.4.2 Mesoporous titania film

1 g P123 was dissolved into 30 g EtOH. 1.8 g HCl (37%) was then added with vigorous stirring for 3 h. After that 3 g TIPO was added drop wise with vigorous stirring. The solution was then kept at 40°C for 20h with vigorous stirring. The result solution was speared into a petri dish at 35°C with water environment for 4 days, transferred into an oven at 80°C for another 6 days. The obtained bulk was then suspended into 28% ammonia solution (10 mL ammonia per 0.1g titania). The mixture was refluxed for 1 day. The final product was calcined at 300 °C (the temperature was increased slowly) for 6 h.

Similar to the silica/titania hybrid material, The SEM (Fig. 2.22 left) also shows no particular morphology after we broke it from the original film form. The TEM image shows us the same not well defined shape of bulk and some pore structures inside (Fig. 2.22 right).

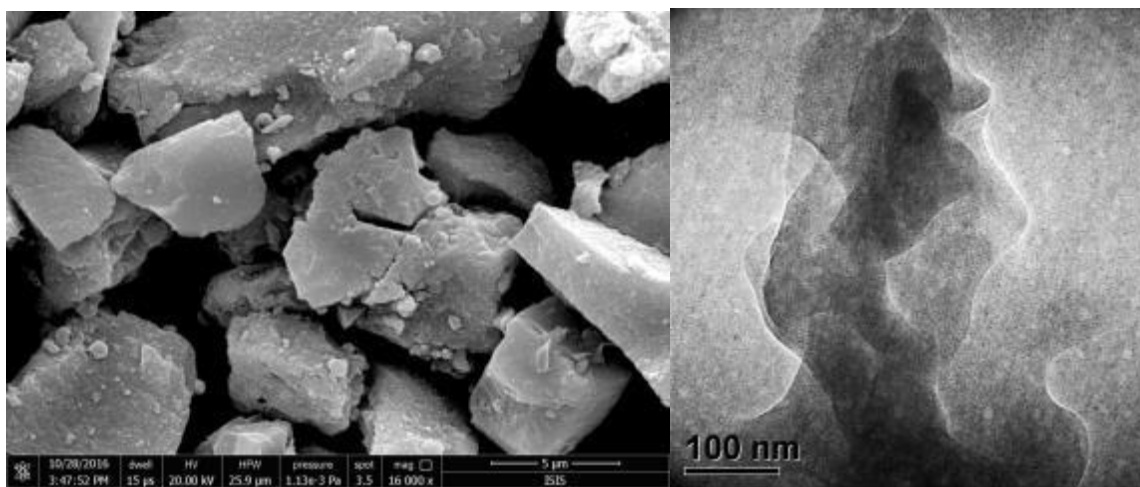


**Fig. 2.22** SEM and TEM images of the fragments of mesoporous titania film.

Like the other porous materials we have introduced before, we have also found a type IV curve from the nitrogen adsorption measurement (Fig. 2.23). Adsorption hysteresis indicated that pore diameter is not constant for each pore. Through the calculated pore distribution we can see the majority of pores have a diameter of 7 nm but in the meantime pores from 2 nm till 20 nm are also found. Same titania crystal change during the heat treatment can be applied here for the explanation of the pore distributions here.

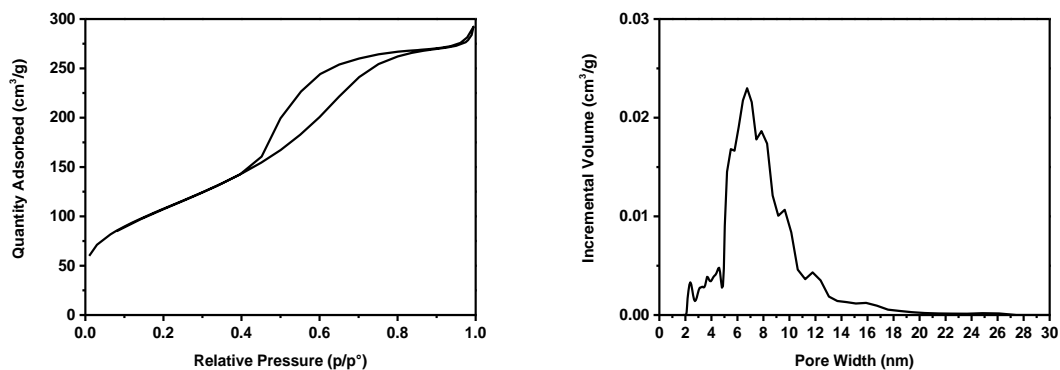


**Fig. 2.23** Nitrogen adsorption isothermal curve and pore distribution of mesoporous titania material.

Solid-state UV-Vis spectrum (Fig. 2.24 left) showed that the absorption is similar to titania material. The slight absorption in the visible region suggested that there were other species doped into the material. Most probably is that the film we have made is relatively thick compare to the micro to nano sized particles, it is difficult to completely remove the surfactant by calcine. Thus some carbon was doped into the material structure which caused the absorption in the visible region. PXRD pattern (Fig. 2.24 right) showed that the crystal type of this material is anatase.

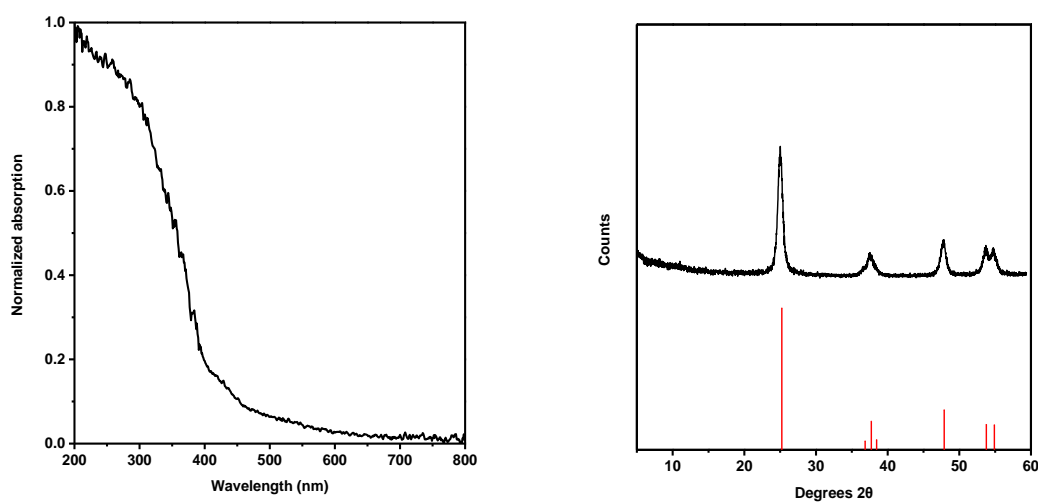


**Fig. 2.24** Solid state UV-Vis spectrum and PXRD pattern of mesoporous titania material.

In general, the quality of mesoporous material made from EISA method is not as good as the normal sol-gel method. The advantage of making mesoporous film through EISA method also gives the disadvantage of less thermal and mechanically stable structure. In this case, based on the purpose of application, the synthesis method of material should be carefully chosen.

## 2.5 Mesoporous silica/titania hybrid film

3 g P123 was dissolved into 90 g EtOH. 5.4 g HCl (37%) was then added with vigorous stirring for 3 h. After that 7.02 g TIPO and 1.29 g TEOS was added drop wise with vigorous stirring. The solution was then heated up and kept at 40°C for 5h with vigorous stirring. The result solution was speared into a petri dish at 35°C with water environment for 4 days, transferred into an oven at 75°C for another 6 days. The final product was calcined at 350 °C (the temperature was increased slowly) for 6 h.

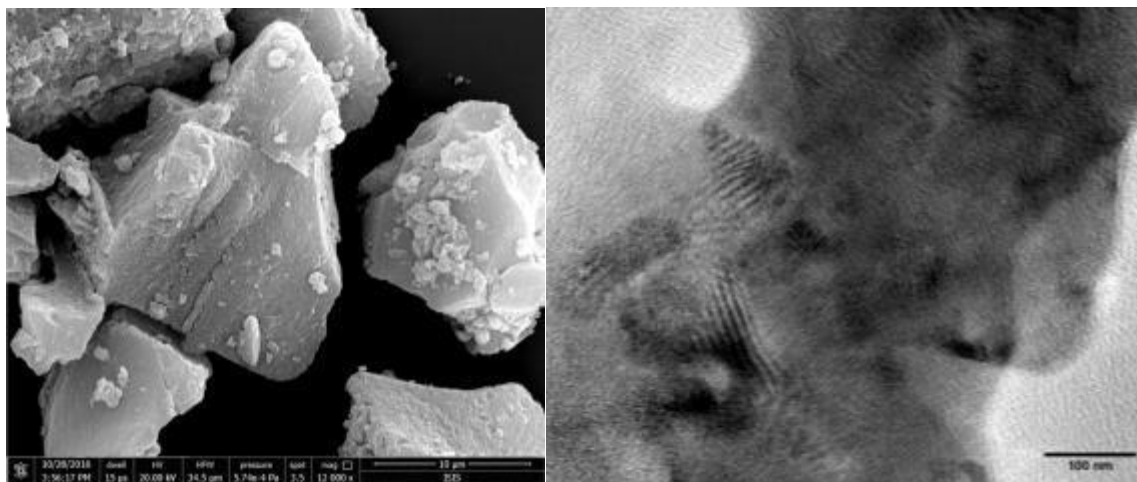


**Fig. 2.25** SEM and TEM images of the fragments of mesoporous silica/titania hybrid film.

The SEM image shows that there is no particular morphology for our silica/titania material after we break the initial film (Fig. 2.25 left). According to the TEM image there are some irregular pores which distribute randomly (Fig. 2.25 right). There are two possible reasons. First is that the material is made from both titania and silica which are

different crystals. Combining the different crystals together gives a lot of structural defects which leads to non-uniformed wall structure. Secondly, same as the titania material, the reorganization of the titania during heat treatment also cause defects and change of the structure.

The nitrogen adsorption measurement also gave us a type IV curve (Fig. 2.26). Unlike the other porous materials we have described before, the capacity condensation process of this silica/titania hybrid material lasts much longer. This is also the proof that in the material the pore size varies a lot. Also, adsorption hysteresis indicated that pore diameter is not constant for each pore. From the calculated pore distribution, we can see that the main pore diameter is about 8 nm but there are pores distribute from 4 nm until more than 40nm which corresponded with what we see from the isothermal curve.

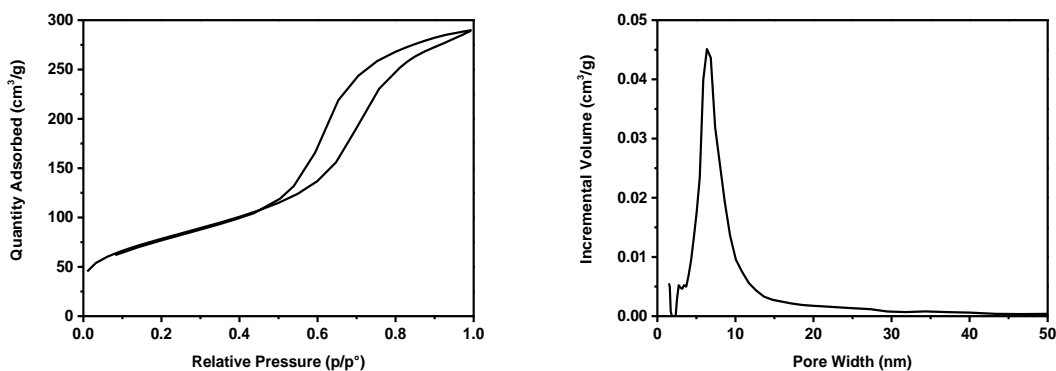


**Fig. 2.26** Nitrogen adsorption isothermal curve and pore distribution of mesoporous silica/titania hybrid material.

Solid-state UV-Vis spectrum (Fig. 2.27 left) showed that the absorption is similar to titania material since titania is one of the component and silica absorbs UV with smaller wavelength. Same slight absorption in the visible region is comparable with the EISA synthesized mesoporous titania. PXRD pattern (Fig. 2.27 right) showed that the major crystal type of this material is anatase. The crystallinity of this silica/titania hybrid is not as good as the other titania or zeolite material we have made. This is due to the fact that most of the silica component is amorphous. Among the amorphous silica structure, only small titania anatase crystals exist.

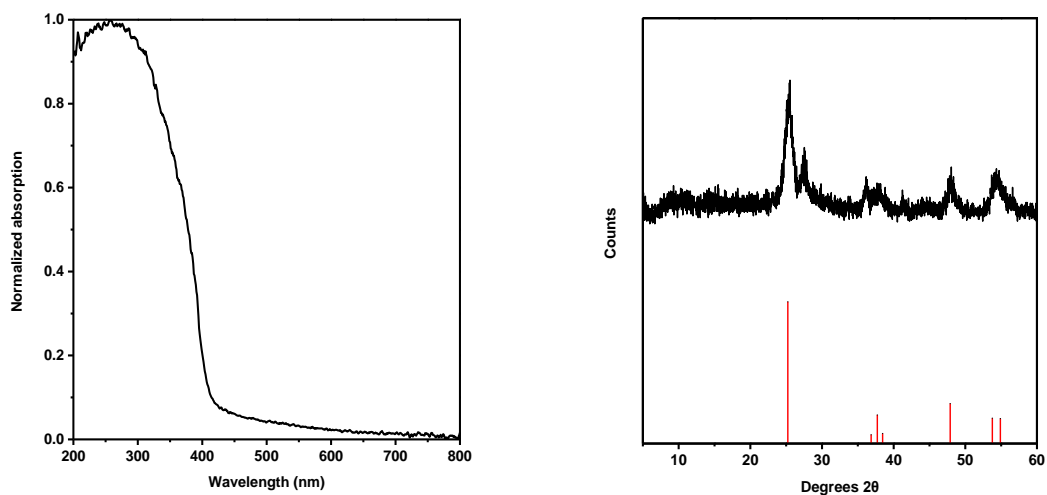


**Fig. 2.27** Solid state UV-Vis spectrum and PXRD pattern of mesoporous silica/titania hybrid material.

## 2.6 Conclusion and perspectives

In this chapter, several different zeolites, silica and titania materials have been successfully synthesized and characterized. The key factors during the synthesis procedure have been studied in detail. It is essential to know how to control the features of these basic inorganic materials. Based on the productions of this chapter, porous materials have been further functionalized and used for several applications in the following chapters.

## 2.7 Experimental section

### *Materials*

KOH (1 kg) and NaOH (1 kg) were bought from VWR chemicals, Al(OH)<sub>3</sub> (500 g, extra pure) and Hexadecyltrimethylammonium bromide (500 g, ≥99%) was purchased from Acros, Aluminum (100 g, grit for synthesis) was bought from Merck, Hexadecylamine (500 g, 90%), Sodium metasilicate nonahydrate (1 kg, ≥98%), Titanium(IV) isopropoxide (100 mL, ≥97%), Tetraethyl orthosilicate (1 L, 98%), (3-Aminopropyl) triethoxysilane (100 mL, 99%), hydrochloric acid (1 L, ≥37%) and Pluronic P-123 were bought from sigma-aldrich, Ludox HS-40 (1 L) was bought from Aldrich chemistry and Aerosil OX-50 was from AEROSIL company.

### *Scanning electron microscope*

Scanning Electron Microscope SEM images were recorded with a FEI Quanta FEG 250 instrument (FEI corporate, Hillsboro, Oregon, USA) with an acceleration voltage of 20kV. The sample is prepared by sputtering coated with Au (Emitech K575X peltier cooled) for 45 s at 60 mA prior to fixation on an Al support.

### *Transmission electron microscope*

TEM images were obtained on a Philips CM120 transmission electron microscope operating at 100 kV with a LaB<sub>6</sub> filament. Areas covered with molecules of interest were recorded under low dose condition, on a Pelletier cooled CCD camera (Model 794, Gatan, Pleasanton, CA).

### *Powder X-ray diffraction*

Powder X-ray diffraction (PXRD) data were collected using a Bruker D2-PHASER diffractometer using CuK $\alpha$  radiation ( $\lambda = 1.5418 \text{ \AA}$ ). The compounds were manually grounded in an agate mortar, then deposited in the hollow of a silicon sample holder.

### *Nitrogen adsorption*

Nitrogen adsorption analysis was performed using a Micromeritics porosimeter (model ASAP-2020). The samples were degassed at 250°C under vacuum for 6h and N<sub>2</sub> adsorption/desorption measurement was done at -196 °C. The surface areas were calculated by BET method. The pore size distributions and pore volume were calculated by DFT methods.

### *Solid-state UV-Vis spectrum*

The UV-Vis absorption spectra were measured by Shimadzu UV-3600 UV-Vis-NIR spectrophotometer. The samples were measured in solid state using integrating sphere and barium sulphate (BaSO<sub>4</sub>) was used as background.

## 2.8 References

1. R. Zhang, A. A. Elzatahry, S. S. Al-Deyab and D. Zhao, *Nano Today*, 2012, **7**, 344-366.
2. P. Innocenzi and L. Malfatti, *Chem. Soc. Rev.*, 2013, **42**, 4198-4216.
3. C. T. Kresge, M. E. Leonowicz, W. J. Roth, J. C. Vartuli and J. S. Beck, *Nature*, 1992, **359**, 710-712.
4. C. T. Kresge and W. J. Roth, *Chem. Soc. Rev.*, 2013, **42**, 3663-3670.
5. L. Han and S. Che, *Chem. Soc. Rev.*, 2013, **42**, 3740-3752.
6. S.-H. Wu, C.-Y. Mou and H.-P. Lin, *Chem. Soc. Rev.*, 2013, **42**, 3862-3875.
7. I. I. Ivanova and E. E. Knyazeva, *Chem. Soc. Rev.*, 2013, **42**, 3671-3688.
8. M. Moliner, C. Martínez and A. Corma, *Chem. Mater.*, 2014, **26**, 246-258.
9. A. F. Cronstedt, J. L. Schlenker and G. Kuhl, *K. vet. akad. handl.*, 1756, **18**, 120-123.
10. J. Smithson, *Philos. Trans. R. Soc. London*, 1811, **101**, 171-177.
11. K. Moller and T. Bein, *Chem. Soc. Rev.*, 2013, **42**, 3689-3707.
12. C. Baerlocher, L. B. McCusker and D. H. Olson, *Atlas of Zeolite Framework Types*, Elsevier, The Netherlands, 2007.
13. D. W. Breck, *Zeolite molecular sieves: structure, chemistry, and use*, John Wiley & Sons, New York, 1974.
14. Z. A. Ruiz, D. Brühwiler, T. Ban and G. Calzaferri, *Monatsh. Chem.*, 2005, **136**, 77-89.
15. R. Martinez-Franco, C. Paris, M. E. Martinez-Armero, C. Martinez, M. Moliner and A. Corma, *Chem. Sci.*, 2016, **7**, 102-108.
16. T. Ennaert, J. Van Aelst, J. Dijkmans, R. De Clercq, W. Schutyser, M. Dusselier, D. Verboekend and B. F. Sels, *Chem. Soc. Rev.*, 2016, **45**, 584-611.
17. P. Cao, O. Khorev, A. Devaux, L. Sägesser, A. Kunzmann, A. Ecker, R. Häner, D. Brühwiler, G. Calzaferri and P. Belser, *Chem. Eur. J.*, 2016, **22**, 4046-4060.
18. K. Kim, T. Lee, Y. Kwon, Y. Seo, J. Song, J. K. Park, H. Lee, J. Y. Park, H. Ihee, S. J. Cho and R. Ryoo, *Nature*, 2016, **535**, 131-135.
19. D. Zhao, J. Feng, Q. Huo, N. Melosh, G. H. Fredrickson, B. F. Chmelka and G. D. Stucky, *Science*, 1998, **279**, 548-552.
20. A. B. D. Nandiyanto, S.-G. Kim, F. Iskandar and K. Okuyama, *Microporous Mesoporous Mater.*, 2009, **120**, 447-453.



21. J. S. Beck, J. C. Vartuli, W. J. Roth, M. E. Leonowicz, C. T. Kresge, K. D. Schmitt, C. T. W. Chu, D. H. Olson, E. W. Sheppard, S. B. McCullen, J. B. Higgins and J. L. Schlenker, *J. Am. Chem. Soc.*, 1992, **114**, 10834-10843.
22. P. Yang, S. Gai and J. Lin, *Chem. Soc. Rev.*, 2012, **41**, 3679-3698.
23. J. M. Rosenholm, T. Gulin-Sarfraz, V. Mamaeva, R. Niemi, E. Özliseli, D. Desai, D. Antfolk, E. von Haartman, D. Lindberg, N. Prabhakar, T. Näreoja and C. Sahlgren, *Small*, 2016, **12**, 1578-1592.
24. Z. Jomeh Farsangi, A. Beitollahi, B. D. Hatton, S. Sarkar, M. R. Jaafari, M. Rezayat, A. Amani and F. Gheybi, *RSC Advances*, 2016, **6**, 67592-67598.
25. T. M. Guardado-Alvarez, W. Chen, A. E. Norton, M. M. Russell, W. B. Connick and J. I. Zink, *Nanoscale*, 2016, DOI: 10.1039/C6NR01640E.
26. S. K. Surmiak, C. Doerenkamp, P. Selter, M. Peterlechner, A. H. Schäfer, H. Eckert and A. Studer, *Chem. Eur. J.*, 2016, DOI: 10.1002/chem.201604508.
27. L. D. Zanatta, I. A. Barbosa, F. B. Zanardi, P. C. de Sousa Filho, L. B. Bolzon, A. P. Ramos, O. A. Serra and Y. Yamamoto, *RSC Advances*, 2016, **6**, 104886-104896.
28. Z. Gao, N. D. Burrows, N. A. Valley, G. C. Schatz, C. J. Murphy and C. L. Haynes, *Analyst*, 2016, **141**, 5088-5095.
29. B. O'Regan and M. Gratzel, *Nature*, 1991, **353**, 737-740.
30. M. R. Hoffmann, S. T. Martin, W. Choi and D. W. Bahnemann, *Chem. Rev.*, 1995, **95**, 69-96.
31. Q. Huo, D. I. Margolese, U. Ciesla, P. Feng, T. E. Gier, P. Sieger, R. Leon, P. M. Petroff, F. Schuth and G. D. Stucky, *Nature*, 1994, **368**, 317-321.
32. P. T. Tanev, M. Chibwe and T. J. Pinnavaia, *Nature*, 1994, **368**, 321-323.
33. D. M. Antonelli and J. Y. Ying, *Angew. Chem. Int. Ed. Engl.*, 1995, **34**, 2014-2017.
34. A. A. Ismail and D. W. Bahnemann, *J. Mater. Chem.*, 2011, **21**, 11686-11707.
35. D. Fattakhova-Rohlfing, A. Zaleska and T. Bein, *Chem. Rev.*, 2014, **114**, 9487-9558.
36. J. L. Vivero-Escoto, Y.-D. Chiang, K. Wu and Y. Yamauchi, *Sci. Tech. Adv. Mater.*, 2012, **13**, 013003.
37. Z. Fei Yin, L. Wu, H. Gui Yang and Y. Hua Su, *PCCP*, 2013, **15**, 4844-4858.
38. T. Zhao, Y. Ren, J. Yang, L. Wang, W. Jiang, A. A. Elzatahry, A. Alghamdi, Y. Deng, D. Zhao and W. Luo, *J. Mater. Chem. A.*, 2016, DOI: 10.1039/C6TA06849A.
39. N. Yantara, D. Sabba, F. Yanan, J. M. Kadro, T. Moehl, P. P. Boix, S. Mhaisalkar, M. Gratzel and C. Gratzel, *Chem. Commun.*, 2015, **51**, 4603-4606.

40. M. Abdi-Jalebi, M. I. Dar, A. Sadhanala, S. P. Senanayak, F. Giordano, S. M. Zakeeruddin, M. Grätzel and R. H. Friend, *J. Phys. Chem. Lett.*, 2016, **7**, 3264-3269.
41. M. Wang, G. Yang, P. Jin, H. Tang, H. Wang and Y. Chen, *Sci. Rep.*, 2016, **6**, 19148.
42. A. Bertucci, E. A. Prasetyanto, D. Septiadi, A. Manicardi, E. Brognara, R. Gambari, R. Corradini and L. De Cola, *Small*, 2015, **11**, 5687-5695.
43. H. Lülff, A. Bertucci, D. Septiadi, R. Corradini and L. De Cola, *Chem. Eur. J.*, 2014, **20**, 10900-10904.
44. N. S. Kehr, B. Ergün, H. Lülff and L. De Cola, *Adv. Mater.*, 2014, **26**, 3248-3252.
45. Q. Cai, Z.-S. Luo, W.-Q. Pang, Y.-W. Fan, X.-H. Chen and F.-Z. Cui, *Chem. Mater.*, 2001, **13**, 258-263.
46. W. Dong, Y. Sun, C. W. Lee, W. Hua, X. Lu, Y. Shi, S. Zhang, J. Chen and D. Zhao, *J. Am. Chem. Soc.*, 2007, **129**, 13894-13904.
47. D. Chen, L. Cao, F. Huang, P. Imperia, Y.-B. Cheng and R. A. Caruso, *J. Am. Chem. Soc.*, 2010, **132**, 4438-4444.
48. *US Pat.*, 909264, 1962.
49. S. Megelski and G. Calzaferri, *Adv. Funct. Mater.*, 2001, **11**, 277-286.
50. O. Larlus and V. P. Valtchev, *Chem. Mater.*, 2004, **16**, 3381-3389.
51. Y.-J. Lee, J. S. Lee and K. B. Yoon, *Microporous Mesoporous Mater.*, 2005, **80**, 237-246.
52. J. H. de Boer, B. C. Lippens, B. G. Linsen, J. C. P. Broekhoff, A. van den Heuvel and T. J. Osinga, *J. Colloid Interface Sci.*, 1966, **21**, 405-414.
53. M. M. J. Treacy and J. B. Higgins, in *Collection of Simulated XRD Powder Patterns for Zeolites (Fifth Edition)*, Elsevier Science B.V., Amsterdam, 2007, pp. 256-257.
54. P. Ekwall, L. Mandell and P. Solyom, *J. Colloid Interface Sci.*, 1971, **35**, 519-528.
55. J. N. Israelachvili, D. J. Mitchell and B. W. Ninham, *J. Chem. Soc. Faraday Trans. 2.*, 1976, **72**, 1525-1568.
56. G. Wanka, H. Hoffmann and W. Ulbricht, *Macromolecules*, 1994, **27**, 4145-4159.
57. A. Firouzi, F. Atef, A. G. Oertli, G. D. Stucky and B. F. Chmelka, *J. Am. Chem. Soc.*, 1997, **119**, 3596-3610.
58. E. P. Barrett, L. G. Joyner and P. P. Halenda, *J. Am. Chem. Soc.*, 1951, **73**, 373-380.
59. M. Kruk, M. Jaroniec and A. Sayari, *J. Phys. Chem. B*, 1997, **101**, 583-589.
60. K. Cassiers, T. Linssen, V. Meynen, P. Van Der Voort, P. Cool and E. F. Vansant, *Chem. Commun.*, 2003, DOI: 10.1039/B302116E, 1178-1179.

## **Chapter 3**

# **Functionalized mesoporous silica for the adsorption of organic dye pollutant**

### **Abstract**

Pollutant of organic dye is harmful for our environment and becomes a highlighted world alarm. Herein, the adsorption of an anionic dye onto different mesoporous silica functionalized with amino groups was studied. UV-Visible analyses were used to quantify the amount of adsorbed dye and thus to infer the adsorption capacity ( $q_t$ ) which shows high adsorption performance. To treat a large amount of dye solution, a prototype device has been designed. Moreover, to enhance the performance of the device, a polymer cross-linked nanoparticle system has been successfully established.

### 3.1 Introduction

Since decades ago the problem related to the wastes introduction in the environment is highlighted as a worldwide alarm. The nature of these wastes is ranging from inorganic to organic products which were used for several applications.<sup>1</sup> Among pollutants, dyes represent an important class of dangerous compounds. And not surprisingly, the discharge of dye-bearing wastewater into natural streams and rivers from textile, paper, carpet, leather, distillery, and printing industries induces problems for human health, such as allergic dermatitis, skin irritation, cancer and mutation, and for aquatic life organisms, inducing additional problems to the aesthetic nature of the environment.<sup>2</sup> More specifically, the discharged wastes containing dyes induces the formation of dangerous by-products from oxidation, hydrolysis, or other chemical reactions in the wastewater phase.<sup>3</sup> It is worth mentioning that, as reported by Singh *et al.*, the wastewater from textile industries is rated as the most polluted among all industrial sectors.<sup>4</sup> In fact, textile industries employ a significant volume of water and chemicals for wet-processing of textiles. The color index listed more than 8,000 chemical products associated with the dyeing process including several structural varieties of dyes.<sup>1</sup> The chemical classes of dyes employed more frequently on industrial scale are the azo, anthraquinone, sulfur, indigoid, triphenylmethyl (trityl), and phthalocyanine derivatives.<sup>5</sup> These considerations rise the importance of the dyes removal from wastewater in which the color greatly affects the water that is highly visible even with the presence of very small concentrations of dyes. Thus, the treatment of wastewaters is considered as a major concern in the environment field.<sup>6</sup> Overall, the removal of color from water is usually associated with the purification process of colored effluents.<sup>7</sup>

In most situations, the use of different methods of treatment is necessary in order to remove all the contaminants presented in the wastewater. However, the physical adsorption is one of the most effective methods to remove color from water.<sup>8</sup> Recently, Seow *et al.*, in their review reported the removal of dye by adsorption processes, empathized that, because of its low price, simple design, easy operation, less energy

consuming, no effect by toxic substances and high quality of the treated effluents, the physical adsorption method is preferred for the treatment of wasted water.<sup>9, 10</sup>

Activated carbon is one of the most used commercial adsorbent materials for these purposes.<sup>11, 12</sup> However, the high cost of production and low level of regeneration tends to replace this adsorbent on the market. It is shown that cyclodextrins and chitosan biofilms have excellent ability for direct dye removal from wasted water.<sup>13, 14</sup> Recently, sorbents based on mesoporous silica has attained considerable attention due to their highly ordered structure, nanometer-sized pores, and their high surface area.<sup>7, 15</sup> More specifically, the presence of an ordered porous structure induces the much easier diffusion of several target molecules into the active sites than other class of adsorbent materials. Therefore, they were extensively used with great performance.<sup>3</sup> Starting from 2006 Wang *et al.* reported the reversible adsorption of organic dye on mesoporous silica in aqueous solution.<sup>16</sup> In 2010, Anbia *et al.* studied the removal of methylene blue from aqueous solution using nanoporous SBA-3.<sup>17</sup> Once again, in 2012, Anbia *et al.* highlighted the removal of acid dyes from aqueous media by adsorption onto amino-functionalized nanoporous silica SBA-3.<sup>2</sup> In 2014, Zarezadeh-Mehrizi *et al.* suggested the use of highly efficient removal of basic blue 41 with porous silica.<sup>18</sup> Last but not least, a large usage of mesoporous silica for this concern appeared from the recent review in 2016 by Nestic *et al.*<sup>7</sup> However, it is worth to mention that the mesoporous silica based adsorbents we discussed above are all nanomaterials. Since the beginning of the 21<sup>st</sup> century, health and environmental risks have been arisen concerning the use of nanoparticles.<sup>19, 20</sup> In this case, it is essential to develop a system for this concern. One possible solution is to transform the bulk particles into a stationary system. On the other hand, the laboratory treatment from powders with stirring or sonication is good for small quantity of dye solution. While for industry, the ability of large quantity treatment of dye solution is needed. For this purpose, an engineer solution is needed.

*In this chapter, we have studied the dye adsorption property by amine functionalized mesoporous silica materials. Based on this study, a device has been made for treating*

large amount of dye polluted solution. In the end, polymer cross-linked nanoparticle have been developed to enhance the adsorption performance and fix the particles.

### 3.2 Dye adsorption study over bulk powder of mesoporous silica

In order to mimic the real pollutant problem, direct blue 78 (DB) is chosen as the dye candidate (Fig. 3.1). DB is a commonly used dye in the textile industry, thus, the problem of this dye pollution exists in real world.

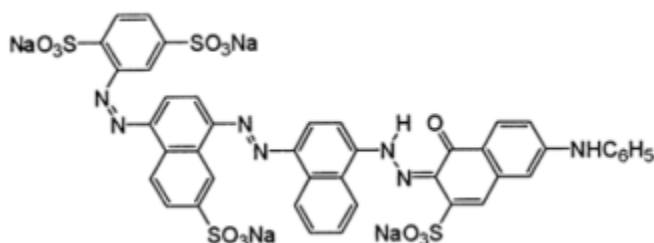


**Fig. 3.1** Chemical structure of the direct blue 78 (DB) dye.

#### 3.2.1 Effect of the functionalization

For the study of the adsorption, MCM-41 mesoporous silica was employed first. This material has been described in chapter 2. To perform the adsorption measurement, a DB dye solution with a concentration of  $5 \times 10^{-5}$  M has been used. A fixed amount of the adsorbent material (12 mg) was dispersed into 2 mL aqueous dye solution. The mixture was kept under sonication for 5 min and stirred for 24 hours. The absence of any adsorption process for the silica materials without functionalization was observed. Zeta-potential measurements showed the negatively charged surface of the MCM-41 mesoporous silica with a value of -38 mV. Results emphasized the negative repulsion between negatively charged dye and the adsorbent materials. As we see from Fig. 3.1, DB has different functional groups. Overall, the key role of negatively charged sulfonic moieties appeared after these considerations.

As a subsequent step of this study, experiments which introduce amine groups were performed. 3-Aminopropyl triethoxysilane (APTES) was used to functionalize amine group on the silica surface (see experimental section for details). In this case, the amine groups were introduced both on the outer surface and the surface of the pore channels. The extraordinary results for the adsorption of amine functionalized MCM-41 mesoporous silica after 5 minutes of sonication is shown in Fig. 3.2. In excellent agreement with literature,<sup>3</sup> the typical absorption band at 600 nm, arising from the characteristic chromospheres of DB was detected. This absorption band is from the interaction between azo functionality ( $-N=N-$ ) and attached aromatic moieties. By using amine functionalized MCM-41, only few minutes were necessary to obtain clean water (Fig. 3.2). Moreover, the picture shows clearly the load of DB on amine functionalized MCM-41 inducing a change in color of from white to blue. Furthermore, the solid state spectrum of amine functionalized MCM41 loaded with DB molecules was acquired which evidencing the typical electronic transition of the dye (Fig. 3.3).<sup>13, 21</sup>

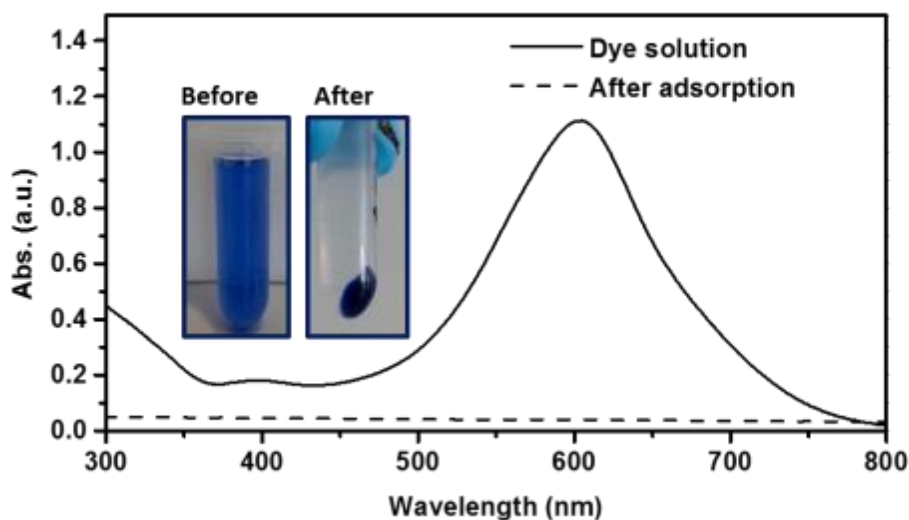


**Fig. 3.2** Comparison between the UV-Vis absorption spectra and picture obtained from  $5 \times 10^{-5}$  M DB aqueous solutions in absence of amine functionalized MCM-41 and after 5 minutes of contact time with 6 mg of amine functionalized MCM-41 (2 mL solution).

It is worthy to mention that the introduction of amine groups increased the Zeta-Potential value to +12 mV for MCM-41 mesoporous silica. As a results, the positively charge

induced by the presence of amine groups was needed to ensure the uptake of the dye. Not surprisingly, after the adsorption of dye the Z-potential values decreased from +12 mV to 7mV. Results showed the presence of electrostatic interactions between DB and amine groups. Two factor contributed to these results: i) the neutralization of charged amine groups by  $\text{SO}_3^-$  ones presents on DB chemical structure and ii) the presence of free negative charges on DB that contributed overall to the global charge decrease on the surface of amine functionalized MCM-41. In order to prove this type of interaction, reference experiments were performed using the naked MCM-41 with only decreasing the pH of dye solution. In this condition, a Zeta-Potential of +4 mV was achieved by MCM-41 at pH of 2. Under this condition, the adsorption of DB did not occur. This indicated and confirmed the main role of amine groups in the adsorption process of DB in water.

After these assessments, nitrogen adsorption measurements were performed in order to investigate the porosity after dye adsorption. From the pore size distribution we can see that both the pore volume and the pore size decreased. This phenomena reflected the occupation of dye molecules in mesopores structure filling the channels.<sup>22</sup>

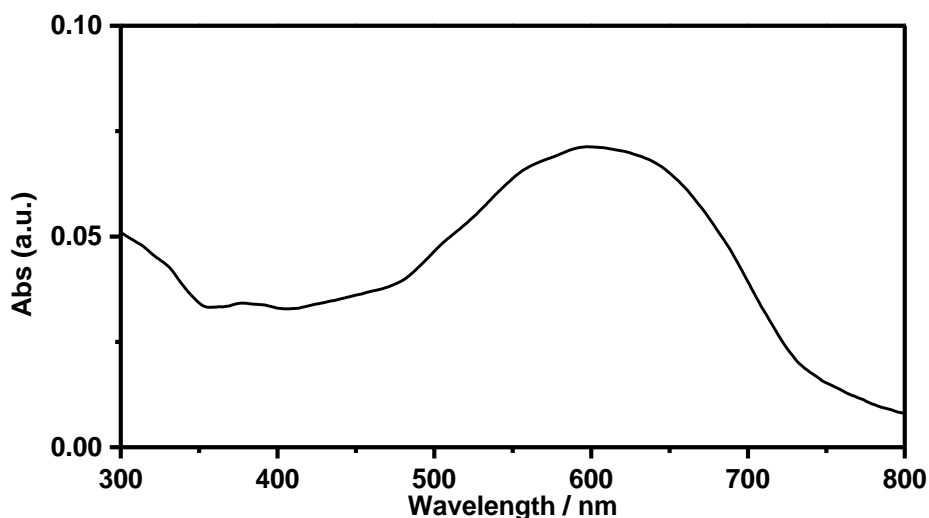


**Fig. 3.3** Solid-state UV-Vis spectrum of amine functionalized MCM-41 after DB dye adsorption.



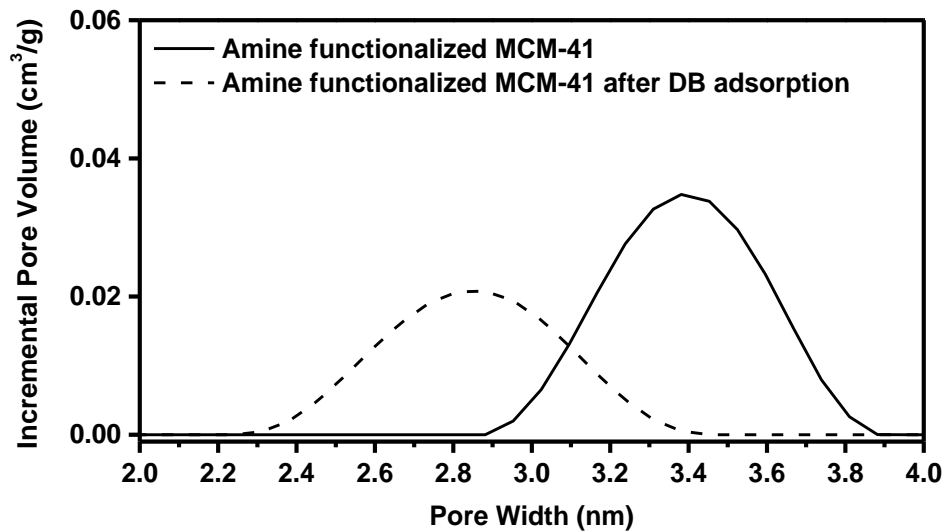


Fig. 3.4 Pore size distribution of amine functionalized MCM-41 before and after DB dye adsorption.

### 3.2.2 Effect of the material dosage and dye concentration

The influence of the amount of amine functionalized MCM-41 on DB adsorption is shown in Fig. 3.5. The quantity of adsorption value  $q_t$  at time  $t$  is expressed as:

$$q_t = \frac{(c_0 - c_t) * V}{W} \quad (1)$$

where  $c_0$  is the initial concentration of the dye,  $c_t$  is the concentration of the dye in solution at time  $t$ ,  $V$  is the volume of the dye solution and  $W$  is the weight of the silica material. The dye solutions were monitored until the complete uptake of dye which indicated by end part of the adsorption process showed a plateau region (region in which the  $q_{max}$  was obtained). The results indicated that at constant concentration of DB ( $5 \times 10^{-5}$  M), by increasing the adsorbent amount of amine functionalized MCM-41 from 0.4 to 12 mg in 2 mL of dye solution, the adsorption of DB molecules increased but the adsorption capacity decreased. From literature, Anbia et al suggested that the increase in adsorption was attributed to the increased surface area and the availability of more free adsorption sites.<sup>2</sup> On the other hand, the decrease in adsorption capacity can be explained considering that some of the adsorption sites remained unsaturated during the adsorption

process.<sup>2, 10</sup> Overall, the recorded trend indicates that the adsorbent dose affects both the percentage of dye removed and the adsorption capacity.<sup>10</sup>

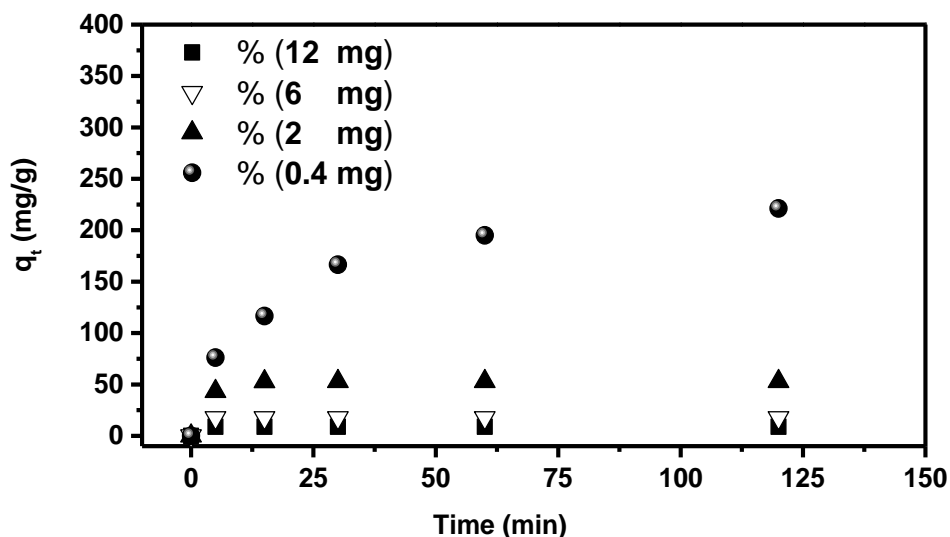


**Fig. 3.5** Adsorption capacity  $q_t$  (mg/g) at  $t$  for different amount of amine functionalized MCM-41 from the adsorption process of a 2 mL of  $5 \times 10^{-5}$  M DB dye solution.

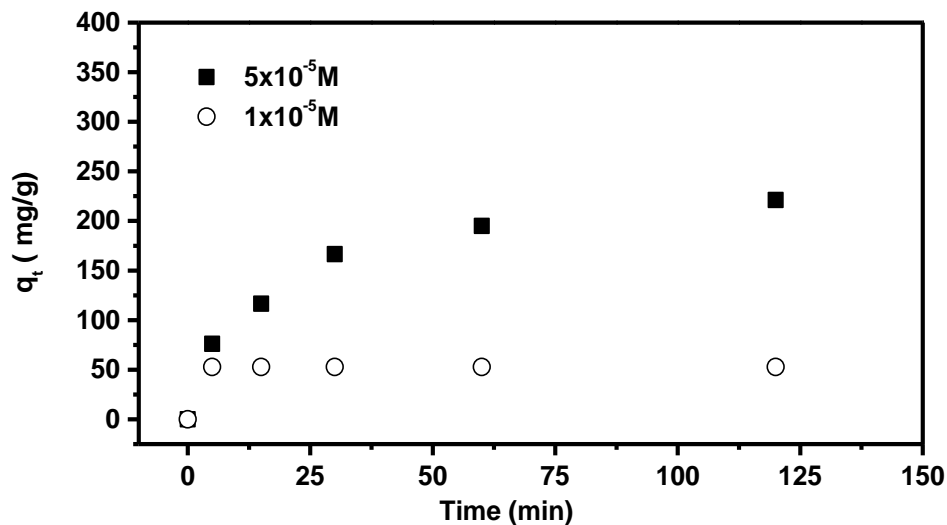


**Fig. 3.6** Effect dye concentration on the adsorption capacity  $q_t$  at time  $t$  of DB removal from 2 mL neutral aqueous solutions onto 0.4 mg amine functionalized MCM-41.

It is worth mentioning that the adsorption rate of amine functionalized MCM-41 from 12 to 2 mg into 2 mL DB solution appeared very fast (15 minutes were enough). But for the 0.4 mg of material into 2 mL dye solution, the rate of adsorption dramatically decreased. Results were in excellent agreement with those obtained decreasing the DB concentration reported in Fig. 3.6. In this case, the smallest amount of the adsorbent material (0.4 mg) was used. The volume of the DB solution remained the same (2 mL) but the concentration was decreased to  $1 \times 10^{-5}$  M. Fig. 3.6 show that the maximum adsorption were obtained quickly, just after few minutes, when a smaller amount of dye was employed. This is not a surprise since by reducing the ratio dye/adsorbent material, relatively more adsorption sites were available per dye molecule.<sup>9</sup> We can also see that the adsorption capacity increased with a more concentrated dye solution ( $5 \times 10^{-5}$  M). This behavior can be explained by the establishment of a higher concentration gradient at the particle–solvent interface due to the higher DB concentration, which enhanced the DB dye removal capacity.<sup>23</sup>

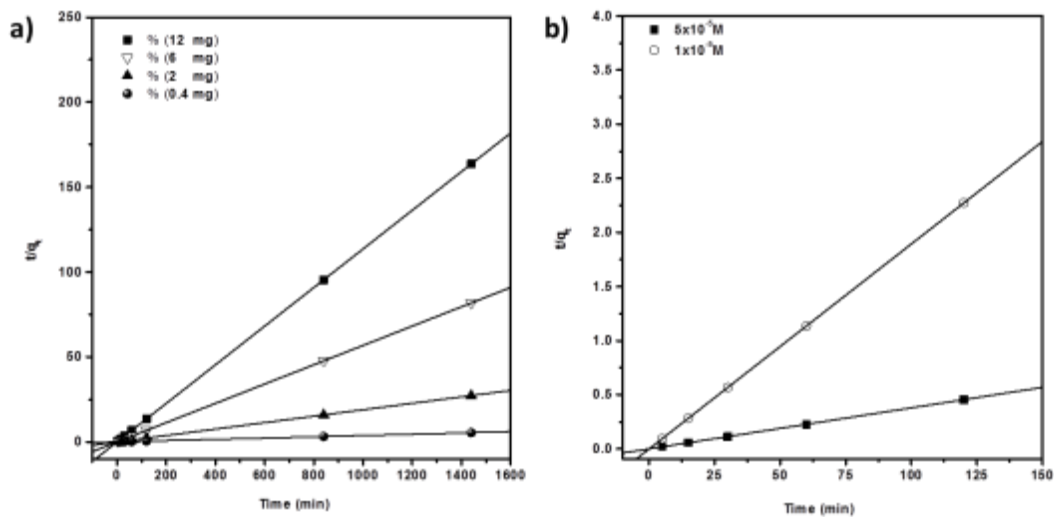


**Fig. 3.7** a) Pseudo-second-order kinetics for the adsorption of DB onto different amount of amine functionalized MCM-41 for 2 mL DB solution ( $5 \times 10^{-5}$  M); b) Pseudo-second-order kinetics for the adsorption of DB onto 0.4 mg amine functionalized MCM-41 for 2 mL DB solution with different concentrations.

Interestingly, the dynamics of the adsorption process can be better understood by the evaluation of kinetic analysis. From literature, both the pseudo first and second order kinetic models could be adopted.<sup>2, 13, 14, 24, 25</sup> As shown in Fig. 3.7, the adsorption of DB dye molecules followed the pseudo-second-order kinetic with excellent regression coefficients. The linear form of the pseudo-second-order kinetic equation is expressed as:

$$\frac{t}{q_t} = \frac{1}{k_2 q_e^2} + \frac{t}{q_e} \quad (2)$$

where  $t$  is the time,  $q_t$  is the adsorption capacity at time  $t$ ,  $q_e$  is the equilibrium adsorption capacity and  $k_2$  is the pseudo-second-order constant.

### 3.2.3 Effect of pH

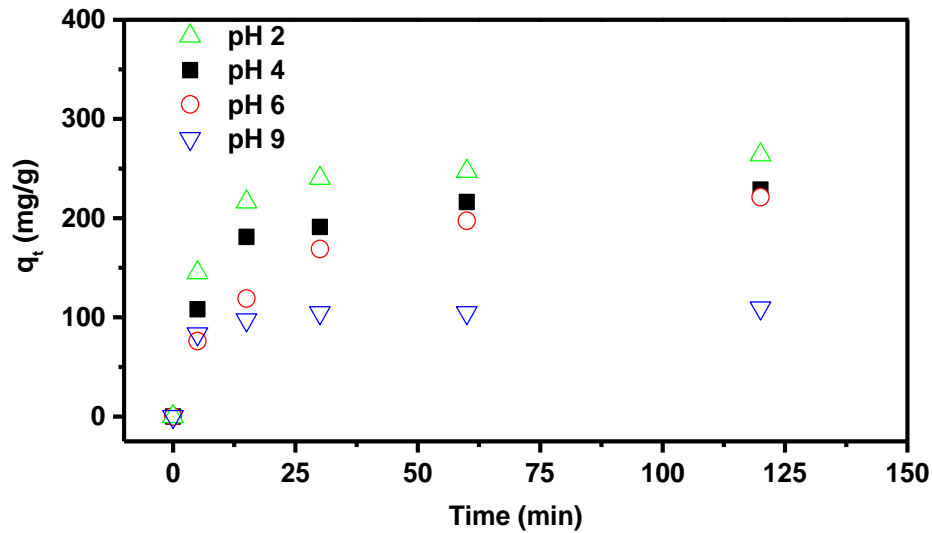


**Fig. 3.8** Effect of pH on the adsorption capacity  $q_t$  at time  $t$  of DB from aqueous solutions (pH 2-12) onto amine functionalized MCM-41. Measurements were performed using 0.4 mg of mesoporous material for 2 mL of DB having a concentration of  $5 \cdot 10^{-5}$  M.

As already known, the pH values affect the charge density both on the surface of the adsorbent material and dye molecules.<sup>10</sup> For studying the effect of the pH on the adsorption capacity of amine functionalized MCM-41, the dye solutions were prepared in the pH ranging from 2 to 12. Not surprisingly, as we can see from Fig. 3.8, the adsorption

capacity increased with decreased pH value and the maximum adsorption capacity for DB was observed at pH 2. Therefore, at lowest pH value, the surface of the material was positively charged via protonation, which increased the electrostatic attractions between negatively charged dye and amine functionalized surface.<sup>10</sup>

At higher pH values the number of positively charged sites were reduced ( $pK_a$  of primary amine groups is 9). Of course this reduced the electrostatic interaction between the material surface and the anionic dyes molecules.<sup>26</sup> Not surprisingly the adsorption at pH 12 didn't occur. Results were well agreed with Zeta-potential measurements of the material in different pH (see Fig. 3.9).

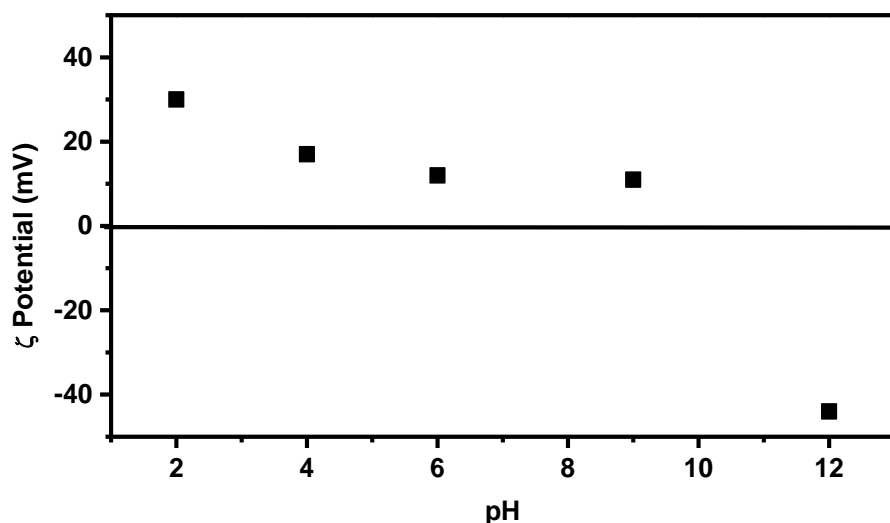


**Fig. 3.9** Zeta-potential value of the amine functionalized MCM-41 in different pH.

In order to better investigate the role of electrostatic interactions, experiments using the phosphate buffer as electrolyte were performed.<sup>27</sup> The amount of both DB solution and the adsorbent were fixed at  $5 \times 10^{-5}$  M, 2 mL for the dye solution and 0.4 mg for the material. Variations were observed for the DB adsorption. Fig. 3.10 shows results related to the effect of an electrolyte on the adsorption process. The obtained capacity values show that when very high concentrations ( $\geq 0.1$  M) of phosphate were adopted, the adsorption process was retarded which suggested, as reported in literature, the screen of

opposite charges in adsorbents and the dye molecules.<sup>28</sup> Indeed, the salts in solution are small ions and thus was expected that they were able to compete efficiently with DB in adsorption process by amine functionalized MCM-41.<sup>29</sup>

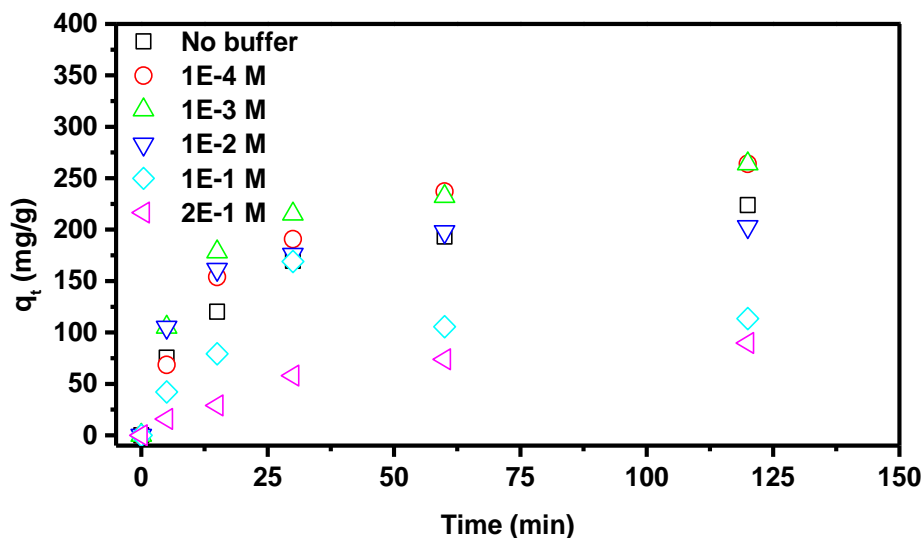


**Fig. 3.10** Effect of phosphate buffer at different concentration on the adsorption capacity  $q_t$  at time  $t$  of DB from aqueous solutions onto amine functionalized MCM-41.

Interestingly, when diluted buffered solutions were adopted, an increase of the adsorption rate of DB was observed. More specifically, when the concentration of the buffer was settled at  $10^{-4}$  M and  $10^{-3}$  M, the adsorption was faster and accomplished in few hours. Due to the amine group in the dye structure, it is suggested that the presence of the slight interaction between protonated amine groups present both in DB structure and the adsorbent was expected to be repulsive electrostatic force. As a result, in the presence of diluted solution which there were just enough ions to eliminate the repulsive force, the adsorption rate increased; on the other hand when the presence of these ions was emphasized, the adsorption rate would reduce.<sup>30</sup>

### 3.2.4 Effect of the dye

As we discussed before, main reason of the adsorption is due to the interaction between amine and the sulfonic group. Here we propose another dye (sulforhodamine B) which also has sulfonic group and can be possible for the adsorption over our amine functionalized MCM-41. As we discussed before, variations such as the amount of dye, the amount of material and the pH could affect the dye adsorption. The adsorption of the dye in solution is an equilibrium process. This means that at a certain amount of material, if more dye was added, more dye would get adsorbed but there would also be more dye remained in the solution. To simplify this problem and to make the results comparable, a term of  $q_c$  is proposed here. The term  $q_c$  means for per gram of material, the maximum quantity of dye it can adsorb under the condition of complete adsorption of dye (no trace of the dye from UV-Vis spectra). For the amine functionalized MCM-41 mesoporous silica, the  $q_c$  value for DB adsorption is 0.88 mg/g (12 mg of functionalized MCM-41 complete adsorbed all the DB dye in 2 mL of  $5 \times 10^{-5}$  M solution).

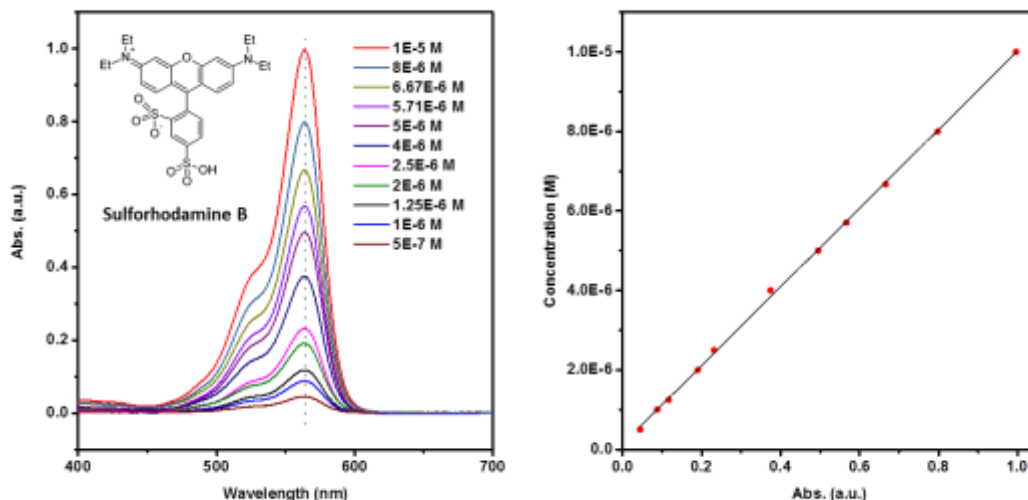


**Fig. 3.11** UV-Vis spectra of sulforhodamine B solution with different concentrations (left). Linear fitting curve shows the relationship between the concentration and the absorption peak height at 564 nm (right).

To investigate the relationship between the concentration of sulforhodamine B and its highest absorption peak height (at 564 nm), several dye solutions with different concentrations were measured by UV-Vis spectroscopy. A linear curve was then fitted to the measured data (Fig. 3.11). With this curve, we can calculate the concentration of the dye by knowing the absorption peak height at 564 nm.

By changing the dye, the adsorption of sulforhodamine B on amine functionalized MCM-41 was also studied. For the complete adsorption of sulforhodamine B, 5 mg of material was able to adsorb all the dye from a 5 mL dye solution of with  $5 \times 10^{-7}$  M concentration (Fig. 3.12). This gave us the  $q_c$  value of 0.28 mg/g. The value for sulforhodamine B is lower compare with DB due to the different structures of the dye. With the structural difference, the number and the position of the effective sulfonic group for adsorption are different which can influence the adsorption process.

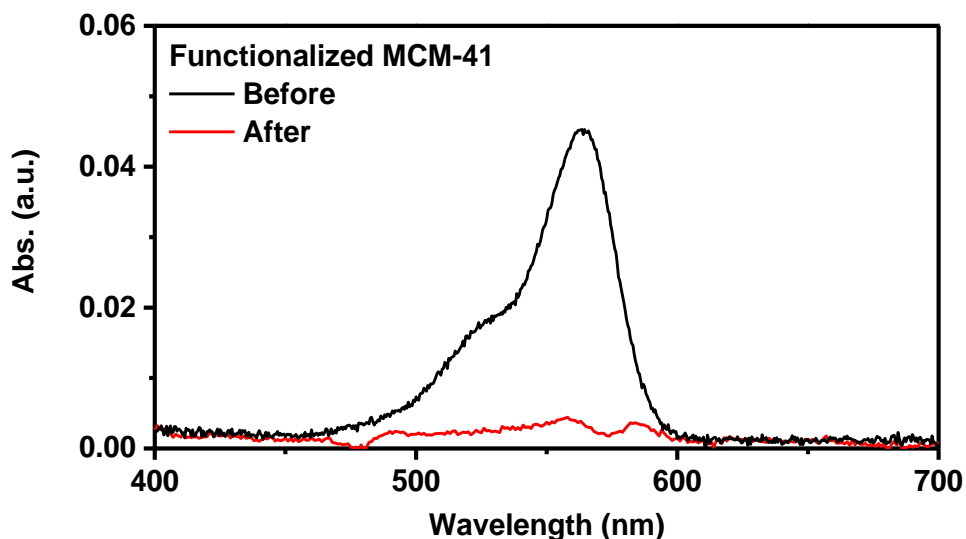


**Fig. 3.12** UV-Vis spectra of sulforhodamine B solution before and after the adsorption by the functionalized MCM-41 (5 mL dye solution with  $5 \times 10^{-7}$  M concentration).

#### 3.2.4 Effect of the porosity of mesoporous silica

As the effective amine group for dye adsorption located both on the surface and in the pores, it could be also interesting to investigate the adsorption with other silica materials



with bigger pores thus bigger effective area. Two types of silica material have been chosen: commercially available silica gel 60 and the SBA-15 we have described in chapter 2. Compare to MCM-41, these two candidates has bigger pores which could give more capacity. APTES was used for the functionalization of amine group (see experimental section for details).

The porosity of these two materials have been investigated by nitrogen adsorption measurement. From the pore distribution we can see that our SBA-15 has bigger pores and larger pore volume (Fig. 3.13). Not surprisingly, our SBA-15 has the BET surface area of 646.8 m<sup>2</sup>/g, bigger than 384.9 m<sup>2</sup>/g for silica gel 60.

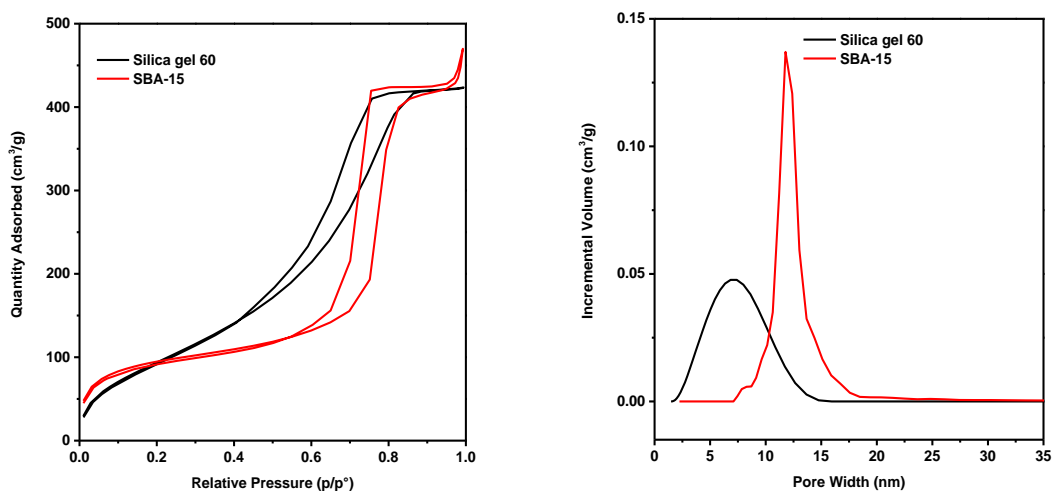


**Fig. 3.13** Nitrogen adsorption isothermal curve and pore distribution of silica gel 60 and SBA-15.

**Table 3.1** Zeta-potential before and after amine functionalization.

Material	Zeta-potential (mV)	Zeta-potential after amine functionalization (mV)
Silica gel 60	-14.45	+12.58
SBA-15	-23.05	+12.64

Zeta-potential measurement was used before and after the functionalization. We can see from Table 3.1 that the surface charge of both silica gel 60 and SBA-15 turned from

negative to positive, which means the successful functionalization of amine group on the surface.

The dye adsorption experiment was done after the relationship between the dye concentration and the UV-Vis spectra had been established. In this case, 5 mg of functionalized silica gel 60 and SBA-15 was used respectively to determine the  $q_c$  value by using  $5 \times 10^{-7}$  M sulforhodamine B solution. For complete adsorption of the dye, 5 mg of functionalized silica gel 60 used 3 mL of dye solution and functionalized SBA-15 used 7 mL. This gave the  $q_c$  value of 0.17 mg/g for functionalized silica gel 60 and 0.39 mg/g for functionalized SBA-15. This is due to the fact that SBA-15 silica has larger surface area than the silica gel 60 ( $646.8 \text{ m}^2/\text{g}$  than  $384.9 \text{ m}^2/\text{g}$ ). If we include functionalized MCM-41 into consideration, both our MCM-41 and SBA-15 have better performance than the commercially available silica gel 60.

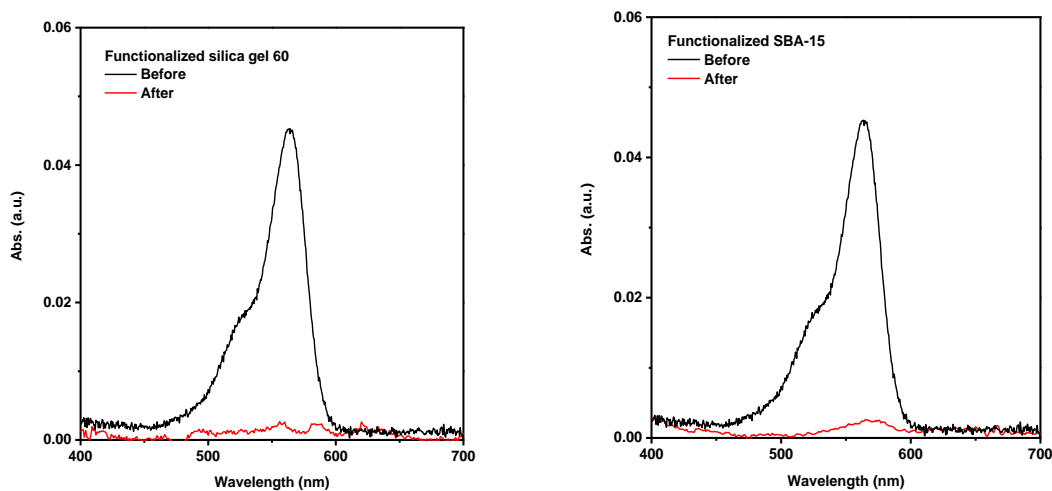


**Fig. 3.14** UV-Vis spectra of sulforhodamine B solution before and after the adsorption by 5 mg of functionalized silica gel 60 (left, 3 mL  $5 \times 10^{-7}$  M dye solution) and 5 mg of functionalized SBA-15 (right, 7 mL  $5 \times 10^{-7}$  M dye solution).

### 3.3 Dye adsorption over stationary phase of mesoporous silica materials

Sonication and centrifugation of the mixture of dye solution and the adsorbent is only suitable in laboratory condition of dye removal. However, it's not applicable for a large quantity of water treatment especially for industrial use. In this case, a device which allows large quantity of dye removal has been designed. The device we've made is shown in Fig. 3.15. The water pump would pump the solution up from the beaker. The solution would then go through the syringe which is filled with our functionalized silica material. The filtrated solution was collected from another beaker.

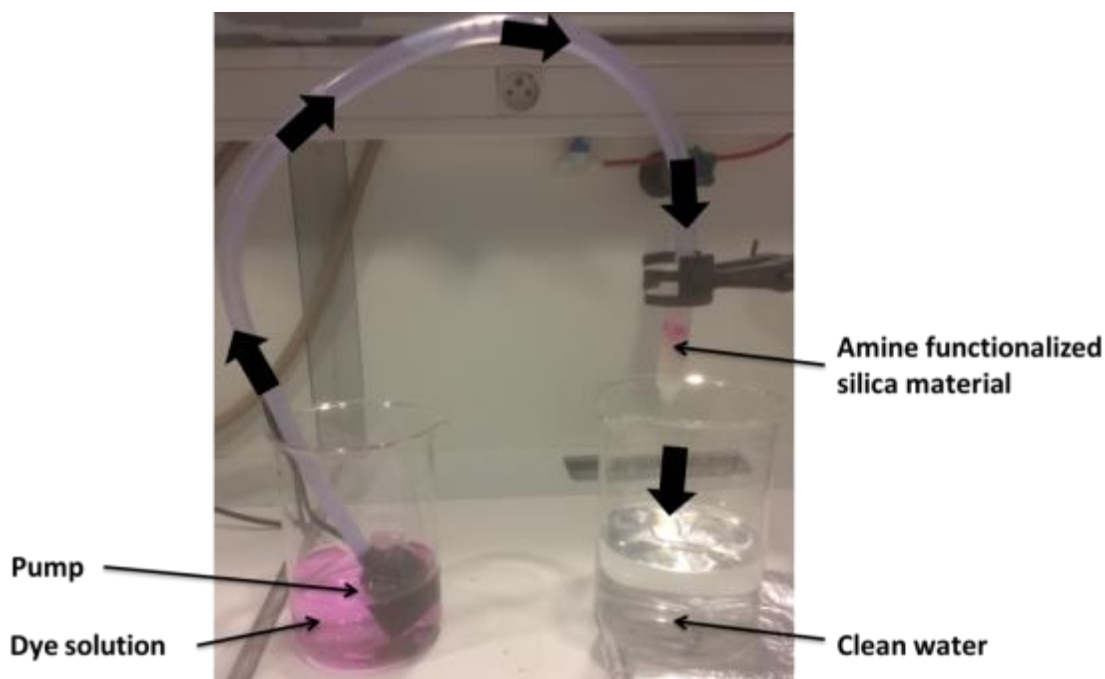


**Fig. 3.15** The setup of dye removal device.

**Table 3.2** Amount of the  $5 \times 10^{-7}$  M sulforhodamine B solution determined by the  $q_c$  values.

Material	$q_c$ (mg/g)	Volume of dye solution (mL)
Functionalized MCM-41	0.28	500
Functionalized silica gel 60	0.17	300
Functionalized SBA-15	0.39	700

To test the performance of our functionalized silica material, 500 mg of each material was added into the filter syringe. Not functionalized silica 60 was used as reference. 1 L of sulforhodamine B solution with  $5 \times 10^{-7}$  M concentration was added into the beaker. To make our results comparable, the pump was turned on until different volumes of purified solution was collected respectively for each material. The volumes were determined by the qc value of each material which shows in Table 3.2. The materials we used are the three functionalized silica described earlier, and not functionalized silica gel 60 as reference. For the functionalized MCM-41, due to its morphology of small sphere, the packing inside the filter syringe is too condensed that the dye solution cannot pass through. Never the less, the filtered solutions from the rest of the materials are shown in Fig. 3.16. We can see that by eye the color from the functionalized SBA-15 is slightly more colorful than pure water, but less colorful than the rest.

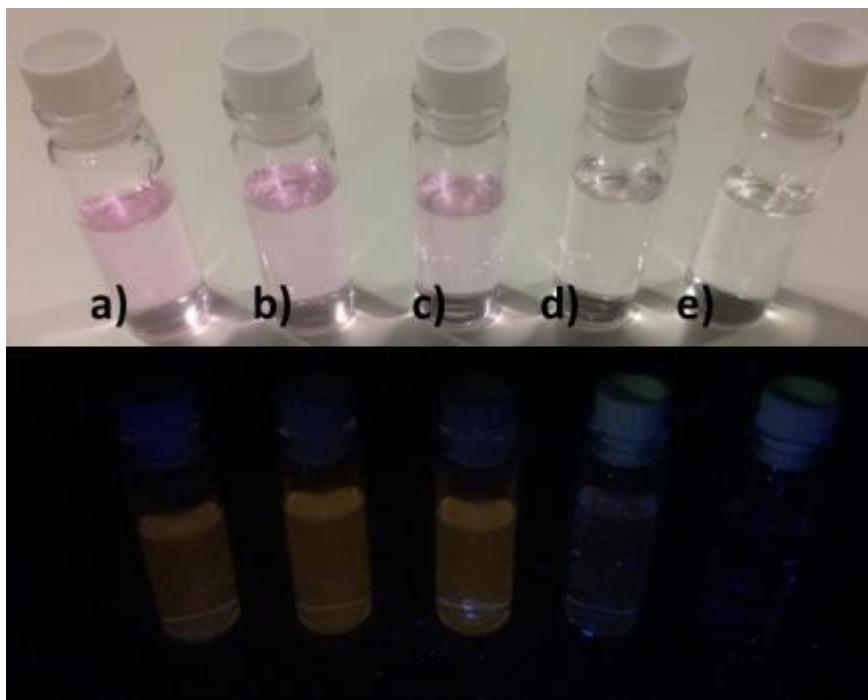


**Fig. 3.16** Pictures of the solutions under ambient light and UV. a) initial dye solution ( $5 \times 10^{-7}$  M); b) dye solution filtered by silica gel 60; c) dye solution filtered by functionalized silica gel 60; d) dye solution filtered by functionalized SBA-15; e) water without dye.

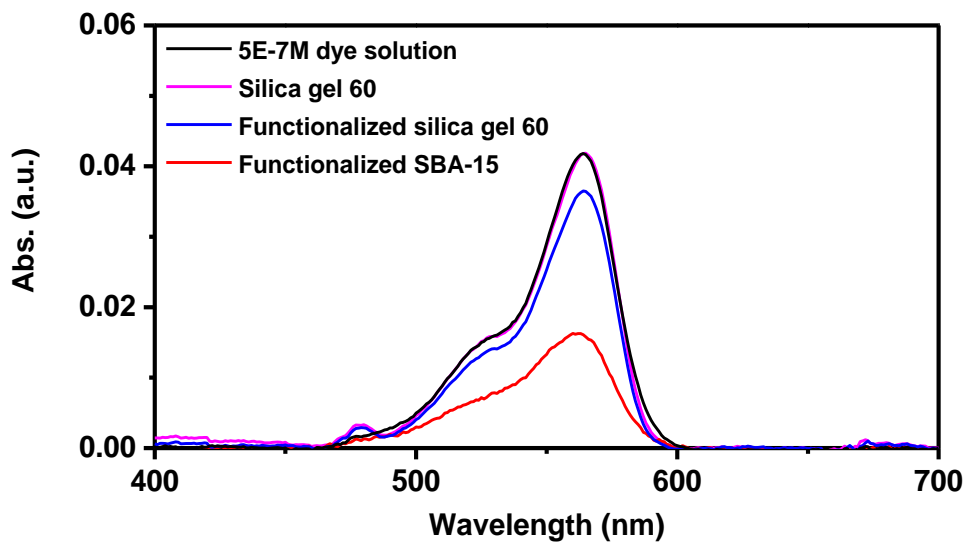


**Fig. 3.17** UV-Vis spectra of the dye solution before and after filtered by different materials.

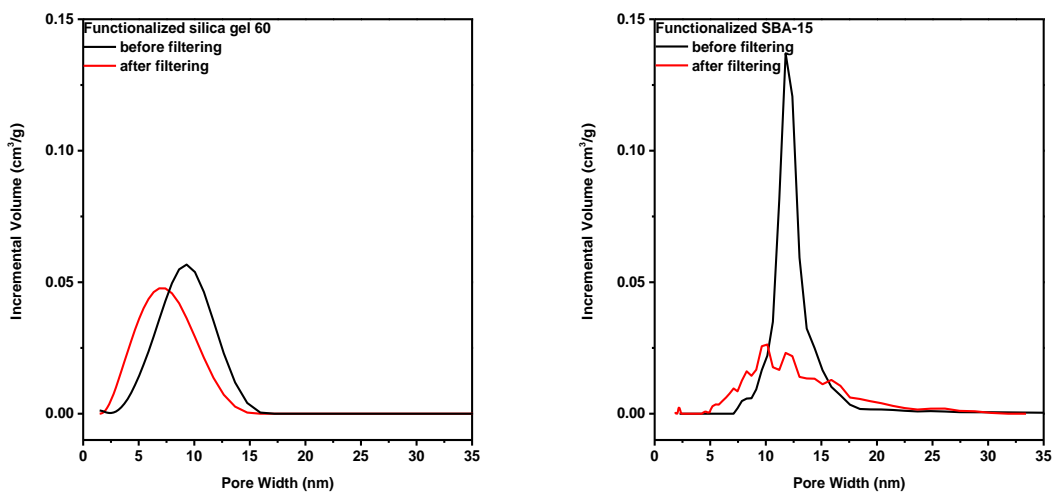


**Fig. 3.18** Pore volume distributions for functionalized silica materials before and after filtering.

To determine the adsorption efficiency, UV-Vis spectra has been used to determine the concentration of the filtered solution (Fig. 3.17). In this case, none of the material shows

complete adsorption. This means the device performance is not as good as the bulk powder sonication system. The reason is that by sonication and stirring, the material and the dye have a long time to interact with each other. But for filtering, the interaction time between the material and the dye solution is much less.

Nitrogen adsorption measurement showed similar results from UV-Vis spectra. We can see that for both materials, pore diameter and pore volume decrease after filtering of the dye solution (Fig. 3.18). Also, it tells us that the dye solution can penetrate through the pores. This feature means that the material surface including the pore surface is fully used, which is the advantage compare to the non-porous materials.

### **3.4 Dye adsorption over stationary powder of mesoporous silica materials with enhanced performance**

By comparing the results from the powder sonication and the device filtering, it is clear that the efficiency for the filtering is lower. To overcome this problem, a polymer cross-linker with amine group is introduced here. The advantage of this system is that extra amine groups from the polymer can also contribute to the adsorption which could enhance the adsorption performance. In the meanwhile, it can also stop the particles from diffusion into the environment which overcome the risk concern of nanomaterials.

The fabrication of the cross-linked silica material system is rather simple (Fig. 3.19). N,N'-methylenebisacrylamide and branched polyethyleneimine (PEI) was mixed at 1:1 weight ratio in water. The functionalized silica material was then added and mixed with the previous solution. The white gel-like product was poured into the filter syringe, and put into oven for the formation of the cross-linked amine functionalized silica materials (see experimental section for details).

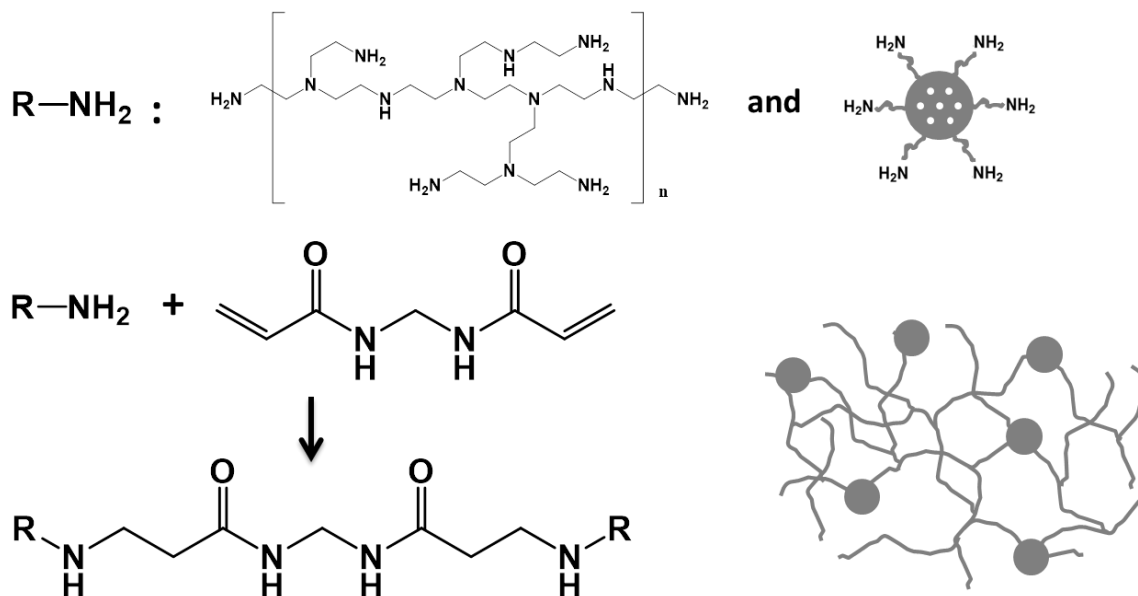


**Fig. 3.19** Schematic representation of the polymer cross-linked amine functionalized silica material.

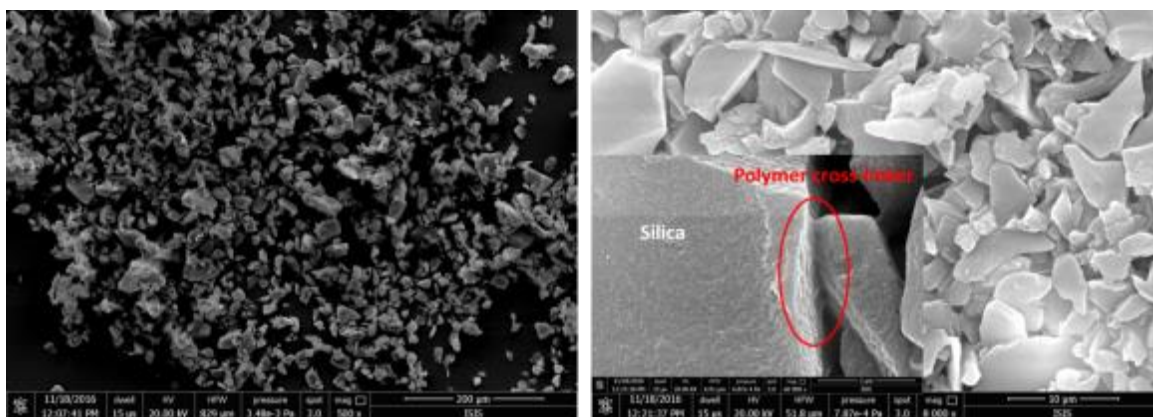


**Fig. 3.20** Silica gel 60 before (left) and after (right) cross-linked by polymer.

Fig. 3.20 shows the SEM image of amine functionalized silica gel 60 before and after put the cross-linker. It is obvious that before cross-linking, the silica gel 60 was just random flakes which distributed everywhere. After treated by the polymer cross-linker, we can see that the silica pieces were hold together. Moreover, if we zoomed in, a clear organic structure was established between the silica pieces. In the meanwhile, the space in between the silica pieces still exists, which could allow water to pass through.

After the crosslinked functionalized silica material was formed in the filtering syringe, same filtering experimental process was done by using our device according to each material. The result picture is shown in Fig. 3.21.



**Fig. 3.21** Pictures of the solutions under ambient light and UV. a) initial dye solution ( $5 \times 10^{-7}$  M); b) dye solution filtered by cross-linked functionalized silica gel 60; c) dye solution filtered by cross-linked functionalized SBA-15; d) water without dye.

The concentration of the filtered solutions was also investigated by UV-Vis spectra (Fig. 3.22). Since the PEI also has a lot of amine groups, we didn't find any dye residuals through UV-Vis spectra. The adsorption performances for both our cross-linked materials were enhanced compare to the not cross-linked material.



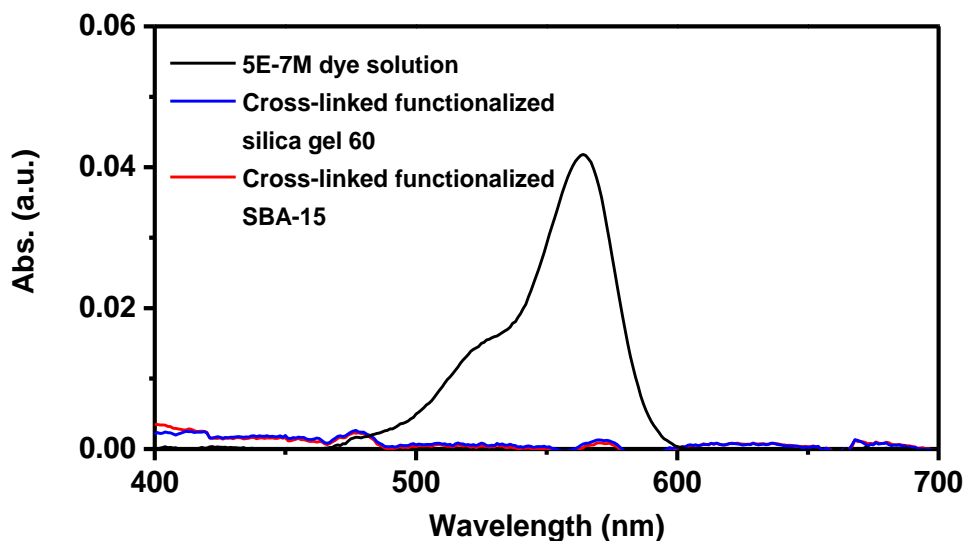


**Fig. 3.22** UV-Vis spectra of the dye solution before and after filtered by different cross-linked functionalized silica materials.

### 3.5 Conclusion and perspectives

By applying the ionic dye adsorption theory, an adsorption system for sulfonic dyes has been established based on amine functionalized silica materials. Effects of functionalization, concentration and pH have been studied in detail between the DB dye and MCM-41 mesoporous silica. Same principle has been used for the study of the adsorption of sulforhodamine B dye from amine functionalized silica gel 60 and SBA-15. Due to the larger surface area, our SBA-15 performs better than the commercially available silica gel 60. A device based on the adsorption system has been built for large quantity of water purification. Moreover, to enhance our device performance and avoid the silica material contaminating the environment, polymer based cross-linker has been used to hold the material together. Further investigation could be focus on the optimization of the system.

### 3.6 Experimental section

#### *Materials*

Silica gel 60 (1 kg) was purchased from Merck, sulforhodamine B (acid form, laser grade, 5 g), polyethylenimine (average  $M_w$  ~25,000 by LS, average  $M_n$  ~10,000 by GPC, branched, 100 mL), N,N'-Methylenebis(acrylamide) (99%, 100 g), (3-Aminopropyl) triethoxysilane (APTES) (99%, 100 mL) was purchased from Sigma-Aldrich. Direct Blue 78 (Color Index Number: 78, chemical formula:  $C_{42}H_{25}N_7Na_4O_{13}S_4$ , MW: 1055.1  $g \cdot mol^{-1}$ ) was received by Colorprint Fashion. The materials above were used as received without any further modification.

#### *Synthesis of the MCM-41 mesoporous silica*

#### *Synthesis of the SBA-15*

Described in chapter 2.

#### *Amine functionalization of silica*

Silica material was suspended in ethanol. With vigorous stirring, APTES was added into the previous suspension with the quantity of 0.1 mL/g silica material. The suspension was heated up to 50 °C and stirred overnight. The result product was washed by centrifugation 5 times with ethanol and dried in vacuum. The amine group of the silica materials was activated by 1 M solution of acidic acid, then the material was washed by water 5 times and dried in oven at 70 °C.

#### *Cross-linked amine functionalized silica gel 60*

30 mg polyethylenimine and 30 mg N,N'-Methylenebis(acrylamide) was dissolved into 1 mL of water. 500 mg of the amine functionalized silica gel 60 was then added and well-mixed. The mixture was added into the filter syringe, and put into an oven at 70 °C overnight.

#### *Cross-linked amine functionalized SBA-15*

30 mg polyethylenimine and 30 mg N,N'-Methylenebis(acrylamide) was dissolved into 1 mL of water. 500 mg of the amine functionalized SBA-15 was then added and well-mixed. The mixture was put into an oven at 70 °C overnight. The cross-linked silica was taken out, break into small pieces (around 1 mm). Again, 30 mg polyethylenimine and 30 mg N,N'-Methylenebis(acrylamide) was dissolved into 1 mL of water. Small pieces of pre-cross-linked amine functionalized SBA-15 were then added. This mixture was added into the filter syringe, and put into an oven at 70 °C overnight.

#### *Nitrogen adsorption*

Nitrogen adsorption analysis was performed using a Micromeritics porosimeter (model ASAP-2020). The samples were degassed at 250°C under vacuum for 6h and N<sub>2</sub> adsorption/desorption measurement was done at -196 °C. The surface areas were calculated by BET method. The pore size distributions and pore volume were calculated by DFT methods.

#### *Scanning electron microscope*

Scanning Electron Microscope SEM images were recorded with a FEI Quanta FEG 250 instrument (FEI corporate, Hillsboro, Oregon, USA) with an acceleration voltage of 20kV. The sample is prepared by sputtering coated with Au (Emitech K575X peltier cooled) for 45 s at 60 mA prior to fixation on an Al support.

#### *Dynamic light scattering and zeta-potential*

DLS and zeta-potential analysis were performed on a Delsa Nano C Particle Analyzer (Beckman Coulter, Brea, CA, USA); all DLS measurements were conducted in water, while zeta-potential analysis in phosphate buffered saline (PBS), pH = 7.

#### *UV-Vis spectrum*

The UV-Vis absorption spectra were measured by Shimadzu UV-3600 UV-Vis-NIR spectrophotometer. The spectra of liquid samples were recorded at a 1 nm/s scan rate in a cuvette with a 1 cm path length.

*Thermogravimetric analysis*

Thermogravimetric (TG) measurements were performed on a TGA instrument NETZSCH STA 449 F3 Jupiter® – TGA. TGA scans were done with a heating rate of 10 °C /min and hold at 1100 °C for 30 min under a synthetic air purge gas flow of 20 mL/min.

### 3.7 References

1. S. P. Buthelezi, A. O. Olaniran and B. Pillay, *Molecules*, 2012, **17**, 14260-14274.
2. M. Anbia and S. Salehi, *Dyes Pigm.*, 2012, **94**, 1-9.
3. C.-H. Huang, K.-P. Chang, H.-D. Ou, Y.-C. Chiang and C.-F. Wang, *Microporous Mesoporous Mater.*, 2011, **141**, 102-109.
4. K. P. Singh, D. Mohan, S. Sinha, G. Tondon and D. Gosh, *Ind. Eng. Chem. Res.*, 2003, **42**, 1965-1976.
5. E. Forgacs, T. Cserhati and G. Oros, *Environ. Int*, 2004, **30**, 953-971.
6. A. R. Cestari, E. F. Vieira, G. S. Vieira, L. P. da Costa, A. M. Tavares, W. Loh and C. Airoidi, *J. Hazard. Mater.*, 2009, **161**, 307-316.
7. A. R. Nestic, M. J. Kokunesoski, T. D. Volkov-Husovic and S. J. Velickovic, *Environ. Monit. Assess.*, 2016, **188**, 1-12.
8. S. Sivamani and B. Leena Grace, *IJBST*, 2009, **2**, 47-51.
9. T. W. Seow and C. K. Lim, *IJAER*, 2016, **11**, 2675-2679.
10. Z. Salahshoor and A. Shahbazi, *Eur. J. Environ. Sci.*, 2014, **4**.
11. C. Namasivayam and D. Kavitha, *Dyes Pigm.*, 2002, **54**, 47-58.
12. B. Hameed, A. M. Din and A. Ahmad, *J. Hazard. Mater.*, 2007, **141**, 819-825.
13. V. Rizzi, A. Longo, P. Fini, P. Semeraro, P. Cosma, E. Franco, R. García, M. Ferrándiz, E. Núñez and J. A. Gabaldón, *Adv. Chem. Engineer. Sci.*, 2014, **4**, 454.
14. P. Semeraro, V. Rizzi, P. Fini, S. Matera, P. Cosma, E. Franco, R. García, M. Ferrándiz, E. Núñez and J. A. Gabaldón, *Dyes Pigm.*, 2015, **119**, 84-94.
15. K. Y. Ho, G. McKay and K. L. Yeung, *Langmuir*, 2003, **19**, 3019-3024.
16. S. Wang and H. Li, *Microporous Mesoporous Mater.*, 2006, **97**, 21-26.
17. M. Anbia and S. A. Hariri, *Desalination*, 2010, **261**, 61-66.
18. M. Zarezadeh-Mehrzi and A. Badiei, *Water Resources and Industry*, 2014, **5**, 49-57.
19. K. L. Dreher, *Toxicol. Sci.*, 2004, **77**, 3-5.
20. M. Hassellöv, J. W. Readman, J. F. Ranville and K. Tiede, *Ecotoxicology*, 2008, **17**, 344-361.
21. A. Hawe, M. Sutter and W. Jiskoot, *Pharm. Res.*, 2008, **25**, 1487-1499.
22. X. Zhuang, Y. Wan, C. Feng, Y. Shen and D. Zhao, *Chem. Mater.*, 2009, **21**, 706-716.

23. S. R. Shirsath, A. P. Patil, R. Patil, J. B. Naik, P. R. Gogate and S. H. Sonawane, *Ultrason. Sonochem.*, 2013, **20**, 914-923.
24. M. Arami, N. Y. Limaee, N. M. Mahmoodi and N. S. Tabrizi, *J. Colloid Interface Sci.*, 2005, **288**, 371-376.
25. Y.-S. Ho and G. McKay, *Process Biochem.*, 1999, **34**, 451-465.
26. K. Bharathi and S. Ramesh, *Appl. water sci.*, 2013, **3**, 773-790.
27. S. Wang, Y. Boyjoo and A. Choueib, *Chemosphere*, 2005, **60**, 1401-1407.
28. G. Crini and P.-M. Badot, *Prog. Polym. Sci.*, 2008, **33**, 399-447.
29. N. M. Mahmoodi, R. Salehi and M. Arami, *Desalination*, 2011, **272**, 187-195.
30. Y. S. Al-Degs, M. I. El-Barghouthi, A. H. El-Sheikh and G. M. Walker, *Dyes Pigment.*, 2008, **77**, 16-23.

## Chapter 4

# Highly selective artificial neurotransmitter receptors from zeolite based nanoporous materials

### Abstract

Despite decades of concentrated efforts, artificial receptors remain inferior compared to their natural counterparts with respect to affinity and selectivity. Receptor candidates whose design was intended to optimize direct receptor-ligand interactions (Emil Fischer's lock and key model)<sup>1</sup> afforded, with the notable exception of multivalent systems,<sup>2</sup> only moderate binding affinities in water, by no means reaching that of protein receptors.<sup>3</sup> Recent (re)discovery of the importance of the non-classical hydrophobic effect in well shielded protein binding pockets and host cavities offers an alternative, biomimetic receptor design strategy.<sup>4-7</sup> Herein, we follow this path and report several extremely selective and strongly binding artificial receptors for aromatic amine neurotransmitters, *e.g.* serotonin, dopamine, (nor)epinephrine and histamine. Importantly, the receptors are functional in buffers and biological media (*e.g.* blood serum) and can be used to study neurotransmitter-degradation or their delivery into living cells in real time.

## 4.1 Introduction

The selective, non-covalent complexation of small organic molecules in aqueous media remains extremely challenging. In fact, it was recently argued that previous knowledge derived for supramolecular complexes in organic solvents is largely irrelevant to molecular interactions in water.<sup>4</sup> Unlike the unsuccessful attempts made by Chemists, nature reaches a high binding-affinity in aqueous media through release of energetically frustrated water molecules from hydrophobic and confined protein cavities. The selectivity for a particular ligand is simultaneously defined through well positioned ligand-binding units (Fig. 4.1a).<sup>4-6</sup> Neurotransmitter binding to protein-receptors is favoured by release of energetically frustrated cavity water and the formation of salt-bridges between protein and ligand. The binding event is transcribed into a biological signal through conformational changes of the receptor. For instance, the binding pocket of the human D3-type dopamine-receptor is confined, hydrophobic and decorated with negatively charged amino acid residues in order to form salt-bridges with the positively charged ammonium moiety of dopamine.<sup>8</sup>

If the release of energetically frustrated cavity water molecules from protein binding pockets is (one of) the main driving forces for protein-ligand complexations, then also artificial receptor analogues should be constructed from synthetic hosts or materials that possess similarly sized, hydrophobic cavities.<sup>4-7</sup> To test this hypothesis, zeolite materials were employed in this study as receptor scaffolds because of *a*) their porosity, shape-stability and crystallinity allows for the creation of robust and molecularly defined binding pockets, and *b*) their permanent negative framework charge mimics the electrostatic-signature of D3-receptor cavity (Fig. 4.1b). Herein, a biomimetic approach is introduced: inorganic nanoporous material contains high-energy water whose displacement by an analyte can be energetically favourable. The negatively charged channels of zeolite materials cause a charge-mediated binding preference for cationic analytes, *e.g.* aromatic amine neurotransmitters. A sensitive signal transduction is



accomplished through co-inclusion of an aryl-moiety-responsive, fluorescent reporter dye into zeolite L or Y.

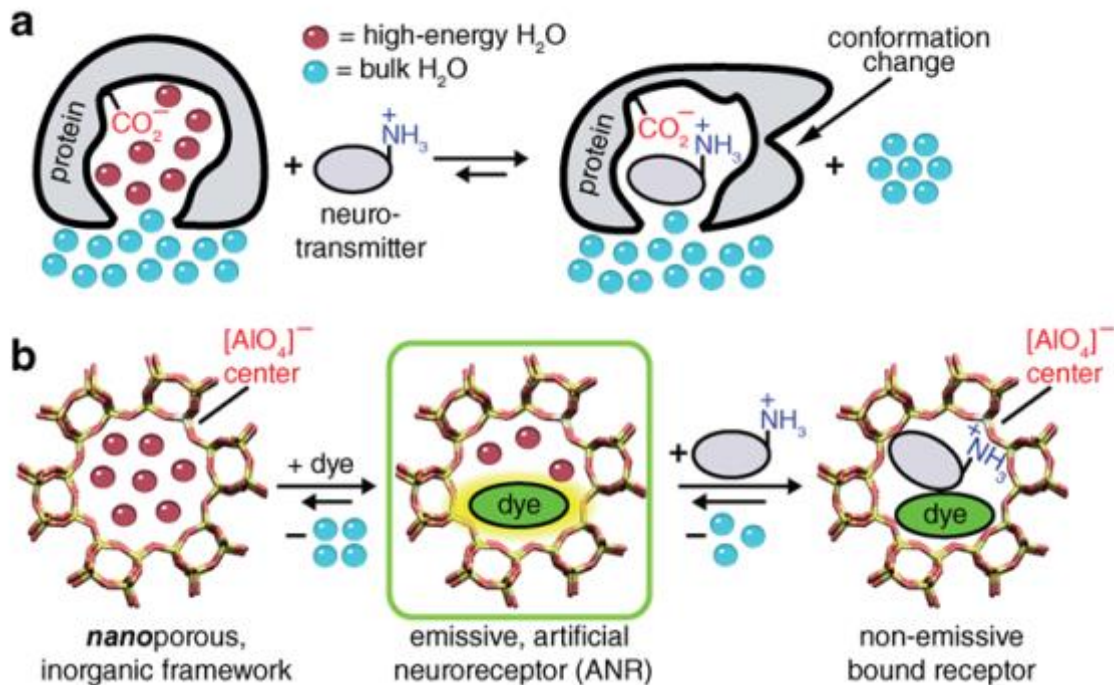


**Fig. 4.1** a) Schematic representation of how the natural neurotransmitters work; b) Artificial neurotransmitter receptor approach via nanoporous zeolite material.

*In this chapter, artificial neurotransmitter receptor based on nanoporous zeolite material has been developed. Different molecules have been tested for both sensitivity and selectivity for the receptors. Several sensing applications have been demonstrated based on our system.*

## 4.2 Proof of concept

It is known that zeolite materials can be loaded with fluorescent dyes,<sup>9, 10</sup> which is extended herein to analyte-responsive reporter dyes that indicate the presence of an aromatic amine neurotransmitter. Specifically, the dicationic reporter dyes (**D1-D5**)

shown in Fig. 4.2 are readily uptaken and strongly bound in the negatively charged zeolite channels. The herein communicated zeolite L (LTL type) -based artificial neuroreceptors (**ANR-L1 – ANR-L5**) and the zeolite Y (FAU type) -based counterparts **ANR-Y1** and **ANR-Y2** were prepared by immersion of zeolite nanocrystals with a solution of the corresponding dyes, followed by simple washing steps via centrifugation. The uptake of dyes by zeolite materials can be readily witnessed by the vanishing of the colour of the supernatant as well as by quantifiable changes of the physical properties of the dye. The effect of solvent on the excitation and emission of the ANR-LX is shown in Fig. 4.3. The excitation and emission spectra change of the dyes encapsulated in different ANRs is shown in Fig. 4.4.

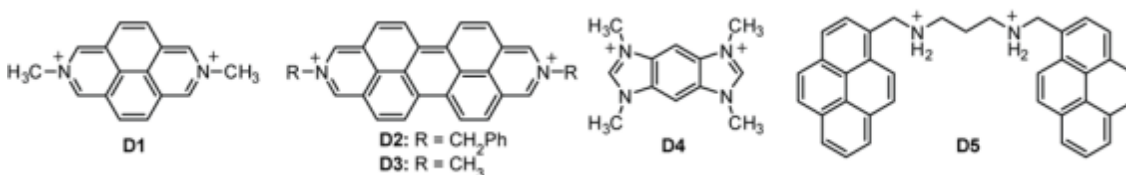


**Fig. 4.2** Chemical structures of the dicationic dyes.

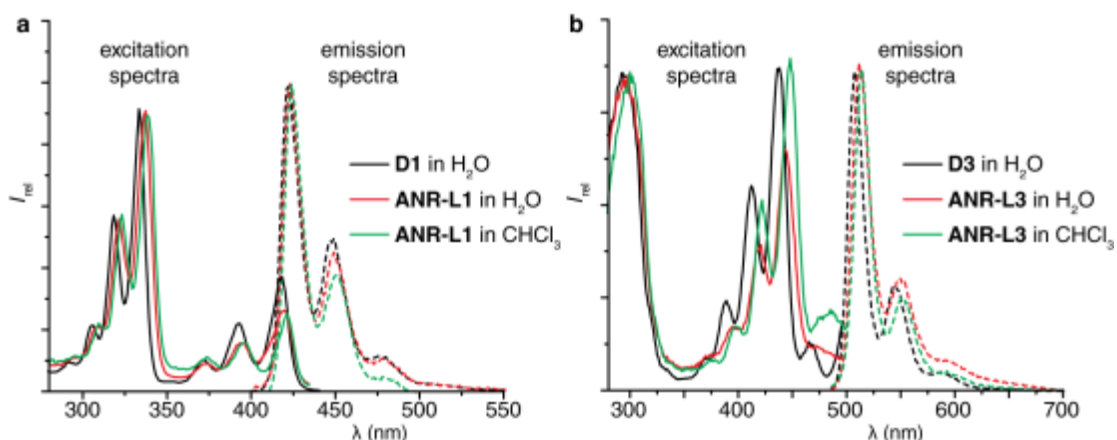


**Fig. 4.3** Normalized emission and excitation spectra of a, dye D1 and b, dye D3 and of their corresponding receptors ANR-L1 and ANR-L3 when dispersed in water or in chloroform.

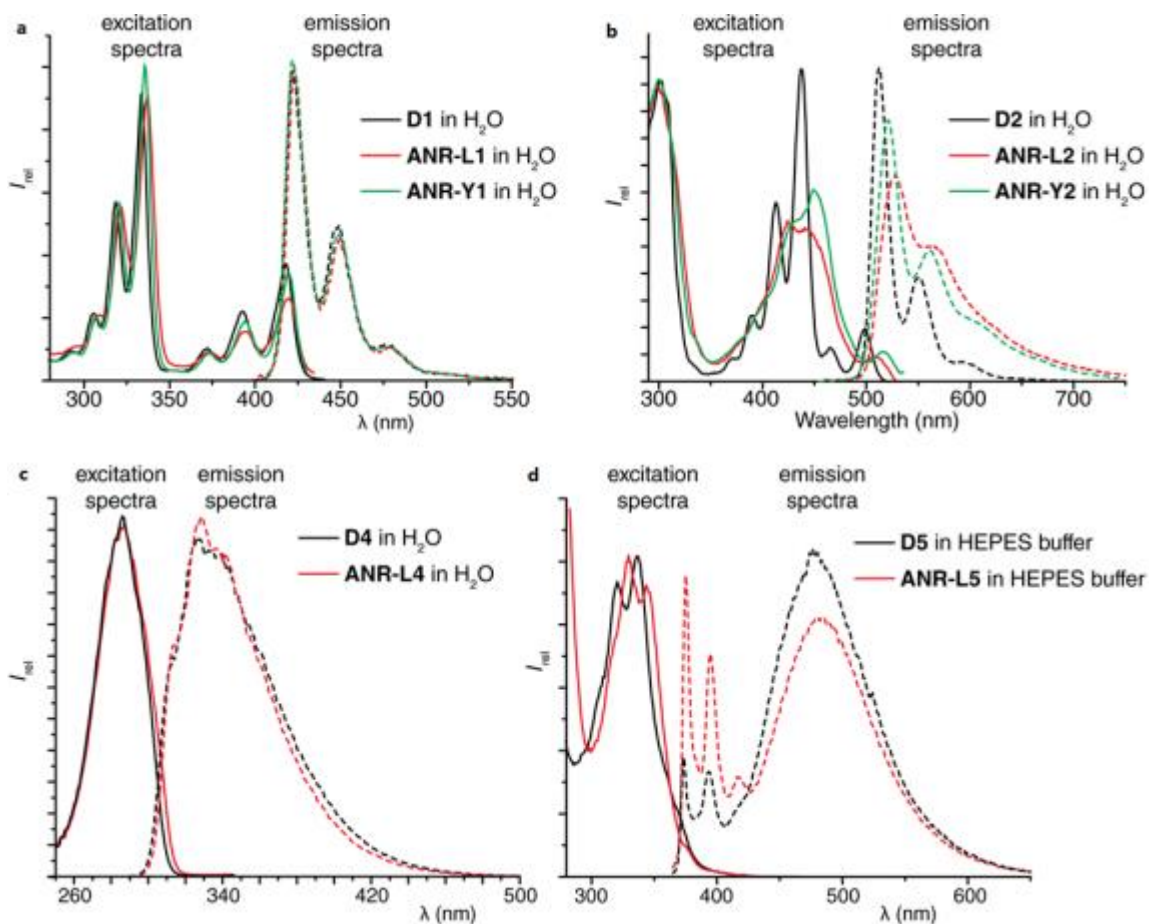


**Fig. 4.4** Normalized emission and excitation spectra of a, dye D1 and its corresponding receptors ANR-L1 (based on zeolite LTL), and ANR-Y1 (based on zeolite Y), b, for dye D2 and its corresponding receptors ANR-L2 (based on zeolite LTL), and ANR-Y2 (based on zeolite Y), c, dye D4 and of its corresponding receptor ANR-L4 in water, and b, of dye D5 and of its corresponding receptor ANR-L5 in aqueous HEPES buffer.

The reporter dyes are known to form stacking complexes with aromatic analytes, accompanied by a strong reduction of the emission of the dye.<sup>11, 12</sup> In fact, zeolite L (max. accessible pore diameter 10.7 Å) and zeolite Y (max. accessible pore diameter 11.9 Å) were chosen because their pores provide sufficient space to arrange a dye molecule and an aromatic amine neurotransmitter in a tight face-to-face stacking arrangement. Table 4.1 show the change quantum yield of the pure dye and the dye loaded in the ANRs, as well as after the addition of quencher.

**Table 4.1** Emission quantum yields (QY) for ANRs and corresponding dyes in water.

<b>System</b>	<b><math>\lambda_{\text{exc}}</math> (nm)</b>	<b>QY</b>
<b>D1</b>	336	0.43
<b>ANR-L1</b>	336	0.52
<b>ANR-L1 + excess dopamine</b>	336	< 0.01
<b>D1</b>	336	0.43
<b>ANR-Y1</b>	336	0.53
<b>ANR-Y1 + excess dopamine</b>	336	< 0.01
<b>D2</b>	420	0.37
<b>ANR-L2</b>	420	0.12
<b>ANR-L2 + excess dopamine</b>	420	< 0.01
<b>D2</b>	420	0.37
<b>ANR-L2</b>	420	0.14
<b>ANR-L2 + excess dopamine</b>	420	< 0.01
<b>D3</b>	440	0.04
<b>ANR-L3</b>	440	< 0.01
<b>ANR-L3 + excess dopamine</b>	440	0.51
<b>D4</b>	300	0.67
<b>ANR-L4</b>	300	0.45
<b>ANR-L4 + excess dopamine</b>	300	< 0.01

By entrapping the reporter dye in the negatively charged zeolites, the resulting artificial receptors can be expected to respond selectively to positively charged species that carry an aromatic moiety. In fact, out of the “zoo” of naturally occurring small molecules in mammals, these features are simultaneously expressed only for aromatic amine neurotransmitters, such as serotonin, dopamine and epinephrine, and some neuroactive trace amines (Fig. 4.5). Indeed, the herein presented receptors are extremely selective for those species.

Having verified the stability of the ANRs in saline buffers, we investigated into their spectroscopic response upon addition of the representative aromatic amine neurotransmitters: In agreement with the expectation from the design, the emission of **ANR1-L1** is nearly fully quenched by dopamine (Fig. 4.6). Emission quenching was generally found for all ANRs in the presence of electron-rich aromatic neurotransmitters such as serotonin, dopamine and norepinephrine (Fig. 4.7). A complementary detection strategy for the electron-poor, non-emission quenching analytes was also developed, which enabled the detection of histamine and phenethylamine through an increase in the

emission of **ANR-L3** and **ANR-Y2**, or through ratiometric changes in the emission spectrum of **ANR-L5** (Fig. 4.8).

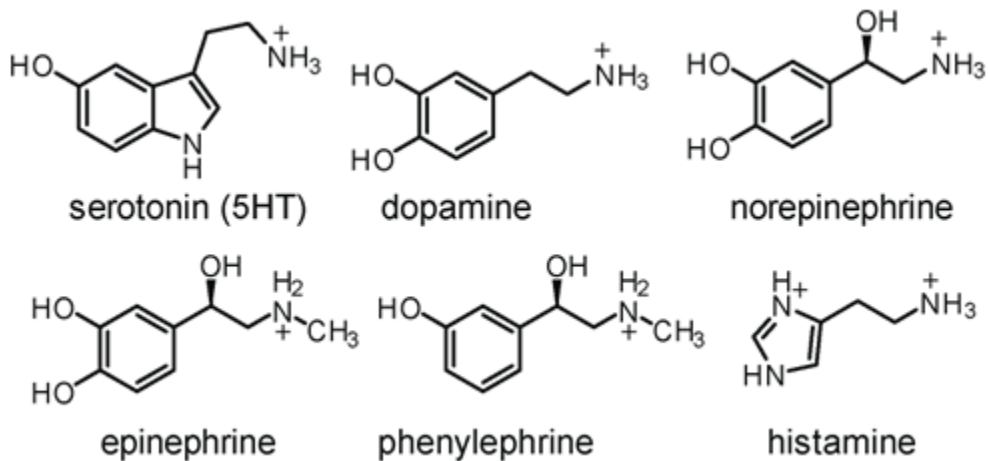


**Fig. 4.5** Selected chemical structures of aromatic amine neurotransmitters/drugs that can be detected by the ANRs and representative dyes employed.

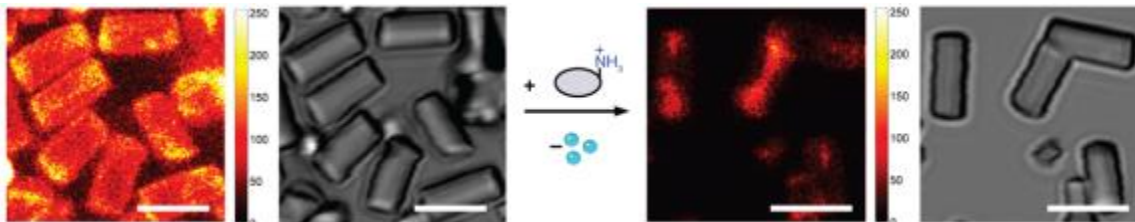


**Fig. 4.6** Intensity coded-confocal micrographs of an aqueous suspension of **ANR-L1** crystals, obtained by immersing dye D1 into zeolite L, prior (left) and after (right) addition of excess dopamine. The scale bar is 5  $\mu\text{m}$ .

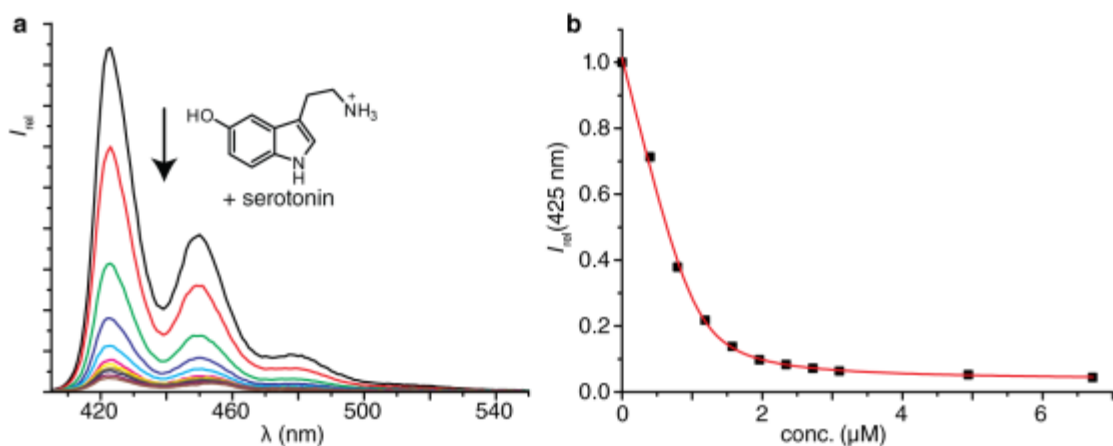


**Fig. 4.7** Example of emission quenching for dye encapsulated ANRs in the presence of electron-rich aromatic neurotransmitters. Emission spectra and binding curve for the titration of **ANR-Y1** (250 µg/mL) with serotonin in 10 mM HEPES buffer (pH 7.3). a, Addition of a solution of serotonin to a suspension of **ANR-Y1** results in a quenching of the emission of **ANR-Y1** ( $\lambda_{exc} = 395$  nm). b, Fit of the relative emission intensity with a 1:1 binding site model yields a single site dissociation constant  $K_d = 70 \cdot nM$ .

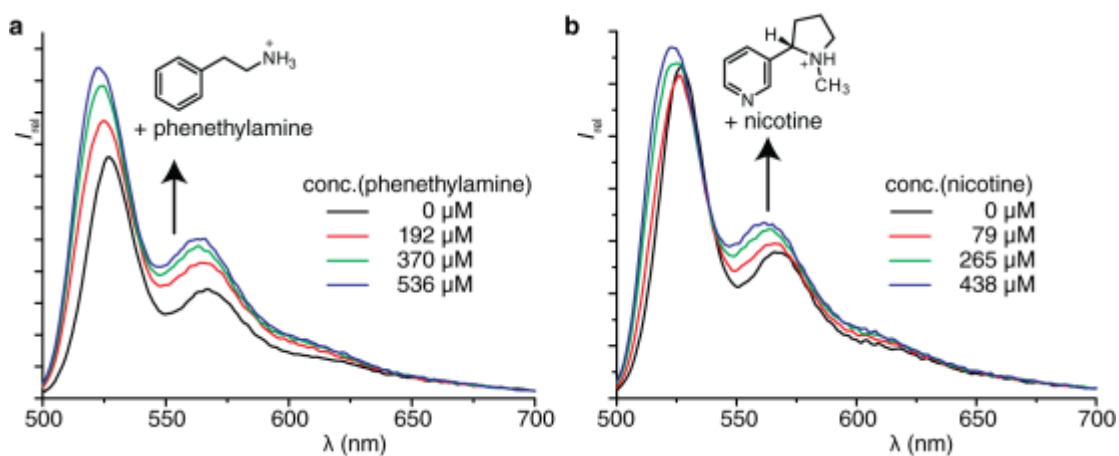


**Fig. 4.8** Emission spectra for the titration of **ANR-Y2** (250 µg/mL) with a, phenethylamine and b, nicotine in 10 mM HEPES buffer (pH 7.3) ( $\lambda_{exc} = 395$  nm).

### 4.3 Detection limit

Low concentration of the neurotransmitters can be readily detected by the ANRs owing to the sensitivity of fluorescence emission, as is exemplified for the response to ultra-low concentration (50 nM) of serotonin (Fig. 4.9). In order to quantify the binding strengths, dissociation constants ( $K_d$ ) were determined from fluorescence titration experiments for various combinations of representative analytes (see Fig. 4.10 for their chemical structures) and six ANRs. High affinities ( $K_d$  ranges from 100 nM to 100  $\mu$ M) were observed for the interactions of the ANRs with the neurotransmitters and trace amines in aqueous media (Table 4.2-4.5). All  $K_d$  values with a  $\gg$  sign denote less than 10% change in emission intensity at  $>50$  molar excess of the analyte. Errors in  $K_d$ , determined by repetitive experiments, are estimated less than  $\pm 20\%$ . Interestingly, a higher binding strength ( $\sim 10x$ ) was found in aqueous than in ethanolic media, which indicates the energetically favourable release of frustrated cavity water molecules from the ANR channels upon neurotransmitter binding (see experimental section for more details).<sup>5, 7, 13</sup>

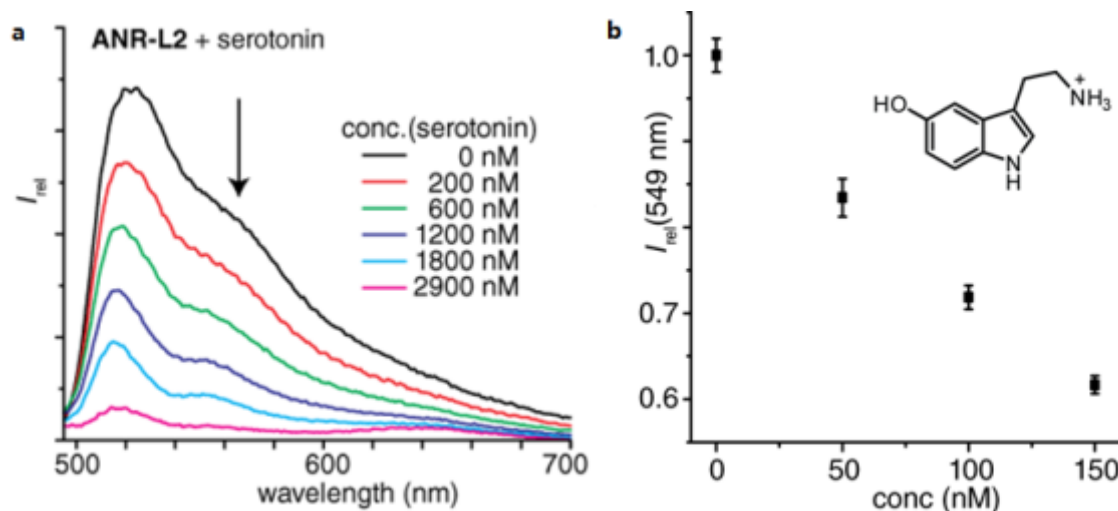


**Fig. 4.9** a, Emission spectra of ANR-L2 (25  $\mu$ g/mL) upon addition of serotonin ( $\lambda_{exc} = 475$  nm). b, Emission response of ANR-L2 (2.5  $\mu$ g/mL) upon addition of serotonin. Error bars were calculated from 3 repetition experiments. The experiments were carried out in aqueous HEPES buffer (10 mM, pH 7.3).

**Table 4.2** Fitted single site dissociation constants ( $K_d$ ) for representative analytes. Zeolite L-system, **ANR-L1**, and zeolite Y-assemblies, **ANR-Y1** (each receptor 250  $\mu\text{g/mL}$  in 10 mM HEPES buffer, pH 7.3).

Analyte	biological function	charge	aryl-unit	$K_d(\text{ANR-L1})$ ( $\mu\text{M}$ )	$K_d(\text{ANR-Y1})$ ( $\mu\text{M}$ )
serotonin (5-HT)	neurotransmitter	+	5HO-indole	3.3	0.07
tryptamine	trace amine	+	indole	10	0.15
dopamine	neurotransmitter	+	catechol	16	3.4
norepinephrine	neurotransmitter	+	catechol	31	11
tyramine	trace amine	+	phenol	27	5.7
octopamine	trace amine	+	phenol	40	11
TrpNH <sub>2</sub>	-	+	indole	32	0.11
epinephrine	neurotransmitter	+	catechol	>100	26
phenylephrine	drug (decongestant)	+	phenol	>100	55
phenethylamine	trace amine	+	benzene	n.s.	n.s.
histamine	neurotransmitter	+	imidazole	n.s.	n.s.
nicotine	stimulant drug, toxin	+	pyridine	n.s.	n.s.
propranolol	drug (beta blocker)	+	1-naphthol	>100	>100
L-DOPA	drug (dopamine precursor)	+ -	catechol	>>1000	>>1000
phenylalanine	amino acid	+ -	benzene	>>1000	>>1000
tyrosine	amino acid	+ -	phenol	>>1000	>>1000
histidine	amino acid	+ -	imidazole	>>1000	>>1000
tryptophan (Trp)	amino acid	+ -	indole	>>1000	>>1000
5-HTP	precursor to 5HT	+ -	5HO-indole	>>1000	>>1000
TrpGly	occurs in hypophysis	+ -	indole	>>1000	>>1000
indole-3-acetic acid	plant hormone	-	indole	>>1000	>>1000
melatonin	hormone	no	5MeO-indole	>>1000	>>1000
adenosine	neuromodulator	no	purine	>>1000	>>1000
estradiol	hormone	no	phenol	>>1000	>>1000
propanil	herbicide	no	benzamide	>>1000	>>1000
indole	-	no	indole	>>1000	>>1000
catechol	-	no	catechol	>>1000	>>1000
paracetamol	drug (analgesic)	no	phenol	>>1000	>>1000
raspberry ketone	natural aroma	no	phenol	>>1000	>>1000
acetylcholin	neurotransmitter	+	no	>>1000	>>1000
glycine (Gly)	neurotransmitter	+ -	no	>>1000	>>1000
D-serine	neurotransmitter	+ -	no	>>1000	>>1000



aspartate	neurotransmitter	+ -	no	>>1000	>>1000
glutamate	neurotransmitter	+ -	no	>>1000	>>1000
GABA	neurotransmitter	+ -	no	>>1000	>>1000
cadaverine	toxin	++	no	>>1000	>>1000
ethanolamine	-	+	no	>>1000	>>1000
glucose	sugar	no	no	>>1000	>>1000

**Table 4.3** Fitted single site dissociation constants ( $K_d$ ) for the binding of zeolite L-based **ANR-L2** and zeolite Y-based **ANR-Y2** (each at 250  $\mu\text{g/mL}$  in 10 mM HEPES buffer, pH 7.3) with representative analytes.

Analyte	biological function	charge	aryl-unit	$K_d(\text{ANR-L2})$ ( $\mu\text{M}$ )	$K_d(\text{ANR-Y2})$ ( $\mu\text{M}$ )
serotonin (5-HT)	neurotransmitter	+	5HO-indole	1.2	0.63
tryptamine	trace amine	+	indole	1.6	0.99
dopamine	neurotransmitter	+	catechol	4.5	9.5
TrpNH <sub>2</sub>	-	+	indole	6.7	2.7
norepinephrine	neurotransmitter	+	catechol	13	26
tyramine	trace amine	+	phenol	13	19
octopamine	trace amine	+	phenol	68	58
epinephrine	neurotransmitter	+	catechol	>100	39
phenylephrine	drug (decongestant)	+	phenol	>100	>100
phenethylamine	trace amine	+	benzene	n.d.*	>100*
histamine	neurotransmitter	+	imidazole	n.d.*	56*
tryptophan (Trp)	amino acid	+ -	indole	>>1000	>1000
TrpGly	occurs in hypophysis	+ -	indole	>>1000	>1000
5-hydroxy tryptophan	precursor to 5HT	+ -	5HO-indole	>>1000	>1000

\* The electron-poor analyte phenethylamine and histamine do not quench the emission of **ANR-L2** and **ANR-Y2**. Conversely, the addition of phenethylamine and histamine to **ANR-Y2**, **ANR-L3** and **ANR-L5** causes an increase in the emission intensity through dye-aggregation, while nicotine gave no appreciable effect at 100  $\mu\text{M}$  concentration. The  $K_d$  values for **ANR-L3** (250  $\mu\text{g/mL}$  in 10 mM HEPES buffer, pH 7.3) with phenethylamine and histamine are 190  $\mu\text{M}$  and 360  $\mu\text{M}$ , respectively. Furthermore, phenethylamine partially quenches the emission of **ANR-L4** (residual emission int. 75% at 25  $\mu\text{M}$  of analyte,  $K_d = 19$   $\mu\text{M}$ ). All other herein shown aryl-moiety containing analytes are known to quench the emission of **D2** when held in close spatial proximity to the dye.<sup>12</sup>

**Table 4.4** Fitted single site dissociation constants ( $K_d$ ) for the binding of zeolite LTL-based **ANR-L2** (250  $\mu\text{g/mL}$  in 10 mM HEPES buffer, pH 7.3) with representative analytes.

analyte	biological function	charge	aryl-unit	$K_d(\text{ANR-L3})$ ( $\mu\text{M}$ )
serotonin (5-HT)	neurotransmitter	+	5HO-indole	2.7
tryptamine	trace amine	+	indole	9.4
tyramine	trace amine	+	phenol	6.9*
dopamine	neurotransmitter	+	catechol	9.7
norepinephrine	neurotransmitter	+	catechol	15
phenethylamine	trace amine	+	benzene	190*
histamine	neurotransmitter	+	imidazole	360*
epinephrine	neurotransmitter, hormone	+	catechol	>100
L-DOPA	drug (dopamine precursor)	+ -	catechol	>>1000
tryptophan (Trp)	amino acid	+ -	indole	>>1000
nicotine	stimulant drug, toxin	+	pyridine	>>1000
indole	-	No	indole	>>1000
catechol	-	No	catechol	>>1000

\* Tyramine quenches the emission of **ANR-L3** by only 30%, but the titration curve shows saturation behaviour.

\*\* The electron-poor analytes phenethylamine and histamine cause an increase in the emission intensity of **ANR-L3** through dye-aggregation.

**Table 4.5** Response of the emission **ANR-L4** (250  $\mu\text{g/mL}$  in 10 mM HEPES buffer, pH 7.3) to representative analytes

analyte	biological function	charge	aryl-unit	$K_d(\text{ANR-L4})$ ( $\mu\text{M}$ )
dopamine	neurotransmitter	+	catechol	3.5
norepinephrine	neurotransmitter	+	catechol	4.5
tyramine	trace amine	+	phenol	5.7
octopamine	trace amine	+	phenol	12
phenethylamine	trace amine	+	benzene	19
epinephrine	neurotransmitter, hormone	+	catechol	11
phenylephrine	drug (decongestant)	+	phenol	>100
histamine	neurotransmitter	+	imidazole	n.d.*
L-DOPA	drug (dopamine precursor)	+ -	catechol	>>1000
phenylalanine	amino acid	+ -	benzene	>>1000
tyrosine	amino acid	+ -	phenol	>>1000

histidine	amino acid	+ -	imidazole	>>1000
adenosine	neuromodulator	No	purine	>>1000
catechol	-	No	catechol	>>1000

\* The electron-poor analyte histamine cannot quench the emission of **ANR-L4**. All other herein shown aryl-moieties are known to quench the emission of **D4** when held in close spatial proximity to the dye.<sup>14</sup>

The autofluorescence of serotonin and tryptamine in the spectral region of the emission of **ANR-L4** has prevented the investigation of their binding to **ANR-L4**.

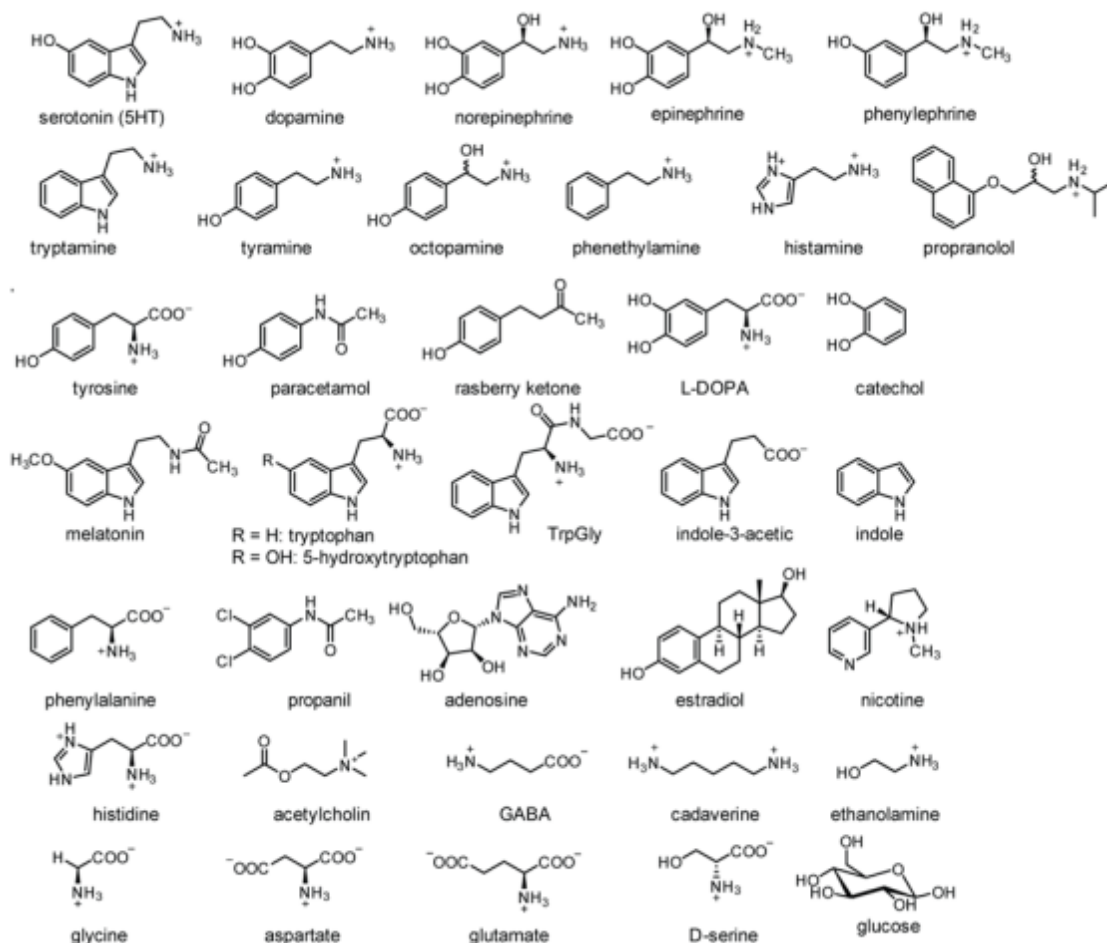


**Fig. 4.10** Chemical structures of the analytes tested in this study.

While not yet achieving the record values of Nature,  $K_d \sim 1$  nM, for serotonin binding to the natural 5-HT<sub>7</sub> receptor protein,<sup>15</sup> for serotonin binding to **ANR-Y1** we observed an impressive  $K_d \sim 70$  nM. Our zeolite-based ANRs are already superior compared to any

other *artificial* neurotransmitter receptor, *e.g.*  $K_d(5\text{-HT}) \sim 15 \mu\text{M}$  with the contemporary “record-affinity” host cucurbit[7]uril.<sup>16</sup> Besides, unlike natural protein receptors or most synthetic hosts, the zeolite-based ANRs have a *built-in* spectroscopic response upon neurotransmitter binding.

#### 4.4 Molecule selectivity

In order to investigate into the selectivity of the ANRs towards the neurotransmitters and structural analogues, ANR-responses to 37 representative substances were determined (Fig. 4.9 and Table 4.2-4.5). A very strong charge-mediated selectivity was generally observed; For instance, the binding affinity of the net positively charged, unnatural, amidated tryptophan ( $\text{TrpNH}_2$ ) with **ANR-Y1** and **ANR-Y2** is large,  $K_d \sim 110 \text{ nM}$  and  $2.7 \mu\text{M}$ , respectively, while its natural counterpart, the essentially isostructural but zwitterionic amino acid tryptophan (Trp) binds very weakly (Fig. 4.10). Notably, our receptor materials can reach charge-selectivity factors in  $K_d$  of about 10,000, whereas selectivity difference of  $\geq 100$  are rarely observed for the complexation of organic molecules by other artificial hosts in water.<sup>17, 18</sup> To exemplify,  $5 \mu\text{M}$  of serotonin could be clearly detected by **ARN-L1** in the presence of  $50,000 \mu\text{M}$  Trp (Fig. 4.11). Moreover, also non-charged species, such as catechol and indole, are only weakly bound by the ANRs, which is in stark contrast to the findings for their derived catecholamine neurotransmitters (dopamine, epinephrine and norepinephrine) and serotonin/tryptamine (Fig. 4.10).

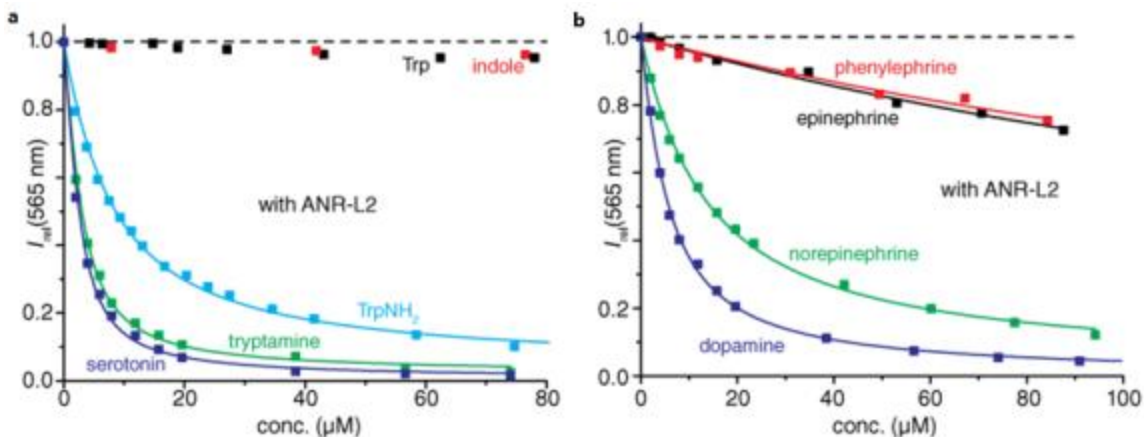


**Fig. 4.10** Binding isotherms for ANR-L2 (250  $\mu\text{g}/\text{mL}$ ) and a, indole-derivatives or b, catechol amines. See Fig. 4.X for their chemical structures. All titration experiments were carried out in aqueous HEPES buffer (10 mM, pH 7.3) and with an excitation wavelength of  $\lambda_{\text{exc}} = 475$  nm.

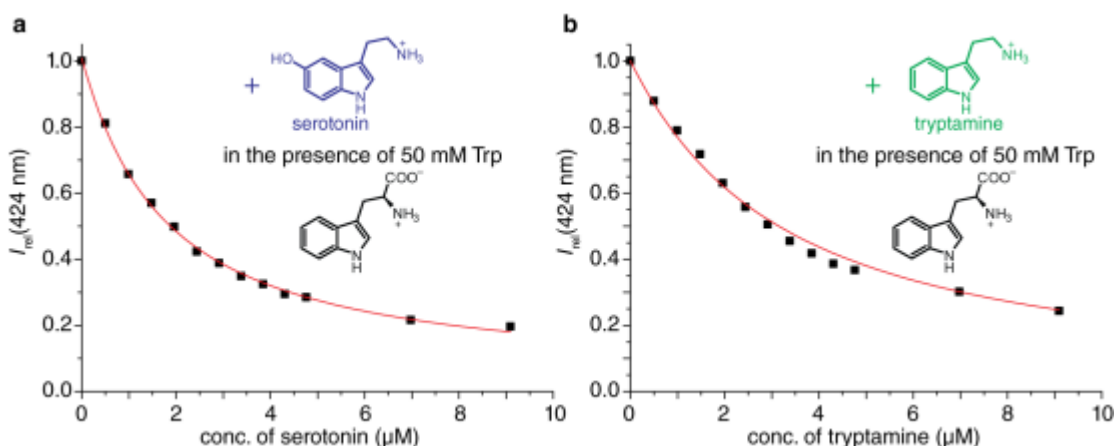


**Fig. 4.11** Binding curves for the titration of ANR-L1 (250  $\mu\text{g}/\text{mL}$ ) with a, serotonin and b, tryptamine, each in 10 mM HEPES buffer (pH 7.3) to which were added 50 mM tryptophan ( $\lambda_{\text{exc}} = 400$  nm). The solid lines represent the least-square fits to a single-site 1:1 binding site model. The binding strength ( $K_d = 14$   $\mu\text{M}$ ) of serotonin in the presence of 50 mM Trp is only by a factor  $\sim 4$  weaker than in the absence of the potential competitor Trp. Similarly, the also the binding of tryptamine ( $K_d = 27$   $\mu\text{M}$ ) and dopamine ( $K_d = 48$   $\mu\text{M}$ ) is still very strong in the presence of 50 mM Trp, and only by a factor  $\sim 3$  weaker than in the absence of the potential competitor Trp (See Table 4.X for comparison).

Equally striking is the much stronger response of **ANR-L1 – ANR-L4** for dopamine and norepinephrine than for the only slightly larger but otherwise very similar epinephrine and phenylephrine (Table 4.6 and Fig. 4.10). Surprisingly, even the natural  $\alpha_{2A}$ -adrenergic receptor and the dopamine D4 receptor show a lower degree of selectivity (Table 4.6). Expectedly, the larger-cavity zeolite-based receptors **ANR-Y1** and **ANR-Y2** are less size selective; with them epinephrine (26  $\mu\text{M}$  and 39  $\mu\text{M}$ , respectively) is strongly bound (see Table 4.2-4.6).

**Table 4.6** Relative binding selectivity for natural receptor proteins and the zeolite-based artificial receptors for dopamine, norepinephrine and epinephrine.

Receptor system	scaffold	Selectivity dopamine vs. (R)-epinephrine	Selectivity (R)-norepinephrine vs. (R)-epinephrine
$\alpha_{2A}$ -adrenergic receptor <sup>19</sup>	protein	13 – 25*	3 – 4*
dopamine D4 receptor <sup>20</sup>	protein	15	3 – 4*
<b>ANR-L1</b>	zeolite L	>50	>50
<b>ANR-L2</b>	zeolite L	52	19
<b>ANR-L3</b>	zeolite L	>50	>50
<b>ANR-L4</b>	zeolite L	32	25
<b>ANR-Y1</b>	zeolite Y	8	<3
<b>ANR-Y2</b>	zeolite Y	4	<2

The protein-based receptor studies were carried out in 50 mM  $\text{K}^+$ -phosphate and in Tris-buffer with added membrane components.<sup>19, 20</sup> The binding assays with the ANRs were performed in 10 mM HEPES buffer.

\* range of selectivity values was reported by different assay types

In addition to charge- and size-mediated selectivity constraints, it should be noted that only analytes that carry an aromatic recognition motif are expected to cause significant changes in the emission intensity of the sensors. Thus, of all naturally occurring substances tested, only the aromatic amine neurotransmitters and aromatic trace amines gave rise to a strong spectroscopic response while other neurotransmitters, hormones, drugs, amino acids, peptides and alkyl amines showed small effects. In fact, the functionality of the ANRs is preserved in cell culture media or blood serum which

verifies the high specificity of the ANRs. It arises as a conclusion that the entrapping of a reporter dye in the negatively charged and confined nanopores of zeolites crystals, guarantees for a very high selectivity for analytes that are small, positively charged and simultaneously possess an aryl-ring as the recognition unit.

## 4.5 Sensing applications

### 4.5.1 Ratiometric sensing

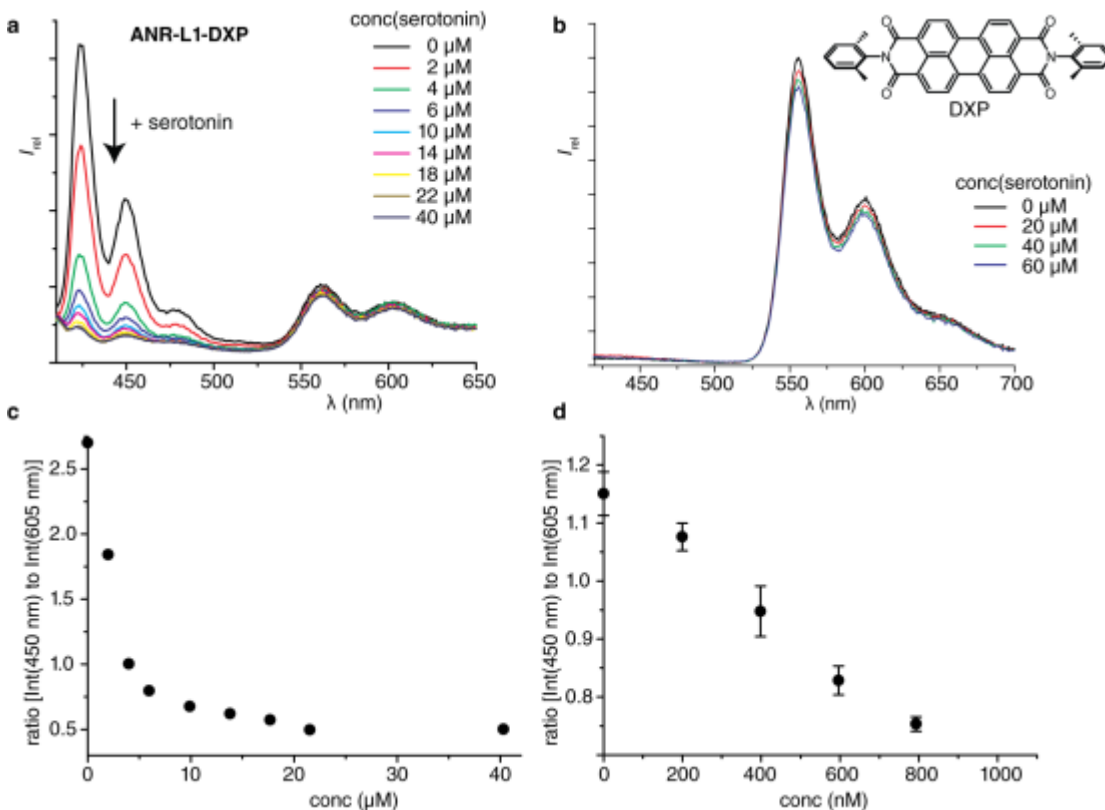


**Fig. 4.12** Ratiometric sensing with ANR-L1 that contains a co-encapsulated, non-analyte responsive reference dye DXP. a, Emission spectra of **ANR-L1-DXP** (=DXP loaded Linde-type zeolite L that was subsequently loaded with **D1**) (250 μg/mL) upon addition of serotonin. b, Control: Emission spectra of DXP loaded Linde-type zeolite L (250 μg/mL) upon addition of serotonin. c, Ratiometric plot for the titration experiment shown in part b of this figure. d, Ratiometric plot for titration experiments at lower **ANR-**

**L1-DXP** concentration ((25  $\mu\text{g}/\text{mL}$ ), allowing for detection of lower concentrations of serotonin.

The modular design of the ANRs allows to address additional requirements for practically applicable sensors. Firstly, co-inclusion of an analyte-responsive reporter dye with a non-responsive reference dye provides a simple access to ratiometric sensing schemes (Fig. 4.12). These experiments were carried out in triple-fold and the error bars are given. All experiments were carried out in 10 mM HEPES buffer and the excitation wavelength  $\lambda_{\text{exc}} = 360 \text{ nm}$  was used.

#### 4.5.2 Release indicator for label-free drugs

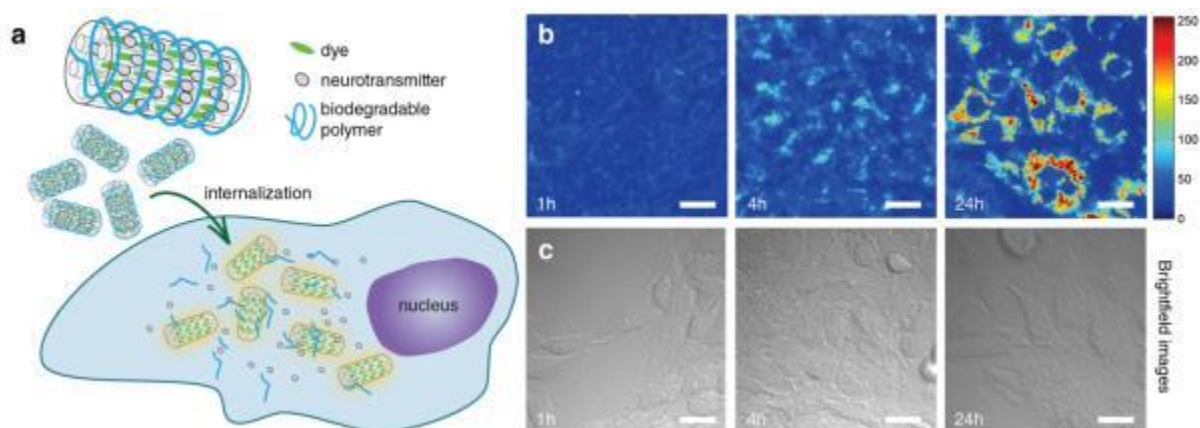


**Fig. 4.13** Fluorescence-based monitoring of the intracellular release of label-free drugs. a) Cellular uptake of drug-loaded and surface-coated ANRs results after release of the drug in an increase in the fluorescence emission of the ANR. b) Intensity coded-confocal micrographs showing cellular uptake experiment of the serotonin-loaded and poly(lysine)-coated **ANR-L1** at different incubation times 1h (left), 4h (center), and 24h (right panel), and c) their corresponding brightfield images. Images were acquired at  $\lambda_{\text{exc}} = 405 \text{ nm}$ . The scale bar is 20  $\mu\text{m}$ .

Surface functionalization of the ANRs is possible, furnishing sensors that are readily uptaken by cells (*e.g.* through coating with polylysine). Porous materials capable of



storing gases<sup>21</sup> or delivering drugs<sup>22</sup> have found wide ranges of industrial and medical applications, but monitoring strategies for cargo-loading and -unloading processes are just emerging.<sup>23, 24</sup> Oftentimes, fluorophore-labelled drug-analogues<sup>25</sup> were employed to study drug-delivery kinetics, however, labelled drugs inevitably show an altered biological profile compared to the parent drug. Employing a porous materials with a built-in fluorescent signal transducer is a promising alternative, allowing for monitoring of cargo-loading and -unloading of label-free drugs. We loaded **ANR-L1** with serotonin (switch off in emission) and surface-coated it with a cell-attracting polylysine layer (Fig. 4.13a). This drug-delivery vehicle was readily uptaken by living *Rattus norvegicus* C6 glioma cells. Then, intracellular-release of the cargo serotonin occurred in the course of 24h hours, as can be inferred from the gradual restoring of the emission of the ANR (Fig. 4.13b, c).

#### **4.6 Conclusion and perspectives**

Applying the lessons learnt for synthetic hosts and natural proteins about the energetic importance of the non-classical hydrophobic effect for binding of analytes/ligands in aqueous media,<sup>4-7</sup> it has been demonstrated that porous inorganic materials provide a platform for high-affinity binding. The herein introduced strategy relies on the use of nanoporous inorganic frameworks (pore size ~ 1 nm) as opposed to the frequently employed mesoporous (pore size > 2 nm)<sup>26</sup> or non-porous spherical nanoparticles.<sup>27</sup> Specifically, highly selective, artificial neurotransmitter receptors were furnished starting from negatively-charged, nanoporous zeolite L and zeolite Y. We believe that this concept is transferable to other nanoporous materials such as silicas, metal organic frameworks (MOFs) or covalent organic frameworks (COFs), which, – depending on their charge and atomic composition – will be high-affinity binders for different analyte classes. Moreover, the herein demonstrated convenient signal transduction strategy, through co-inclusion of an emissive reporter dye into the porous framework, can find important applications because of its sensitivity and practical ease.

## 4.7 Experimental section

### *Materials*

The zeolite host (Lucidot® NZL 40) was provided by Clariant. Zeolite Y was purchased as its sodium salt from Alfa Aesar. Analytes (e.g. neurotransmitters) were purchased from Sigma Aldrich with the highest purity grade available, typically as analytical standard grade, but in all cases at least 99%, and used as received. D1-D5 have been provided by Dr. Frank Biedermann.

### *Preparation of large, barrel-shaped zeolite L crystals*

Described in chapter 2.

### *Preparation of the ANRs*

A dicationic dye (**D1-D5**) was solubilized in 10 mL deionized water to reach a concentration of 5 mM. Then, commercial zeolite L powder (500 mg) was added to the solution. After 5 min of sonication, the suspension was shaken overnight. Then, the sample was centrifuged, decanted and washed several times with water to remove surface-adsorbed dye. This sequence was repeated until the supernatant became colourless and non-emissive. Finally, the solids were dried in vacuum to yield the corresponding **ANR-LX** ( $X = 1 \dots 5$ ). The same procedure was applied for the preparation of **ANR-Y1** and **ANR-Y2** starting from zeolite Y. The included dye was on the order of 0.5% per weight, see the section “Discussion of the number of binding sites ( $c_B$ )”, below. Table SEM measurements confirmed that no significant change in the morphology occurred upon dye uptake, as was expected.

### *Preparation of ANR-L1-DXP*

#### *1. Insertion of reference dye DXP by sublimation*

The DXP dye (0.1 mg) is mixed with commercial zeolite-L (100 mg) in a glass ampoule.<sup>28</sup> The amount of DXP loading is calculated by considering that one DXP molecule occupies 3 unit cells and a loading of 20% corresponds to the highest loading

possible. We aimed for a loading of 1%. The ampoule was dehydrated at about  $4.0 \times 10^{-6}$  mbar for 12 hours and sealed. The ampoule was then heated at 300 °C for 12 hours in the rotating oven. Afterwards the zeolite-L crystals were washed with n-butanol until the supernatant showed no absorbance anymore and the zeolites were finally dried in vacuum.

### *2. Loading of DXP-zeolite with **D1***

To a suspension of DXP-loaded zeolite L in water (200 mg in 10 mL) was added dye **D1** to achieve a concentration of 1 mM. The suspension was shaken overnight at room temperature, centrifuged and the solids were treated 4x with a washing-centrifugation-decanting sequence. The so prepared **ANR-L1-DXP**, suitable for ratiometric sensing, (Fig. S26), was then dried in vacuum.

### *Preparation of PEGylated **ANR-L1-PEG***

To a suspension of **ANR-L1** (40 mg) in 1.5 mL of anhydrous chloroform and the suspension was sonicated with a tip sonicator for 2 min. Then 40 mg of MeO-PEG-silane ( $M_w = 5$  kDa) were added and the suspension was stirred with a magnetic stirrer bar at 40 °C overnight and then centrifuged. The solids were washed 2x with chloroform and 2x with ethanol (each 1.5 mL) and then dried under vacuum. The presence of surface-grafted PEG on the ANR was confirmed by TGA (weight loss 6.8%) and SEM experiments, showing substantially less particle agglomeration than for the parent **ANR-L1**.

### *Preparation of polylysine-coated **ANR-L1***

To a suspension of **ANR-L1** (40 mg) in 1 mL of deionized water was added 500 µL of an aqueous solution of polylysine (0.1% (w/v), Santa Cruz Biotechnology). The suspension was sonicated in a sonication bath for 2 min and then shaken for 2 hours and centrifuged. The solids were washed 3x with deionized water and then dried under vacuum. The presence of a polylysine coating layer on the ANR was confirmed by the positive zeta potential of the coated, and negative zeta potential of the parent **ANR-L1**.

The polylysine-coated **ANR-L1** can be readily loaded with serotonin as a model drug by suspending the material in a 1 mM serotonin solution in water, followed by a centrifugation and washing step.

*Stability and Functionality of ANR-L1 particles in blood serum and culture media*

50  $\mu$ l of dispersion of ANR-L1 particles in blood serum (at concentration 1 mg/ml) was placed on glass cover slips and analyzed directly by confocal microscope. Next, 50  $\mu$ l of serotonin solution in HEPES buffer (at concentration 1mM) was mixed to the droplet and the confocal microscopy experiment was performed. Finally, 50  $\mu$ l of histamine solution HEPES buffer (at concentration 10mM) was extra added to the sample and the sample further analyzed by microscope. The same experiment was conducted for the same system in the presence of culture media.

*C6 Glioma cell culture*

Rattus norvegicus brain glioma (C6 Glioma) cells were grown inside culture media containing 88% Dulbecco's Modified Eagle Medium (DMEM), 10% Fetal Bovine Serum (FBS), 1% Penicillin-Streptomycin, and 1% L-Glutamine 200mM (all materials were purchased from Gibco), under 37°C and 5% CO<sub>2</sub> condition, until reaching 80 to 90% cell confluency. The cells were washed twice with phosphate buffered saline (PBS, Gibco), trypsinated, and 50,000 cells were seeded on the rectangular glass cover slip (VWR) inside six-well plate culture dish and glass bottom dishes (MatTek). Fresh culture medium (2 was added gently and cells were grown overnight.

*Stability and Functionality of ANR-L1 in the presence of culture media and cells*

Culture media were removed from glass bottom dish and 1 mL of nanoparticles dispersion (ANR-L1-PEG at concentration 0.1 mg/ml) was gently added onto cells. Cells were left at 37°C and 5% of CO<sub>2</sub> for 2 to 5 minutes to let the particles sediment on the glass surface. The sample was imaged subsequently by confocal microscope. In addition, the behavior of the system after addition of serotonin and histamine (at concentration 1mM and 10mM, respectively) were also analyzed.

### *Cellular uptake experiments*

Culture media were removed from the cell well plates and 1 mL of a serotonin loaded and polylysine coated **ANR-L1** dispersion was gently added onto cells (concentration 0.1 mg/ml). Cells were incubated at 37°C and 5% of CO<sub>2</sub> for 1, 4, and 24 hours and after each of the incubation is finished, the media was removed and the cell layer on glass cover slips was gently washed three times with fresh PBS. Cell layer was fixed with 4% paraformaldehyde (PFA) solution for 10 minutes. The layer was rewashed with PBS and rinsed in 0.1% Triton X-100 in PBS for 5 minutes, washed twice with PBS and followed in 1% bovine serum albumin, BSA (Sigma Aldrich), in PBS solution for 20 minutes. Cells were gently washed with PBS three times and the cell layer on glass cover slip was directly stained with Phalloidin Alexa Fluor® 647 (Invitrogen), for f-actin/membrane staining, for 20 minutes, in the dark at room temperature, and washed again twice with PBS and once with water. The cover slips were mounted onto glass slides for microscopy experiments.

### *Confocal microscopy*

Fluorescence images were acquired using Zeiss LSM 710 confocal microscope system with 63x magnification, numerical aperture 1.3 of Zeiss LCI Plan-NEOFLUAR water immersion objective lens (Zeiss GmbH). The samples were excited by a continuous wave (cw) laser operated at wavelength 405 nm and the emission of the system was collected widely in the range 412 nm to 735 nm. The emission spectra were acquired using lambda mode acquisition and the signal was reprocessed by Zen 2011 software (Zeiss GmbH).

### *Dynamic light scattering and zeta-potential*

DLS and zeta-potential analysis were performed on a Delsa Nano C Particle Analyzer (Beckman Coulter, Brea, CA, USA); all DLS measurements were conducted in water, while zeta-potential analysis in phosphate buffered saline (PBS), pH = 7.

### *Thermogravimetric analysis*

Thermogravimetric (TG) measurements were performed on a TGA instrument NETZSCH STA 449 F3 Jupiter® – Simultaneous TGA-DSC. TGA scans were done with a heating rate of 10 °C /min and hold at 550 °C for 30 min under a synthetic air purge gas flow of 20 mL/min.

### *UV-Vis spectrum*

The UV-Vis absorption spectra were measured by Shimadzu UV-3600 UV-Vis-NIR spectrophotometer. The spectra of liquid samples were recorded at a 1 nm/s scan rate in a cuvette with a 1 cm path length.

### *Fluorescence steady state spectrofluorometer*

Steady-state emission spectra were recorded on a Horiba Jobin–Yvon IBH FL-322 Fluorolog 3 spectrometer equipped with a 450 W xenon arc lamp, double-grating excitation, and emission monochromators (2.1 nm mm<sup>-1</sup> of dispersion; 1200 grooves mm<sup>-1</sup>) and a TBX-04 single photoncounting detector. Emission and excitation spectra were corrected for source intensity (lamp and grating) and emission spectral response (detector and grating) by standard correction curves.

### *Fluorescence lifetime spectrometer*

Time-resolved measurements were performed using either the time-correlated single-photon counting (TCSPC) electronics PicoHarp 300 or the Multi-Channel Scaling (MCS) electronics NanoHarp 250 of the PicoQuant FluoTime 300 (PicoQuant GmbH, Germany), equipped with a PDL 820 laser pulse driver. A pulsed laser diode LDH-P-C-375 ( $\lambda_{\text{exc}} = 375$  nm, pulse FWHM <70 ps, repetition rate 40 kHz) was used to excite the sample and mounted directly on the sample chamber at 90°. The photons were collected by a PMA-C-192 photomultiplier (PMT) single-photon-counting detector. The data were acquired by using the commercially available software EasyTau (PicoQuant GmbH, Germany), while data analysis was performed using the commercially available software FluoFit (PicoQuant GmbH, Germany).

### Fluorescence Titration Experiments

Analyte-ANR response experiments were carried out in a fluorescence quartz cuvette (3.5 mL) by titrating a suspension of the ANR in buffer with a stock solution of the analyte. The excitation and emission wavelengths were chosen outside the absorbance window of the analyte while simultaneously avoiding the contribution of the Raman scattering peak to spectral area of interest. It was found that repetitive measurements of the ANR suspension gave essentially identical spectra and intensities, confirming that the ANR suspensions are stable. It was also confirmed that repetitive addition of buffer to the ANR suspension did not affect the measurable emission intensity beyond dilution effects. After addition of aliquots of the stock solution of the analyte to the ANR suspension, the cuvette was shaken for about 3 seconds and the emission spectra was recorded. By comparison with longer waiting times (*e.g.* 10 s, 5 min, 30 min) it is clear that the binding equilibrium was already established after 3 seconds (possibly faster), *i.e.* within manual mixing time.

Stern-Volmer analysis of the emission data shows the expected linear behaviour between the concentration of the quencher and the ratio of the emission intensities  $F_0/F$ .

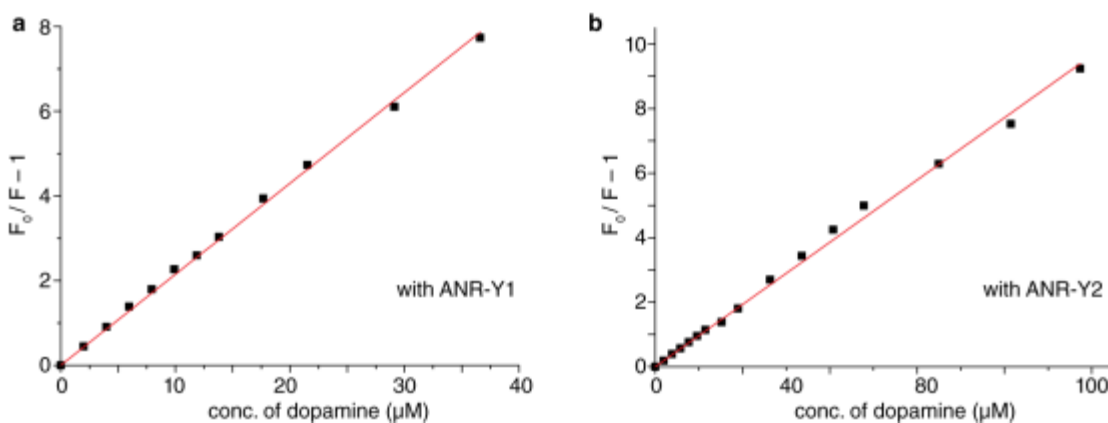


**Fig. 4.15** Example of a Stern-Volmer plot for a, **ANR-Y1** with dopamine and b, **ANR-Y2** with dopamine. The approximated dissociation constants ( $K_d = 1/\text{slope}$ ) of 4  $\mu\text{M}$  and 10  $\mu\text{M}$ , respectively, are qualitatively in good agreement with the ones obtained by the preferred non-linear least square fit.

The binding isothermes were obtained then by plotting relative emission intensity at a suitable wavelength against the analyte concentration and were then fitted by equation (1), see below.

This fitting procedure was used in favour of a Stern-Volmer analysis, because linearized binding plots are known to produce errors in  $K_d$ .

*Data analysis and extraction of the affinity constants  $K_d$*

The binding isotherms were fitted by a least square fit through a binding equation for a single site 1:1 binding model ( $A+B \rightarrow AB$ ) under the assumption that only the components B and AB are emissive.

$$\frac{F_A}{F_0} = 1 + \frac{\Delta F [(c_A + c_B + K_d) - \sqrt{(c_A + c_B + K_d)^2 - 4 \cdot c_A \cdot c_B}]}{2 \cdot c_B} \quad (1)$$

Herein,  $F_A$  is the intensity at a given analyte concentration and  $F_0$  is the emission intensity before analyte addition.  $\Delta F$  is a measure of the relative emission increase or decrease caused by the analyte. For fully non emissive AB complexes, *i.e.* when the analyte A is an efficient quencher,  $\Delta F$  reaches  $-1$ . The quantity  $c_A$  denotes the concentration of the analyte A and  $c_B$  denotes the concentration of the “binding stations” in the ANR.

The values  $K_d$  and  $\Delta F$  result from the non-least square fit given the input  $F_A$ ,  $F_0$ ,  $c_A$  and  $c_B$ .

The concentration  $c_A$  of the analyte follows directly from the concentration of the stock solution and the added volume to the cuvette with the suspension of the ANR. The concentration  $c_B$  of the single binding sites per ANR suspension is a priori not known. However,  $c_B$  is directly and unambiguously obtained from the fitting of the fluorescence binding isotherms for the case of strongly binding analytes, e.g. serotonin and tryptamine. This so obtained value  $c_B$  was then used as a constant for the fitting of the binding isotherms of the weaker binding analytes. Notably, in all cases were fits observed with an adjusted R-square value  $> 0.98$ , which cooperates that all binding sites inside the zeolite crystal can be treated as independent and equal. In addition, it is reassuring to note that



the value of the affinity constant  $K_d$  is rather insensitive to the concentration  $c_B$ . The so determined  $c_B$  values are tabulated below.

ANR suspension (250 $\mu\text{g/mL}$ )	$c_B$ from fitting / $\mu\text{M}$
<b>ANR-L1</b>	6.6
<b>ANR-L1-DXP</b>	4.0
<b>ANR-L2</b>	2.6
<b>ANR-L3</b>	3.2
<b>ANR-L4</b>	5.5
<b>ANR-Y1</b>	1.1
<b>ANR-Y2</b>	1.0

*Discussion of the number of binding sites ( $c_B$ )*

Based on the simplified schematic description in Fig. 1b in the main text, one would expect that the number of binding sites in the ANRs is closely related to the number of included dye molecules. This assumption was tested for **ANR-L1** and **ANR-Y1** by determining the dye concentration independently. In particular **D1** shows similar photophysical properties (*e.g.* emission quantum yield (Table S4), and emission and excitation spectra (Fig. S2) as its aqueous solution and inside the zeolite L and Y crystal. Thus, a stock solution of **D1** in 10 mM HEPES buffer was diluted as such that the recorded fluorescence emission intensity nearly equals that of an **ANR-L1** suspension (250  $\mu\text{g/mL}$ ) or that of an **ANR-Y1** suspension (250  $\mu\text{g/mL}$ ) in the same buffer. Because the concentration of the stock of **D1**, the quantum yields and the dilution factors are known, we could arrive at an approximate concentration of the dye component in the ANRs. For **ANR-Y1** (250  $\mu\text{g/mL}$ ), the dye concentration was  $c_{\text{dye}} = 1.1 \mu\text{M}$ , which coincides with the concentration of the binding sites,  $c_B$ , see the table above. This suggests that indeed every cavity-bound dye molecule can act as an independent binding station within the zeolite Y crystals. For **ANR-L1** (250  $\mu\text{g/mL}$ ), the dye concentration was  $c_{\text{dye}} = 0.37 \mu\text{M}$ , which is substantially lower than that of the binding stations,  $c_B$ . In this case, it is therefore plausible, that analytes can also bind in other parts of the zeolite L channels and do not only form face-to-face stacking complexes with the dye.

## 4.8 References

1. E. Fischer, *Berichte der deutschen chemischen Gesellschaft*, 1894, **27**, 2985-2993.
2. J. Rao, J. Lahiri, L. Isaacs, R. M. Weis and G. M. Whitesides, *Science*, 1998, **280**, 708-711.
3. H.-J. Schneider, P. Agrawal and A. K. Yatsimirsky, *Chem. Soc. Rev.*, 2013, **42**, 6777-6800.
4. P. Snyder, M. Lockett, D. Moustakas and G. Whitesides, *Eur. Phys. J. Spec. Top.*, 2014, **223**, 853-891.
5. E. Persch, O. Dumele and F. Diederich, *Angew. Chem. Int. Ed.*, 2015, **54**, 3290-3327.
6. D. Chandler, *Nature*, 2005, **437**, 640-647.
7. F. Biedermann, W. M. Nau and H.-J. Schneider, *Angew. Chem. Int. Ed.*, 2014, **53**, 11158-11171.
8. E. Y. T. Chien, W. Liu, Q. Zhao, V. Katritch, G. Won Han, M. A. Hanson, L. Shi, A. H. Newman, J. A. Javitch, V. Cherezov and R. C. Stevens, *Science*, 2010, **330**, 1091-1095.
9. B. Schulte, M. Tsotsalas, M. Becker, A. Studer and L. De Cola, *Angew. Chem. Int. Ed.*, 2010, **49**, 6881-6884.
10. R. N. Mahato, H. Lülfi, M. H. Siekman, S. P. Kersten, P. A. Bobbert, M. P. de Jong, L. De Cola and W. G. van der Wiel, *Science*, 2013, **341**, 257-260.
11. V. Sindelar, M. A. Cejas, F. M. Raymo, W. Chen, S. E. Parker and A. E. Kaifer, *Chem. Eur. J.*, 2005, **11**, 7054-7059.
12. F. Biedermann and W. M. Nau, *Angew. Chem. Int. Ed.*, 2014, 5694-5699.
13. D. B. Smithrud and F. Diederich, *J. Am. Chem. Soc.*, 1990, **112**, 339-343.
14. F. Biedermann, U. Rauwald, M. Cziferszky, K. A. Williams, L. D. Gann, B. Y. Guo, A. R. Urbach, C. W. Bielawski and O. A. Scherman, *Chemistry – A European Journal*, 2010, **16**, 13716-13722.
15. M. Ruat, E. Traiffort, R. Leurs, J. Tardivel-Lacombe, J. Diaz, J. M. Arrang and J. C. Schwartz, *Proceedings of the National Academy of Sciences*, 1993, **90**, 8547-8551.
16. S. Kasera, L. O. Herrmann, J. d. Barrio, J. J. Baumberg and O. A. Scherman, *Sci. Rep.*, 2014, **4**.
17. H.-J. Schneider, *Angew. Chem. Int. Ed.*, 2009, **48**, 3924-3977.
18. D. A. Dougherty, *Acc. Chem. Res.*, 2012, **46**, 885-893.

19. T. Nyrönen, M. Pihlavisto, J. M. Peltonen, A.-M. Hoffrén, M. Varis, T. Salminen, S. Wurster, A. Marjamäki, L. Kanerva, E. Katainen, L. Laaksonen, J.-M. Savola, M. Scheinin and M. S. Johnson, *Mol. Pharmacol.*, 2001, **59**, 1343-1354.
20. F. Lanau, M.-T. Zenner, O. Civelli and D. S. Hartman, *J. Neurochem.*, 1997, **68**, 804-812.
21. R. E. Morris and P. S. Wheatley, *Angew. Chem. Int. Ed.*, 2008, **47**, 4966-4981.
22. M. Vallet-Regí, F. Balas and D. Arcos, *Angew. Chem. Int. Ed.*, 2007, **46**, 7548-7558.
23. J. Kärger, T. Binder, C. Chmelik, F. Hibbe, H. Krautscheid, R. Krishna and J. Weitkamp, *Nat Mater*, 2014, **13**, 333-343.
24. N. Yanai, K. Kitayama, Y. Hijikata, H. Sato, R. Matsuda, Y. Kubota, M. Takata, M. Mizuno, T. Uemura and S. Kitagawa, *Nat Mater*, 2011, **10**, 787-793.
25. N. G. Gubernator, H. Zhang, R. G. W. Staal, E. V. Mosharov, D. B. Pereira, M. Yue, V. Balsanek, P. A. Vadola, B. Mukherjee, R. H. Edwards, D. Sulzer and D. Sames, *Science*, 2009, **324**, 1441-1444.
26. F. Hoffmann, M. Cornelius, J. Morell and M. Fröba, *Angew. Chem. Int. Ed.*, 2006, **45**, 3216-3251.
27. L. Bau, P. Tecilla and F. Mancin, *Nanoscale*, 2011, **3**, 121-133.
28. G. Calzaferri, S. Huber, H. Maas and C. Minkowski, *Angew. Chem. Int. Ed.*, 2003, **42**, 3732-3758.

## **Chapter 5**

# **X-Ray induced luminescent Cu(0) clusters inside porous materials**

### *Abstract*

Herein, we report the formation of air stable luminescent Cu(0) clusters by in situ X-ray irradiation inside various porous materials. The photoluminescent properties were further investigated by both steady state and time-resolved spectroscopic techniques.

## 5.1 Introduction

Ultra small metal clusters are attracting more and more research interests because of their unique size-dependence optical and electrical properties that differs them from the bulk materials and metal complexes.<sup>1, 2</sup> This leads to the promising application of the metal clusters on catalysis, bio-imaging, optical and electrical applications.<sup>3-8</sup>

Among all the metals, the synthesis of the noble metal clusters have been well established by various methods<sup>4</sup> which can be used in fluorescence based sensing,<sup>9</sup> bio-imaging<sup>10</sup> and catalysis applications.<sup>11</sup> For example, red emissive silver clusters were used for microRNA detection.<sup>12</sup> The luminescent property of 28-atom gold clusters has been investigated.<sup>13</sup> Since we know that silver or gold is relatively expensive, copper which is not a precious element could be an alternative to create luminescence metal cluster. It is cheap and already widely used in our daily life. However, compared to the noble metals, copper is known to be easily oxidized which results with non-emissive materials. This makes it difficult to obtain the pure Cu(0) clusters. This is the main reason that up till now, emissive copper materials are mainly Cu(I) complexes which can be useful in OLED and other applications.<sup>14-16</sup>

For emissive Cu(0) clusters, due to the ultra-small size and the high reactivity which makes it easily oxidized, the synthesis cannot be easily done through a simple approach.<sup>17</sup> It make the copper based emissive cluster not really well developed. In the past few years, a few stable and small Cu(0) synthesis have been successfully produced. It is described that by using the micro-emulsions method, the formation of Cu(0) clusters with controlled size smaller than 3 nm could be achieved.<sup>18</sup> Sub nanometer-sized copper nanoclusters were prepared by a one-pot procedure based on wet chemical reduction.<sup>19</sup> Via electrochemistry, it is reported that Cu(0) cluster which has less than 14 Cu atom have been synthesized.<sup>20</sup> More recently, Cu(0) 5 atom cluster has been successfully synthesized in water also by using electrochemistry method.<sup>21</sup> Usually within the liquid phase synthesis, stabilizer is usually needed to prevent the aggregation of clusters.<sup>22</sup> This could eventually be the potential limitation on the application of the clusters.

Compare to the other reducing agent, photo assisted reduction have the advantage on the control of reduction position and purification, which is very suitable for the cluster formation in a confined space or template. A. Katrib discovered in the 1980s that by exposure to X-ray, Pt(IV) can be reduced to Pt(II).<sup>23</sup> Since then, several researches showed the possibility the reduction of platinum, gold or silver under X-ray irradiation.<sup>24</sup> In 2014, J. Hofkens and co-workers developed the method of silver cluster formation inside zeolite material by X-ray irradiation.<sup>25</sup> The advantage of using X-ray is that the reduction can be controlled in situ, which is not possible for hydrogen or other chemical reducing agent. With tunable size and shape of the X-ray source, different patterns of the reduced species can be spatially created. This could end up with applications such as encrypted message and anti-counterfeit. However, there is no report of forming Cu(0) clusters inside porous materials by X-ray irradiation yet.

*In this chapter, we explored the formation of luminescence Cu(0) cluster via different loading methods and reducing in different porous materials via X-ray irradiation.*

## **5.2 General approach for the synthesis of Cu(0) cluster inside porous materials**

The synthesis of emissive Cu(0) cluster, initially, can be done by loading potentially emissive source (Cu ions or salts) into the porous materials. There are several advantages of forming the emissive part inside the porous material. First, the clusters will be stabilized and protected inside the channels to avoid the extra oxygen and water from air. This is one of the major reason why Cu(0) clusters are not stable in air thus most of the synthesis was done in solution and surfactant or ligand is needed for protection. Secondly, each of the porous material we use has a unique pore size. This means that we can tune the size of the cluster and the formation of the cluster formation cannot exceed a certain scale. Big aggregation which is common for small particles can be avoided. This is a good aspect on the cluster formation because with larger size there is less quantum confinement effect which leads to poorer performance of the clusters.<sup>18</sup> Moreover, for

certain applications such as catalysis for oil industry, porous material can provide the space which gives the full contact between the reactant and the catalyst. Especially for zeolite material, product can escape from smaller pore in the framework.<sup>26</sup> This improves the reaction efficiency and leads to higher yield.

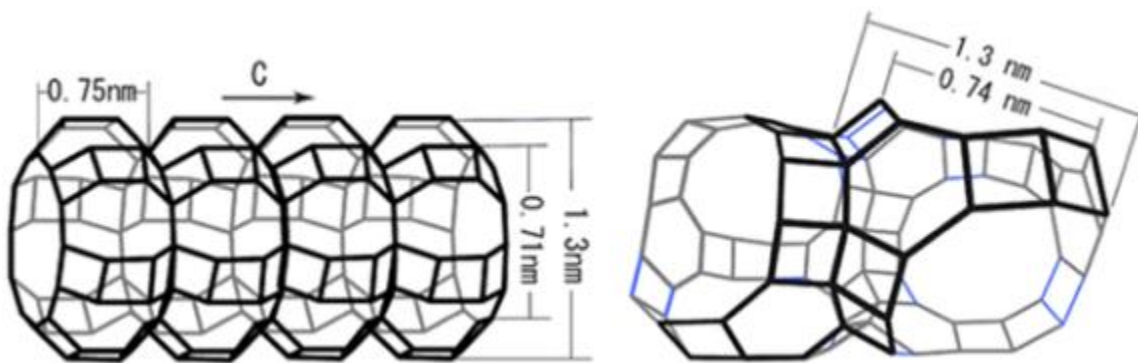


**Fig. 5.1** Zeolite LTL (left) and zeolite FAU (right) framework and their dimensions. Adapted from Ruiz, A., Brühwiler, D., Ban, T. et al. Monatshefte für Chemie (2005) 136: 77, with permission from Springer Link.

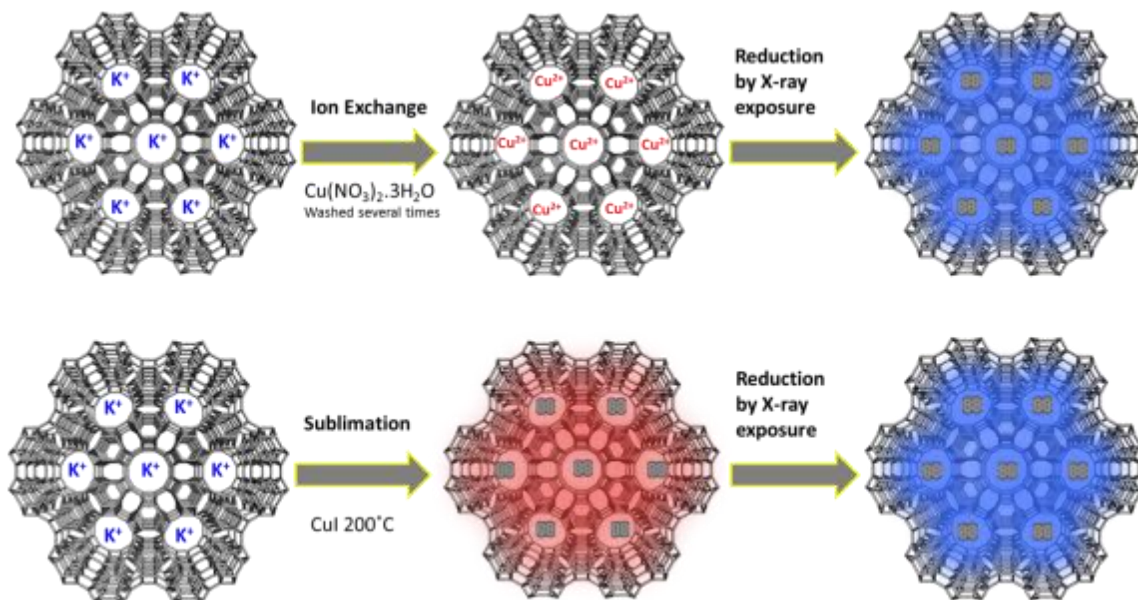


**Fig. 5.2** Schematic synthetic procedure of the reduced Cu(0) cluster by ion exchange and CuI loading.

To load other ions/molecules into the porous material, several methods have been developed. Ion exchange for zeolite material have been established in the 1940s,<sup>27</sup> followed by lots of examples.<sup>28,29</sup> For the gas phase loading, sublimation is usually used to disperse the guest molecules into the host material.<sup>30,31</sup> In our case, both methods are used for loading copper source.

To investigate different copper species by different loading methods, both ion exchange and sublimation were applied. The counter ions which exist in zeolite framework make it possible for ion exchange. As for mesoporous silica, there is no counter ion in the framework. Sublimation which requires no counter ion was applied for both silica and zeolite material. For zeolite material, we use zeolite LTL (Si/Al=3:1) and zeolite FAU (Si/Al=5.1:2) (Fig. 5.1) which have pore size of 0.7 nm and 1.2 nm respectively. Mesoporous silica materials we employed have the average pore size of 3 nm and 12 nm. This could help us to understand the size dependence of the cluster formation. To load the copper source, we used two methods which we can see from Fig. 5.2. For zeolite materials, the natural  $\text{Al}^{3+}$  ion site in the zeolite crystals gives itself a negative charge with the presence of the  $\text{O}^{2-}$ . In this case, charge-balance ions are needed to compensate the negative charge. Since the counter-balancing ions (in our case  $\text{Na}^+$  or  $\text{K}^+$ ) are already presented in the zeolite materials, ion exchange method with  $\text{Cu}^{2+}$  contained solution was used. Two original counter ions ( $\text{Na}^+$  or  $\text{K}^+$ ) can be replaced by  $\text{Cu}^{2+}$ . Since it is not possible to load copper into mesoporous silica by ion exchange, gas phase loading by sublimation method was used to load the copper source into both zeolite and silica materials. The salt we chose to sublime was  $\text{CuI}$ , there are several reasons for that. Firstly, among all the  $\text{Cu(I)}$  halogen salts such as  $\text{CuBr}$  or  $\text{CuCl}$ ,  $\text{CuI}$  has the lowest boiling point which means we can use the lowest temperature for sublimation. The loading can be beneficial from minimum decomposition of  $\text{Cu(I)}$  salt. Secondly, we have discovered that the  $\text{CuI}$  cluster inside the zeolite framework gives a red emission which is different from the  $\text{Cu(0)}$  clusters that usually emits in the UV/blue/green area.<sup>32</sup> This makes it easier for us to distinguish the reduced and the not reduced part in the following experiments. Thirdly, compare to  $\text{Cu(II)}$ ,  $\text{Cu(I)}$  is easier to reduce. After the loading of  $\text{CuI}$ , the reduction happened while the samples were exposed by X-ray in XPS. For each point



reduced, 2 times if survey scan and 10 times of Cu 3p elemental scan were applied. The final sample was taken out from the XPS chamber without any modification and used for further characterizations. The characterization was done by using SEM, XPS and nitrogen adsorption from the material point of view, and fluorescence microscope, fluorescence steady state spectrofluorometer and fluorescence lifetime spectrometer for the photophysics point of view.

### **5.3 Luminescence Cu(0) clusters from Cu<sup>2+</sup>**

Zeolite samples were ion exchanged by Cu<sup>2+</sup> and reduced by X-ray. The elemental composition of the materials has been studied by X-ray photoelectron spectroscopy. The elemental composition of the ion exchanged samples can be found in Table 5.1. From there we see all the elements inside our system which are the zeolite itself (Al, Si, O, K and Na), the exchanged and reduced Cu and the adventitious carbon from air. Due to the crystal structure difference of the two zeolites and the two plus charge Cu ion other than the original one plus charged counter ion, we had higher ion exchange rate for the zeolite FAU (68.4%) than zeolite LTL (27.4%). This is due to the zeolite FAU has bigger pores which can be accessible more easily.

To study the chemical state of the copper, elemental scan of the X-ray photoelectron spectroscopy measurement was carried out. The spectra revealed the reduction of Cu(II) in the ion exchanged samples, see (Fig. 5.3). From the Cu 2p<sub>3/2</sub> scan, the small satellite peaks and the peak shoulder which are very common for Cu<sup>2+</sup> were decreasing during the X-ray exposure, and completely disappeared in the end. This indicates the reduction of Cu(II) to Cu(0).

**Table 5.1** Elemental composition of the Cu(0) clusters contained porous materials by X-ray reduction of the Cu<sup>2+</sup> counter-ion.

Material	Element	Atomic %	Material	Element	Atomic %
Zeolite LTL	O	57.37	Zeolite FAU	O	57.27
	Si	21.02		Si	17.67
	Al	7.74		Al	9.23
	C	6.68		C	9.07
	K	5.20		Na	2.50
	N	1.01		N	2.71
	Cu	0.98		Cu	1.55

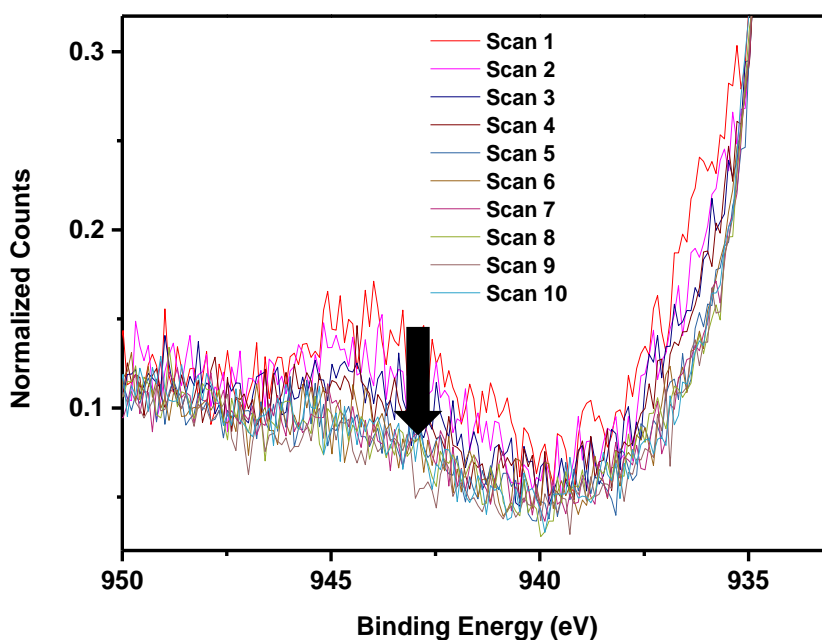


**Fig. 5.3** The change of XPS spectra of the ion exchanged zeolite LTL sample by 10 scans.

Metal clusters due to its small size have their unique size-dependence optical properties. Among developed metal clusters, different emission wavelengths have been discovered. Usually the emission can be tuned by adjust the size of the metal clusters.<sup>33</sup>

The picture of the X-ray reduced emissive Cu(0) clusters inside zeolite samples can be seen as following. The ion exchanged sample showed green emission under fluorescence

microscope with 475 nm filter. For comparison, the samples without any X-ray exposure didn't show any emission at all (Fig. 5.4).

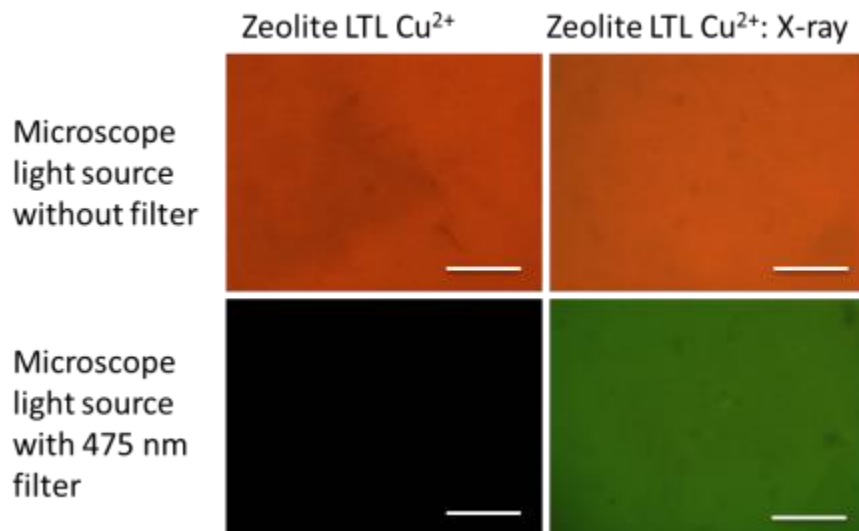


**Fig. 5.4** Comparison of fluorescence microscope image of ion exchanged samples before and after X-ray exposure with/without 475 nm filter (scale bar 50  $\mu\text{m}$ ).

Zeolite itself could be emissive if electrical hole is created inside the material. To make sure that the emission is really coming from the copper source, reference experiments with X-ray exposure were also carried out. We have tried to expose the zeolite LTL with  $\text{K}^+$  as counter ion under X-ray using the same condition as the zeolite LTL with copper source. From fluorescence microscope we can see that there was no green emission observed with the 475 nm filter (Fig. 5.5a). From the emission spectrum, there was no emission until 470 nm by applying the 270 nm wavelength of excitation (Fig. 5.5b). This indicates that the reduced copper source was the reason for the green emission.

Because of the existence of the ion gun in the XPS instrument which is used for compensate the plus charge on the measuring surface caused by the loss of electrons,  $\text{Ar}^-$  ion could also be a source to give electrons to copper ions for the reduction. To investigate which is the real source for the reduction, we have deployed the X-ray beam size of 400  $\mu\text{m}$  and the  $\text{Ar}^-$  ion gun beam of 2nm. By combining several fluorescence microscope picture we obtained the image in Fig. 5.6. The size of the reduced area which

was correlated with the X-ray beam size (400  $\mu\text{m}$ ) gave us the solid proof that the reduction process was done by X-ray.

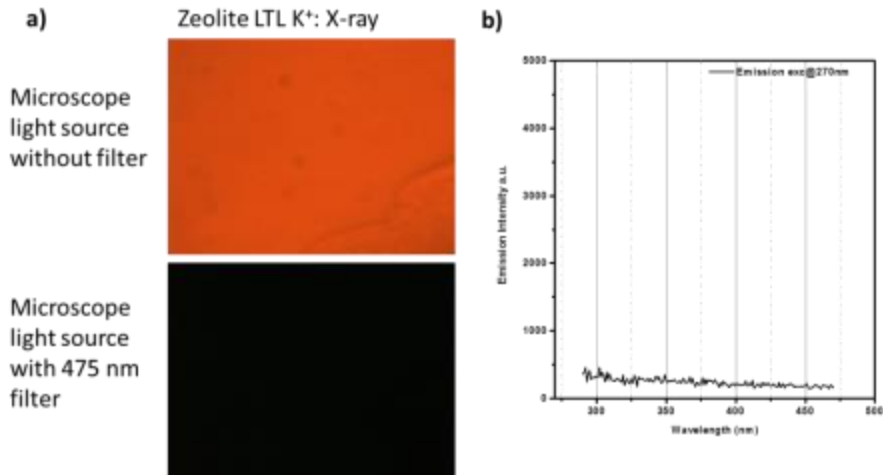


**Fig. 5.5** a) Zeolite LTL with  $\text{K}^+$  as counter ion after X-ray exposure; b) emission spectra of the  $\text{K}^+$  zeolite LTL (excitation at 270 nm).

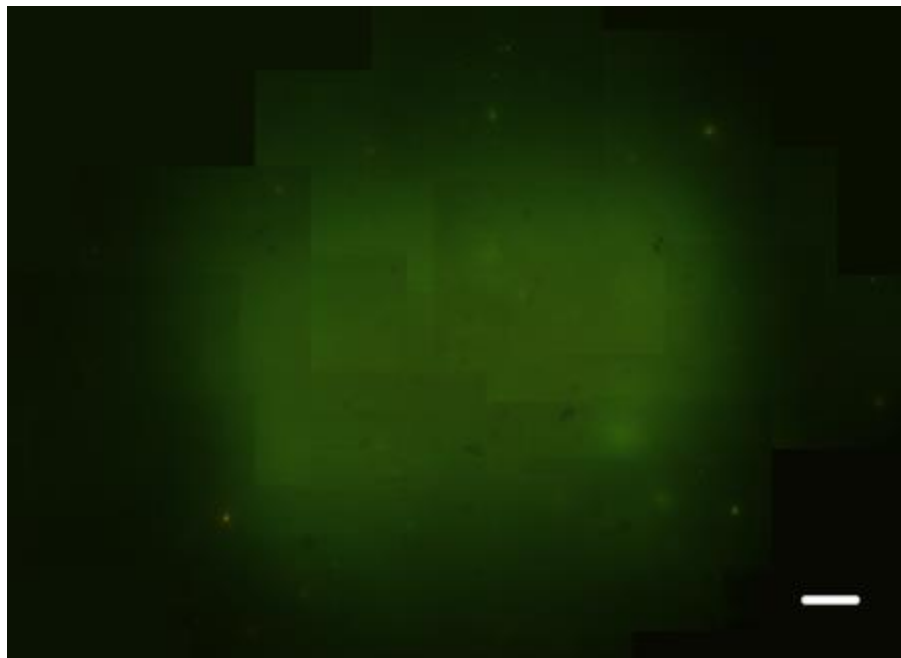


**Fig. 5.6** Fluorescence microscope image of the reduced spot of the ion exchanged zeolite LTL. (Scale bar: 50  $\mu\text{m}$ )

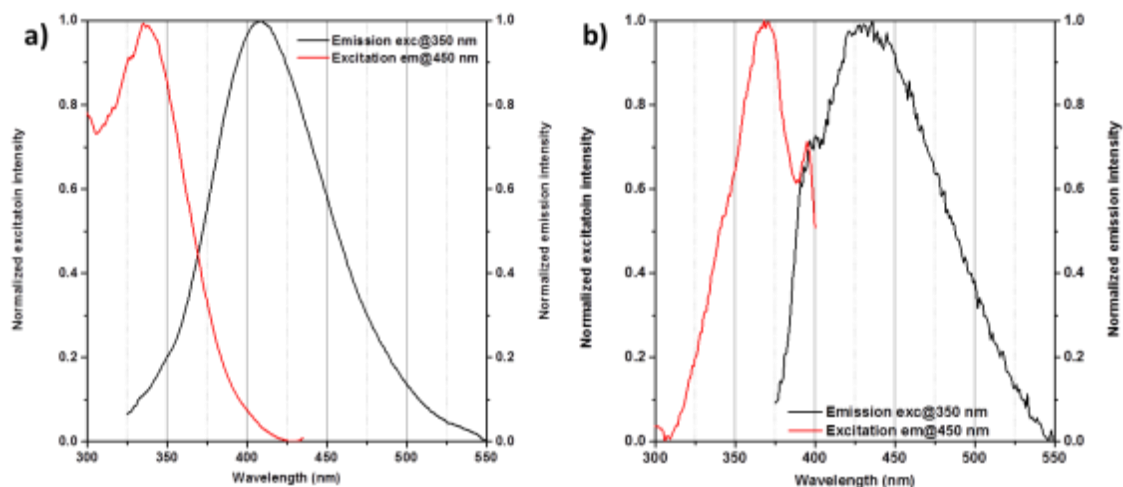


**Fig. 5.7** Excitation/emission spectra of the reduced ion exchanged zeolite LTL from a) X-ray; b) hydrogen.

The excitation and emission spectra of the ion exchanged sample is shown in Fig. 5.7. The ion exchanged sample has emission at 410 nm. This is comparable to our previous result of the hydrogen reduced ion exchanged sample which has the emission at around 420 nm. The sample we synthesized has low quantum yield which the emission is not really visible by naked eye but only by fluorescence microscope which is also similar with the hydrogen reduced sample.

The relationship of the emission energy and the number of atoms in the cluster was investigated by Zheng and co-workers.<sup>33</sup> The relationship is shown as following:

$$E_{em} = \frac{E_f}{N^{1/3}} \quad (1)$$

Where  $E_{em}$  is the emission energy,  $E_f$  is the Fermi energy of the metal and  $N$  is the number of atom in the cluster. In this case, our ion exchanged zeolite LTL should have 12 atoms (410 nm emission). One unit cell of zeolite LTL contains 9 Al atoms thus there are 9 counter ions if the ion is 1+ charged.<sup>34</sup> There could only be 4.5 Cu atoms per unit cell which is less than the copper cluster estimated. The XPS survey showed that there was around 1% of nitrogen remained in the material, indicated that the  $\text{Cu}(\text{NO}_3)_2$  was not completely removed which is the possible source of the exceeded Cu atoms.

## 5.4 Luminescence Cu(0) clusters from CuI

CuI was sublimed into both zeolite and silica materials. The CuI inside the loaded porous materials were reduced by X-ray. Through the SEM images we can see that the morphology of the zeolite or silica material didn't change before and after the loading and reduction of the copper source (Fig. 5.8), indicates that the loading of CuI didn't destroy the porous structure of our materials. Meanwhile we have obtained red emission from the loaded CuI which indicated that our copper source was successfully loaded inside the porous material which we will discuss in the photophysical characterization part later.

The elemental composition of the CuI reduced samples can be found in Table 5.2. There we observed the elements from the material themselves (Al, Si, O, K and Na for zeolites, Si, O for silica), the loaded Cu and I, and of course the adventitious carbon from air. From the zeolite materials, the atomic ratio of the original counter ion shows that they are still occupying the counter ion site in the zeolite framework. This indicates that the CuI are loaded in the pores.

**Table 5.2** Elemental composition of the Cu(0) clusters contained porous materials by X-ray reduction of the loaded CuI.

Material	Element	Atomic %	Material	Element	Atomic %
Zeolite LTL	O	45.03	Zeolite FAU	O	46.72
	C	22.15		C	21.37
	Si	18.77		Si	17.91
	Al	6.69		Al	6.69
	K	5.18		Na	6.51
	Cu	0.61		Cu	0.51
	I	0.58		I	0.28
MCM-41 silica	O	57.85	SBA-15 silica	O	59.31
	Si	28.51		Si	29.13
	C	12.56		C	9.34
	Cu	0.61		Cu	1.23
	I	0.47		I	0.99

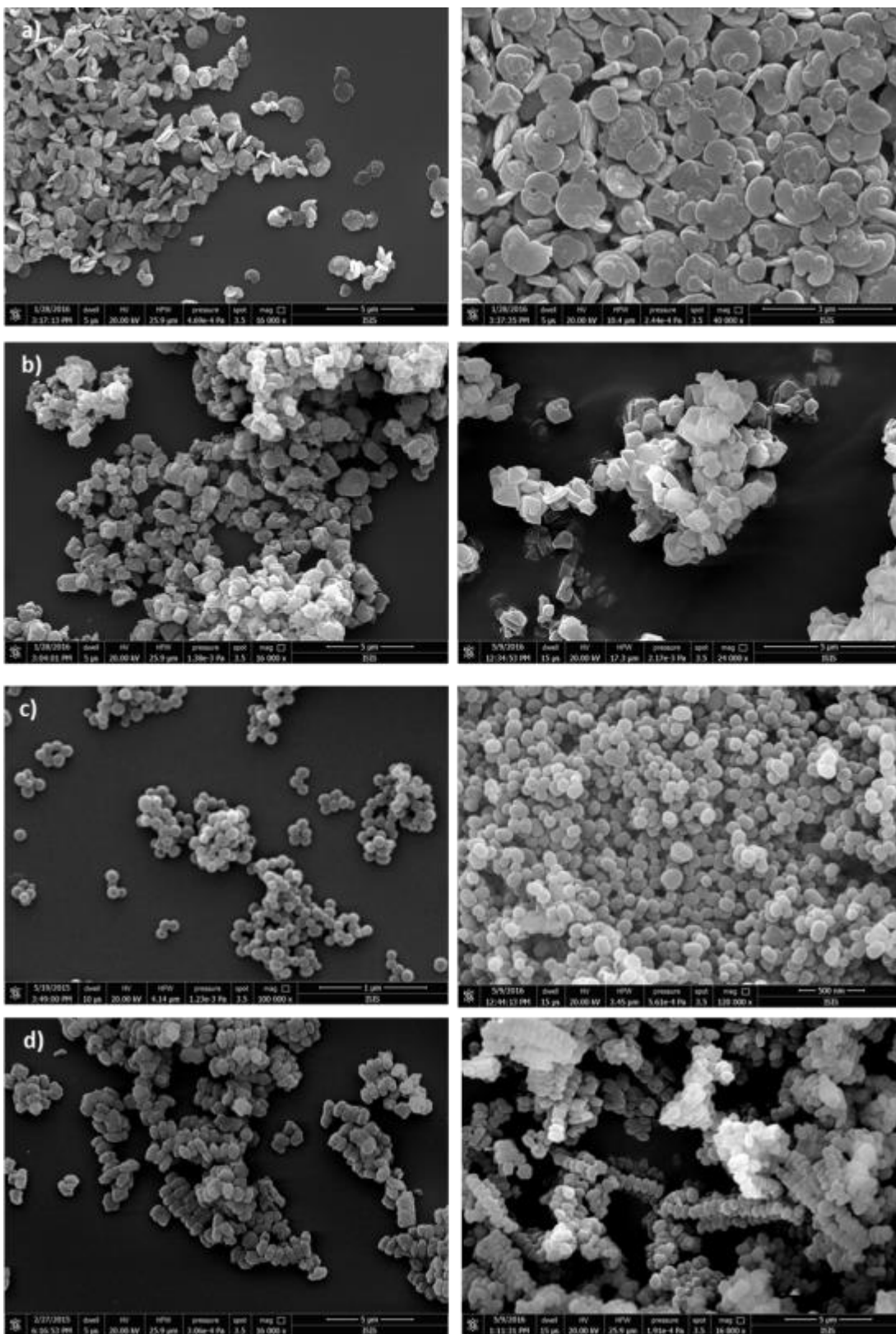


**Fig. 5.8** SEM images of a) zeolite LTL; b) zeolite FAU; c) MCM-41 silica; d) SBA-15 silica before (left) and after (right) the loading of CuI.

Compared to the ion exchanged samples, no satellite peak was observed before or after the X-ray exposure from the CuI loaded samples. As we can see from Fig. 5.9, there is also no significant change of the Cu 2p spectra since it is well-known that the binding energy of Cu(I) and Cu(0) is very similar (only 0.1 eV difference).<sup>35</sup> In this case, the reduction cannot be seen by XPS in an obvious way. Further characterization is needed.

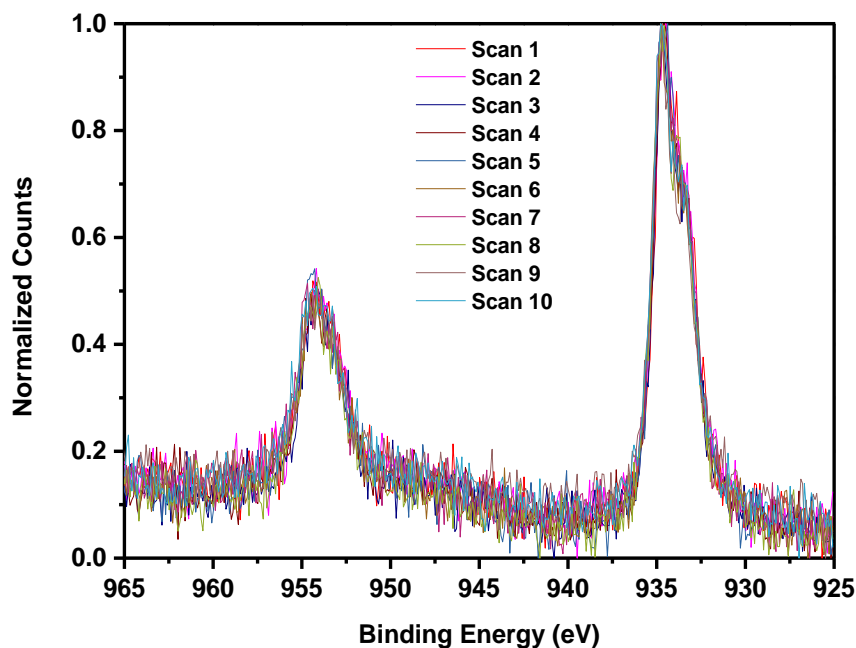


**Fig. 5.9** The change of the XPS spectra of the CuI loaded zeolite LTL sample by 10 scans.

N<sub>2</sub> adsorption measurement showed the loading of the CuI inside the pores of the porous material. The isothermal curve and pore distribution can be found in Fig. 5.10, the type of the curve didn't change before and after the loading suggesting that the sublimation of CuI didn't change the porosity and it was partially loaded into the porous structure. The decrease of the pore volume before and after loading also indicated that pores were partially loaded (Table 5.3).



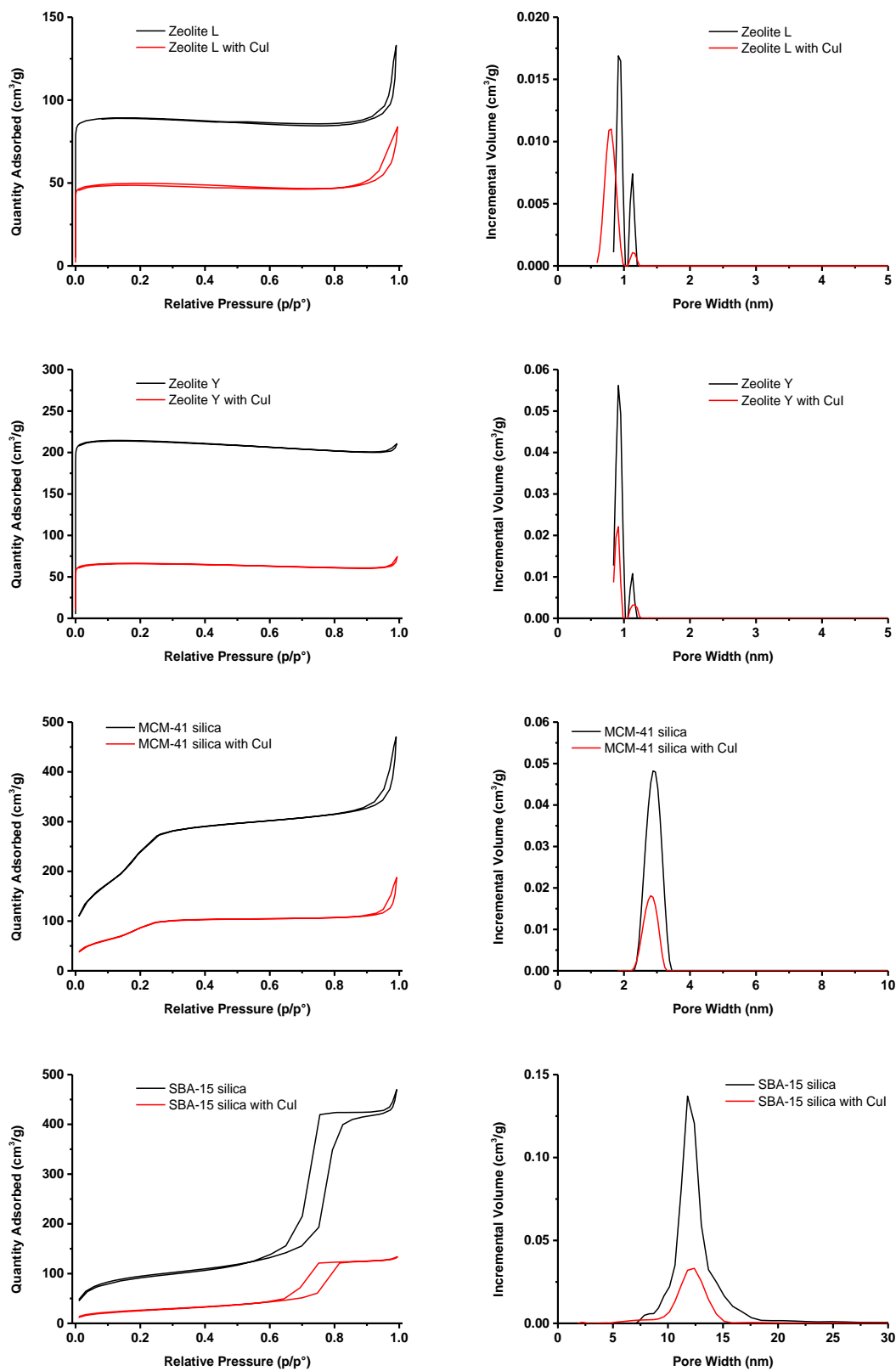
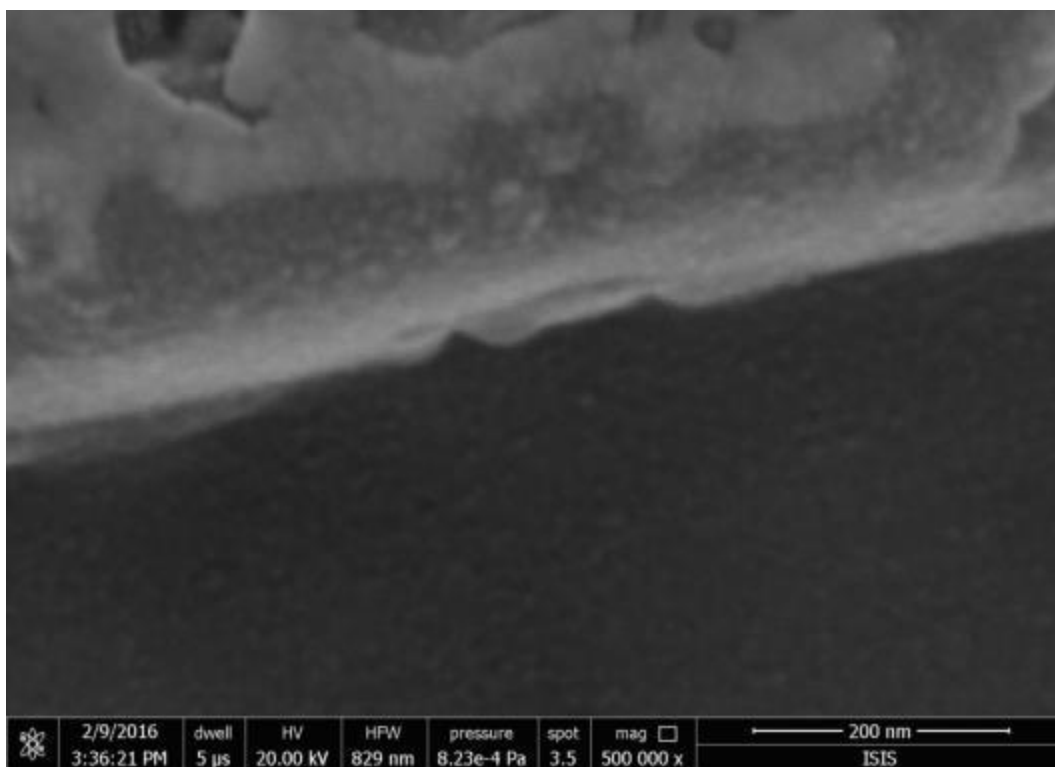


Fig. 5.10 N<sub>2</sub> adsorption isotherm and pore distributions of different porous materials.

**Table 5.3** Pore volume of the porous material before and after loading of CuI

Sample	Pore Volume (cm <sup>3</sup> /g of material)	Loading rate
Zeolite LTL	0.13125	44%
Zeolite LTL loaded with CuI	0.07350	
Zeolite FAU	0.31803	70%
Zeolite FAU loaded with CuI	0.09552	
MCM-41 silica	0.42002	65%
MCM-41 silica loaded with CuI	0.14682	
SBA-15 silica	0.65027	70%
SBA-15 silica loaded with CuI	0.19310	

To investigate if we can see anything inside the material, focused ion beam have been used for etching on the reduced CuI loaded zeolite LTL sample. And we can see that there is no significant difference between the etched (down) and the not etched part (up) (see Fig. 5.11). Thus the CuI is homogeneously loaded inside the porous material.



**Fig. 5.11** SEM image of the FIB etched sample of the reduced CuI loaded zeolite LTL.

The CuI reduced sample show bright blue/green emission under UV (Fig. 5.12). Even though based on the XPS spectrum we were not sure if CuI samples were reduced or not.

The bright blue emission on the spot where there was X-ray exposure shows us the existence of the reduction. Outside the reduced CuI spot we can see the original red emission of the unreduced CuI cluster.

Compare to the reduced Cu(0) cluster from the ion exchanged zeolite, the emission of the CuI reduced Cu(0) clusters is much more complicated. From the excitation and emission spectra of the reduced CuI in zeolite LTL (Fig. 5.13), it is shown that there are at least two emissions separately at around 355 nm and 425 nm which have been excited from two different bands according to the excitation spectra. This gave us an idea that inside our system, at least two kinds of Cu(0) clusters with different sizes were formed. As a reference, originally there is the unreduced CuI emission which can be found from Fig. 5.14. It doesn't overlap with our reduced cluster emission.

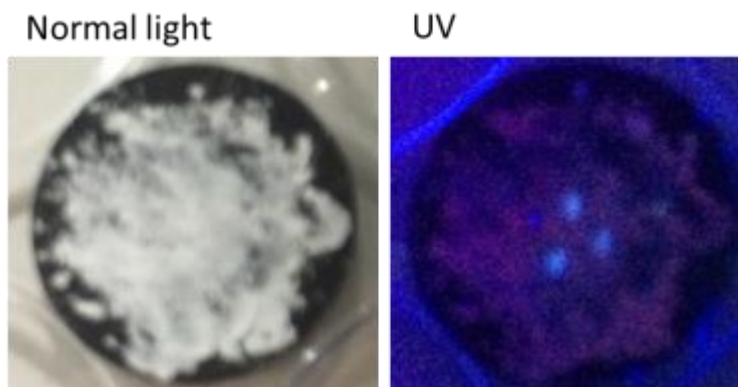


**Fig. 5.12** X-ray exposed CuI loaded zeolite LTL under normal light and UV. Bright blue spots are the reduced part and the red emission comes from the not reduced CuI cluster.

To investigate the effect of the pore size on the formation of the Cu(0) clusters, CuI has been loaded into the porous material with 0.7 nm (zeolite LTL), 1.2 nm (zeolite FAU), 3 nm (MCM-41 mesoporous silica, CTAB as surfactant) and 12 nm (SBA-15 mesoporous silica, P123 as surfactant) pore sizes. To make sure the CuI can be loaded into the zeolite and to exclude the possibility of cluster forming outside the pores, relatively low weight ratio between porous material and CuI (1:1) has been used. The emission spectra of these samples are shown in Fig. 5.15. From the spectra we can see that the emission between 400 nm to 440 nm increases while the pore size increases. This indicates that with bigger

pore size, we form more clusters with larger size which emit between 400 nm to 440 nm. But in this case, the reduced CuI inside zeolite LTL has an unusual shoulder at these wavelengths which could most probably due to the space in between the zeolite discs according to N<sub>2</sub> adsorption measurement (Fig. 5.10). These bigger spaces make the bigger clusters formed at the space in between the zeolite LTL discs which can be similar with the silica material with bigger pores. Above all, we always obtain the small clusters which emit at 355 nm no matter what is the pore size of the material. The number of atoms of each cluster species is also estimated from equation 1. The emission from 330 nm to 355 nm corresponds to Cu<sub>6</sub>, Cu<sub>7</sub> and Cu<sub>8</sub>. The emission from 410 nm and 425 nm corresponds to Cu<sub>12</sub> and Cu<sub>13</sub>. This result is supported by literature which suggested that Cu(0) clusters which has more than 13 atoms are not emissive.<sup>18</sup> In our case, Cu(0) clusters more than 13 atoms could also be formed in the meantime.

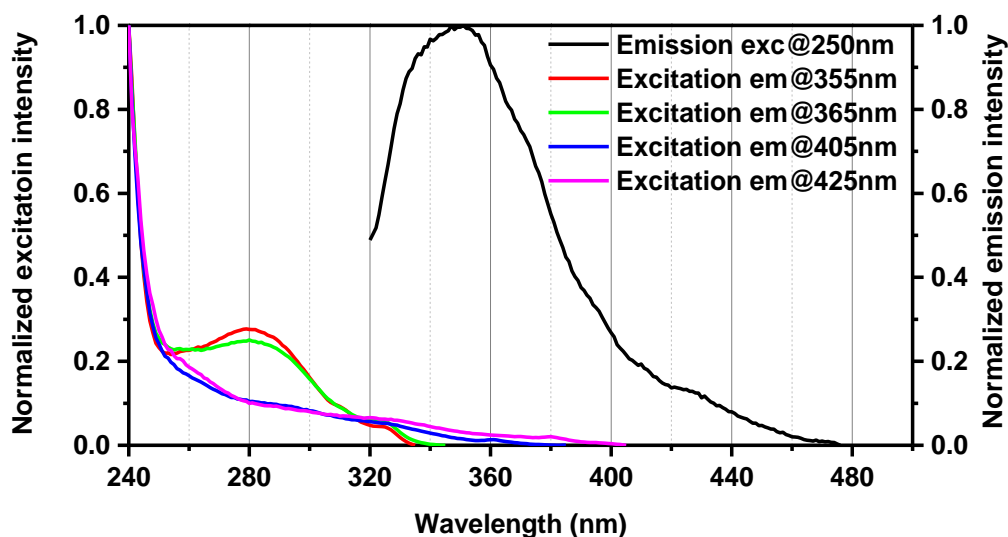


**Fig. 5.13** Excitation/emission spectra of the reduced CuI loaded zeolite LTL.

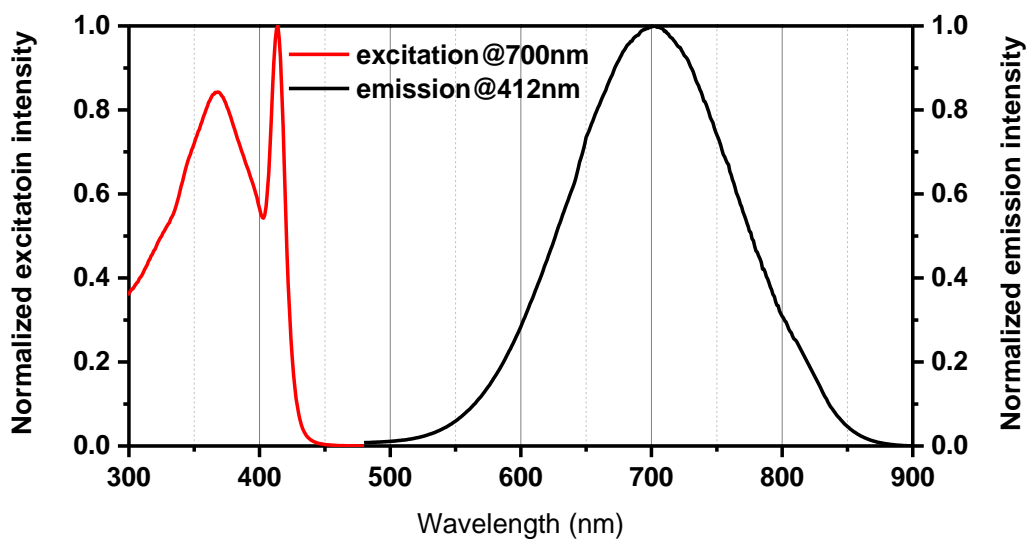


**Fig. 5.14** Excitation/emission spectra of the unreduced CuI clusters inside zeolite LTL.

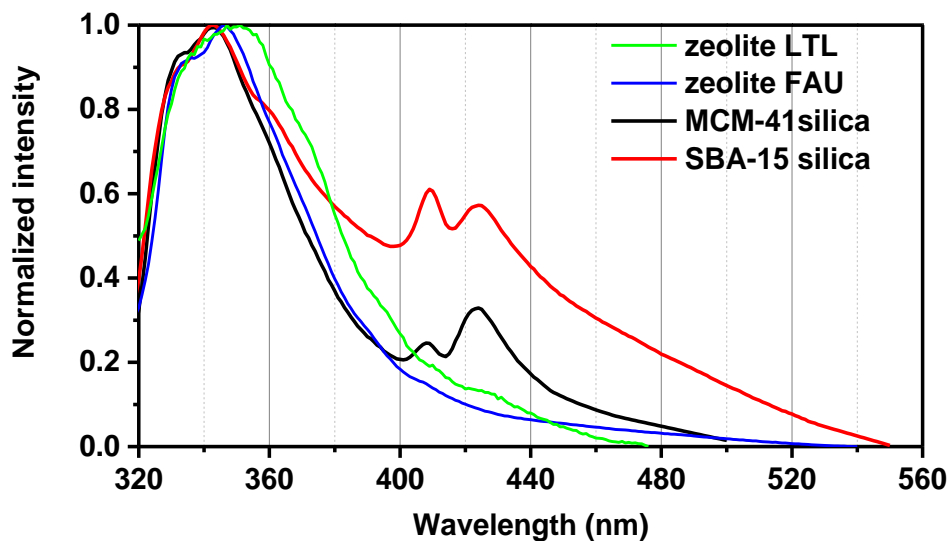


**Fig. 5.15** Emission spectra of Cu(0) clusters in different porous materials (excitation at 270nm).

Time-resolved luminescence measurements of the X-ray activated samples were performed by FluoTime 300. By the emission spectra we knew that despite the pore size difference for the porous materials, we always obtain the small Cu(0) species. Regardless

the size, all the clusters we obtained have a major lifetime component of less than 1 ns which is common for metal clusters (Table 5.4).

**Table 5.4** Lifetime of different Cu(0) clusters in different porous materials.

Emission	Lifetime (ns)		
	$\tau_1$	$\tau_2$	$\tau_3$
Zeolite LTL 355nm	0.7 (66.9%)	9.0(24.0%)	24.4 (9.1%)
Zeolite FAU 355nm	0.8 (65.3%)	8.3 (22.4%)	22.8 (12.3%)
MCM-41 silica 355nm	0.6 (93.2%)	7.7 (5.2%)	33.0 (1.6%)
SBA-15 silica 355nm	0.6 (92.2%)	6.3 (5.5%)	27.6 (2.3%)
Zeolite LTL 425nm	0.8 (73.7%)	4.3 (20.8%)	18.2 (5.5%)
MCM-41 silica 425nm	0.6 (79.0%)	3.0 (17.7%)	15.5 (3.3%)
SBA-15 silica 425nm	0.5 (53.2%)	1.2 (44.5%)	8.2 (2.3%)

For the clusters that emit at 355 nm, there are more components of longer lifetime from the zeolites than from the silica. This tells us that in the zeolite material, there is higher chance for the clusters to have interaction with the environment because of the ultra-small pore size which result with longer lifetime components. In the case of the clusters that emit between 400 nm to 440 nm, clusters inside the zeolite LTL and the MCM-41 silica were similar while there appeared to be more interaction between the cluster and the material environment in the SBA-15 silica. This could be due to the large variety distribution of the pores in the SBA-15 silica material.

To prove that the Cu(0) clusters are stable, we left them under air for more than 1 month. From Fig. 5.16 we can see that under UV there are still visible blue emission coming from the reduced Cu(0) clusters while the red emission coming from the CuI clusters are almost gone compare to the fresh prepared sample in Fig. 5.12. This gives us the solid proof that our Cu(0) clusters are stable through a relatively long period of time under room temperature and exposed with normal air.

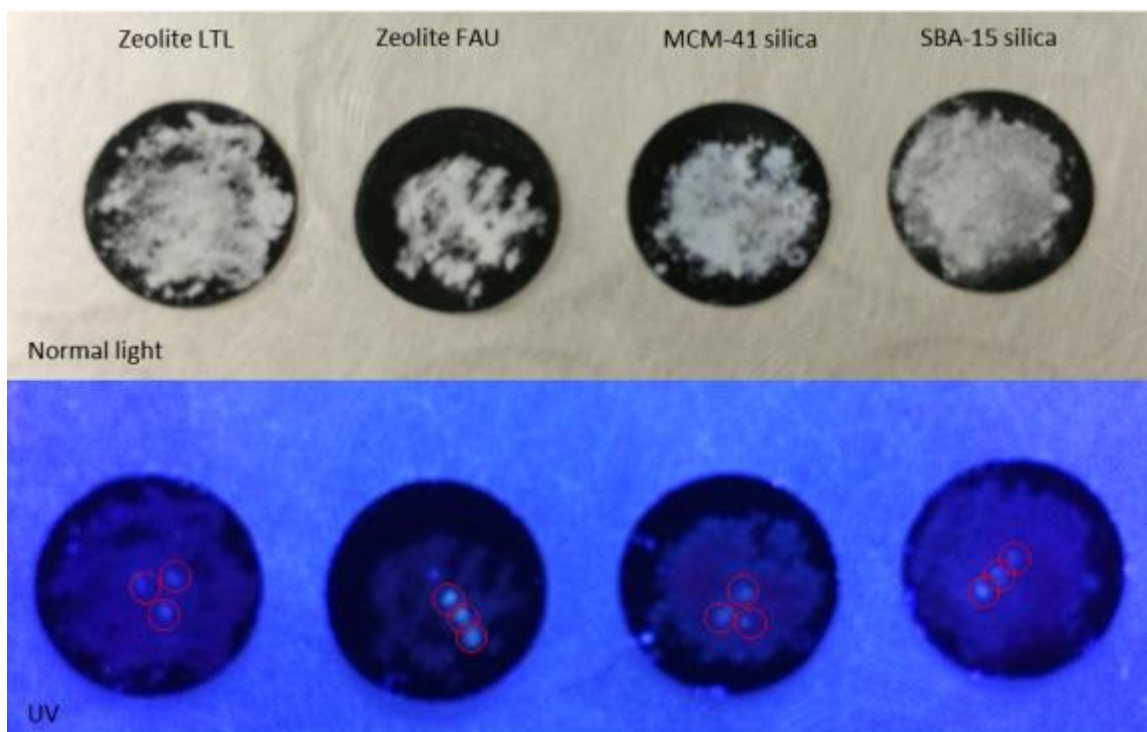


**Fig. 5.16** Image taken one month after the reduction process, Cu(0) clusters inside different materials under normal light and UV.

#### 5.4 Conclusion and perspectives

In summary, we report for the first time the in situ formation of luminescent Cu(0) cluster inside porous materials by X-ray irradiation. The clusters are stable in air. Furthermore, photophysics properties of the Cu(0) clusters have been measured. Also we investigate the size dependence of the porous materials on the different cluster formation.

As we have described, this Cu(0) cluster can be fabricated in situ and the emission can be tuned by using different porous materials. These unique properties could lead us to further application such as specific lighting devices or creating certain emissive patent such as anti-counterfeit application. Also, if we mix our blue/green emissive Cu(0) clusters with other yellow/orange emissive species, white emitter could be created. As the metal clusters are inside the porous framework, it could also be used in certain Cu(0) based catalysis applications.<sup>36</sup> Last but not least, more metal compound could be reduced

by the X-ray assisted reduction. The size of the cluster could also be controlled by the size of the porous space. In this way, more metal clusters could be in situ fabricated under size control. More applications could be developed based on different metal.



## 5.5 Experimental section

### *Materials*

KOH (1 kg) and NaOH (1 kg) were bought from VWR chemicals,  $\text{Al}(\text{OH})_3$  (500 g, extra pure) and Hexadecyltrimethylammonium bromide (500 g, 99+%) was purchased from Acros, CuI (100 g, 99%),  $\text{Cu}(\text{NO}_3)_2 \cdot 3\text{H}_2\text{O}$  (100 g, 99%), Sodium metasilicate nonahydrate (1 kg,  $\geq 98\%$ ), Tetraethyl orthosilicate (1 L, 98%), (3-Aminopropyl)triethoxysilane (100 mL, 99%), hydrochloric acid (1 L,  $\geq 37\%$ ) and Pluronic P-123 were bought from sigma-aldrich,  $\text{Cu}(\text{Ac})_2 \cdot \text{H}_2\text{O}$  (500 g, 99%) was purchased from merck, and Ludox HS-40 (1 L) was bought from Aldrich chemistry. Zeolite Y (FAU) was from Alfa Aesar GmbH & Co KG. All the products above were used as bought without any modification.

### *Synthesis of disc shaped zeolite L*

### *Synthesis of the MCM-41 silica*

### *Synthesis of the SBA-15 silica*

### *Ion exchange*

These contents have been described in chapter 2.

### *Synthesis of CuI cluster contained material*

Porous material (zeolite LTL, zeolite FAU, MCM-41 silica and SBA-15 silica) was mixed with CuI powder with 1:1 weight ratio. The mixture was degased under a high vacuum until the pressure is lower than  $1 \cdot 10^{-5}$  mbar. The mixture was then sealed at high vacuum and transferred into a rotating oven for sublimation at  $200^\circ\text{C}$  for 2 hours. The final product was then taken out from the vacuum after cooled down.

### *X-ray photoelectron spectroscopy*

All the X-ray Photoelectron Spectroscopic (XPS) measurements were done by a Thermo Scientific K-Alpha X-ray Photoelectron Spectrometer using a monochromatic  $\text{AlK}\alpha$  radiation ( $h\nu = 1486.6$  eV). Survey measurements were performed with 200 eV analyser pass energy and a 1 eV energy step size to calculate the atomic concentrations. Element

scans were performed with 50 eV analyser pass energy and a 0.1 eV energy step size to obtain the chemical state information. X-ray beam size was 400  $\mu\text{m}$ . All the obtained binding energies were referenced to  $\text{sp}^3$  carbon 1s peak at 284.8 eV.

#### *Scanning electron microscope*

Scanning Electron Microscope SEM images were recorded with a FEI Quanta FEG 250 instrument (FEI corporate, Hillsboro, Oregon, USA) with an acceleration voltage of 20kV. The sample is prepared by sputtering coated with Au (Emitech K575X peltier cooled) for 45 s at 60 mA prior to fixation on an Al support.

#### *Fluorescence microscope*

Fluorescence microscopy images were taken using an Olympus inverted research microscope BX51M with a digital Olympus XC10 camera for image acquisition. All the fluorescence microscopy images were acquired in air. The filter we use was the build-in WB filter which has the excitation wavelength at the range of 460-490 nm and emission cut-off at 520 nm.

#### *Fluorescence steady state spectrofluorometer*

Steady-state emission spectra were recorded on a Horiba Jobin–Yvon IBH FL-322 Fluorolog 3 spectrometer equipped with a 450 W xenon arc lamp, double-grating excitation, and emission monochromators (2.1  $\text{nm mm}^{-1}$  of dispersion; 1200 grooves  $\text{mm}^{-1}$ ) and a TBX-04 single photoncounting detector. Emission and excitation spectra were corrected for source intensity (lamp and grating) and emission spectral response (detector and grating) by standard correction curves.

#### *Fluorescence lifetime spectrometer*

Timeresolved measurements were performed using either the time-correlated single-photon counting (TCSPC) electronics PicoHarp 300 or the Multi-Channel Scaling (MCS) electronics NanoHarp 250 of the PicoQuant FluoTime 300 (PicoQuant GmbH, Germany), equipped with a PDL 820 laser pulse driver. A pulsed laser diode LDH-P-C-375 ( $\lambda_{\text{exc}} = 375 \text{ nm}$ , pulse FWHM  $<70 \text{ ps}$ , repetition rate 40 kHz) was used to excite the sample and

mounted directly on the sample chamber at 90 °. The photons were collected by a PMA-C-192 photomultiplier (PMT) single-photon-counting detector. The data were acquired by using the commercially available software EasyTau (PicoQuant GmbH, Germany), while data analysis was performed using the commercially available software FluoFit (PicoQuant GmbH, Germany).

#### *Nitrogen adsorption*

Nitrogen adsorption analysis was performed using a Micromeritics porosimeter (model ASAP-2020). The samples were degassed at 250°C under vacuum for 6h and N<sub>2</sub> adsorption/desorption measurement was done at -196 °C. The surface areas were calculated by BET method. The pore size distributions and pore volume were calculated by DFT methods.

## 5.6 References

1. Y. Lu and W. Chen, *Chem. Soc. Rev.*, 2012, **41**, 3594-3623.
2. G. Schmid, *Chem. Rev.*, 1992, **92**, 1709-1727.
3. S. Choi, R. M. Dickson and J. Yu, *Chem. Soc. Rev.*, 2012, **41**, 1867-1891.
4. E. C. Tyo and S. Vajda, *Nat Nano*, 2015, **10**, 577-588.
5. K. Bourhis, A. Royon, G. Papon, M. Bellec, Y. Petit, L. Canioni, M. Dussauze, V. Rodriguez, L. Binet, D. Caurant, M. Treguer, J.-J. Videau and T. Cardinal, *Mater. Res. Bull.*, 2013, **48**, 1637-1644.
6. E. Maik, R. Klaus, H. Armin, M. T. Dragomir, W. Wilfried, S. Reinhard and P. Gianfranco, *Nanotechnology*, 2008, **19**, 135701.
7. T. P. Bigioni, R. L. Whetten and Ö. Dag, *J. Phys. Chem. B*, 2000, **104**, 6983-6986.
8. J. D. Aiken Iii and R. G. Finke, *J. Mol. Catal. A: Chem.*, 1999, **145**, 1-44.
9. E. M. Nolan and S. J. Lippard, *Chem. Rev.*, 2008, **108**, 3443-3480.
10. X. Michalet, F. F. Pinaud, L. A. Bentolila, J. M. Tsay, S. Doose, J. J. Li, G. Sundaresan, A. M. Wu, S. S. Gambhir and S. Weiss, *Science*, 2005, **307**, 538-544.
11. T. Sun and K. Seff, *Chem. Rev.*, 1994, **94**, 857-870.
12. P. Shah, A. Rørvig-Lund, S. B. Chaabane, P. W. Thulstrup, H. G. Kjaergaard, E. Fron, J. Hofkens, S. W. Yang and T. Vosch, *ACS Nano*, 2012, **6**, 8803-8814.
13. S. Link, A. Beeby, S. FitzGerald, M. A. El-Sayed, T. G. Schaaff and R. L. Whetten, *J. Phys. Chem. B.*, 2002, **106**, 3410-3415.
14. P. C. Ford, E. Cariati and J. Bourassa, *Chem. Rev.*, 1999, **99**, 3625-3648.
15. K. Tsuge, *Chem. Lett.*, 2013, **42**, 204-208.
16. M. Wallesch, D. Volz, D. M. Zink, U. Schepers, M. Nieger, T. Baumann and S. Bräse, *Chem. Eur. J.*, 2014, **20**, 6578-6590.
17. D.-W. Shin, S. X. Wang, A. F. Marshall, W. Kimura, C. Dong, A. Augustsson and J. Guo, *Thin Solid Films*, 2005, **473**, 267-271.
18. C. Vázquez-Vázquez, M. Bañobre-López, A. Mitra, M. A. López-Quintela and J. Rivas, *Langmuir*, 2009, **25**, 8208-8216.
19. W. Wei, Y. Lu, W. Chen and S. Chen, *J. Am. Chem. Soc.*, 2011, **133**, 2060-2063.
20. N. Vilar-Vidal, M. C. Blanco, M. A. López-Quintela, J. Rivas and C. Serra, *J. Phys. Chem. A*, 2010, **114**, 15924-15930.

21. S. Huseyinova, J. Blanco, F. G. Requejo, J. M. Ramallo-López, M. C. Blanco, D. Buceta and M. A. López-Quintela, *J. Phys. Chem. A*, 2016, DOI: 10.1021/acs.jpcc.5b12227.
22. C. Wang, Y. Yao and Q. Song, *Colloids Surf., B*, 2016, **140**, 373-381.
23. A. Katrib, *J. Electron. Spectrosc. Relat. Phenom.*, 1980, **18**, 275-278.
24. M. Fujiwara, H. Fujii, K. Tainaka, T. Matsushita and S. Ikeda, *Analytical Sciences/Supplements*, 2002, **17icas**, i1065-i1067.
25. E. Coutino-Gonzalez, D. Grandjean, M. Roeffaers, K. Kvashnina, E. Fron, B. Dieu, G. De Cremer, P. Lievens, B. Sels and J. Hofkens, *Chem. Commun.*, 2014, **50**, 1350-1352.
26. M. Guisnet and P. Magnoux, *Applied Catalysis*, 1989, **54**, 1-27.
27. H. C. Thomas, *J. Am. Chem. Soc.*, 1944, **66**, 1664-1666.
28. B. Schulte, M. Tsotsalas, M. Becker, A. Studer and L. De Cola, *Angew. Chem. Int. Ed.*, 2010, **49**, 6881-6884.
29. M. Iwamoto, H. Furukawa, Y. Mine, F. Uemura, S.-i. Mikuriya and S. Kagawa, *J. Chem. Soc., Chem. Commun.*, 1986, DOI: 10.1039/C39860001272, 1272-1273.
30. K. i. Kuge and G. Calzaferri, *Microporous Mesoporous Mater.*, 2003, **66**, 15-20.
31. E.-M. El-Malki, R. A. van Santen and W. M. H. Sachtler, *J. Phys. Chem. B.*, 1999, **103**, 4611-4622.
32. E. A. Prasetyanto, L. Donato, C. Hsu, P. Chen and L. D. Cola, *manuscript in preparation*.
33. J. Zheng, P. R. Nicovich and R. M. Dickson, *Annu. Rev. Phys. Chem.*, 2007, **58**, 409-431.
34. M. M. J. Treacy and J. B. Higgins, in *Collection of Simulated XRD Powder Patterns for Zeolites (Fifth Edition)*, Elsevier Science B.V., Amsterdam, 2007, pp. 256-257.
35. J. Chastain, R. C. King and J. Moulder, *Handbook of X-ray photoelectron spectroscopy: a reference book of standard spectra for identification and interpretation of XPS data*, Physical Electronics Eden Prairie, MN, 1995.
36. P. Maity, S. Yamazoe and T. Tsukuda, *ACS Catalysis*, 2013, **3**, 182-185.

## **Chapter 6**

# **Multi-functionalized mesoporous titania for bio-application**

### **Abstract**

Mesoporous material due to its large surface area, biocompatibility and possibility of functionalization, makes it a good candidate for bio-application. Herein, multi-functionalized mesoporous titania particle has been developed for drug delivery application. Compare with the widely used mesoporous silica, titania which is photoactive could provide extra advantages in bio-application. On the other hand, the widely used titania material e.g. in sunscreen also bring health concerns. In this case, the release of the reactive oxygen species (ROS) by titania material under UV irradiation has been studied in vitro. These results could be further applied for intercellular reaction, inhibition of drug resistance and so on.

## 6.1 Introduction

Mesoporous titania materials find different applications in various photo induced functions such as dye sensitized solar cells,<sup>1, 2</sup> water splitting<sup>3, 4</sup> and degradation of organic pollutions<sup>5, 6</sup> due to its unique semiconducting properties. According to FDA (21CFR73.575), titania is also considered to be safe and indeed has been used in tooth paste and cosmetic products. However so far very little has been explored related to the possibility of functionalization and the use of photo-active properties, applied in biomedical applications.<sup>7, 8</sup> Compared to the semiconductor field, there are fewer examples for mesoporous titania used in bio-applications. Compare to the semiconductor field, in the bio-area mesoporous titania have been used only as a matrix for sustained drug delivery<sup>9</sup> or in antibacterial usse<sup>10</sup> in the form of membranes or films. On the other hand porous silica has been widely used as drug delivery agent in the form of nanoparticles.<sup>11</sup> However, since silica materials are electrically “dead” and not photoactive, the employment of the titania in this field could bring new aspects to the drug delivery system. Thus, mesoporous particles of titania could represent an interesting material to compare with similar size silica systems. In chapter 2 we have introduced the mesoporous titania particles which could be ideal for this purpose. In fact, the hybrid porous titania particles can be used as drug delivery material,<sup>12</sup> but more interestingly as killing agents in bio-applications. This unique property is demonstrated to be useful to solve the problem of multidrug resistance developed by cells or bacteria.<sup>13</sup> Compared with titania particles which have no porous structure, spatial functionalization of the pores and the possibility to entrap molecules such as drugs in the channels makes these particles quite attractive.<sup>7</sup>

To use the titania material as killing agent, it is essential to know the release of the ROS under UV irradiation inside the cells. The production of ROS by titania material under UV irradiation have been discovered in the 1970s.<sup>14</sup> The photo induced process of the creation of electron/hole pairs by titania material was studied later.<sup>15</sup> It was suggested that both HO· and HOO· were produced in the aqueous suspension of anatase titania after UV exposure.<sup>16</sup> Through the years, the different ROS production by titania under UV

exposure was studied by many researchers in different solvents such as water,<sup>17, 18</sup> ethanol<sup>19</sup> and DMSO.<sup>20</sup> Of all these studies, electron spin resonance (ESR) spectroscopy was used as the detection technique for the different ROS which is suitable in pure solvents. However, as titania material has already been used widely in bio-medical field,<sup>21, 22</sup> the release of ROS bring both challenges (e.g. cytotoxicity) and opportunities (e.g. killing agent). In this case, it is necessary to study the release of ROS in cells. As intracellular environment is much more complicated than pure solvent, ESR is not applicable for our purpose. Studies from biologists proposed that ROS which the mitochondrial produced can be detected by fluoresce probe.<sup>23</sup> Same principle could be applied into our system. To our knowledge, up till now, there is no kinetic study reported on the ROS release by titania under UV exposure in vitro. Also, as the toxicity of titania in sunscreen has been debated for many years,<sup>24</sup> this study can therefore bring some useful information.

*In this chapter, a drug delivery system based on multi-functionalized mesoporous titania is described. Moreover, due to the unique photocatalytic property of the titania material, the kinetic of ROS release in vitro under UV was also investigated.*

## **6.2 Functionalization and characterization**

As we mentioned in chapter 2 we have synthesized and characterized mesoporous titania particle 400 nm in diameter and with pores of 11 nm. The surface of the particles has been functionalized and the schematic procedure is shown in Fig. 6.1. The mesoporous titania particle was first covered with alanine by the interaction between the carboxylic acid and titania surface.<sup>25</sup> The fluorescein isothiocyanate isomer was then reacted with the -NH<sub>2</sub> group of alanine and covalently attached. In the end, the whole system was covered with a biocompatible polymer (polylysine) which could hold the whole system together. Polylysine also gave a positively charged surface which makes the particle easier to be internalized in the cells. The concept is that alanine and the mesoporous titania particles were not covalently attached. After the degradation of polylysine inside



the cells, alanine and its attachment would be released from the mesoporous titania particle which could potentially act as drug. The fluorescein molecule attached with alanine would make the release visible by microscopic methods.

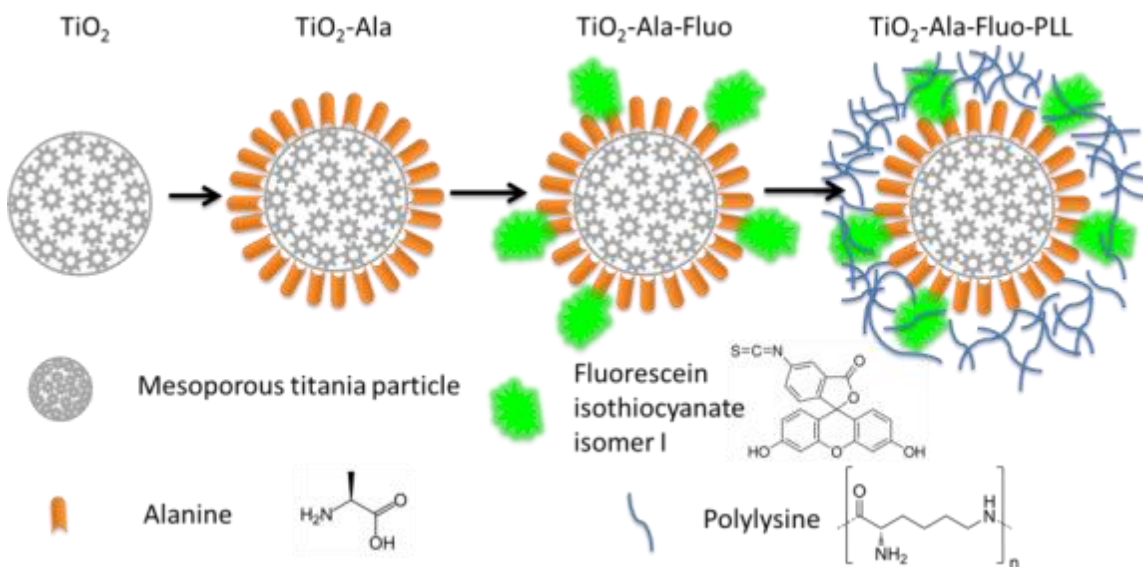


**Fig. 6.1** Schematic procedure of the functionalization of mesoporous titania particle.

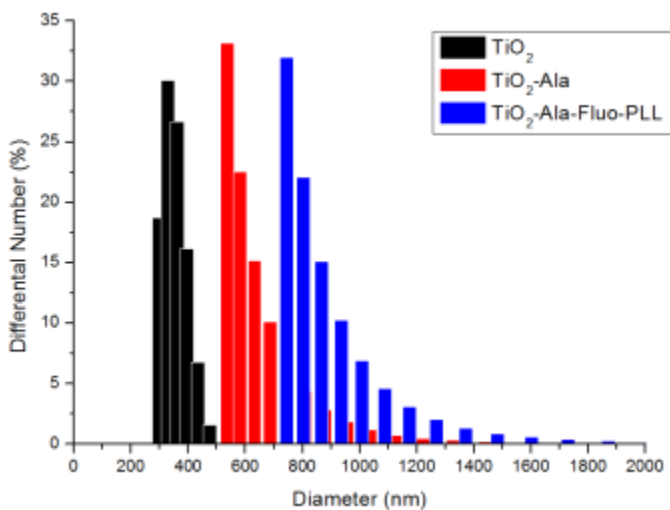


**Fig. 6.2** DLS number distribution of the original and functionalized mesoporous titania.

To determine size change of the functionalization of each step, dynamic light scattering (DLS) was employed. We can see that as expected, with further functionalization the particles get bigger (Fig. 6.2). The hydrodynamic diameter of starting mesoporous titania

was around 400 nm. The alanine attached particle was around 600 nm and the final polylysine covered particle was around 800 nm. The “tail” we have seen on the distribution was due to the bigger aggregates.

The surface charge of the particles was characterized by zeta-potential measurement (Table 6.1). The naked mesoporous titania particles showed negatively charged surface. After the alanine and fluorescein functionalization, the fluorescein molecules on the particle surface still showed negative charge. In the end, positive charge was obtained due to the amine groups from the surrounded polylysine.

**Table 6.1** Zeta-potential of the original and functionalized mesoporous titania.

Name	Zeta-potential (mV)
TiO <sub>2</sub>	-65.73
TiO <sub>2</sub> -Ala-Fluo	-34.5
TiO <sub>2</sub> -Ala-Fluo-PLL	+13.26

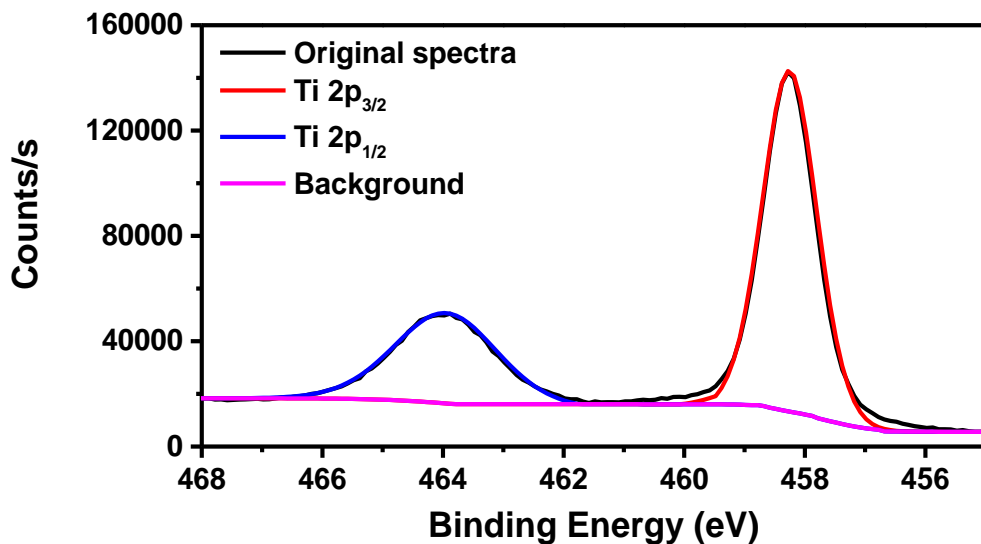


**Fig. 6.3** XPS titanium 2p spectra of TiO<sub>2</sub>-Ala.

To prove that the alanine was not covalently attached onto the titania surface which could make the release possible, X-ray photoelectron spectroscopy (XPS) measurement was used to measure the alanine functionalized titania. We can see that from the Ti 2p scan,

the spectra can be fitted with one Gaussian peak (Fig. 6.3). This gave us the idea that there was only one kind of titanium species which clearly only from titania. The interaction of the alanine and titania was most likely electrostatic interaction between the Ti(IV) ion with positive charge and the -COOH group which show negative charge in water after the loss of H<sup>+</sup>.

### 6.3 In vitro bio-application

#### 6.3.1 Drug delivery

Even through titania material is FDA approved, cytotoxicity of our functionalized titania particle was unknown. In this case, cytotoxicity study was done in the first place. The cells we have chosen were HeLa cells. The functionalized particles have been dispersed in PBS solution with two different concentrations: 0.01 mg/mL and 0.05 mg/mL. The

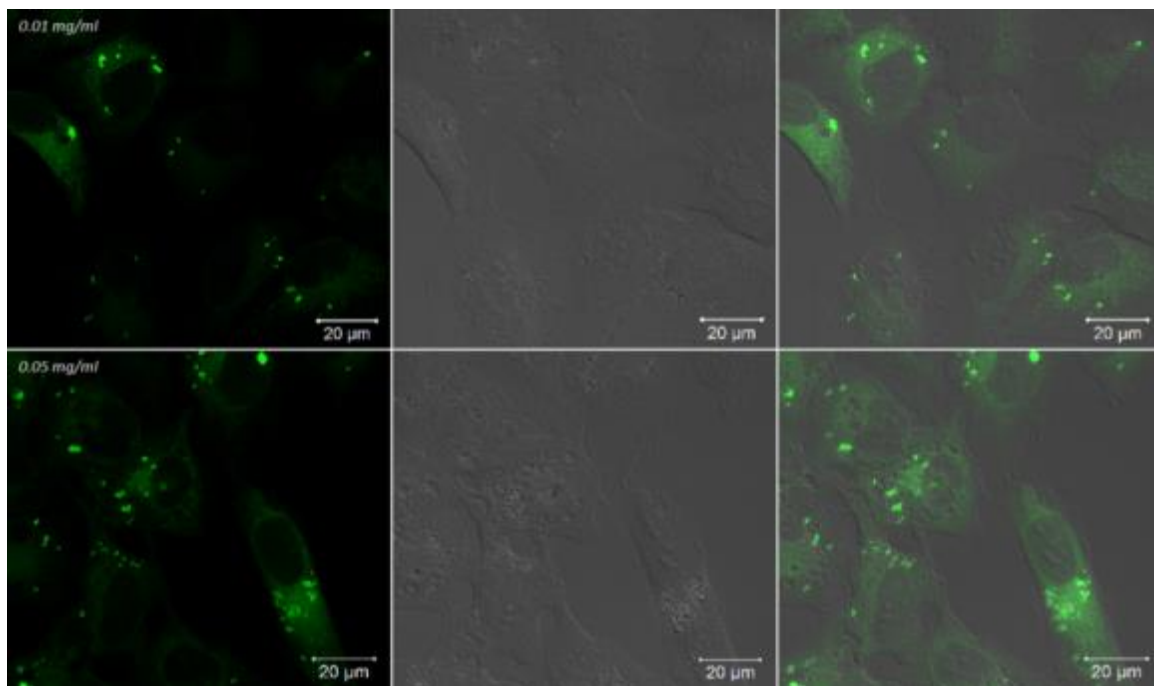


**Fig. 6.4** Confocal microscopic image of the functionalized mesoporous titania particle cytotoxicity study. HeLa cells were incubated for 24 hours with 0.01 mg/mL and 0.05 mg/mL concentration. 0.1 µg/mL of DAPI was added as staining agent.

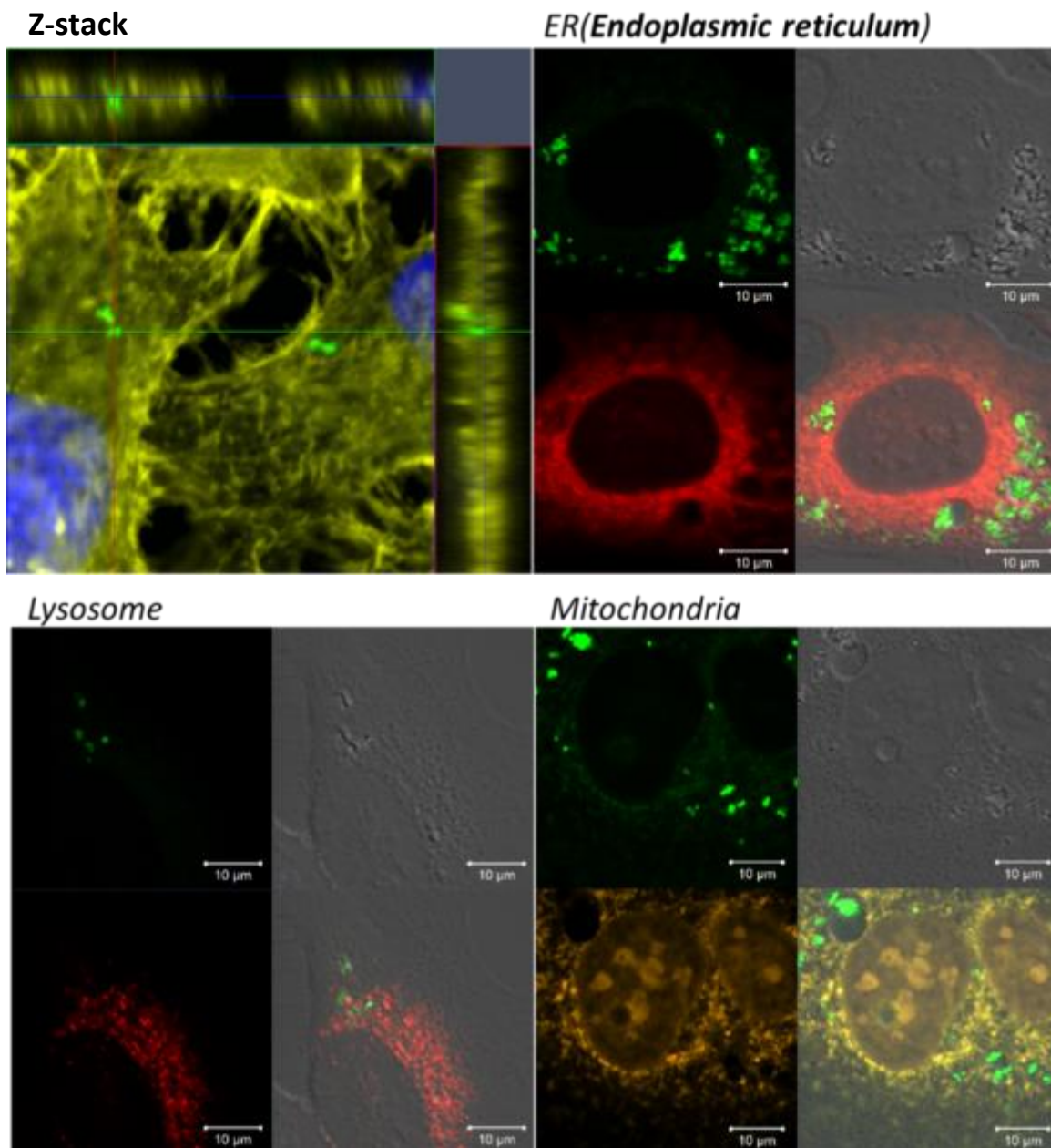


**Fig. 6.5** Confocal microscopic image of the functionalized mesoporous titania particle co-localization study with different cell organs.

particles were incubated with cells for 24 hours. Afterwards, DNA staining agent DAPI (4',6-diamidino-2-phenylindole) was added to see the cell viability. It is known that very high concentration ( $>25 \mu\text{g/mL}$ ) of DAPI is needed to stain living cells due to its low membrane permeability.<sup>26</sup> In our experiments,  $0.1 \mu\text{g/mL}$  was used that would be able to label only dead cells. From the confocal microscope image Fig. 6.4 we can see clearly

that after 24 hours of incubation, no blue emission from the cell nucleus was observed which means that cells under both particle concentrations were not stained. This indicated that our functionalized mesoporous titania was not toxic to HeLa cells with 0.05 mg/mL concentration or lower.

To make sure that the particles were inside the cells, z-stack pictures using the confocal microscope were taken. We can see clearly that our particles were inside the cells (Fig. 6.5). To investigate which cell organ was favorable for the functionalized mesoporous titania particles, co-localization study by confocal microscope was applied. It was shown that the particles were not co-localized with ER (endoplasmic reticulum), lysosome and mitochondria. This indicated that the titania particle and the functionalized molecules don't have specific interactions with the cell organs.

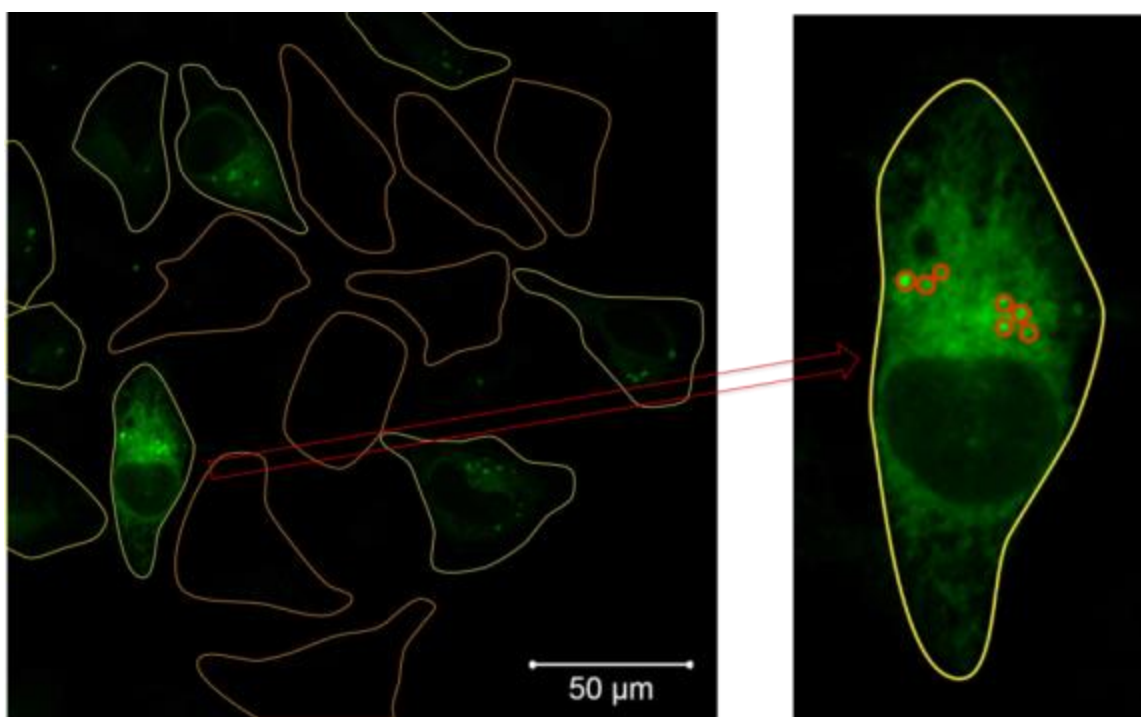


**Fig. 6.6** Confocal microscopic image of the HeLa cells incubated with 0.01 mg/mL functionalized mesoporous titania particles for 24 hours.

As we have discussed before, alanine was not covalently attached with titania particle. It could be released after the surrounding polymer (polylysine) has been degraded. In this

experiment, HeLa cells were incubated with 0.1 mg/mL functionalized mesoporous titania particles for 24 hours. Fig. 6.6 shows the confocal microscopic image of the HeLa cells with particles inside. The fluorescein color was only found in some cells. If we zoom in one of the cells with green color, particles can be found inside the cells. This gave us the clear clue that the fluorescein was released after the cell uptake of particles. This means that our multi-functionalized mesoporous titania could be used for drug delivery applications.

### 6.3.2 ROS release under UV irradiation

It is well known that under UV irradiation, titania could produce reactive oxygen species (ROS).<sup>19</sup> Compare with silica material which is usually just a host of drugs in the drug delivery system,<sup>12</sup> the property of releasing ROS could make titania also act as a killing agent.

To investigate the killing of cells by titania under UV irradiation, a HQRP 12 LED flashlight which emits 365 nm wavelength light was employed. Reference experiment was firstly carried out to prove that the cells were not killed by the UV. The cells were exposed for 2 hours under UV irradiation. DAPI was also added. No DAPI signal was observed indicated that the cells were still alive under our conditions (Fig. 6.7). For the cells with titania particles, after 2 hours of UV exposure, blue emissive DAPI was staining the cell nucleus which indicated that most of the cells were killed (Fig. 6.8).

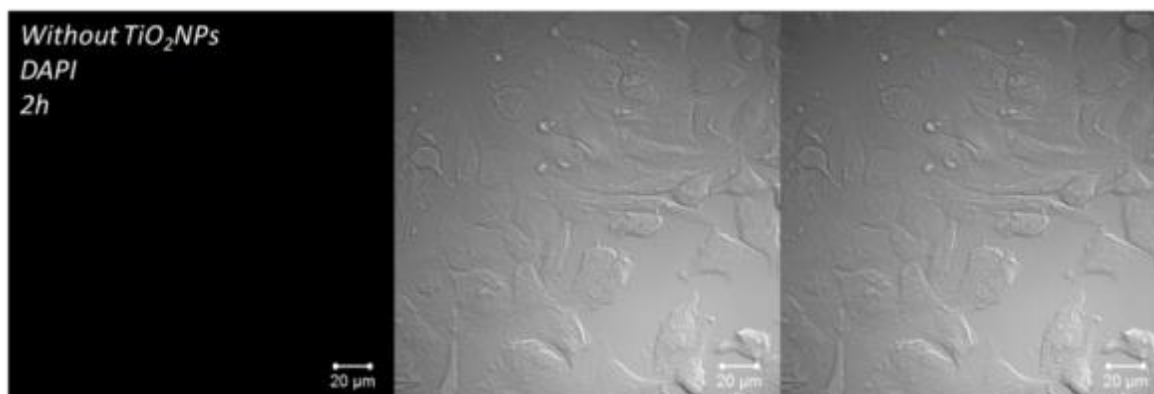


**Fig. 6.7** HeLa cell without titania particle exposed under UV light for 2 hours, stained with DAPI.

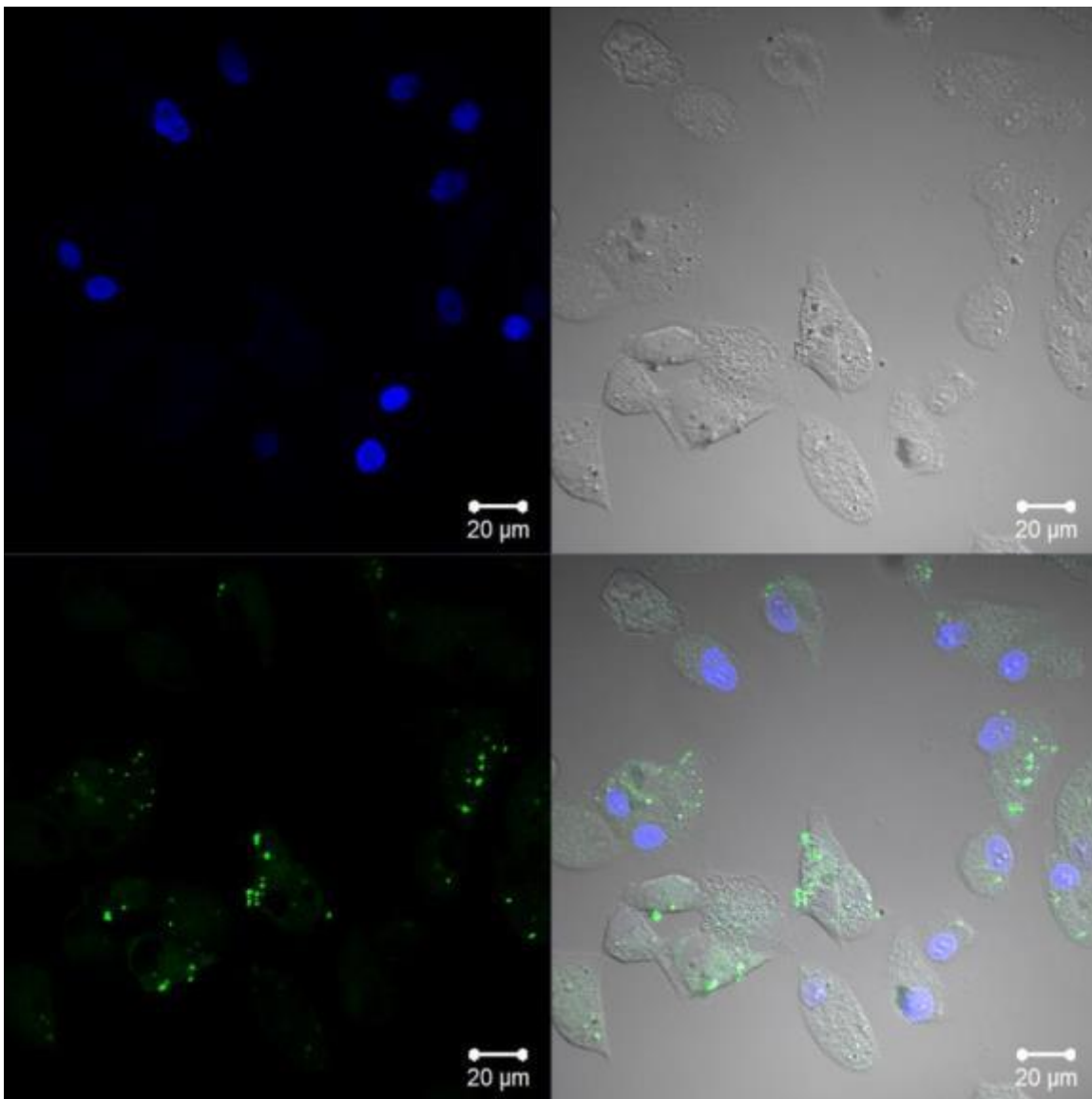


**Fig. 6.8** Confocal microscopic images of the HeLa cells incubated with functionalized mesoporous titania particles after 2 hours of UV exposure, stained with DAPI.

The kinetic of the ROS release through titania under UV irradiation was studied by an oxidation sensitive dye which is called Cell-ROX. Cell-ROX is not emissive initially, but emits red light after oxidation. Fig. 6.9 shows the red emission which means cell-ROX has been oxidized. This indicated that under UV exposure, ROS had been produced which kill the cells.

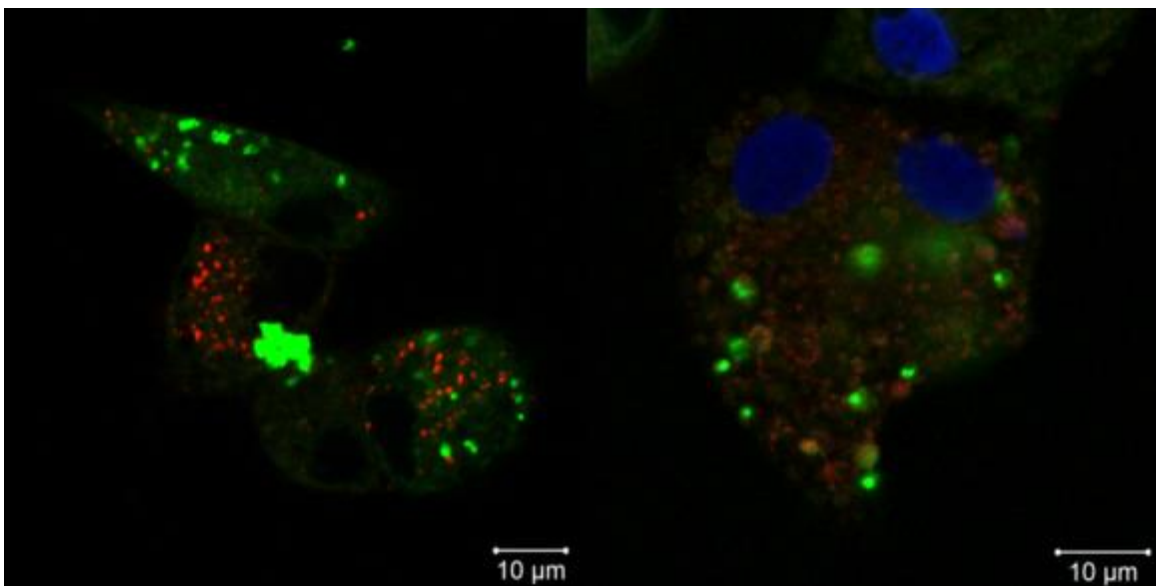


**Fig. 6.9** Functionalized mesoporous titania particles contained HeLa cells treated with Cell-ROX after UV exposure. Red emission indicates the production of ROS.

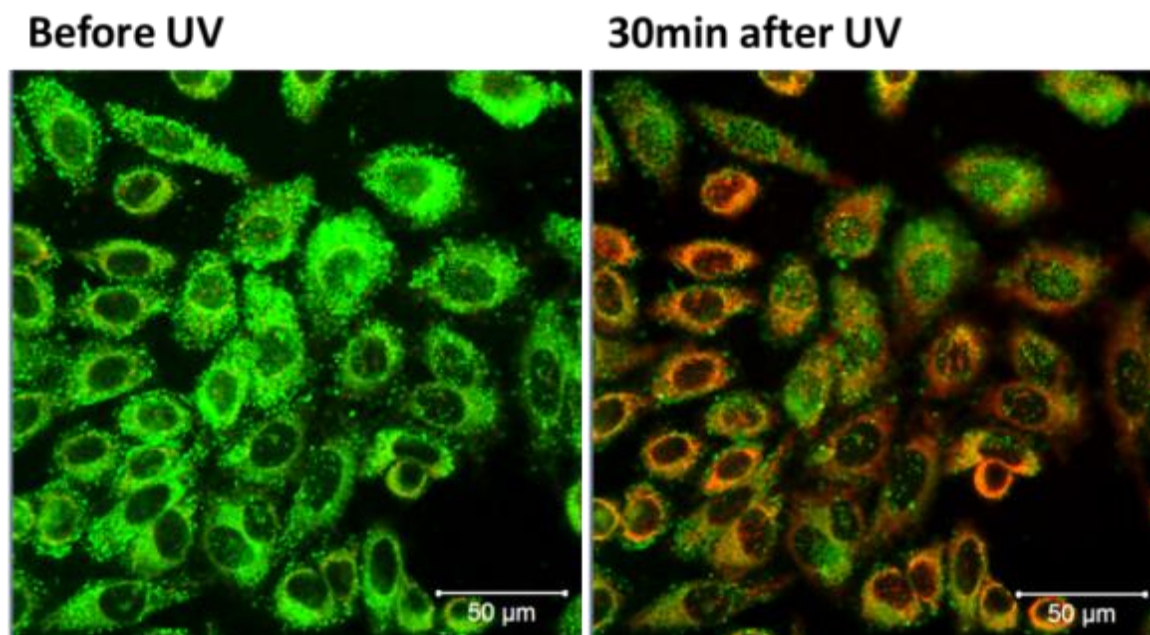


**Fig. 6.10** Confocal microscopic image of the ROS release indicated by cell-ROX (red).

To investigate the kinetics of the ROS release in vitro, cell-ROX has been used as an indicator of the ROS. HeLa cells were incubated by 0.05 mg/mL functionalized mesoporous titania particles for 24 hours. The cells were then exposed with an 8 mW UV



with 355 nm wavelength mounted with the confocal microscope. The picture was taken every 5 minutes. The red component of the picture was taken out for further analysis (Fig. 6.10).

To determine the ROS release kinetic in vitro, several cells have been picked up and the emission intensity of the cell-ROX has been analyzed. A typical red signal from one cell is shown in Fig. 6.11. As the particles never enter the nucleus, we only pick up the strongest signal from the cytoplasm. The initial value of the Cell-ROX can be explained by the ROS produced by mitochondria which was first discovered in the 1960s.<sup>27</sup> First order reaction rate was applied to determine the ROS releasing rate which was suggested by several literatures.<sup>18, 20, 28</sup>

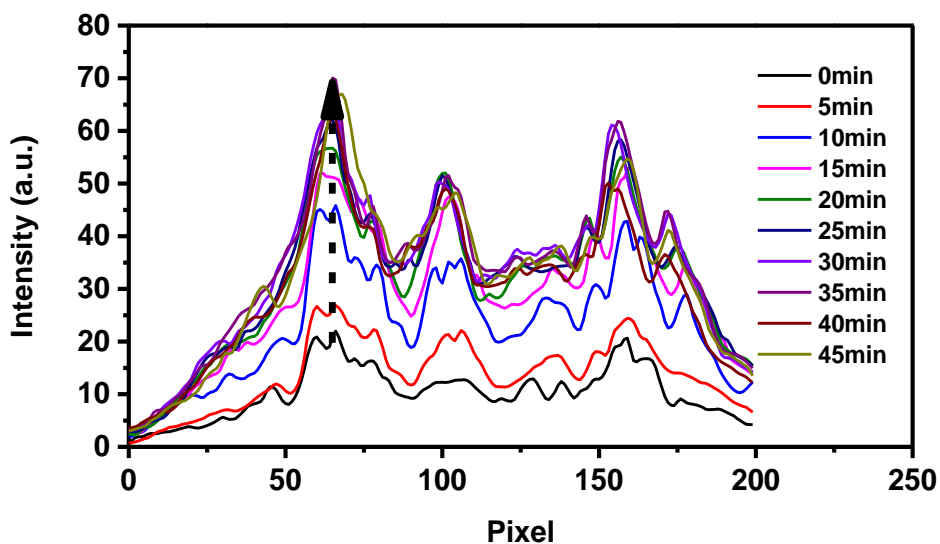


**Fig. 6.11** An example of the intensity of Cell-ROX dye increasing with UV exposure.

The kinetic of the ROS release in vitro is shown in Fig. 6.12. We have similar shape of curve compare with the previous researchers which have investigate the release of ROS from titania by UV irradiation in ethanol or in water.<sup>18-20</sup> Previous studies suggested that in aqueous solution, both hydrogen peroxide and singlet oxygen were produced by titania under UV exposure.<sup>18</sup> The production of ROS has been fitted with first-order reaction rate.<sup>20</sup> As we used the same fitting to our curve, a rate of  $15.25 \text{ min}^{-1}$  was obtained.

Compare to literature for ROS release, which reported that  $15000 \text{ s}^{-1}$  reaction rate was achieved in DMSO at  $0.1 \text{ mg/mL}$  of titania,<sup>20</sup> our reaction rate in vitro is much slower. This could be explained mainly by two reasons. First, much more oxygen which is the reactant to create the ROS, can be dissolved DMSO than in water (e.g.  $9.2 \text{ mg O}_2 \text{ dm}^{-3}$  at  $20 \text{ }^\circ\text{C}$  in water,<sup>29</sup>  $67 \text{ mg O}_2 \text{ dm}^{-3}$  at  $25 \text{ }^\circ\text{C}$  in DMSO<sup>30</sup>). Also, a much less powerful light source was used in our experiments than the literature ( $8 \text{ mW}$  compare to  $300 \text{ mW}$ ).

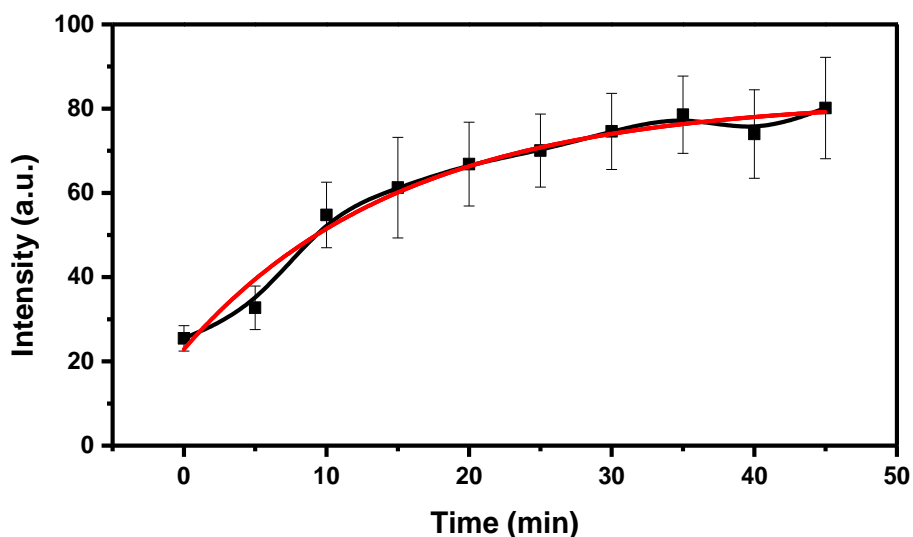


**Fig. 6.12** Experimental and the fitting data of the ROS release (fitted by first-order reaction rate).

#### 6.4 Conclusion and perspectives

In this chapter, multi-functionalized mesoporous titania have been successfully made. The application of drug delivery has been demonstrated. Furthermore, compared with the widely used silica material, the ability of being “killing agent” has been proved. Finally, the in vitro kinetic of the ROS release by titania under UV exposure has been investigated. This multi-functionalized mesoporous titania can be potentially used for intercellular reaction, inhibition of drug resistance and so on.

## 6.5 Experimental section

### *Materials*

L-Alanine ( $\geq 98\%$ , 1g), Fluorescein isothiocyanate isomer I (90%), Poly-L-lysine was purchased from Sigma-Aldrich without further modification.

Cell media is made of 88% Dulbecco's Modified Eagle Medium (DMEM), 10% of fetal bovine serum (FBS), 1% of L-glutamine and 1% of penicillin.

### *Synthesis of the mesoporous titania particle*

Described in chapter 2.

### *Functionalization of mesoporous titania particle*

100 mg particles were suspended into 1 mL of EtOH, 5 mg of alanine was then added. The mixture was stirred in the dark for 2 hours. The product was washed by centrifugation 3 times with ethanol to remove the free alanine. The obtained TiO<sub>2</sub>-Ala was suspended into ethanol, 0.1 mg of fluorescein isothiocyanate isomer I was added. The mixture was stirred in the dark overnight. The free fluorescein was removed by centrifugation 3 times with ethanol. TiO<sub>2</sub>-Ala-Fluo was then suspended into 10 mL solution of polylysine water solution (1 mg/mL) and stirred overnight. Final product TiO<sub>2</sub>-Ala-Fluo-PLL was washed with water by centrifugation 3 times. The functionalized particles were suspended into PBS solution at certain concentration for the in vitro experiments.

### *X-ray photoelectron spectroscopy*

All the X-ray Photoelectron Spectroscopic (XPS) measurements were done by a Thermo Scientific K-Alpha X-ray Photoelectron Spectrometer using a monochromatic AlK $\alpha$  radiation ( $h\nu = 1486.6$  eV). Survey measurements were performed with 200 eV analyser pass energy and a 1 eV energy step size to calculate the atomic concentrations. Element scans were performed with 50 eV analyser pass energy and a 0.1 eV energy step size to obtain the chemical state information. Valence band spectra were performed with 50 eV

analyser pass energy and 0.2 eV step size. X-ray beam size was 400  $\mu\text{m}$ . All the obtained binding energies were referenced to  $\text{sp}^3$  carbon 1s peak at 284.8 eV.

#### *Confocal microscopy*

Fluorescence images were acquired using Zeiss LSM 710 confocal microscope system with 63x magnification, numerical aperture 1.3 of Zeiss LCI Plan-NEOFLUAR water immersion objective lens (Zeiss GmbH). The samples were excited by a continuous wave (cw) laser operated at wavelength 405 nm and the emission of the system was collected widely in the range 412 nm to 735 nm. The emission spectra were acquired using lambda mode acquisition and the signal was reprocessed by Zen 2011 software (Zeiss GmbH).

#### *Dynamic light scattering and zeta-potential*

DLS and zeta-potential analysis were performed on a Delsa Nano C Particle Analyzer (Beckman Coulter, Brea, CA, USA); all DLS measurements were conducted in water, while zeta-potential analysis in phosphate buffered saline (PBS), pH = 7.

## 6.6 References

1. M. Grätzel, *Curr. Opin. Colloid Interface Sci.*, 1999, **4**, 314-321.
2. M. Zukalová, A. Zuka, L. Kavan, M. K. Nazeeruddin, P. Liska and M. Grätzel, *Nano Lett.*, 2005, **5**, 1789-1792.
3. P. Hartmann, D.-K. Lee, B. M. Smarsly and J. Janek, *ACS Nano*, 2010, **4**, 3147-3154.
4. G. Liu, Y. Zhao, C. Sun, F. Li, G. Q. Lu and H.-M. Cheng, *Angew. Chem. Int. Ed.*, 2008, **47**, 4516-4520.
5. D. P. Sawant, J. Justus, V. V. Balasubramanian, K. Ariga, P. Srinivasu, S. Velmathi, S. B. Halligudi and A. Vinu, *Chem. Eur. J.*, 2008, **14**, 3200-3212.
6. R. J. Tayade, R. G. Kulkarni and R. V. Jasra, *Ind. Eng. Chem. Res.*, 2006, **45**, 5231-5238.
7. K. C. W. Wu, Y. Yamauchi, C.-Y. Hong, Y.-H. Yang, Y.-H. Liang, T. Funatsu and M. Tsunoda, *Chem. Commun.*, 2011, **47**, 5232-5234.
8. Z. Fei Yin, L. Wu, H. Gui Yang and Y. Hua Su, *PCCP*, 2013, **15**, 4844-4858.
9. E. Gultepe, D. Nagesha, S. Sridhar and M. Amiji, *Adv. Drug Deliv. Rev.*, 2010, **62**, 305-315.
10. Y. Liu, X. Wang, F. Yang and X. Yang, *Microporous Mesoporous Mater.*, 2008, **114**, 431-439.
11. I. I. Slowing, B. G. Trewyn, S. Giri and V. S. Y. Lin, *Adv. Funct. Mater.*, 2007, **17**, 1225-1236.
12. F. Tang, L. Li and D. Chen, *Adv. Mater.*, 2012, **24**, 1504-1534.
13. M. Song, R. Zhang, Y. Dai, F. Gao, H. Chi, G. Lv, B. Chen and X. Wang, *Biomaterials*, 2006, **27**, 4230-4238.
14. A. Fujishima and K. Honda, *Nature*, 1972, **238**, 37-38.
15. D. Dung, J. Ramsden and M. Graetzel, *J. Am. Chem. Soc.*, 1982, **104**, 2977-2985.
16. C. D. Jaeger and A. J. Bard, *J. Phys. Chem.*, 1979, **83**, 3146-3152.
17. J. R. Harbour, J. Tromp and M. L. Hair, *Can. J. Chem.*, 1985, **63**, 204-208.
18. R. Konaka, E. Kasahara, W. C. Dunlap, Y. Yamamoto, K. C. Chien and M. Inoue, *Redox Report*, 2001, **6**, 319-325.
19. R. Konaka, E. Kasahara, W. C. Dunlap, Y. Yamamoto, K. C. Chien and M. Inoue, *Free Radical Biol. Med.*, 1999, **27**, 294-300.
20. V. Brezová, S. Gabčová, D. Dvoranová and A. Staško, *J. Photochem. Photobiol., B*, 2005, **79**, 121-134.

21. E. Moschini, M. Gualtieri, M. Colombo, U. Fascio, M. Camatini and P. Mantecca, *Toxicol. Lett.*, 2013, **222**, 102-116.
22. R. Y. Prasad, K. Wallace, K. M. Daniel, A. H. Tennant, R. M. Zucker, J. Strickland, K. Dreher, A. D. Kligerman, C. F. Blackman and D. M. DeMarini, *ACS Nano*, 2013, **7**, 1929-1942.
23. D. B. Zorov, M. Juhaszova and S. J. Sollott, *BBA-Bioenergetics*, 2006, **1757**, 509-517.
24. M. D. Newman, M. Stotland and J. I. Ellis, *J. Am. Acad. Dermatol.*, 2009, **61**, 685-692.
25. U. Diebold, *Surf. Sci. Rep.*, 2003, **48**, 53-229.
26. D. Zink, N. Sadoni and E. Stelzer, *Methods*, 2003, **29**, 42-50.
27. P. Jensen, *BBA-Proteins and Proteomics*, 1966, **122**, 157-166.
28. A. Fujishima, T. N. Rao and D. A. Tryk, *J. Photochem. Photobiol. C.*, 2000, **1**, 1-21.
29. M. Crosson and R. Gibb, *J. Chem. Educ.*, 1992, **69**, 830.
30. D. T. Sawyer, G. Chiericato Jr, C. T. Angelis, E. J. Nanni Jr and T. Tsuchiya, *Anal. Chem.*, 1982, **54**, 1720-1724.

## **Chapter 7**

# **Organotitania material for photocatalytic application(s)**

### *Abstract*

The reduction of the band gap of titania material is important to fully utilize its photocatalytic properties especially under visible light. Herein, we report the synthesis which introduces organic compounds to the organotitania precursor. The polymerization of the organotitania precursor would end up with the titania framework which has organic linkers. In the end, organotitania with benzene and/or thiophene linker have been produced. Photocatalytic activities under both UV and visible-light have been tested.

## 7.1 Introduction

Titanium dioxide ( $\text{TiO}_2$ ) is a strategic material for many conventional usage (plastics, paintings, paper, cosmetics, medical products etc.) and advanced applications such as photocatalysis,<sup>1, 2</sup> water photo-splitting,<sup>3</sup> dye-sensitized solar cells<sup>4</sup> (DSSC) and superhydrophilic coatings.<sup>5</sup> This metal dioxide is known in its three different polymorphs (rutile, anatase and brookite).<sup>1</sup> Anatase and rutile are the most interesting  $\text{TiO}_2$  phases under the point of view of the photochemical applications. In addition, the most stable thermodynamic phase: rutile, has been much more investigated by surface scientists due to the fact that growing single crystals and/or single crystalline layers of this polymorph is significantly easier.<sup>1</sup>

Titania as highly promising material is mainly used for photochemical applications and as a photocatalyst because of its excellent functionality, long term stability, and nontoxicity.<sup>6, 7</sup> Nevertheless,  $\text{TiO}_2$  becomes active only under UV light, whose energy is greater than the band gap of  $\text{TiO}_2$  (around 3.0 eV).<sup>8</sup> The effective utilization of visible light occupying the main part of the solar beams is one of the important subjects for the increased utility of  $\text{TiO}_2$ . In many previous studies, in order to improve the photoreactivity of  $\text{TiO}_2$  and to extend its absorption edge into the visible-light region, doping of various transition metal cations has been intensively attempted.<sup>6, 9-11</sup> For a few cases, the photoactivity of the cation-doped  $\text{TiO}_2$  decreased even in the UV region.<sup>6, 10, 11</sup> This is because the doped materials suffer from a thermal instability.<sup>6</sup> Solution of these problems could be found in the hybrid organotitania nanomaterials, which expect to be more effective due to the combination of organic - inorganic bonded parts through covalent bonds or coordination-covalent bonds. Hybrid nanomaterials based on titanium dioxide containing incorporated organic molecules are well known in different forms and structures (nanolayers,<sup>12, 13</sup> nanoparticles-NPs,<sup>12-14</sup> nanofibers<sup>12, 15</sup> and nanocomposites<sup>12, 13</sup>), started to be promising for different types of applications not only in chemistry, but also in physics<sup>6, 7, 16, 17</sup> and in medicine.<sup>16, 18</sup> Many successful strategies have been developed to modify titania by the incorporation of other functional metal ions,



molecules and components with TiO<sub>2</sub> frameworks, which allow in many cases a priori design of better photocatalysts.<sup>16, 19, 20</sup>

From the structure point of view, titanium is a transition element with its valence electrons divided between the III. and IV. principal quantum group, it cannot be expected to bear more than a superficial resemblance to other group IV elements such as silicon, germanium and tin which readily form stable covalent bonds with carbon. The consequent lack of stability and difficulty to form the titanium-carbon bond is the crucial reason for the repeated failures reported in the literature since the first attempt by Cahours in 1861.<sup>21</sup> Study of the organic compounds of titanium has been carried out resulting in isolation of a compound containing the covalent titanium-carbon bond. A series of exploratory reactions between butyl titanate with various organomagnesium and organolithium reagents in 1:1 to 4:1 molar ratios substantiated this assumption and showed that the most stable carbon to metal bonds were formed with aromatic R groups.<sup>21</sup> However due to complicated synthesis route of organotitanium compounds, repeated failures have been reported in the literature until 60 years ago when Herman and Nelson (1953) isolated the first organometallic titanium compounds incorporating a Ti-C  $\sigma$ -bond by reacting titanium tetraisopropoxide with phenyllithium.<sup>22</sup> Furthermore, more general study has been done to investigate the stability of the Ti-C  $\sigma$ -bond in the class of compounds represented by the general formula R<sub>n</sub>TiX<sub>4-n</sub>. The stability of the organotitanium compounds is attributed to the initial formation of a stable lithium-monophenyltitanium complex which apparently has no magnesium counterpart. The reduction of titanium to the titanous state is considered to parallel the decomposition of the R-Ti  $\sigma$ -bond. Herman and Nelson<sup>23</sup> also confirmed that, R-Ti compounds formed from 1:1 molar ratios of Grignard reagent to butyl titanate increase in stability in the following order: butyl < methyl < acetylenyl < p-anisyl < phenyl <  $\alpha$ -naphthyl < indenyl compounds, the increasing stability parallels the increasing electronegativity of the R groups as given by Kharasch.<sup>24</sup> The order of increasing stability is in general agreement with the published results on organogold<sup>25</sup> and organosilver<sup>26</sup> compounds. In a general way the stability is decreased with increasing electronegativity of the X group. However, additional information is required to fully substantiate this observation. A sufficiently

high electronegative field is required surrounding the titanium to stabilize it in the tetravalent state. The R groups in themselves are not sufficiently electronegative to supply this field and accordingly, a compound such as  $R_4Ti$  is unstable. Increasing electronegativity of the R group is paralleled by the increasing stability of the organometallic bond. Thus aryl compounds are more stable than alkyl compounds. A delicate balance of the electronegativity of the R and X group appears to be necessary in order to stabilize  $RTiX_3$ . It is suggested that although the electronegativity of an -OR group such as  $-OC_4H_9$  is necessary for the stabilization of the R-Ti bond, a second mechanism plays tending to weaken the bond when groups of greater electronegativity such as  $-OCH_3$ ,  $-Cl$  and  $-F$  are used. The strong electron attraction of three F atoms, for example, should cause a decrease of the screening effect of the three binding electron pairs. As a result, the electron pair forming the R-Ti  $\sigma$ -bond should move closer to the titanium, the net effect being to weaken the organotitanium bond. While the structure which contains more than one R group causes marked instability in a tetravalent titanium compound, there are indications that compounds of the type  $R_2Ti$  or  $R_3Ti$  are relatively stable.

Band gap of titania materials can be tuned by the insertion of different types of metals and/ or organic molecules.<sup>6, 7, 12, 16</sup> The reduction of the band gap of titanium is critically important to fully utilize its photocatalytic properties.<sup>6, 12</sup> The search for titania based materials with a smaller band gap, enabling absorption in the 400–900 (visible and near-IR) spectral range, is of prime importance for improving their efficiency.<sup>12</sup> One of the real examples recently published also by George S. et al.<sup>18</sup> They reduced band gap of  $TiO_2$  with aim to use it for a macrophage cell line evaluation of cytotoxic and ROS production, that showed increase oxidant injury and cell death in parallel with. Mentioned findings demonstrate the importance of band gap energy in the phototoxic response of the cell to  $TiO_2$  nanoparticles and reflect potential of this material to generate adverse effects in humans and the environment during high-intensity light exposure. A wide range of nanocomposites based on titania are used in photovoltaic applications. Santos J.-M. et al.<sup>27</sup> describe donor–acceptor composites based on the combination of a thiophene system and  $TiO_2$  anatase nanostructure. Thiophene systems absorb light in the visible region<sup>27, 28</sup>

and can attain high hole mobilities,<sup>27, 29, 30</sup> whereas TiO<sub>2</sub> nanoparticles or nanosystems – nanocomposites are a common choice for bulk heterojunction solar cells.<sup>27, 31-33</sup> It is a kind of hybrid combinations of organic–inorganic interfaces relevant for photovoltaic applications.<sup>27</sup> Compounds containing thiophene are in high interest due to their possibility to make electron-transport layers and/or blue light emitters. They possess relatively low LUMO energy levels while maintaining high HOMO-LUMO gaps. In recent years, the use of organic semiconducting materials for applications in “plastic electronics”, such as field effect transistors (FETs), organic light emitting diodes (OLEDs), and photovoltaics (PVs), has gained increasing interest.<sup>34, 35</sup> Organic and/ or hybrid systems offer the possibility for cheap raw materials and processing costs and are readily tailored to access a wide range of physical, optical, and electrical properties in the final device.<sup>34, 36-38</sup>

*In this chapter, we would like to present completely new class of nanostructured organotitania materials with narrower band gap compare to the inorganic titania. We have successfully designed new hybrid organotitania nanomaterials namely 1,4-bis-triethoxytitanyl benzene and 2,5-bis-triethoxytitanyl thiophene which have exceptional properties beyond classical TiO<sub>2</sub> broadening application possibility of titanium based materials in different fields. In particular, photocatalytic activity will be discussed.*

## **7.2 Synthesis and characterization**

### *7.2.1 Ti-Ben*

The synthesis of 1,4-bis-triethoxytitanyl benzene is shown as following (Fig. 7.1). The synthesis was done by exchange the iodide from 1,4-diiodobenzene with lithium by lithiation reaction.<sup>39</sup> The 1,4-dilithiobenzene thus obtained was subsequently used for the reaction with Ti(OEt)<sub>4</sub> to get our final organotitania precursor 1,4-bis-triethoxytitanyl benzene.<sup>40</sup> Detailed synthetic procedure can be found in the experimental section. By exposure with air, the water from the air could hydrolyse the –OEt group, and a hybrid titania framework with both Ti-O-Ti and Ti-Benzene-Ti (Ti-Ben) can be obtained.

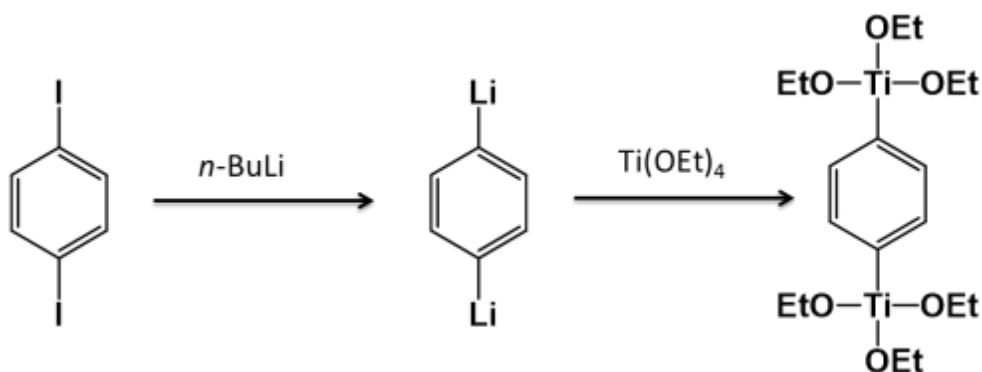


**Fig. 7.1** Scheme of the 1,4-bis-triethoxytitanyl benzene synthesis.

For our organotitania material, the critical characterization is the Ti-C bond. X-ray Photoelectron Spectroscopy (XPS) was used to see if we obtained the Ti-C bond. Since we are analysing carbon, 1,4-bis-triethoxytitanyl benzene was transferred in sealed bottle from the synthetic glove box to the glove box mounted with XPS in order to avoid the adventitious carbon from air.<sup>41</sup> From the titanium point of view, several very early literature at 1980s suggested that for the pure  $\text{TiO}_2$ , the Ti  $2p_{3/2}$  peak located around 458.5 eV, if we use the  $\text{sp}^3 \text{C } 1s$  peak reference at 284.8eV.<sup>42,43</sup> If we change Ti-O to Ti-C, compare to oxygen, carbon has less electronegativity which means the binding energy of electrons from titanium in Ti-C would be lower than Ti-O. Here we found out exactly that the binding energy of Ti  $2p_{3/2}$  electrons was lower than 458.5 eV (Fig. 7.2 left), which indicates the existence of Ti-C bond. From the carbon point of view, by analysing the C 1s spectra, we can see the composition of different carbon bonds. In our 1,4-bis-triethoxytitanyl benzene sample, four different types of carbon bond can be identified from the C 1s spectra, which are the aromatic C-C (2) in the benzene ring, aromatic Ti-C, aliphatic C-O and aliphatic C-C in the  $-\text{OEt}$  group (Fig. 7.2 right). The composition can be found in Table 7.1. For pure 1,4-bis-triethoxytitanyl benzene, the ratio between aromatic Ti-C and C-O should be 1:3 but what we obtained is around 1:5, which means that the obtain material is a mixture of 1,4-bis-triethoxytitanyl benzene and  $\text{Ti}(\text{OEt})_4$ .

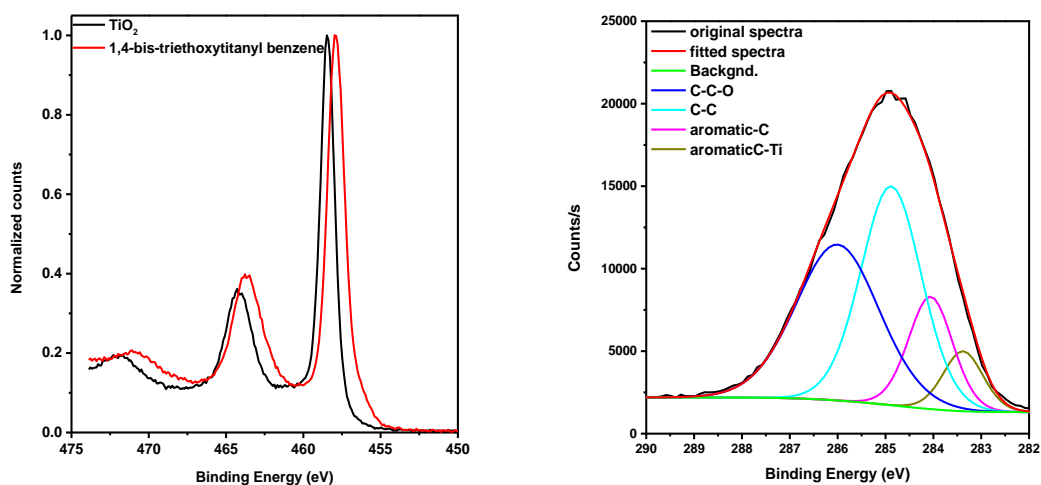
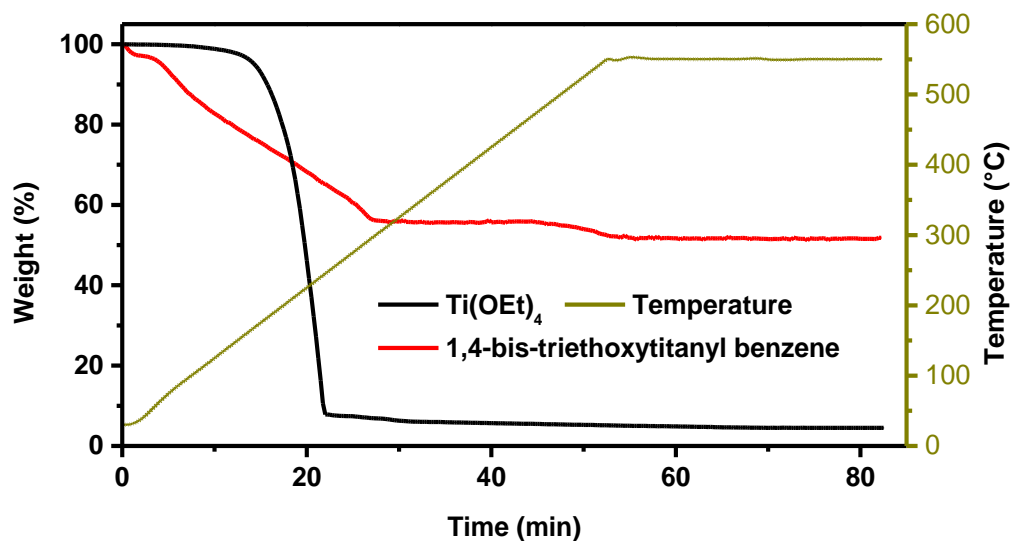


**Fig. 7.2** Comparison of XPS spectra of Ti 2p scan between inorganic  $\text{TiO}_2$  and 1,4-bis-triethoxytitanyl benzene (left); C 1s scan deconvolution of 1,4-bis-triethoxytitanyl benzene (right).

**Table 7.1** Composition of carbon species from 1,4-bis-triethoxytitanyl benzene.

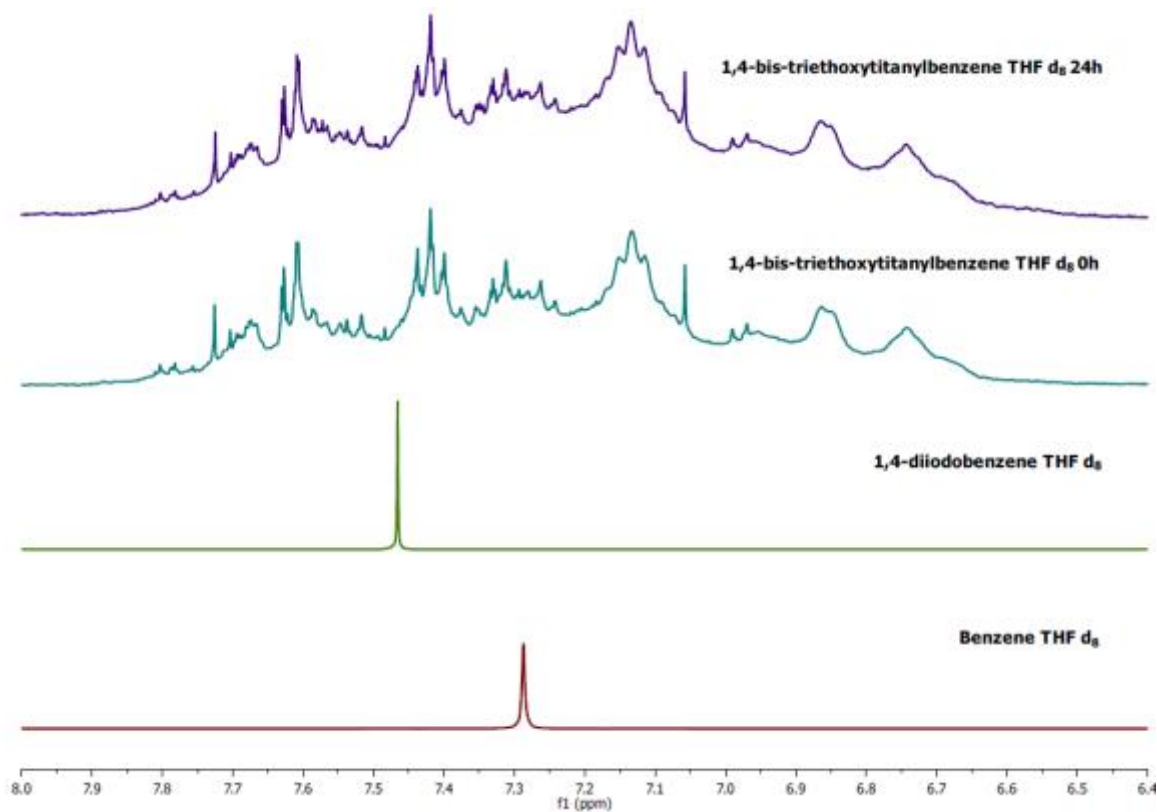
C 1s scan	Aromatic C-Ti	Aromatic C	C-C	C-C-O
Binding energy (eV)	283.38	284.06	284.88	286.00
Atomic ratio (%)	7.11	14.78	39.52	38.59

Fig. 7.3 shows the thermal analysis data of 1,4-bis-triethoxytitanyl benzene, with  $\text{Ti}(\text{OEt})_4$  as reference. From the curve of  $\text{Ti}(\text{OEt})_4$ , we can see that the organic part (-OEt group) of the material was fully decomposed before 300 °C. There was no weight loss observed in higher temperature which means that only pure titania remained. For 1,4-bis-triethoxytitanyl benzene, when the temperature is lower than 300 °C, we have observed the degradation of aliphatic carbon groups (-OEt). Between 450 °C and 550 °C, another decomposition step was observed, which indicates the presence of Ti-C bond. Afterwards, no weight loss was observed in the end of the procedure which indicates us the formation of pure  $\text{TiO}_2$ .



**Fig. 7.3** Comparison of TGA curves between  $\text{Ti}(\text{OEt})_4$  and 1,4-bis-triethoxytitanyl benzene.

As proved by XPS, our 1,4-bis-triethoxytitanyl benzene was not pure, nuclear magnetic resonance spectroscopy (NMR) and mass spectrometry (MS) have been done as supporting information for our material characterization. From the aromatic region of NMR spectra, the peaks are really complicated, but we can see that the signal was shifted and different than both benzene and 1,4-diiodobenzene which indicates the formation of aromatic Ti-C (Fig. 7.4). The spectra for 1,4-bis-triethoxytitanyl benzene didn't change after 24 hours in THF which indicates that it's stable in THF. In Fig. 7.5, the mass signals at  $m/z$  443.3 and  $m/z$  480.9 correspond to  $[\text{1,4-bis-triethoxytitanyl benzene H}]^+$  and  $[\text{1,4-bis-triethoxytitanyl benzene K}]^+$ , respectively. For direct analysis of 1,4-bis-triethoxytitanyl benzene spray ambient ionization mass technique was performed with 50% acetonitrile as ionizing solvent. The results clearly show the molecule of 1,4-bis-triethoxytitanyl benzene divided into many clusters, containing at least two different types of cations ( $\text{H}^+$  and  $\text{K}^+$ ).



**Fig. 7.4**  $^1\text{H}$  NMR spectra comparison in the aromatic region from Ti-Ben synthesis.

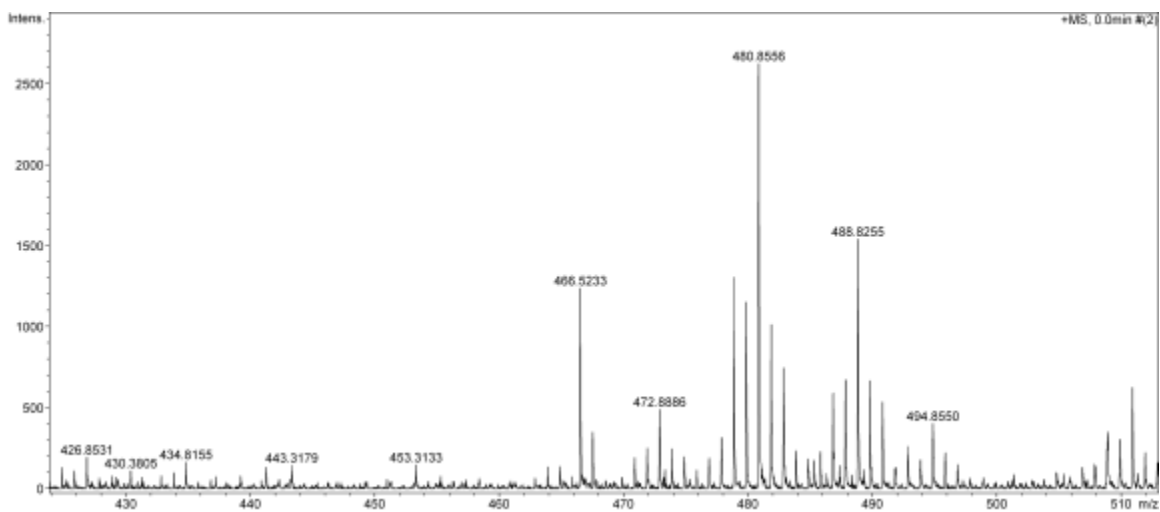


**Fig. 7.5** ESI-MS spectrum of 1,4-bis-triethoxytitanyl benzene created in positive-ion mode.

After dispersion in water with sonication, the –OEt groups from 1,4-bis-triethoxytitanyl benzene were hydrolyzed and a network of TiO<sub>2</sub> and Ti-Benzene organic linker was then formed. This material has been named as Ti-Ben. To make sure that the Ti-C bond is still there after water treatment, XPS was carried out again. From the Ti 2p scan it is shown that the binding energy is still lower than TiO<sub>2</sub> (Fig. 7.6). This gives the proof that there are still Ti-C bonds in Ti-Ben. C 1s scan analysis was not performed because of the adventitious carbon contamination from air exposure which has both C-C and C-O bonds.<sup>41</sup>

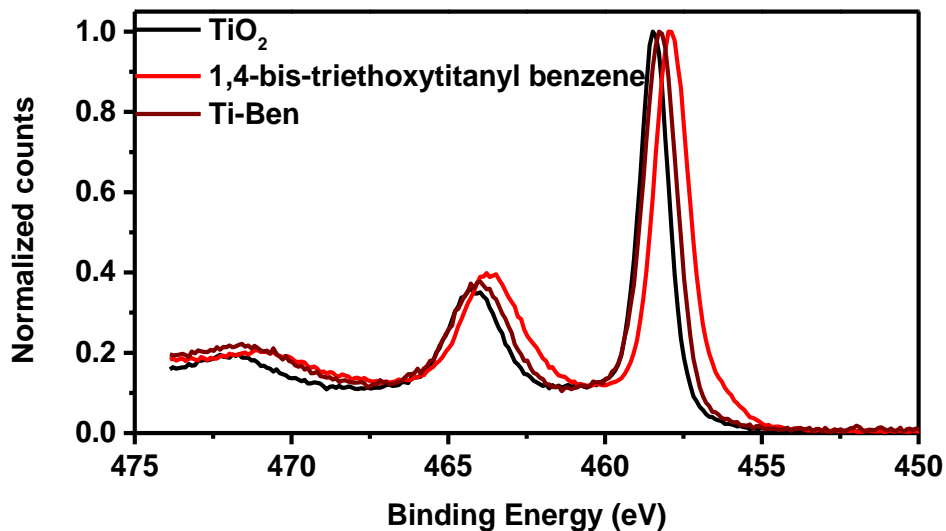


**Fig. 7.6** XPS Ti 2p spectra of TiO<sub>2</sub>, 1,4-bis-triethoxytitanyl benzene and Ti-Ben.

From SEM image (Fig. 7.7), we can see a mixed crystal system which is not well defined. This also suggested presence of our organic linker.



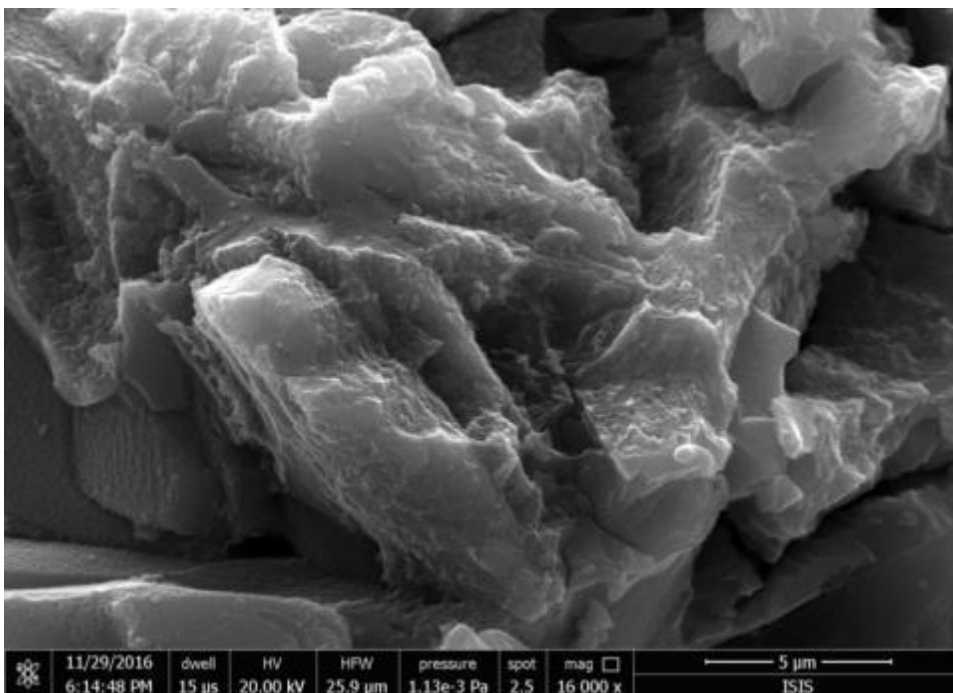


**Fig. 7.7** SEM image of Ti-Ben.

### 7.2.2 Ti-Thio

Synthesis of the 2,5-bis-triethoxytitanyl thiophene can be found from Fig. 7.8. It is similar with the synthesis of 1,4-bis-triethoxytitanyl benzene. Firstly, 2,5-dilithiothiophene was obtained by lithiation of thiophene.<sup>44</sup> Then lithium have been exchanged with titanium from  $\text{Ti}(\text{OEt})_4$ . Detailed procedure can be found in the experimental section. Similarly, a hybrid titania framework with both Ti-O-Ti and Ti-Thiophene-Ti (Ti-Thio) can be obtained by air exposure.

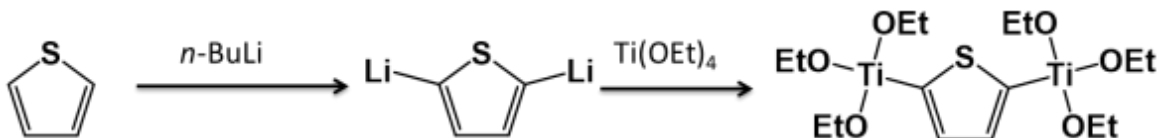


**Fig. 7.8** Scheme of the 2,5-bis-triethoxytitanyl thiophene synthesis.

XPS has been use for Ti-C bond characterization. From the titanium point of view, we have found out that the binding energy of Ti  $2p_{3/2}$  electrons was lower than 458.5 eV (Fig. 7.9 left), which indicates the existence of Ti-C bond. From the carbon point of view, we

analysed the C 1s spectra of 2,5-bis-triethoxytitanyl thiophene sample. Four different types of carbon bond were identified from the C 1s spectra, which are the aromatic C-C in the thiophene ring, aromatic Ti-C, aliphatic C-O and aliphatic C-C in the -OEt group (Fig. 7.9 right). The composition can be found in Table 7.2. For pure 2,5-bis-triethoxytitanyl thiophene, the ratio between aromatic Ti-C and C-O should be 1:3 but what we obtained was around 1:6, which means that the obtained material is a mixture of 2,5-bis-triethoxytitanyl thiophene and  $\text{Ti}(\text{OEt})_4$ .

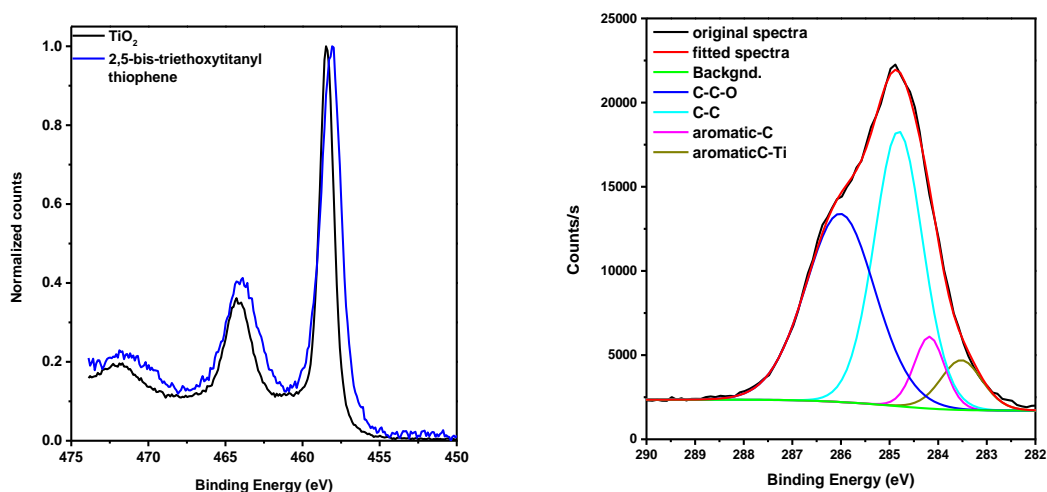


**Fig. 7.9** Comparison of XPS spectra of Ti 2p scan between inorganic  $\text{TiO}_2$  and 2,5-bis-triethoxytitanyl thiophene (left); C 1s scan deconvolution of 2,5-bis-triethoxytitanyl thiophene (right).

**Table 7.2** Composition of carbon species from 2,5-bis-triethoxytitanyl thiophene.

C1s scan	Aromatic C-Ti	Aromatic C	C-C	C-C-O
Binding energy (eV)	283.52	284.18	284.81	286.01
Atomic ratio (%)	6.71	7.16	43.41	42.73

Fig. 7.10 shows the thermal analysis data of 2,5-bis-triethoxytitanyl thiophene, with  $\text{Ti}(\text{OEt})_4$  as reference. As we discussed before, the -OEt group from  $\text{Ti}(\text{OEt})_4$  was fully decomposed before 300 °C. As for our 2,5-bis-triethoxytitanyl thiophene, we have found the aliphatic carbon groups (-OEt) also decomposed before 300 °C. Between 450 °C and 500 °C, similarly with 1,4-bis-triethoxytitanyl benzene, another decomposition step was

found, which indicates the Ti-C bond. No weight loss was observed in the end of the procedure. This indicates us the formation of pure TiO<sub>2</sub> after 500 °C.

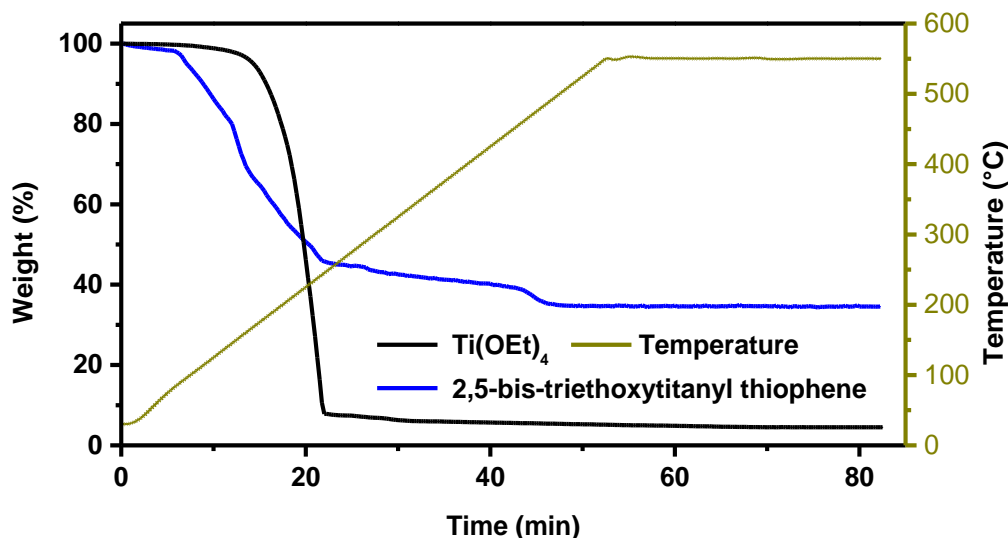


**Fig. 7.10** Comparison of TGA curves between Ti(OEt)<sub>4</sub> and 2,5-bis-triethoxytitanyl thiophene.

As proved by XPS, our 2,5-bis-triethoxytitanyl thiophene was not pure, nuclear magnetic resonance spectroscopy (NMR) and mass spectrometry (MS) have been done as supporting information for our material characterization. From the <sup>1</sup>H NMR spectra (Fig. 7.11), the 2,5-bis-triethoxytitanyl thiophene sample has a very weak original thiophene signal. There are significant changes in the <sup>1</sup>H NMR spectra before and after 24h in THF<sub>d</sub><sub>8</sub> in nitrogen environment. Sample of 2,5-bis-triethoxytitanyl thiophene (two dark-blue spectra) has peaks in the region between 6.80-7.05 ppm. Difference between the as made and 24 h THF aged spectra indicates us reversibility of the reaction in the solution in time. In case of 2,5-bis-triethoxytitanyl thiophene, the situation was more difficult (Fig. 7.12). In many cases, we got spectra of partly polymerized samples. The targeted molecule was not clearly observed in this case.

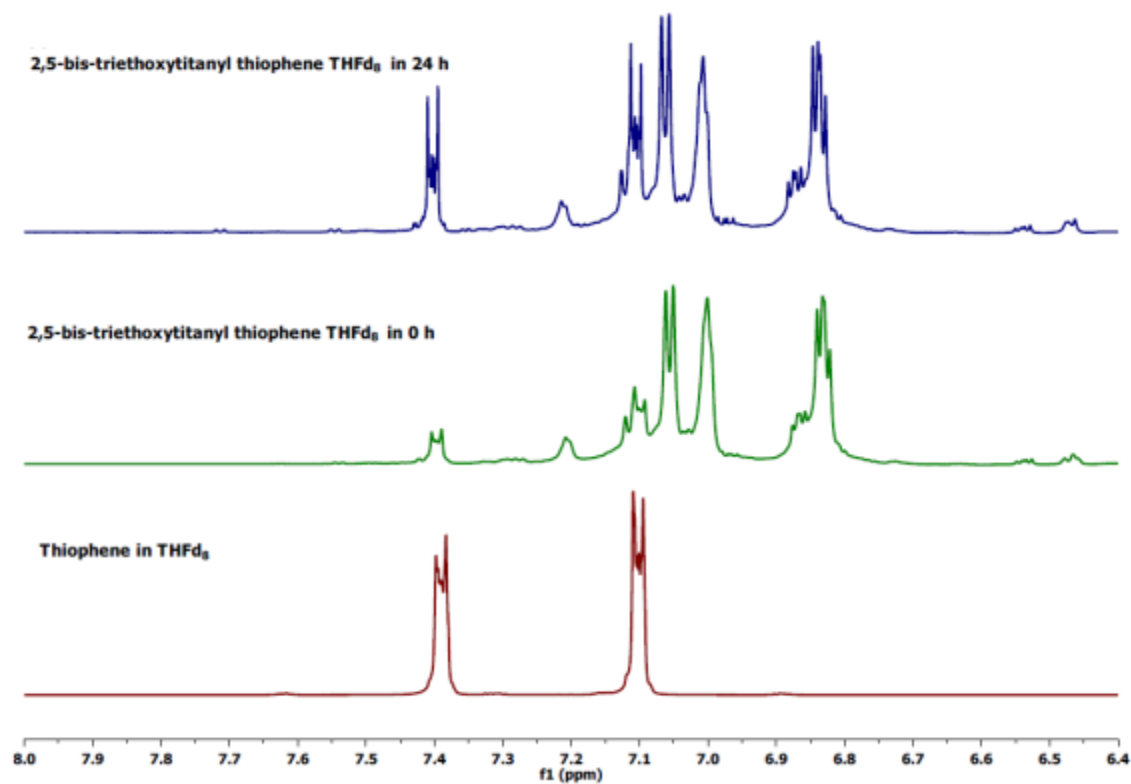


**Fig. 7.11**  $^1\text{H}$  NMR spectra comparison in the aromatic region from Ti-Thio synthesis.

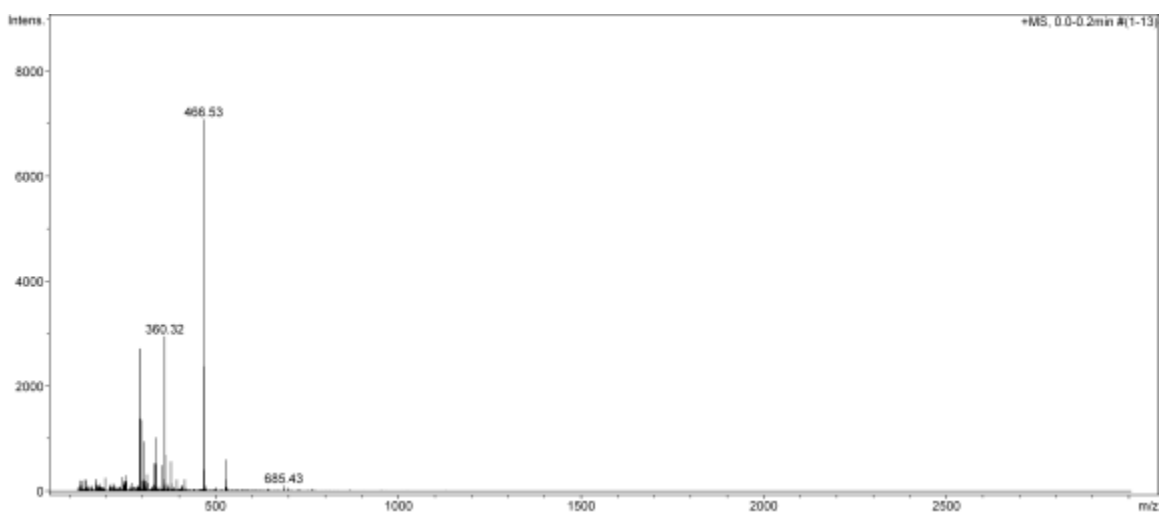


**Fig. 7.12** ESI-MS spectrum of 2,5-bis-triethoxytitanyl thiophene measured in positive-ion mode.

A network of  $\text{TiO}_2$  and Ti-Thiophene organic linker was formed similarly as Ti-Ben. This material has been named as Ti-Thio. To make sure that the Ti-C bond is still there after

water treatment, XPS is carried out again. From the Ti 2p scan we see that the binding energy didn't change between 2.5-bis-triethoxytitanyl thiophene and Ti-Thio (Fig. 7.13). This gives the proof that there were still Ti-C bonds in Ti-Thio. C 1s scan analysis was not performed because of the adventitious carbon contamination from air exposure which contains both C-C and C-O bonds.<sup>41</sup>

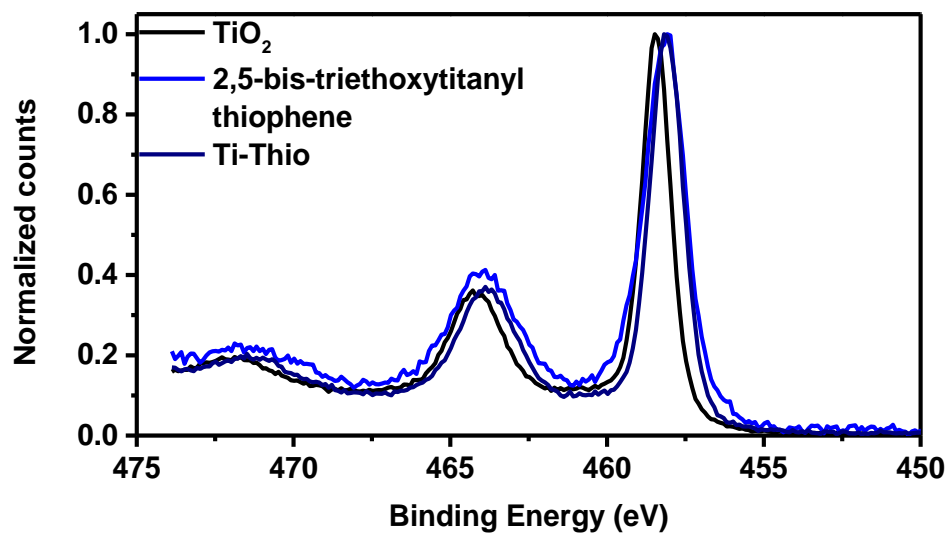


Fig. 7.13 XPS Ti 2p spectra of TiO<sub>2</sub>, 2.5-bis-triethoxytitanyl thiophene and Ti-Thio.

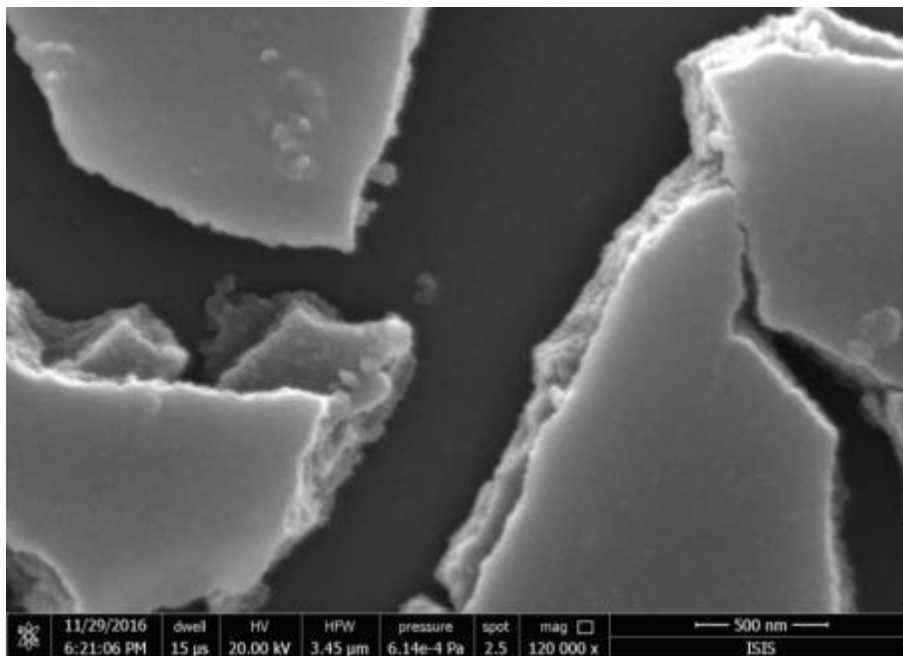


Fig. 7.14 SEM image of Ti-Thio.

From SEM image (Fig. 7.14), we can see a smooth structure resembling cracked nanolayer which indicated that this material is more hydrophilic. Well defined crystal structure was not seen. This could be also a proof of the presence organic linker in the structure.

## 7.3 Photocatalysis

### 7.3.1 Photophysics properties

The term “band gap” refers to the energy difference between the top of the valence band to the bottom of the conduction band; electrons are able to jump from one band to another. In order for an electron to jump from a valence band to a conduction band, it requires a specific minimum amount of energy for the transition, which is called the band gap energy<sup>45</sup>. Measurement of the band gap is important in the semiconductor and nanomaterial industries. The UV-Vis spectra of different TiO<sub>2</sub> and organotitania compounds are shown in Fig. 7.15. According to UV-Vis measurement, all our organotitania powders have significantly higher photo activity in region 400 - 600 nm due to the Ti-C bonds of organic linkers (benzene and thiophene) into the titania framework. The organotitania samples were compared with two types of inorganic TiO<sub>2</sub> material: 100 nm particles which are commercially available from Sigma-Aldrich and the 400 nm mesoporous titania particles, which we produced and are described in chapter 2. From the UV-Vis spectra we can see that the inorganic titania material didn't show photo activity in the region of visible light. On the other hand, our organotitania samples have absorption in the visible light region. To determine the band gap, the UV-Vis spectra have been transformed into Tauc plot (Fig. 7.15 right).<sup>46</sup> We can see that the inorganic titania particles from Sigma-Aldrich and our inorganic mesoporous titania show similar band gap energy (2.96 and 3.03 eV respectively). The band gap energies of our organotitania materials are significantly reduced compare to inorganic titania. The band gap of the direct transition was observed at 2.43 eV for Ti-Ben and 2.05 eV for Ti-Thio, which give them significantly enhanced reactivity under the visible light region than the inorganic titania material.

All our titania VB XPS spectra (Fig. 7.16) which can be used for determine the highest occupied molecular orbital (HOMO) show the edge of the maximum energy at about 2.5 eV, similar to that found for other titania materials.<sup>12</sup> The titania from Sigma-Aldrich show the energy around 1 eV which is comparable with other doped titania materials.<sup>47</sup>

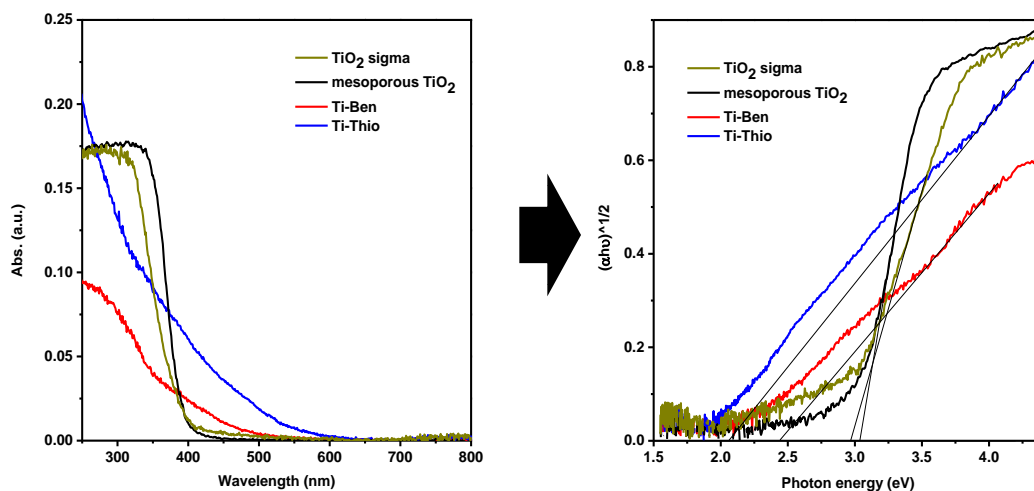


**Fig. 7.15** Solid state UV-Vis spectra of different titania materials (left); band gap energy is determined by Tauc plot transferred from the UV-Vis spectrum (right).

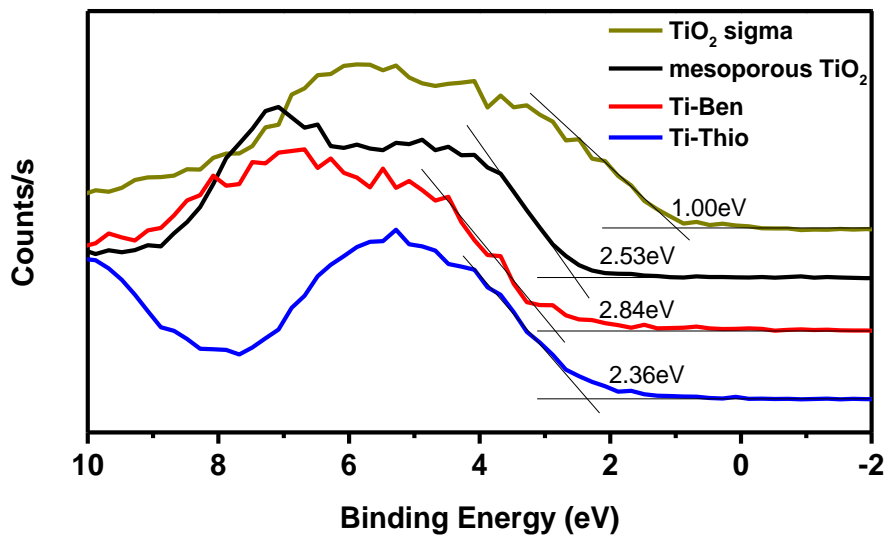


**Fig. 7.16** Valence band XPS spectra of different titania materials.

Confocal microscopy was used to see the real colour and emission spectra of our organotitania compounds (Fig. 7.17). Ti-Ben showed blue emission and Ti-Thio showed more greenish emission. The co-localization of the emitted light and the sample indicated that the emission was coming from the sample.

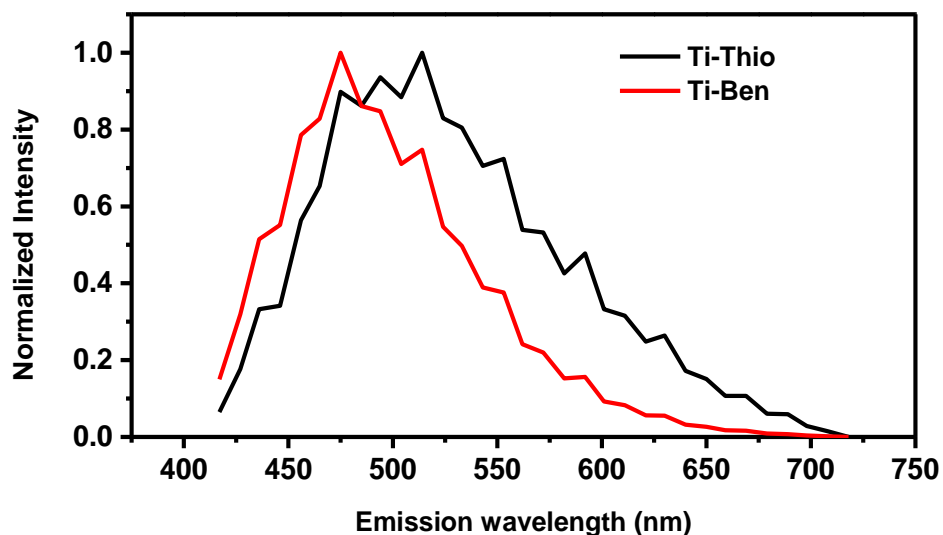
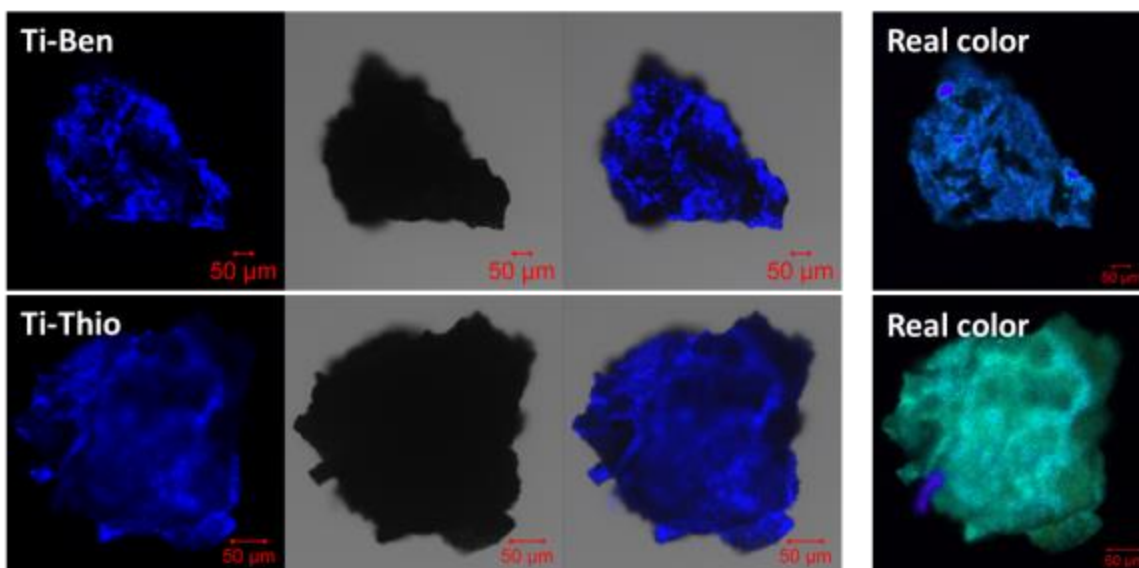


**Fig. 7.17** Confocal microscope image of Ti-Ben and Ti-Thio powder (up); emission spectra (350 nm excitation) of Ti-Ben and Ti-Thio (down).



### 7.3.2 Photocatalysis under UV

Photocatalytic activity of the materials was evaluated by photocatalytic degradation of Rhodamine B molecules in aqueous solution under an Olympus high pressure mercury lamp (100 W). For a typical test, the mixed solution contains  $10^{-5}$  M concentration of Rhodamine B and 0.15 g/L of material. The mixed solution was stirred in the dark for 3 hours to reach the adsorption/desorption equilibrium of the dye and the material. After the process was finished, the final solution was centrifuged to remove the material. The concentration of the remaining dye was determined via UV-Vis spectroscopy by using the obtained supernatant. To investigate the relationship between the concentration of Rhodamine B and its highest absorption peak height (at 554 nm), several dye solutions with different concentrations were measured by UV-Vis spectroscopy. A linear curve was then fitted to the measured data (Fig. 7.18). With this curve, we can calculate the concentration of the dye by knowing the absorption peak height at 554 nm.

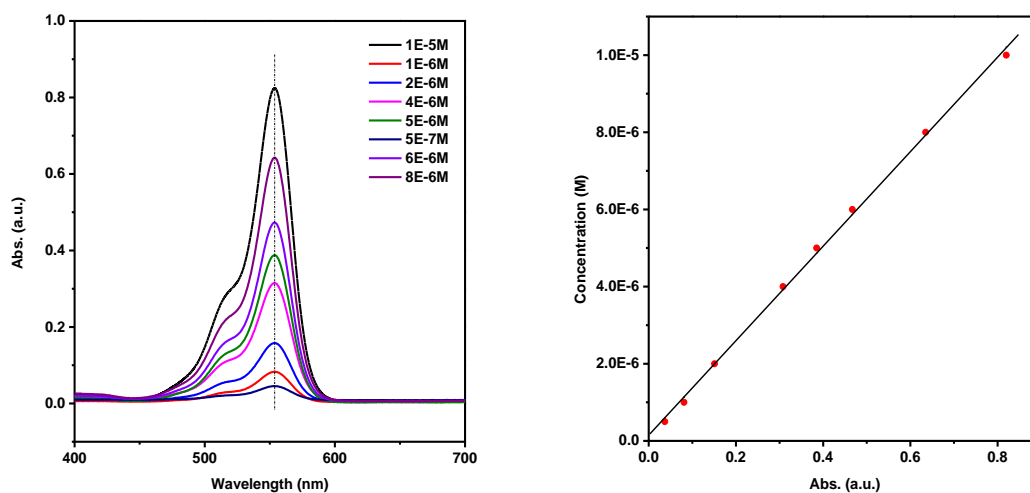


**Fig. 7.18** UV-Vis spectra of Rhodamine B solution with different concentrations (left). Linear fitting curve shows the relationship between the concentration and the absorption peak height at 554 nm (right).

The change of concentration of Rhodamine B with the photocatalyst under UV exposure is shown in Fig. 7.19. The photodegradation process of Rhodamine B was well

investigated by literature, and the pseudo-first-order reaction rate should be applied for the process.<sup>48</sup> The photocatalytic constant  $k'$  was thus calculated by linear fitting of  $\ln(c_0/c)$  versus time (Fig. 7.19 right). Table 7.3 shows the photocatalytic constant of each material calculated from the fitted curves. Surprisingly, the  $\text{TiO}_2$  from Sigma-Aldrich showed very low photocatalytic performance. The reason was unclear but we suppose that it was because of the doped manganese. Due to its porosity and large surface area, the mesoporous titania showed the best performance as expected, which is more than 30 times faster compare to the  $\text{TiO}_2$  from Sigma-Aldrich. Our Ti-Ben showed reasonable performance which is about half of the mesoporous titania. Ti-Thio showed relatively low photocatalytic activity but still more than 3 times better compare to the commercial titania. As we discussed earlier, our titania materials are emissive under UV. The loss of energy by emission could be one of the reason that the organotitanias were less active than the mesoporous titania.

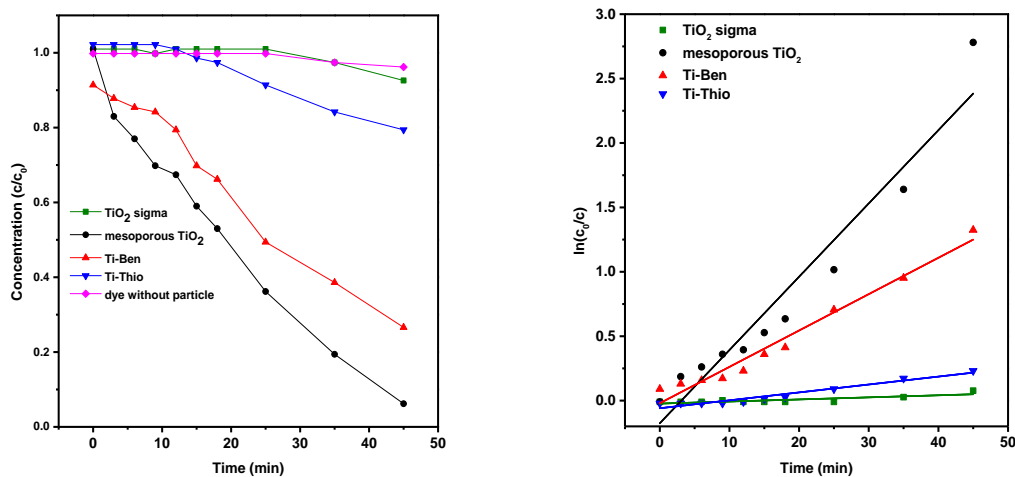


**Fig. 7.19** Photocatalytic reaction of titania materials under UV irradiation with the pure Rhodamine B solution as reference (left); fitted pseudophotocatalytic constant ( $k'$ ) of titania materials under UV (right).

**Table 7.3** Photocatalytic constant  $k'$  for different titania materials under UV.

Material	Band gap (eV)	UV photocatalytic constant $k'$ ( $\text{min}^{-1}$ )
TiO <sub>2</sub> sigma	2.96	0.0016
Mesoporous TiO <sub>2</sub>	3.03	0.0569
Ti-Ben	2.43	0.0282
Ti-Thio	2.05	0.0061

### 7.3.3 Photocatalysis under visible light

The photocatalysis under visible light was done similar with the experiments under UV. The same concentration of material and dye was used (0.15 g/L and  $10^{-5}$  M respectively). The suspension was also stirred in the dark for 3 hours. Same light source of the Olympus high pressure mercury lamp was used but added with a 450 nm longpass optical filter to get rid of the UV. Fig. 7.20 shows the experimental data and the fitting of the photocatalytic constant  $k'$ . Table 7.4 show the calculated  $k'$  values. In this condition, our Ti-Ben showed good performance under visible light which is two times faster than the mesoporous titania. Ti-Thio was not really comparable with the other two even though it has the lowest band gap. The reason is discussed later with the UV spectra. Nevertheless, with the reduction of the band gap from Ti-C, our Ti-Ben showed better photocatalytic performance than inorganic titania under visible light exposure.

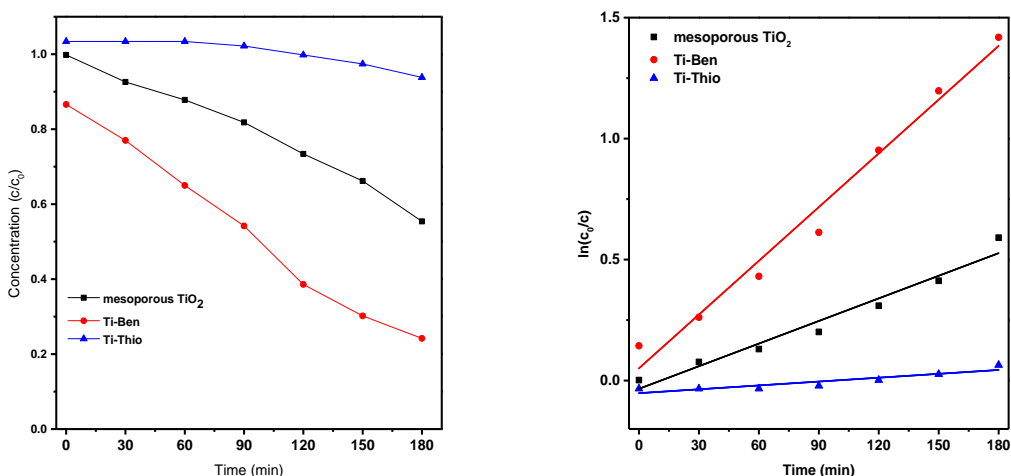


**Fig. 7.20** Photocatalytic reaction of titania materials under visible light irradiation (left); fitted pseudophotocatalytic constant ( $k'$ ) of titania materials under visible light (right).

**Table 7.4** Photocatalytic constant  $k'$  for different titania materials under Visible light.

Material	Band gap (eV)	Visible light photocatalytic constant $k'$ ( $\text{min}^{-1}$ )
Mesoporous $\text{TiO}_2$	3.03	0.0031
Ti-Ben	2.43	0.0074
Ti-Thio	2.05	0.0005

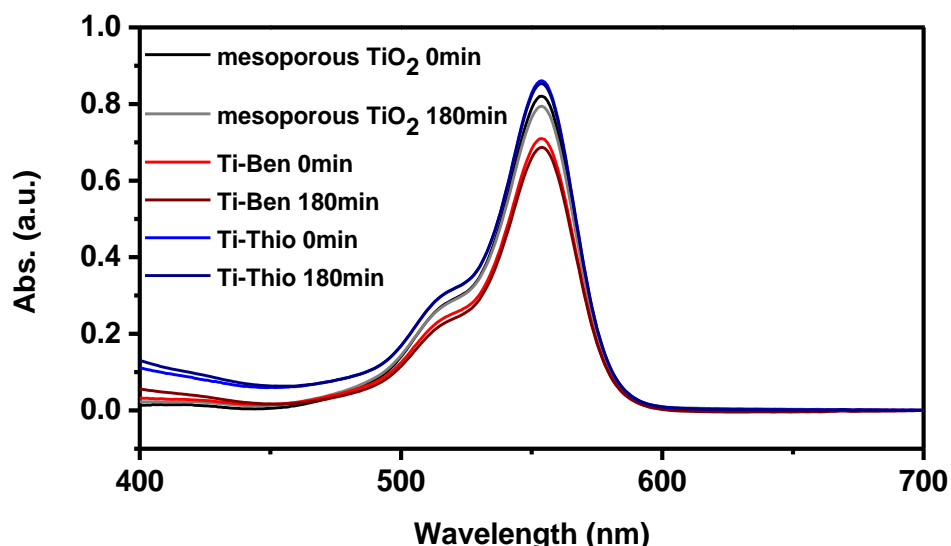


**Fig. 7.21** Reference UV-Vis absorption spectra of the mixed dye and photocatalysts solution stirred in the dark before and after the photocatalytic reaction.

To prove that the dye was degraded because of the photocatalyst but not the adsorption, a reference experiment was carried out. While the photo degradation was going on, a part of the starting solution which contained the material and the dye was continued stirring in the dark until the end of the whole process (180 min). As we can see from Fig. 7.21, the dye concentration from the final solution shows no significant difference compare to the starting solution. This indicates that the dye was degraded by our photocatalysts, not escaped from the solution by physical adsorption.

#### 7.3.4 Discussion of photocatalysis reaction

The final product of dye degradation during the photocatalysis was investigated by many researchers.<sup>48-50</sup> In general, the complete disappearance of the adsorption peak means the full degradation of the dye.<sup>12</sup> The detailed UV-Vis spectra of each photodegradation

process are shown in Fig. 7.22. For mesoporous titania, due to its large surface area and strong photocatalytic property, the Rhodamine B molecule is considered to be fully degraded into small molecules under UV irradiation (Fig. 7.22a). While under visible light irradiation, we can see a blue shift of the peak. Several literatures suggested that this is due to the photodegradation from Rhodamine B to Rhodamine which has the absorption peak at 499 nm.<sup>48, 51</sup> Same but more obvious phenomenon has been observed from Ti-Ben both under UV and visible light exposure (Fig. 7.22b). This means that the photodegradation process done by Ti-Ben was not all the way to small molecules. And finally for Ti-Thio, we have observed a decrease of the absorption band between 400 nm and 450 nm (Fig. 7.22c). If we re-look at the solid state UV-Vis spectra (Fig. 7.15), this band clearly belongs to Ti-Thio itself. We suggest that, the Ti-Thio was not stable at all under light irradiation, it decomposes itself. It also explained why we have observed poor photocatalytic ability in case of Ti-Thio.

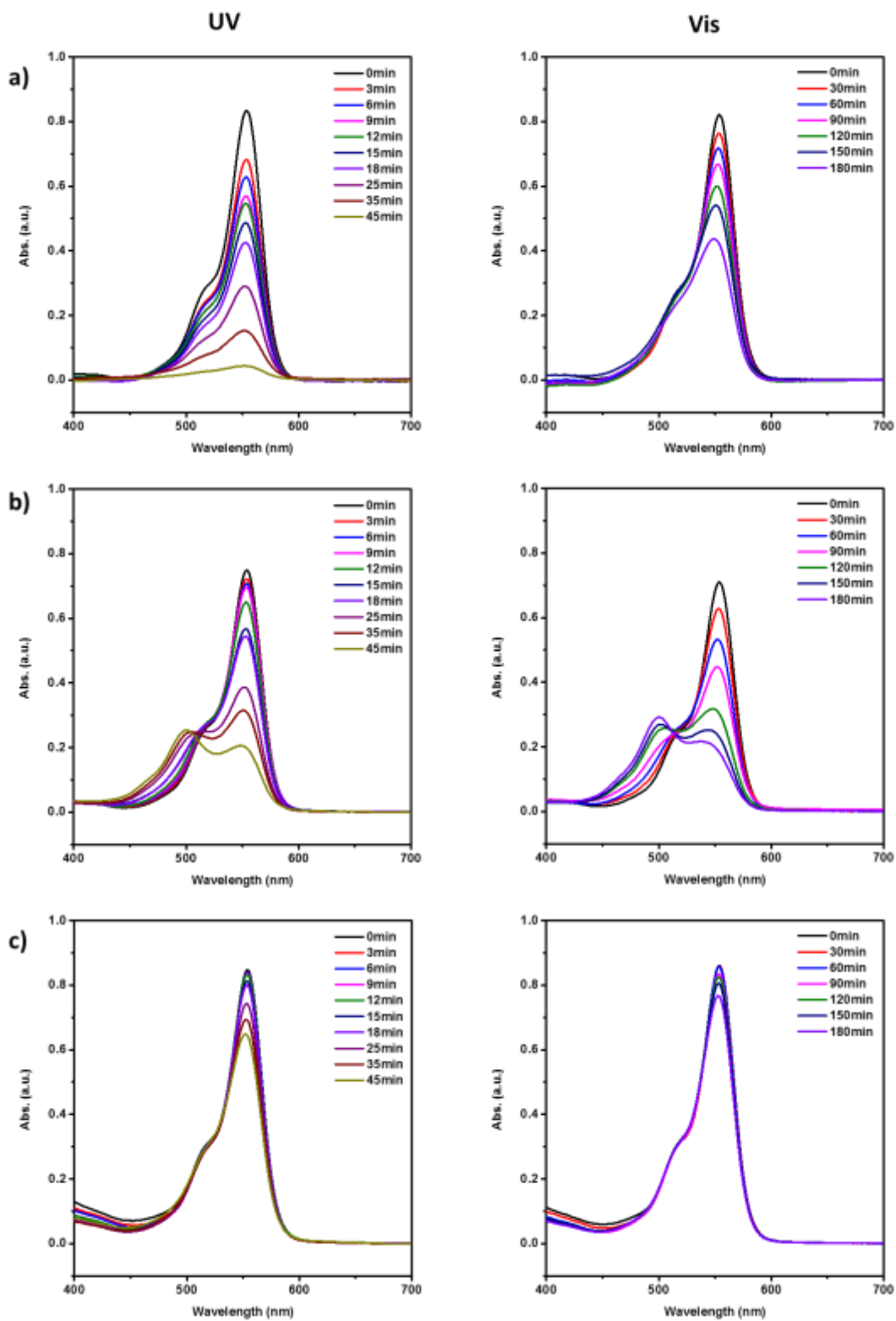


**Fig. 7.22** UV-Vis spectra of rhodamine B aqueous solution in presence of a) mesoporous TiO<sub>2</sub> b) Ti-Ben and c) Ti-Thio under UV (left) and visible light (right).

## 7.4 Conclusion and perspectives

Herein we report the synthesis of two new types of organotitania material: 1,4-bis-triethoxytitanyl benzene and 2,5-bis-triethoxytitanyl thiophene. In both cases we observed the reduction of the band gap compare to inorganic titania. Photocatalysis of the materials were tested both under UV and visible light. Under UV, our inorganic mesoporous titania showed the better photocatalytic ability compare to our organotitania and commercially available titania nanoparticles from Sigma-Aldrich. Under visible light, our Ti-Ben performed the better than our inorganic mesoporous titania. The fact is that, our organotitania, which has high reactivity under visible light, would bring promising applications compare to the traditional inorganic titania.

## 7.5 Experimental section

### *Materials*

*n*-Butyllithium – *n*-BuLi, (Sigma-Aldrich, 1.6 M solution in hexane), diethylether - Et<sub>2</sub>O (Sigma-Aldrich, 1 ppm BHT as inhibitor, anhydrous, ≥99.7%), 1,4-diodobenzene (ABCR, 98%), *n*-hexane (Roth, 99,99%, <30ppm of H<sub>2</sub>O), titanium(IV) ethoxide – Ti(OEt)<sub>4</sub> (Sigma-Aldrich, >97%), cyclohexane (Sigma-Aldrich, anhydrous, 99.5%), dibutylether (Sigma-Aldrich, anhydrous, 99.3%), toluene (Sigma-Aldrich, anhydrous, 99.8%), tetrahydrofuran - THF (Sigma-Aldrich, anhydrous, ≥99.9%), 2,5-dibromothiophene (Sigma-Aldrich, 95%), thiophene (Sigma-Aldrich, ≥ 99%), pentane (Sigma-Aldrich, anhydrous, ≥99%), 1,2-dichloroethane (Sigma-Aldrich, anhydrous, ≥99.8%), Petroleum ether (Sigma-Aldrich, anhydrous), 1,4-dioxane (Sigma-Aldrich, anhydrous, ≥99,8%). All the products above were used as bought without any purification.

Titania nanoparticle (Sigma-Aldrich, Mn doped, 100 nm size) was calcined at 350 °C for 3 hours to remove the organic residuals.

### *Synthesis of 1,4-bis-triethoxytitanyl benzene*

*n*-BuLi 1.6 M solution in *n*-hexane (10 ml, 16 mmol) was added in one portion into the Schlenk flask (100 ml) filled with Ar (5.0 purity). The hexane from *n*-BuLi was evaporated through vacuum, thus the yellow, oily *n*-BuLi was obtained at r.t. Then Et<sub>2</sub>O (12 ml, 115.4 mmol) was added to *n*-BuLi. The solution was cooled in acetone bath to -20 °C. 1,4-diodobenzene (2.66 g, 8 mmol) was evacuated for 20 min in the second Schlenk flask, then refilled with Ar. 1,4-diodobenzene was added in one portion into the cooled reaction kept under Ar,. The reaction was stirred for 1h/ 450 rpm at -20 °C. After the cool bath was removed, precipitation of 1,4-dilithiobenzene has immediately started. ½ Et<sub>2</sub>O was evaporated through vacuum and hexane (2x 20 ml, 304 mmol) was added into the mixture kept under the Ar. The second part of Schlenk apparatus with frita S4 filled with Ar, was quickly connected to the Schlenk flask, the apparatus was turned over, 1,4-dilithiobenzene was collected on the frita, then was washed carefully with hexane (3 x 6 ml, 136.7 mmol) and dried overnight in the vacuum<sup>39</sup>. 1,4-dilithiobenzene (10 mg,



110  $\mu\text{mol}$ ) was dissolved in the mixture of cyclohexane and diethylether with a 7:3 ratio (3.5 mL and 1.5 mL) stirred at 300 rpm for 24 h in glove box, filtrated and subsequently dropped into  $\text{Ti}(\text{OEt})_4$  (0.17 mL, 230  $\mu\text{mol}$ ). The reaction was stirred for additional 24h/300 rpm in the glove box at r. t., yellow solution was obtained. Glass substrates were dipped into the solution, left there 30 s and removed, carefully dipped into the same solvents as were used in the reaction, and washed 1x. Rest of the solution was recrystallized. Yellow crystals were formed in the vacuum in the pre-cooled flask, when 2/3 of the solvents were evaporated. Yellow crystals were dried in the vacuum and stored in glove box for further use.

#### *Synthesis of 2,5-bis-triethoxytitanyl thiophene*

Thiophene (0.4 ml, 5 mmol) was added into the round bottom flask (50 ml) placed in the glove box, subsequently diethylether (10 ml, 96.2 mmol) was added. The mixture was stirred at 450 rpm/30 min/18 °C. *n*-BuLi 1.6M solution in hexane (0.9 ml, 9.54 mmol) was dropped into reaction mixture at r.t., the colour has immediately changed into yellow. Lithiated thiophene was subsequently dropped within 5 minutes into the 2M solution of  $\text{Ti}(\text{OEt})_4$  in hexane, (0.2 ml solution of  $\text{Ti}(\text{OEt})_4$  with diethylether (4 ml, 38.5 mmol)/ 450 rpm. Whole reaction mixture was covered with aluminium foil and reacted for 2 h, the colour has changed into yellow-green. Recrystallization was done from anhydrous Petroleum ether (5 ml). Petroleum ether was added under Ar 5.0, when the 2/3 of diethylether was evaporated through vacuum. Yellow crystals were dried overnight in the vacuum and stored in the glove box.

#### *X-ray photoelectron spectroscopy*

All the X-ray Photoelectron Spectroscopic (XPS) measurements were done by a Thermo Scientific K-Alpha X-ray Photoelectron Spectrometer using a monochromatic  $\text{AlK}\alpha$  radiation ( $h\nu = 1486.6$  eV). Survey measurements were performed with 200 eV analyser pass energy and a 1 eV energy step size to calculate the atomic concentrations. Element scans were performed with 50 eV analyser pass energy and a 0.1 eV energy step size to obtain the chemical state information. Valence band spectra were performed with 50 eV

analyser pass energy and 0.2 eV step size. X-ray beam size was 400  $\mu\text{m}$ . All the obtained binding energies were referenced to  $\text{sp}^3$  carbon 1s peak at 284.8 eV.

#### *Nuclear magnetic resonance spectroscopy*

$^1\text{H}$  Nuclear Magnetic Resonance (NMR) spectra were acquired on a Bruker Avance 400 spectrometer, the NMR chemical shifts were given in ppm, using the residual proton of the solvent as internal standard (2.31 ppm for tetrahydrofuran  $\text{d}_8$ ).

#### *UV-Vis spectrum*

The UV-Vis absorption spectra were measured by Shimadzu UV-3600 UV-Vis-NIR spectrophotometer. The spectra of liquid samples were recorded at a 1 nm/s scan rate in a cuvette with a 1 cm path length. The solid samples were measured in solid state using integrating sphere and barium sulphate ( $\text{BaSO}_4$ ) was used as background.

#### *Thermogravimetric analysis*

Thermogravimetric (TG) measurements were performed on a TGA instrument NETZSCH STA 449 F3 Jupiter® – Simultaneous TGA-DSC. TGA scans were done with a heating rate of 10  $^\circ\text{C}/\text{min}$  and hold at 550  $^\circ\text{C}$  for 30 min under a synthetic air purge gas flow of 20 mL/min.

#### *Confocal microscopy*

Fluorescence images were acquired using Zeiss LSM 710 confocal microscope system with 63x magnification, numerical aperture 1.3 of Zeiss LCI Plan-NEOFLUAR water immersion objective lens (Zeiss GmbH). The samples were excited by a continuous wave (cw) laser operated at wavelength 405 nm and the emission of the system was collected widely in the range 412 nm to 735 nm. The emission spectra were acquired using lambda mode acquisition and the signal was reprocessed by Zen 2011 software (Zeiss GmbH).

#### *Mass spectrometry*

Experiments were performed on a Bruker Daltonics microTOF spectrometer (Bruker Daltonik GmbH, Bremen, Germany) equipped with an orthogonal electrospray (ESI)

interface. Calibration was performed using a solution of 10 mM sodium formiate. Sample solutions were introduced into the spectrometer source with a syringe pump (Harvard type 55 1111: Harvard Apparatus Inc., South Natick, MA, USA) with a flow rate of 5  $\mu\text{L}\cdot\text{min}^{-1}$ .

## 7.6 References

1. S. Livraghi, M. Rolando, S. Maurelli, M. Chiesa, M. C. Paganini and E. Giamello, *J. Phys. Chem. A*, 2014, **118**, 22141-22148.
2. A. Fujishima, T. N. Rao and D. A. Tryk, *J. Photochem. Photobiol. C.*, 2000, **1**, 1-21.
3. A. Fujishima and K. Honda, *Nature*, 1972, **238**, 37-38.
4. A. Hagfeldt and M. Graetzel, *Chem. Rev.*, 1995, **95**, 49-68.
5. M. Takeuchi, G. Martra, S. Coluccia and M. Anpo, *J. Phys. Chem. A*, 2007, **111**, 9811-9817.
6. T. Umebayashi, T. Yamaki, H. Itoh and K. Asai, *Appl. Phys. Lett.*, 2002, **81**, 454-456.
7. Z. Fei Yin, L. Wu, H. Gui Yang and Y. Hua Su, *PCCP*, 2013, **15**, 4844-4858.
8. J. Pascual, J. Camassel and H. Mathieu, *Phys. Rev. Lett.*, 1977, **39**, 1490-1493.
9. W. Choi, A. Termin and M. R. Hoffmann, *J. Phys. Chem.*, 1994, **98**, 13669-13679.
10. J.-M. Herrmann, J. Disdier and P. Pichat, *Chem. Phys. Lett.*, 1984, **108**, 618-622.
11. H. Yamashita, Y. Ichihashi, M. Takeuchi, S. Kishiguchi and M. Anpo, *J. Synchrotron Radiat.*, 1999, **6**, 451-452.
12. M. Rico-Santacruz, A. E. Sepulveda, E. Serrano, E. Lalinde, J. R. Berenguer and J. Garcia-Martinez, *J. Mater. Chem. A.*, 2014, **2**, 9497-9504.
13. K. Lee, A. Mazare and P. Schmuki, *Chem. Rev.*, 2014, **114**, 9385-9454.
14. E. Filippo, C. Carlucci, A. L. Capodilupo, P. Perulli, F. Conciauro, G. A. Corrente, G. Gigli and G. Ciccarella, *Appl. Surf. Sci.*, 2015, **331**, 292-298.F
15. O. L. Galkina, V. K. Ivanov, A. V. Agafonov, G. A. Seisenbaeva and V. G. Kessler, *J. Mater. Chem. B.*, 2015, **3**, 1688-1698.
16. X. Liu, J. Guo, L. Xiao and J. Fan, *Chem. Commun.*, 2010, **46**, 6729-6731.
17. A. S. Shebanova, A. G. Bogdanov, T. T. Ismagulova, A. V. Feofanov, P. I. Semenyuk, V. I. Muronets, M. V. Erokhina, G. E. Onishchenko, M. P. Kirpichnikov and K. V. Shaitan, *Biophysics*, 2014, **59**, 284-292.
18. S. George, S. Pokhrel, Z. Ji, B. L. Henderson, T. Xia, L. Li, J. I. Zink, A. E. Nel and L. Mädler, *J. Am. Chem. Soc.*, 2011, **133**, 11270-11278.
19. K. E. Karakitsou and X. E. Verykios, *J. Phys. Chem.*, 1993, **97**, 1184-1189.
20. O. Carp, C. L. Huisman and A. Reller, *Prog. Solid State Chem.*, 2004, **32**, 33-177.
21. D. F. Herman and W. K. Nelson, *J. Am. Chem. Soc.*, 1952, **74**, 2693-2693.

22. B. Weidmann, L. Widler, A. G. Olivero, C. D. Maycock and D. Seebach, *Helv. Chim. Acta*, 1981, **64**, 357-361.
23. D. F. Herman and W. K. Nelson, *J. Am. Chem. Soc.*, 1953, **75**, 3882-3887.
24. M. S. Kharasch and A. L. Flenner, *J. Am. Chem. Soc.*, 1932, **54**, 674-692.
25. M. S. Kharasch and H. S. Isbell, *J. Am. Chem. Soc.*, 1930, **52**, 2919-2927.
26. H. Gilman and J. M. Straley, *Recl. Trav. Chim. Pays-Bas*, 1936, **55**, 821-834.
27. M. Alves-Santos, L. M. M. Jorge, M. J. Caldas and D. Varsano, *J. Phys. Chem. A*, 2014, **118**, 13539-13544.
28. J. Roncali, *Chem. Rev.*, 1992, **92**, 711-738.
29. R. A. Street, J. E. Northrup and A. Salleo, *Phys. Rev. B.*, 2005, **71**, 165202.
30. B. S. Ong, Y. Wu, P. Liu and S. Gardner, *Adv. Mater.*, 2005, **17**, 1141-1144.
31. Y.-G. Kim, J. Walker, L. A. Samuelson and J. Kumar, *Nano Lett.*, 2003, **3**, 523-525.
32. P. Ravirajan, S. A. Haque, J. R. Durrant, D. Poplavskyy, D. D. C. Bradley and J. Nelson, *J. Appl. Phys.*, 2004, **95**, 1473-1480.
33. C.-H. Wu, H. Li, H. H. Fong, V. A. Pozdin, L. A. Estroff and G. G. Malliaras, *Org. Electron.*, 2011, **12**, 1073-1079.
34. K. Geramita, J. McBee, Y. Shen, N. Radu and T. D. Tilley, *Chem. Mater.*, 2006, **18**, 3261-3269.
35. D.-H. Hwang, J.-D. Lee, J.-M. Kang, S. Lee, C.-H. Lee and S.-H. Jin, *J. Mater. Chem.*, 2003, **13**, 1540-1545.
36. D.-H. Hwang, S.-K. Kim, M.-J. Park, J.-H. Lee, B.-W. Koo, I.-N. Kang, S.-H. Kim and T. Zyung, *Chem. Mater.*, 2004, **16**, 1298-1303.
37. M. Schwartz, G. N. Srinivas, A. T. Yeates, R. J. Berry and D. S. Dudis, *Synth. Met.*, 2004, **143**, 229-236.
38. Y. Zhu, M. M. Alam and S. A. Jenekhe, *Macromolecules*, 2003, **36**, 8958-8968.
39. K. R. Flower, A. T. McGown, P. J. Miles, R. G. Pritchard and J. E. Warren, *Dalton Trans.*, 2010, **39**, 3509-3520.
40. B. Weber and D. Seebach, *Tetrahedron*, 1994, **50**, 7473-7484.
41. T. L. Barr and S. Seal, *J. Vac. Sci. Technol., A*, 1995, **13**, 1239-1246.
42. E. Rodenas, H. Hattori and I. Toyoshima, *React. Kinet. Catal. Lett.*, 1981, **16**, 73-76.
43. S.-H. Chien, B. N. Shelimov, D. E. Resasco, E. H. Lee and G. L. Haller, *J. Catal.*, 1982, **77**, 301-303.

44. J. L. Wardell, in *Organometallic Chemistry: Volume 22*, ed. E. W. Abel, The Royal Society of Chemistry, 1993, vol. 22, pp. 1-12.
45. M. R. Hoffmann, S. T. Martin, W. Choi and D. W. Bahnemann, *Chem. Rev.*, 1995, **95**, 69-96.
46. J. Tauc, *Mater. Res. Bull.*, 1968, **3**, 37-46.
47. X. Chen, L. Liu, P. Y. Yu and S. S. Mao, *Science*, 2011, **331**, 746-750.
48. P. Wilhelm and D. Stephan, *J. Photochem. Photobiol., A*, 2007, **185**, 19-25.
49. J. Yu, Q. Li, S. Liu and M. Jaroniec, *Chem. Eur. J.*, 2013, **19**, 2433-2441.
50. Z. He, S. Yang, Y. Ju and C. Sun, *J. Environ. Sci.*, 2009, **21**, 268-272.
51. Q. Wang, C. Chen, D. Zhao, W. Ma and J. Zhao, *Langmuir*, 2008, **24**, 7338-7345.

# **Chapter 8**

## **Instruments**

### *Abstract*

In this thesis, many experimental techniques were used in order to characterize the properties of materials. Here we explain the most important instrumental methods and their principles.

## 8.1 UV-Vis spectroscopy

When a light with a given wavelength pass through a solution, the absorbance can be expressed as:

$$\text{Abs}(\lambda) = \lg \frac{I_0}{I_t} \quad (1)$$

where  $I_0$  is the intensity of light measured without the sample and  $I_t$  is the intensity of light measured with sample.

The relationship between the sample concentration ( $C$ ) and the absorbance can be expressed by Beer-Lambert law<sup>1</sup>:

$$\text{Abs} = \epsilon CL \quad (2)$$

where  $\epsilon$  is the sample's absorption coefficient and  $L$  is the length of the cell's optical path. This is an idea equation which assumes that there's no intensity of the light loss due to other phenomenon such as scattering.

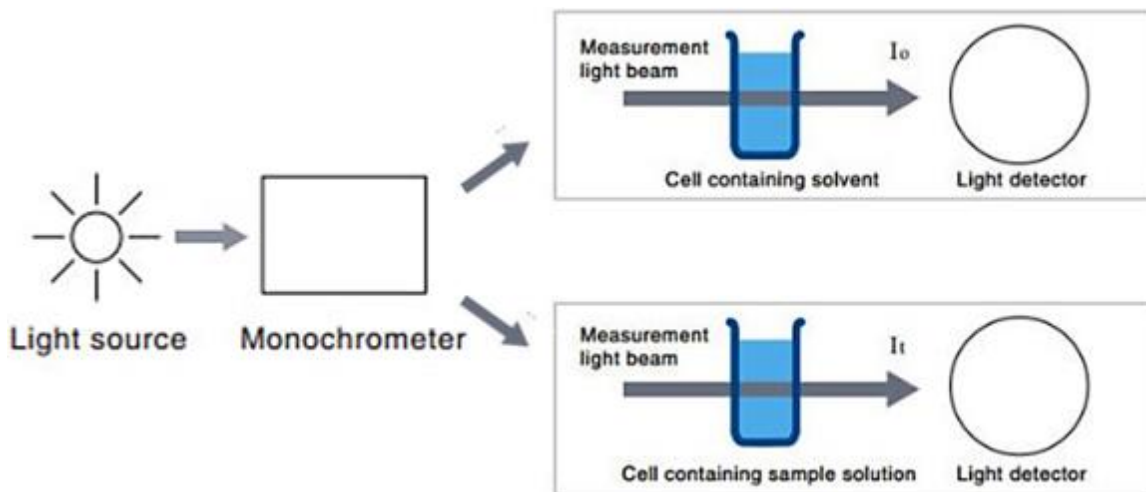


**Fig. 9.1** Configuration and the measurement of UV-Vis spectroscopy. Copyright: shimadzu.com.

The configuration of a UV-Vis spectroscopy is shown in Fig. 9.1. The wavelength of the light is adjusted by the monochromator and then divided into two equal parts which go



through the reference and the sample respectively. The lights are then detected by the light detectors and used for further analysis.

## 8.2 Steady-state emission spectroscopy

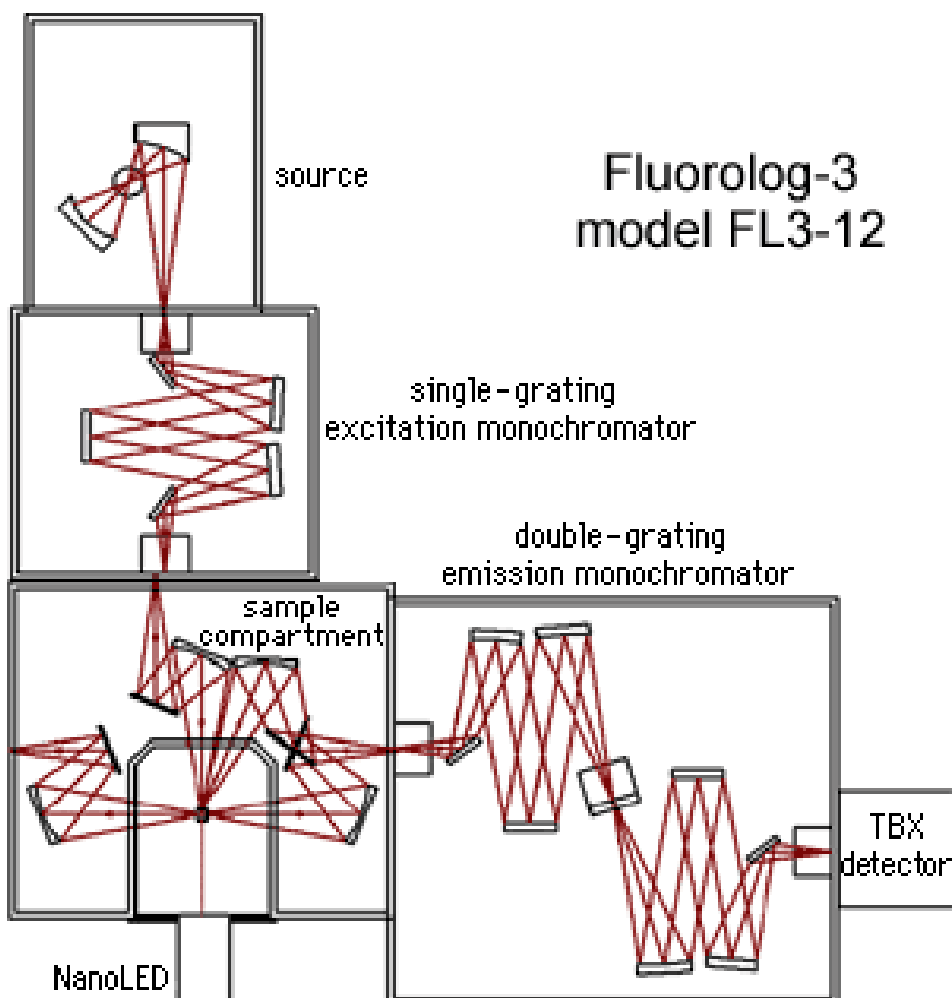


**Fig. 8.2** Configuration of Fluorolog-3 steady-state emission spectroscopy. Copyright: horiba.com.

An emission spectrum describes the wavelength distribution of emission under a constant excitation wavelength. Conversely, an excitation spectrum is measured by scanning the excitation wavelength at a constant emission wavelength. In the system, the spectral output of the light source, the wavelength dependent efficiency of the monochromators

and the detector tubes are not uniformed. In this case, the instrument doesn't show the real excitation or emission spectra. The polarization of the emitted light can affect the detection of the fluorescence due to the polarization dependence of the grating efficiency. Also, the emission spectra from different instrument could be different because of the sensitivity of the detector on different wavelength is different. Since the sensitivity of the detector on different wavelength is different, depends on the region of the light spectrum, different detectors are used. In our Fluorolog 3 equipment, for UV-Vis range, a TBX-04 single photon-counting detector is used and for the NIR, a Hamamatsu R2658P photomultiplier is used. The configuration of the instrument is shown in Fig. 8.2. During the measurement, different optical filters are also used to remove the unwanted lights.

### **8.3 Scanning electron microscopy (SEM)**

SEM is a microscopic method used to investigate the surface microstructure of various types of materials.<sup>2</sup> A typical configuration of SEM is shown in Fig. 8.3. Generally, the main components of SEM are source of electrons, electromagnetic lenses, sample chamber and holder, electron detector, and computer for control. Electrons are produced by the electron gun. Then the electrons are accelerated down and passed through a combination of lenses and coils to form a focused beam. The focused electron beam (typically with 100 - 30000 eV energy) hits the surface of the sample. In this process, electrons from the sample such as secondary electrons and backscattered electrons are produced. These electrons can be detected by the electron detector. With the beam moving, a full image of the sample structure in a certain area would be displayed.

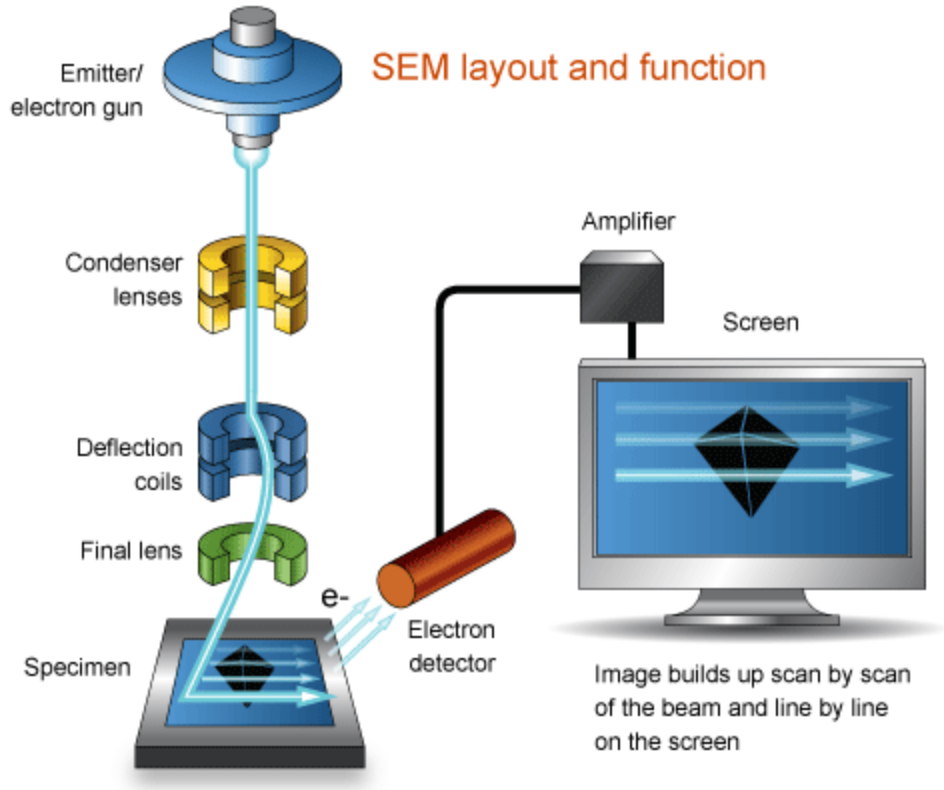


**Fig. 8.3** Configuration of SEM. Copyright: ammrf.org.au.

#### 8.4 Transmission electron microscopy (TEM)

TEM is a microscopic technique to investigate the microstructure of materials. The energy of the beam is typically very high (100000 - 400000 eV) compare to SEM.<sup>3</sup> TEM uses the same principle of normal optical microscope but use electron beam instead of visible light. The configuration of TEM is shown in Fig.8.4. Similar with SEM, the electrons produced by the electron gun are accelerated through a complicated lens system to form a focused beam. When the electron beam transmits a small specimen of the sample, some electrons are scattered. These transmitted electrons are again treated by a lens system to give an image of the sample on the image plate.

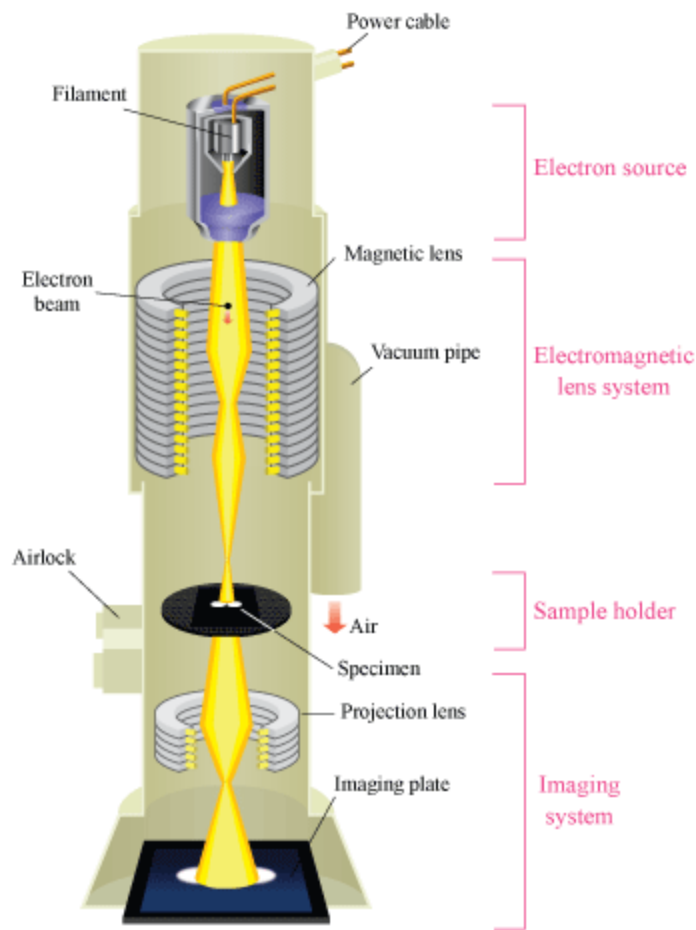


**Fig. 8.4** Configuration of TEM. Copyright: hk-phy.org.

### 8.5 Laser scanning confocal microscope

Compare with the conventional fluorescence microscope, laser scanning confocal microscope gives several advantages such as controllable depth of field, the elimination of the image degrading out-of-focus information and the ability to collect serial optical sections from thick specimens. The confocal approach makes it possible to use a spatial filtering system to eliminate out-of-focus light by illuminating the objective through a pinhole (Fig. 8.5). From the pinhole, only the reflection from the focused spot can get through. Other light from the out-of-focus spot are blocked. In this way, the final picture

is only made of the light coming from the focused spots. By adjusting the focus point, information of the specimen from different planes can be collected.

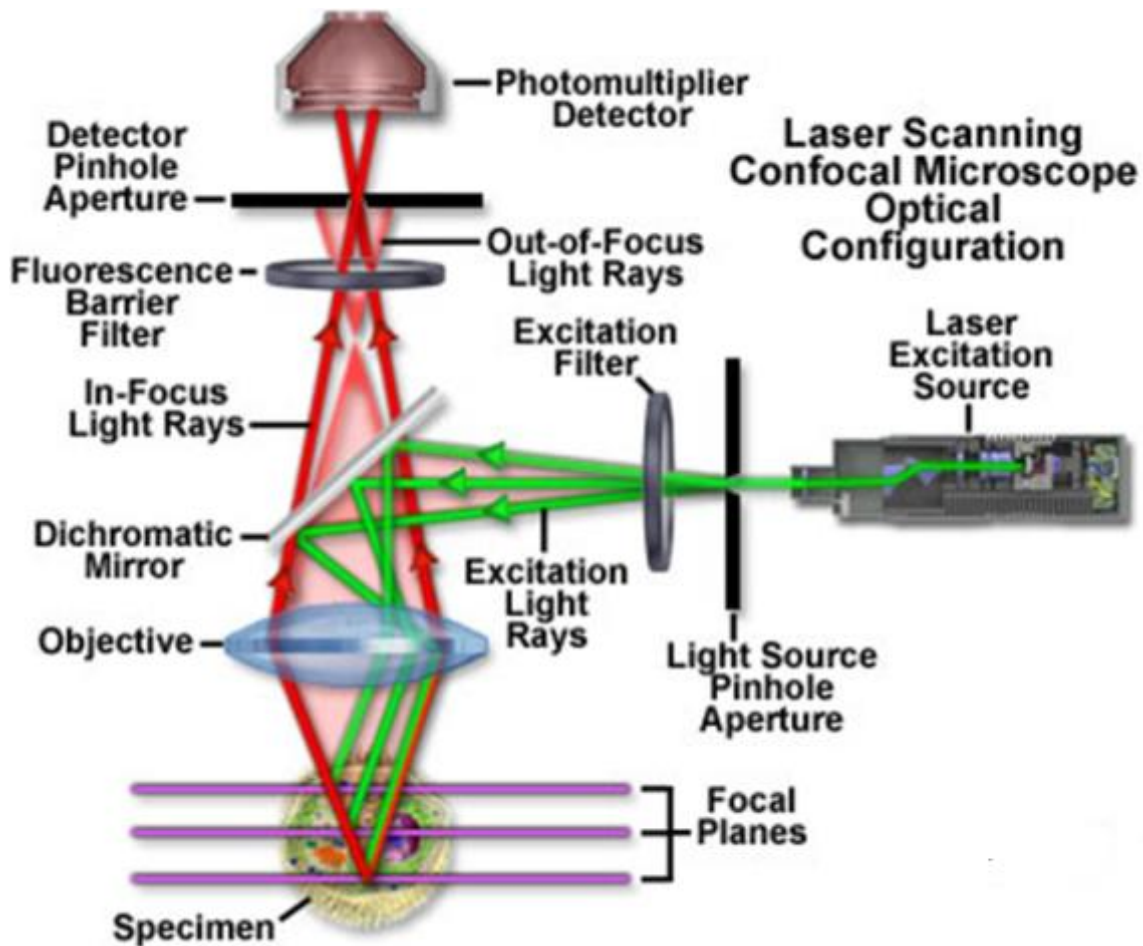


**Fig. 8.5** Configuration of laser scanning confocal microscope. Copyright: zeiss.com.

### 8.6 Dynamic light scattering (DLS)

Small particulates dispersed in a solution are normally subject to Brownian motion. In solution, the diffusion coefficient ( $D$ ) can be expressed as a function of the hydrodynamic particle size ( $d$ ), known as Stokes-Einstein equation:

$$D = \frac{kT}{3\pi\eta d} \quad (3)$$

where  $D$  is the diffusion coefficient,  $k$  is the Boltzmann's constant,  $T$  is the temperature of the medium,  $\eta$  is the viscosity of the medium and  $d$  the hydrodynamic diameter of the particle. From this equation, it's clear that in the same solution, for smaller particles the diffusion is faster and for bigger particles the diffusion is slower. When a laser beam passes through the particle suspension under the influence of the Brownian motion, the light will get scattered by the particles (Fig. 8.6). Each scattered light is corresponded to individual particles that move through the initial light path. In this way, the fluctuation of the scattered light corresponds with the size of the particles. The fluctuation of scattered light can be detected by detector and the size distribution of particles can be calculated.

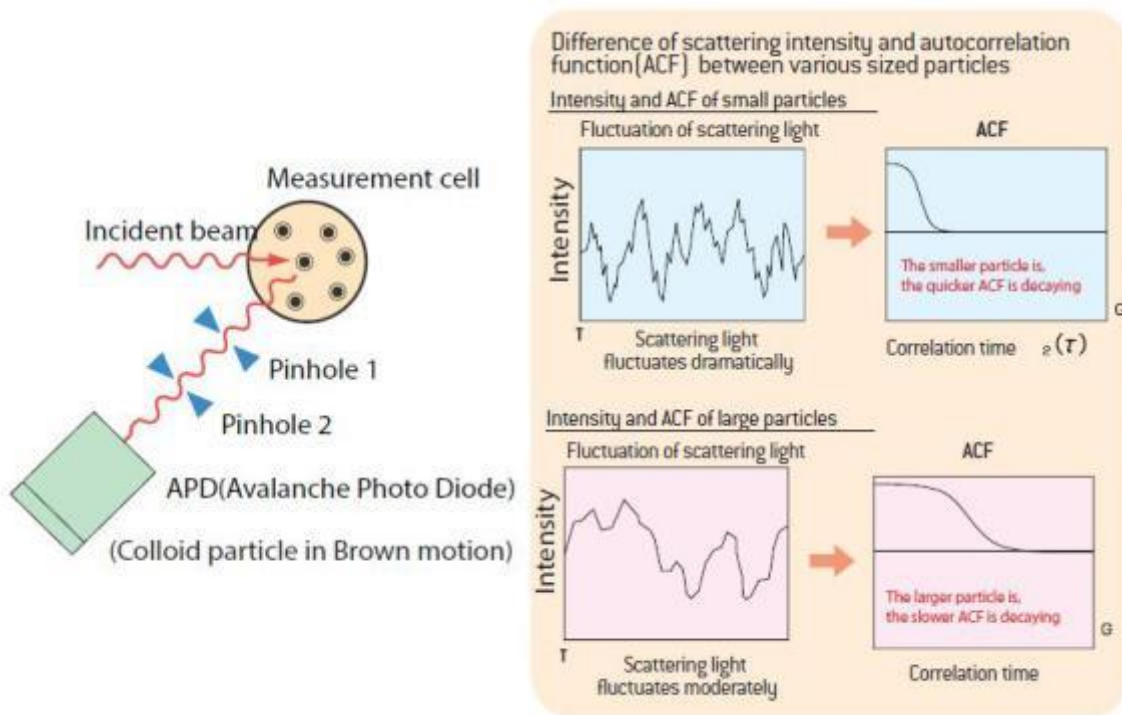


**Fig. 8.6** Principle of DLS measurement. Copyright: particulatesystems.com.

## 8.7 Zeta-potential

Colloidal particles usually possess a positive or negative electrostatic charge on its surface. When an electrical field is applied to the particle suspension, the particles will

migrate to the opposite charged direction (Fig. 8.7). At this point, a laser is shining through the system. The light is scattered by the particles in the solution. Due to the mobility of particles, Doppler effect is created on the scattered light. The shift of light frequency ( $\Delta\nu$ ) is measured by the detector, and the velocity of the particle ( $V$ ) can be calculated as:

$$\Delta\nu = 2Vn \sin\left(\frac{\theta}{2}\right) / \lambda \quad (4)$$

where  $n$  is the refractive index,  $\theta$  is the detect angle and  $\lambda$  is the wavelength of the initial light. The electrophoresis mobility  $U$  equals to  $V/E$  ( $E$  is the electrical field). Finally, zeta-potential ( $\zeta$ ) is expressed as Smoluchowski equation:<sup>4</sup>

$$\zeta = \eta U / \epsilon \quad (5)$$

where  $\eta$  is the viscosity of the solution and  $\epsilon$  is the permittivity of the solution.

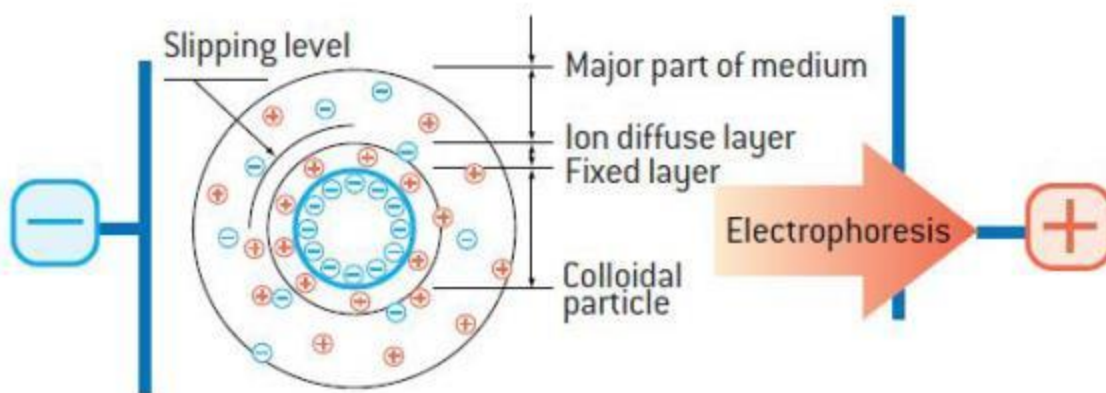


**Fig. 8.7** Principle of zeta-potential measurement. Copyright: particulatesystems.com.

## 8.8 Thermogravimetric analysis (TGA)

TGA measures mass changes of a material as a function of temperature (sometimes also of time) under a controlled atmosphere. Information of both physical and chemical, such as adsorption/desorption, vaporization, decomposition and solid-gas reactions can be provided by TGA measurement. The configuration of TGA is shown in Fig. 8.8. In this specific instrument, the gas atmosphere can be also chosen by purging different gases

into the chamber. In a typical measurement, a crucible without anything inside is measured through the whole procedure of the temperature change. This result is used as background. Then the crucible filled with sample is measured through the same procedure. Final result is corrected from the reference background.

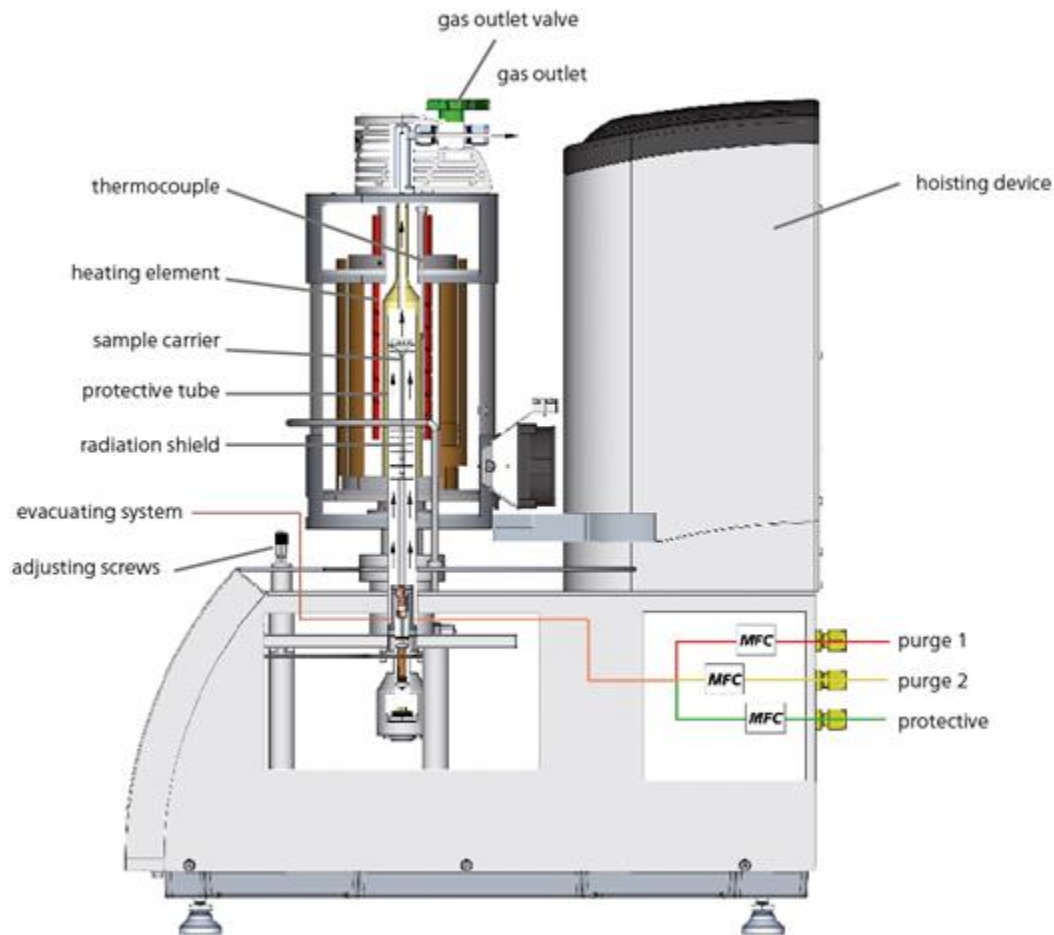


**Fig. 8.8** Configuration of TGA. Copyright: netzsch-thermal-analysis.com.

### 8.9 Powder X-ray diffraction (PXRD)

PXRD is a useful tool to determine the crystal structure of the material. Crystal structures are regular arrays of atoms/ions. X-ray is one kind of electromagnetic radiation. In this case the electrons from the atoms or ions which form the crystal structure can scatter X-ray. Through this procedure, scattered X-ray emanates from the material. This



phenomenon is known as elastic scattering, and the electron which scatters the X-ray is known as the scatterer. Through a regular array of scatterer, a regular pattern of scattered X-ray can be obtained. The relationship between the X-ray and the arrays of scatterer can be expressed by Bragg's law (Fig. 8.9):<sup>5</sup>

$$2d \sin\theta = n\lambda \quad (6)$$

where  $d$  is the spacing between diffracting arrays,  $\theta$  is the incident angle,  $n$  is any integer, and  $\lambda$  is the wavelength of the initial X-ray. For a certain crystal, distances ( $d$ ) between different diffraction planes are different. This will result for a unique PXRD pattern. Thus, PXRD pattern can give the crystal lattice information.

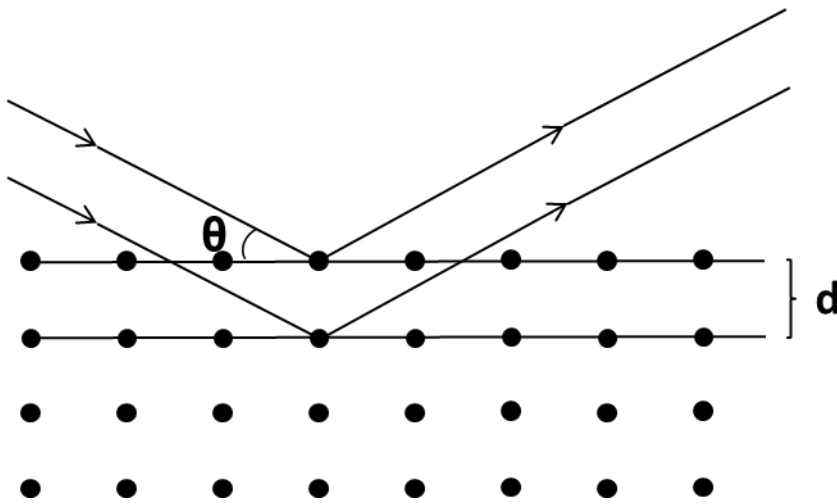


**Fig. 8.9** Principle of the X-ray diffraction.

## 8.10 References

1. A. Beer, *Ann. Phys. Chem*, 1852, **86**, 78-88.
2. C. Oatley, W. Nixon and R. Pease, *Adv. Electron. El. Phys.*, 1966, **21**, 181-247.
3. D. B. Williams and C. B. Carter, in *Transmission electron microscopy*, Springer, 1996, pp. 3-17.
4. A. Sze, D. Erickson, L. Ren and D. Li, *J. Colloid Interface Sci.*, 2003, **261**, 402-410.
5. W. H. Bragg and W. L. Bragg, *Proceedings of the Royal Society of London. Series A, Containing Papers of a Mathematical and Physical Character*, 1913, **88**, 428-438.

# Summary

## Introduction

In 1992, the oil company Mobil discovered a new class of porous materials which were based on silica and has uniform pores, named as the M41S family.<sup>1</sup> Since then, porous nanomaterials have attracted a lot of research interests due to their ability to entrap molecules, large surface area, rather easy functionalization and other unique properties.<sup>2</sup> Afterwards, several other porous materials have been developed,<sup>3</sup> as well as, microporous materials such as zeolite have been employed for other type of research than catalysis, in the last few decades.<sup>4</sup> Nowadays porous materials are widely applied to many fields such as catalysis, photovoltaics, sensing, bio imaging and drug delivery, just to cite few of them.<sup>5,6</sup>

In our group, previous researchers have developed functionalized mesoporous silica particles for drug delivery,<sup>7</sup> and also, zeolites LTL functionalized in different ways have been used in as carriers system for imaging agents and for gene therapy.<sup>8</sup> In addition such systems have been developed as substrates for cell adhesion in bio-application.<sup>9</sup> Based on the existing results, my PhD thesis **aims to develop new porous materials based on hybrid silica and titania, control their shape and porosity, use them in various applications.**

## Result and discussions

### *Synthesis of porous materials*

A big effort has been devoted to control the morphology and properties of porous materials based on silica, titania and to a less extent on zeolites. All the systems prepared and characterized are summarized in Table 1.

As can be seen, depending on the materials, each series of porous materials have been synthesized via a different approach. For microporous materials such as zeolite, since the pore size is based on the crystal structure itself, gel crystallization under hydrothermal condition has been used for the synthesis.<sup>10</sup> As for mesoporous materials such as silica and titania, we have employed surfactant template based sol-gel synthesis and evaporation induced self-assembly (EISA) methods.<sup>11-13</sup> In all cases, modification and optimization have been applied to each synthesis route. The morphology of the materials was characterized by scanning electron microscope (SEM) and transmission electron microscope (TEM). The pores (size and shape) were characterized by TEM, Small Angle X-ray Scattering (SAXS) and nitrogen adsorption measurements. The crystal structure was obtained by powder X-ray diffraction (PXRD). As an example of a characterization of a mesoporous silica material, Fig. 1 shows the different information obtained with our techniques.

**Table 1** List of the synthesized porous materials and their properties.

Material	Description	Pore size	Synthesis method
Zeolite LTL	Disc shaped, 1 $\mu\text{m}$ diameter, 200 nm or less thickness	0.7 nm	Hydrothermal
Zeolite LTL	Barrel shaped, 800 nm diameter, 400 nm thickness	0.7 nm	Hydrothermal
Zeolite LTL	Hexagonal shaped, 2 $\mu\text{m}$ diameter, 5 $\mu\text{m}$ length	0.7 nm	Hydrothermal
MCM-41 silica	Sphere, 100 nm diameter	3 nm	Sol-gel
SBA-15 silica	Hexagonal interconnected	12 nm	Sol-gel
Titania particle	Sphere, 400 nm diameter	11 nm	Sol-gel
P123-titania	Film	7 nm	EISA
P123-silica/titania	Film	8 nm	EISA

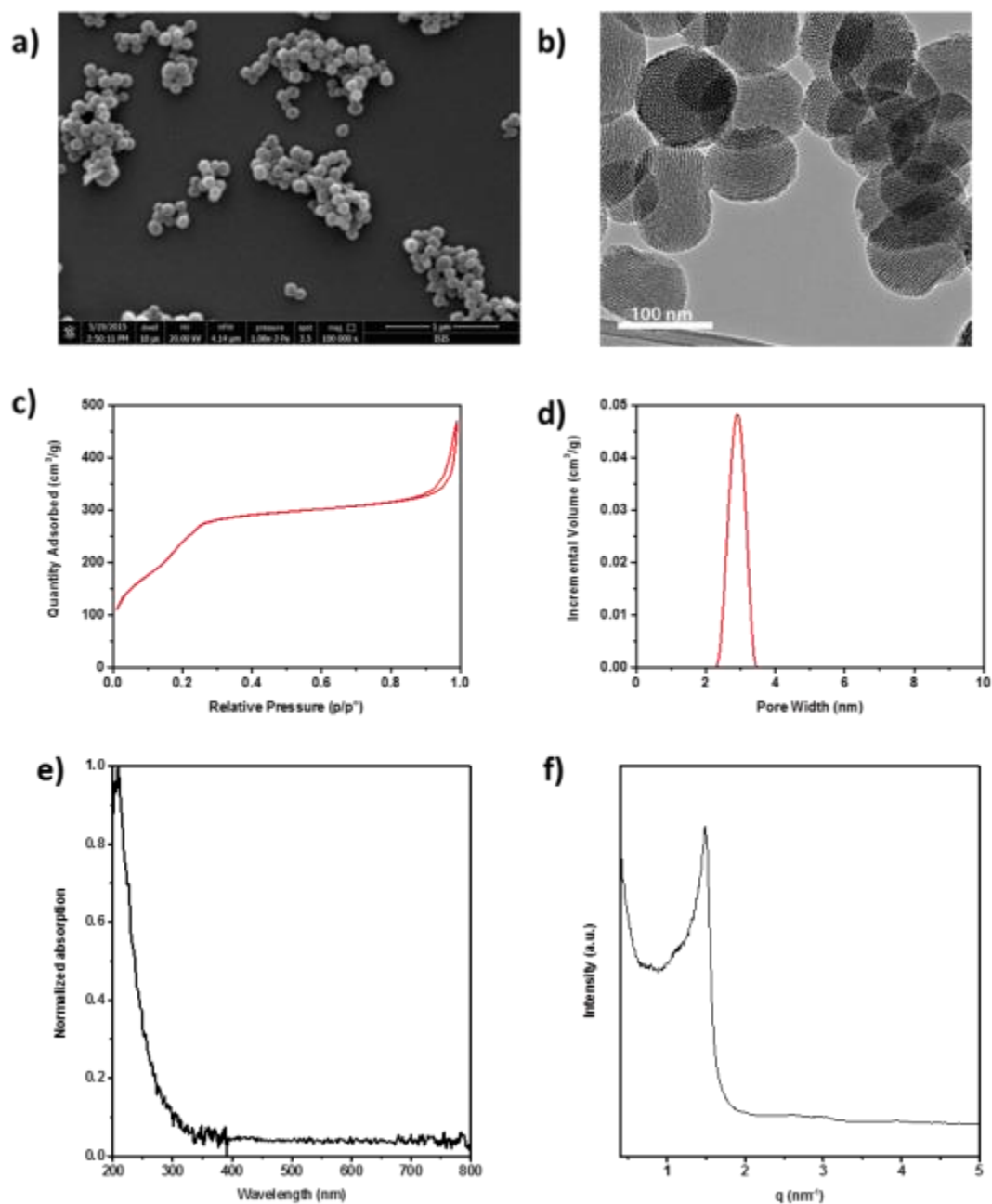


**Fig. 1** Typical characterizations for a porous material. a) SEM image of MCM-41 silica; b) TEM image of MCM-41 silica; c) Nitrogen adsorption isothermal curve of MCM-41 silica; d) Pore distribution of MCM-41 silica; e) solid-state UV-Vis spectra of MCM-41 silica; f) SAXS pattern of MCM-41 silica.

### *Dye adsorption based on functionalized silica materials*

Since decades ago the problem related to the wastes introduction in the environment is highlighted as a worldwide alarm. The nature of these wastes is ranging from inorganic to organic products which were used for several applications.<sup>14</sup> Among pollutants, dyes represent an important class of dangerous compounds. And not surprisingly, the discharge of dye-bearing wastewater into natural streams and rivers from textile, paper, carpet, leather, distillery, and printing industries induces problems for human health, such as allergic dermatitis, skin irritation, cancer and mutation, and for aquatic life organisms, inducing additional problems to the aesthetic nature of the environment.<sup>15</sup> More specifically, the discharged wastes containing dyes induces the formation of dangerous by-products from oxidation, hydrolysis, or other chemical reactions in the wastewater phase.<sup>16</sup> It is worth mentioning that, as reported by Singh *et al.*, the wastewater from textile industries is rated as the most polluted among all industrial sectors.<sup>17</sup> In fact, textile industries employ a significant volume of water and chemicals for wet-processing of textiles. The color index listed more than 8,000 chemical products associated with the dyeing process including several structural varieties of dyes.<sup>14</sup> In most situations, the use of different methods of treatment is necessary in order to remove all the contaminants presented in the wastewater. However, the physical adsorption is one of the most effective methods to remove color from water.<sup>18</sup> Recently, sorbents based on mesoporous silica has attained considerable attention due to their highly ordered structure, nanometer-sized pores, and their high surface area.<sup>19, 20</sup> The adsorption of dyes with sulfonic group by functionalized silica materials has been studied (Fig. 2a, b). The sonication and stirring methods have their own limitations and cannot be applied for water treatment with large quantity. A device was developed by using filtering method (Fig. 2c). While this device can treat a large amount of water, a decrease of performance was seen due to the less contacting time between the adsorbent and the dye solution. To solve this problem, a cross-linked polymer system was developed to add more amine site which is the effective group for the dye adsorption. Compare to the simply filtering, the adsorption capacity was enhanced. In the meanwhile, since the health and environment concern is rising up in the recent years,<sup>21</sup> the creation of this cross-linked particle network could

prevent the particles from escaping the device and diffusing into environment which might create environmental issues.

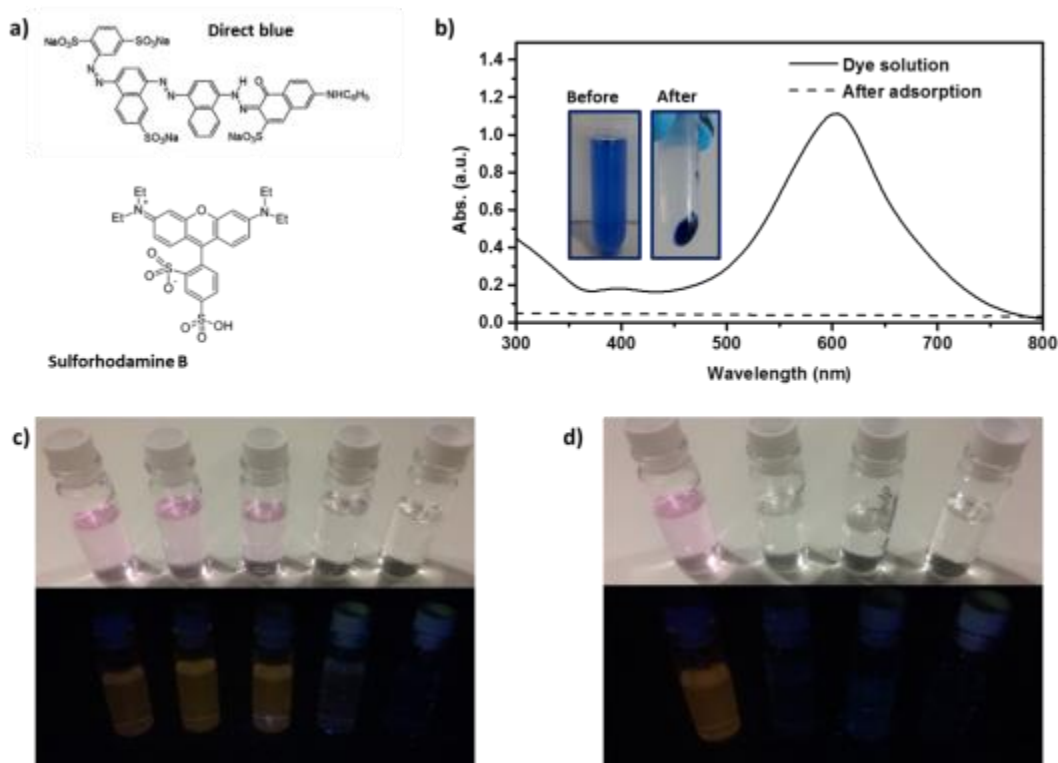


**Fig. 2** a) Chemical structures of direct blue dye and the sulforhodamine dye; b) comparison between the UV-Vis absorption spectra and picture obtained from  $5 \times 10^{-5}$  M DB aqueous solutions in absence of amine functionalized MCM-41 and after 5 minutes of contact time with 12 mg of amine functionalized MCM-41 (2 mL solution); c) pictures of the sulforhodamine B solutions under ambient light and UV, from left to right: initial dye solution ( $5 \times 10^{-7}$  M), dye solution filtered by silica gel 60, dye solution filtered by functionalized silica gel 60, dye solution filtered by functionalized SBA-15, water without dye; d) pictures of the solutions under ambient light and UV, from left to right: initial dye solution ( $5 \times 10^{-7}$  M), dye solution filtered by cross-linked functionalized silica gel 60, dye solution filtered by cross-linked functionalized SBA-15 mesoporous silica, water without dye.

### *Highly selective sensing for small biomolecules by zeolite based nanoporous materials*

Despite decades of concentrated efforts, artificial receptors remain inferior compared to their natural counterparts with respect to affinity and selectivity. Receptor candidates whose design was intended to optimize direct receptor-ligand interactions (Emil Fischer's lock and key model)<sup>22</sup> afforded, with the notable exception of multivalent systems,<sup>23</sup> only moderate binding affinities in water, by no means reaching that of protein receptors.<sup>24</sup> Recent (re)discovery of the importance of the non-classical hydrophobic effect in well shielded protein binding pockets and host cavities offers an alternative, biomimetic receptor design strategy.<sup>25-28</sup> Herein, we follow this path and report several extremely selective and strongly binding artificial receptors for aromatic amine neurotransmitters, *e.g.* serotonin, dopamine, (nor)epinephrine and histamine (Fig. 3).

The concept (shown in Fig. 3a) is based on the entrapment of positively charged dyes inside the zeolites, which are negatively charged, and the interaction with the neurotransmitters, possessing also a positively charged structure (the protonated amine), and result in a quenching of the emission of the dye. Importantly, the receptors are functional in buffers and biological media (*e.g.* blood serum) and can be used to study neurotransmitter-degradation or their delivery into living cells in real time. It is known that zeolite materials can be loaded with fluorescent dyes, which is extended herein to analyte-responsive reporter dyes that indicate the presence of an aromatic amine neurotransmitter. Notably, our receptor materials can reach charge-selectivity factors in  $K_d$  of about 10,000, whereas selectivity difference of  $\geq 100$  are rarely observed for the complexation of organic molecules by other artificial hosts in water.<sup>29, 30</sup>

Several applications have been developed based on this artificial neurotransmitter receptors. Porous materials capable of storing gases<sup>31</sup> or delivering drugs<sup>32</sup> have found wide ranges of industrial and medical applications, but monitoring strategies for cargo-loading and -deloading processes are just emerging.<sup>33, 34</sup> Oftentimes, fluorophore-labelled drug-analogues<sup>35</sup> were employed to study drug-delivery kinetics, however, labelled drugs inevitably show an altered biological profile compared to the parent drug. Employing a porous material with a built-in fluorescent signal transducer is a promising alternative,



allowing for monitoring of cargo-loading and -unloading of label-free drugs. We loaded ANR-L1 with serotonin (switch off in emission) and surface-coated it with a cell-attracting polylysine layer (Fig. 3e). This drug-delivery vehicle was readily uptaken by living *Rattus norvegicus* C6 glioma cells. Then, intracellular-release of the cargo serotonin occurred in the course of 24h hours, as can be inferred from the gradual restoring of the emission of the ANR (Fig. 3f).

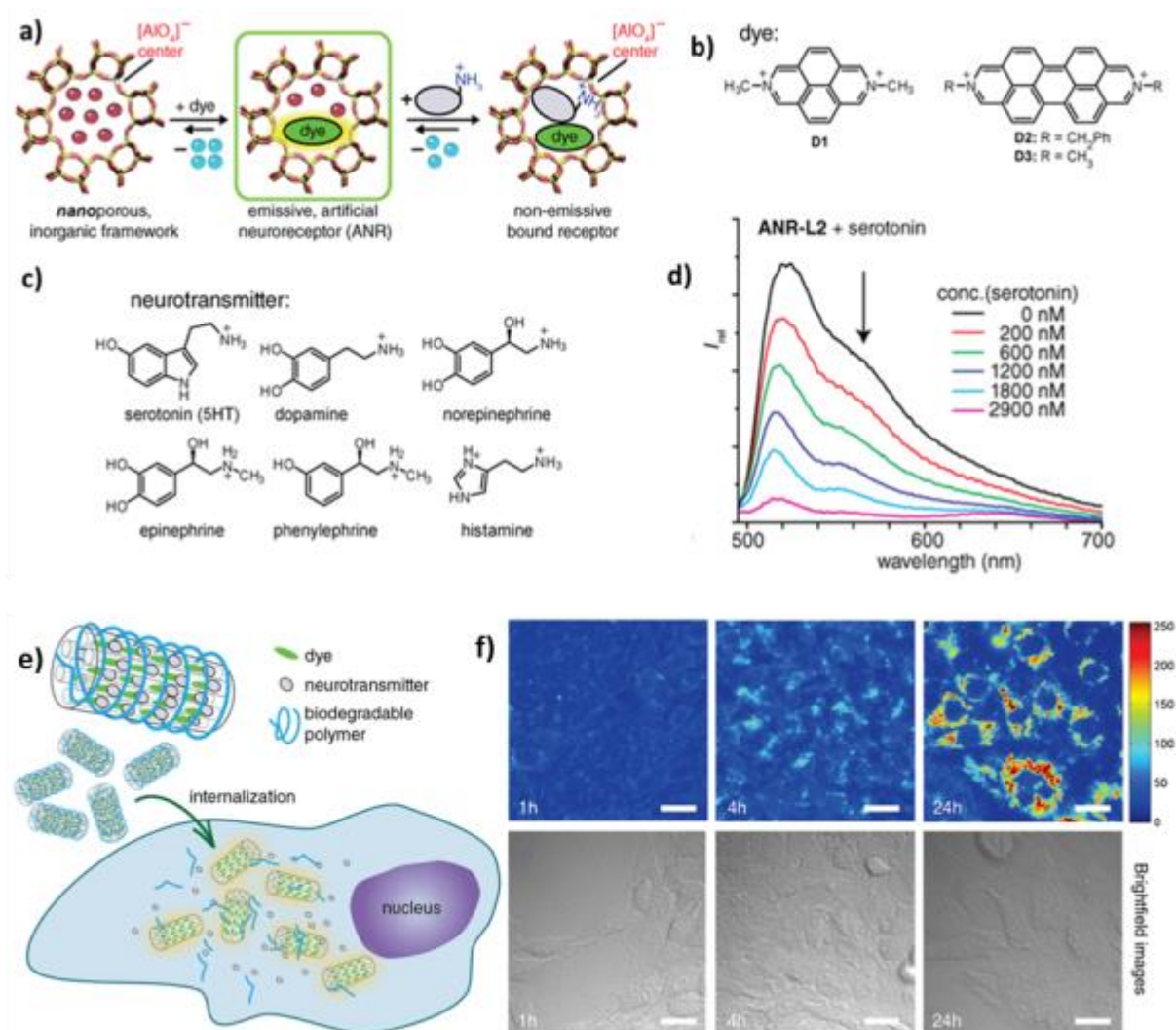


**Fig. 3** a) Schematic representation of the concept for neurotransmitters sensor. A dye encapsulated in the channels of a zeolite can be quenched upon insertion of the biomolecule. b)-c) chemical structures of aromatic amine neurotransmitters/hormones that can be detected by the ANRs, and representative dyes; d) emission spectra of ANR-L2 (25  $\mu g/mL$ ) upon addition of serotonin; e) cellular uptake of drug-loaded and surface-

coated ANRs results after release of the drug in an increase in the fluorescence emission of the ANR. e) Intensity coded-confocal micrographs showing cellular uptake experiment of the serotonin-loaded and poly(lysine)-coated ANR-L1 at different incubation times 1h (left), 4h (center), and 24h (right panel), and their corresponding brightfield images. Images were acquired at  $\lambda_{\text{exc}} = 405 \text{ nm}$ . The scale bar is  $20 \mu\text{m}$ .

#### *Formation of luminescence Cu(0) clusters in porous materials induced by irradiation of X-Ray*

By taking the advantage of different pore size, Cu(0) clusters have been successfully synthesized under exposure of X-ray. Metal clusters have been widely used in catalysis, bio-imaging, optical and electrical applications.<sup>36, 37</sup> Compare to the well-established noble metal clusters, Cu could be a good alternative in different applications because it is cheap and environmentally friendly. In the past years, only a few papers reported the successful synthesis of luminescent Cu(0) clusters.<sup>38, 39</sup> The main problem is that compare to gold or silver, copper is relatively easy to oxidize resulting in the loss of its optical and electrical properties. Most of the reported synthesis was done in solution by reduction agent and the clusters were protected by surfactant or ligand molecules.<sup>38, 40</sup> Compare to the other reducing agent, photo assisted reduction have the advantage on the control of reduction position and purification, which is very suitable for the cluster formation in a confined space or template. A. Katrib discovered in the 1980s that by exposure to X-ray, Pt(IV) can be reduced to Pt(II).<sup>41</sup> Since then, several researches showed the possibility the reduction of platinum, gold or silver under X-ray irradiation.<sup>42</sup> In 2014, J. Hofkens and co-workers developed the method of silver cluster formation inside zeolite material by X-ray irradiation.<sup>43</sup> The advantage of using X-ray is that the reduction can be controlled in situ, which is not possible for hydrogen or other chemical reducing agent. With tunable size and shape of the X-ray source, different patterns of the reduced species can be spatially created. In our case, we use the photo induced reduction method (X-ray) to reduce the loaded Cu(I) species to Cu(0) clusters inside our porous materials (zeolite and silica) (Fig. 4a).

The clusters were protected by their encapsulation and remain stable in air for months. The samples were characterized as materials and for their spectroscopic properties. From the fluorescence microscope, we observed that the parts which there are X-ray exposure showed the emission but not the unexposed part (Fig. 4b). From the CuI reduced sample, the reduced part was clearly visible under UV by naked eye (Fig. 4d). According to XPS, the copper we obtained was Cu(0). Very short life time (nano-seconds) of the emission suggested that the copper has a cluster form. The Cu(0) cluster emission according to the pore size have been studied. It is clear that with bigger pore size, the emission of wavelength longer than 400 nm increases (Fig. 4c). In this case, we have successfully developed the method to form Cu(0) clusters in situ by using X-ray. The color of the clusters changed according to different pore size. Potential applications such as catalysis or anti-counterfeit could be possible via our Cu(0) clusters.

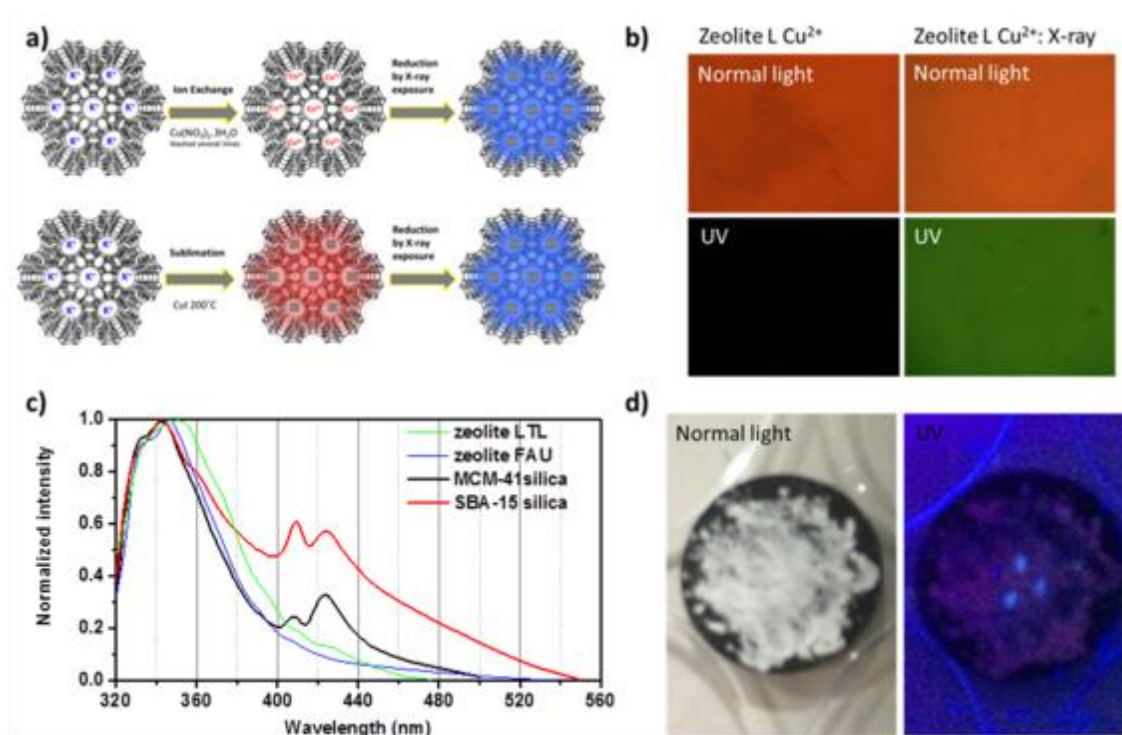


**Fig. 4** a) Synthetic procedure of the reduced Cu(0) cluster by ion exchange and CuI loading; b) Fluorescence microscope image of Cu(II) ion exchanged samples before and after X-ray exposure; c) Emission spectra (excitation @ 270 nm) of Cu(0) clusters in different porous materials from the reduction of Cu(I); d) Cu(0) cluster by X-ray exposure from Cu(I) loaded zeolite LTL under normal light and UV (bright blue: copper clusters; red: not reduced CuI clusters).

### *Multifunctional mesoporous titania for bio-application*

It is well-known that silica has been widely used as drug delivery agent.<sup>44</sup> However, since silica material are electrically “dead”, the employment of the titania in this field could bring new aspects to the drug delivery system. In fact, the hybrid porous titania particles have been tested as drug delivery materials, but more interestingly as *killing agents* in bio-applications. Titania due to its biocompatibility, possibility of functionalization and photo-active properties, could become an interesting candidate for bio-applications.<sup>45, 46</sup> Compared with titania particles which have no porous structure, spatial functionalization of the pores and the possibility to entrap molecules in the channels makes these particles quite attractive. Since titania particles are not emissive, fluorescein was used as both optical marker of the particle and to simulate a drug encapsulation of which we can trace the fate. To obtain this goal, the 400 nm mesoporous titania sphere (pore size of 11 nm) with further surface functionalization of organic molecules have been used for this purpose.

We functionalized the surface by an amino acid in order to have a better biocompatibility. The mesoporous titania particle was therefore decorated with alanine anchoring the –COOH group to the titania surface, and coupling the free –NH<sub>2</sub> group of alanine with fluorescein isothiocyanate isomer. At last the whole functionalized particle was covered by polylysine for protection and to impart a positive charge to the surface in order to facilitate cell internalization. From in vitro experiments, we confirmed that the particles are uptaken inside the cells, as can be seen by the emission of the bounded fluorescein. Among all the cells, fluorescein (green) was found only inside the cells which contain titania particles (Fig. 5a). This suggests that the fluorescein was released after cell uptake. The confocal microscopy co-localization studies showed that the particle did not have a preference for any specific cell organ.

Since titania has a well-known property of releasing reactive oxygen species (ROS) by UV irradiation,<sup>47</sup> the particle itself could be the killing agent. We can see that the cells were killed after UV irradiation. To study the kinetics of ROS release in vitro under UV, a special type of dye called cell-ROX was employed. The cell-ROX is not emissive

normally but becomes red emissive after oxidation (Fig. 5b). The detailed kinetics of ROS release under UV irradiation has been studied by measuring the emission intensity of cell-ROX through time (Fig. 5c).

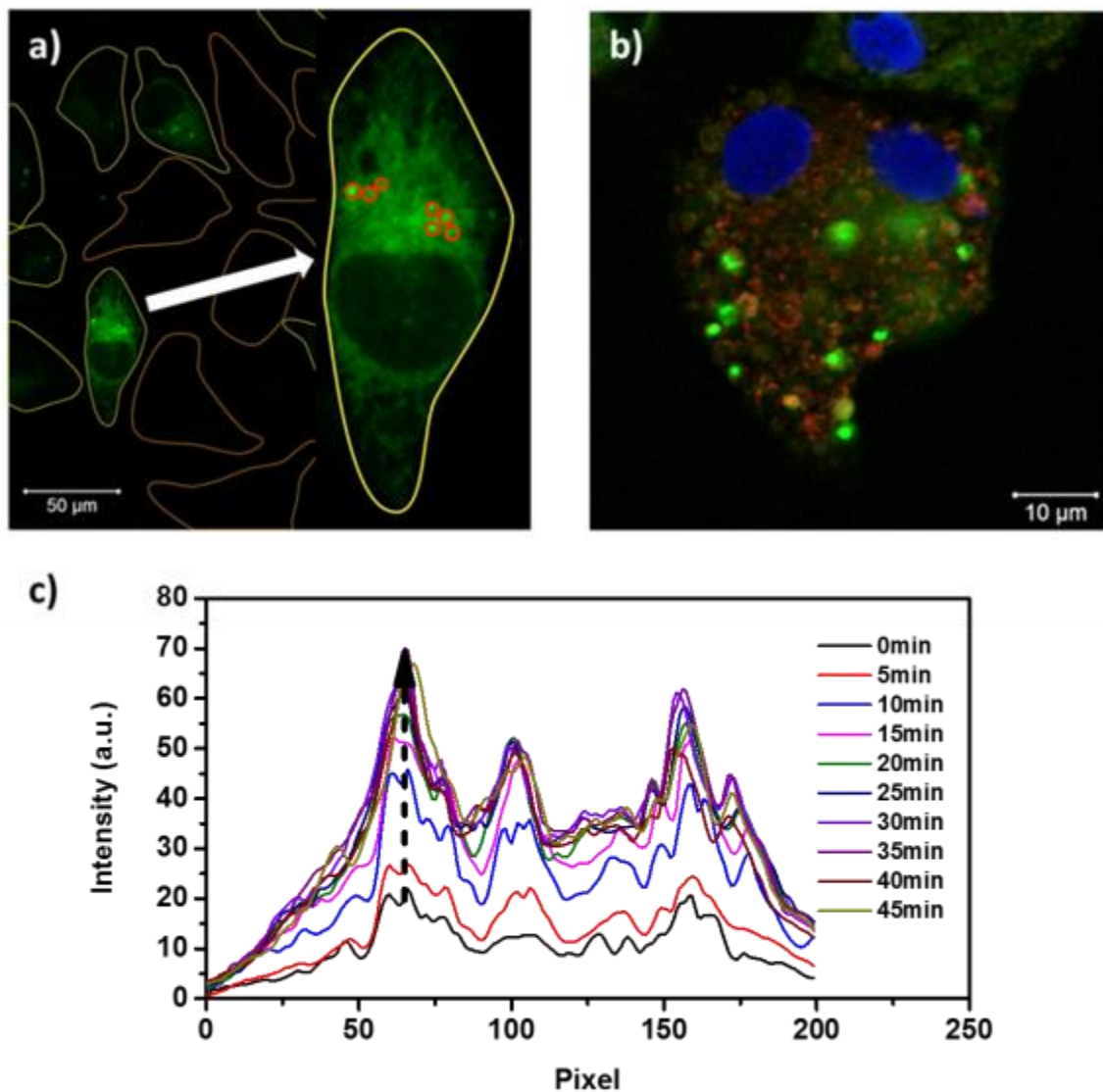


**Fig. 5** In vitro experiments of the multifunctionalized mesoporous titania particle, a) cell uptake and release of fluorescein inside Hela cells; b) the cells contained titania particles were killed after UV irradiation (green: fluorescein, blue: DAPI, red: cell-ROX); c) Intensity of cell-ROX dye through time under UV exposure indicates the kinetics of ROS formation.

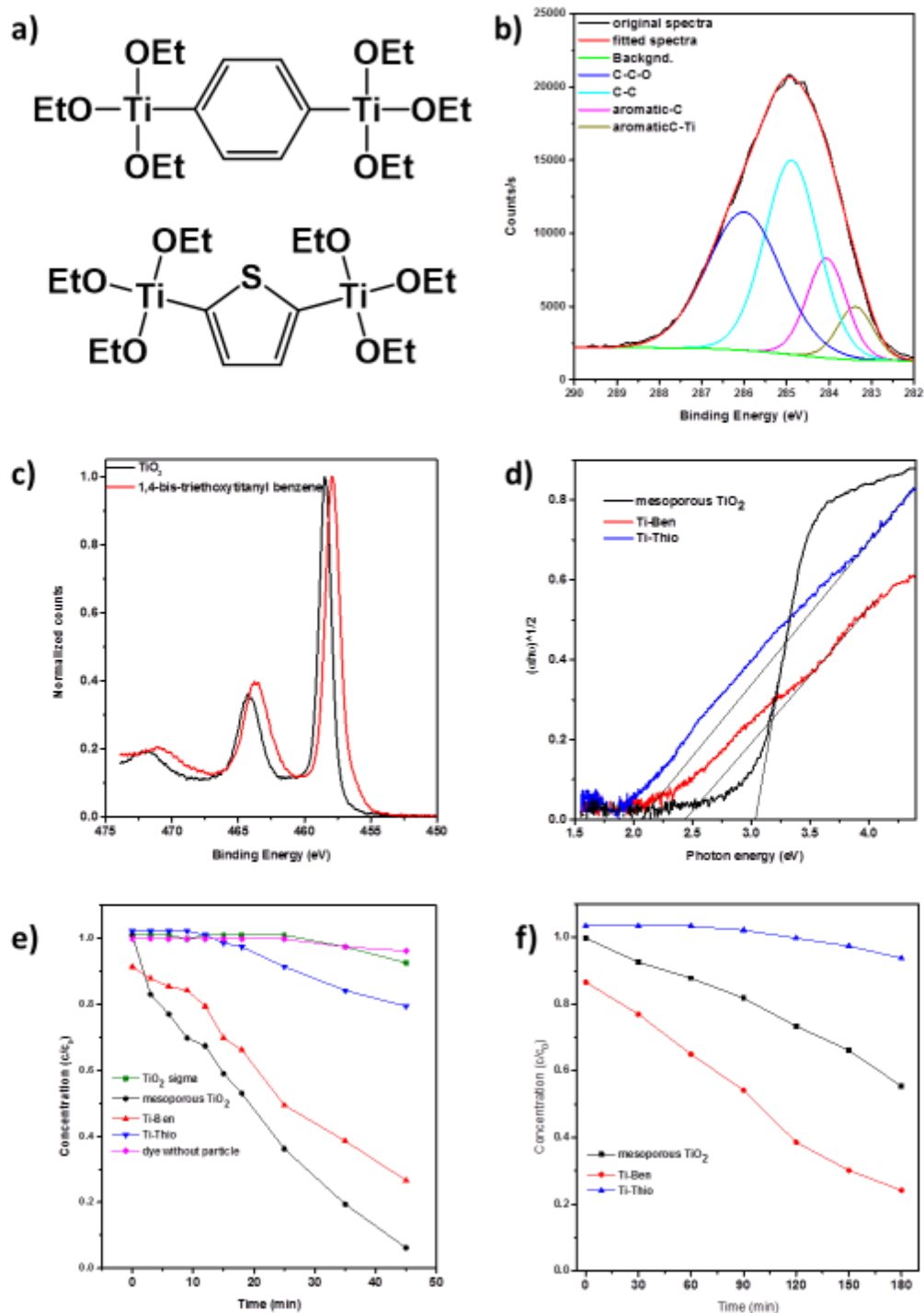


**Fig. 6** a) Structure of 1,4-bis-triethoxytitanyl benzene and 2,5-bis-triethoxytitanyl thiophene; b) deconvolution of XPS carbon elemental scan of 1,4-bis-triethoxytitanyl

benzene; c) XPS Ti elemental scan for titania and 1,4-bis-triethoxytitanyl benzene; d) band gap energy is determined by Tauc plot transferred from the UV-Vis spectrum; e) photocatalytic reaction of degradation of rhodamine B by titania materials under UV irradiation; f) photocatalytic reaction of degradation of rhodamine B by titania materials under visible light irradiation.

A big challenge in the modification of titania is the possibility to tune the band gap by introducing some chemical groups in the  $\text{TiO}_2$  structure. Due to the different reactivity of titania vs silica, the normal procedure described for the hybrid silica cannot be applied and therefore we have developed a strategy to achieve organotitania complex which has Ti-C covalent bond using organic molecules as linkers. Titania as highly promising material is mainly used for photochemical applications such as dye-sensitized solar cells and as a photocatalyst because of its excellent functionality, long term stability, and nontoxicity.<sup>48, 49</sup> In order to improve the photoreactivity of  $\text{TiO}_2$  and to extend its absorption edge into the visible-light region, doping of various transition metal cations has been intensively attempted.<sup>50, 51</sup> However, due to the thermal instability of the doped material, the photoactivity of the cation-doped  $\text{TiO}_2$  decreased even in the UV region.<sup>52</sup> Therefore hybrid organotitania nanomaterials, are expected to be more effective due to the combination of organic - inorganic parts through covalent bonds.

By using synthesized organolithium reagents, organotitania which contains Ti-C bond have been synthesized. The linker molecules we used were benzene and thiophene (Fig. 6a). The products have been characterized by several methods. Through X-ray photoelectron spectroscopy, XPS, we can clearly see the difference between titania and organotitania. From the titanium side we can monitor the lower binding of Ti-C compare to Ti-O (Fig. 6c). From the carbon point of view the component of the aromatic C-Ti bond was found (Fig. 6b). From UV-Vis measurement, we can transfer the spectra into Tauc plot.<sup>53</sup> The band gap was calculated. The Ti-benzene has a band gap of 2.43 eV and Ti-thiophene has a band gap of 2.05 eV which are significantly lower than pure titania which is 3.03 eV (Fig. 6d). Furthermore, the monomer of the organotitanium we obtained

can be polymerized and a hybrid titania network with benzene or thiophene linker can be established.

The photocatalytic properties of the Ti-Ben and Ti-Thio material have been investigated. In our case, mixtures of rhodamine B dye solution with fixed concentration and our titania based materials with fixed weight were exposed under UV or visible light respectively. Not surprisingly, we found out that under UV irradiation, the inorganic titania material showed the best photocatalytic property (Fig. 6e). But under visible light irradiation, our Ti-Ben showed the best photocatalytic performance because of its lower band gap compared with the inorganic titania material (Fig. 6f). Other applications based on the photoactivity under visible light could be developed according to our discovery.

## **Conclusion**

To conclude, my PhD research focus on the synthesis, characterization and applications of silica, titania and zeolite based porous materials.

Porous silica, titania and zeolite have been synthesized using different methodologies. Functionalized silica materials have been used for dye adsorption application which is useful for water treatment. A new cross-linked system and device have been created to enhance the adsorption ability and for large quantity of water treatment. By taking advantage of the pores, new method for Cu(0) cluster formation have been established. The photophysics of the Cu(0) clusters reduced from different copper source in different porous materials has been investigated. The use of the confinement for sensing has been demonstrated for small bio molecules, such as neurotransmitters. Several applications have been developed based on this artificial neurotransmitter receptors. Multi-functionalized mesoporous titania material has been used for bio-applications. Compare to the widely used silica material, its photoactivity could bring extra advantages. Finally, new types of hybrid organotitanium materials have been developed and their



photocatalytic properties have been investigated. In the meantime, deeper knowledge and skills on characterization instruments have also been obtained.

## References

1. C. T. Kresge, M. E. Leonowicz, W. J. Roth, J. C. Vartuli and J. S. Beck, *Nature*, 1992, **359**, 710-712.
2. C. T. Kresge and W. J. Roth, *Chem. Soc. Rev.*, 2013, **42**, 3663-3670.
3. L. Han and S. Che, *Chem. Soc. Rev.*, 2013, **42**, 3740-3752.
4. I. I. Ivanova and E. E. Knyazeva, *Chem. Soc. Rev.*, 2013, **42**, 3671-3688.
5. R. Zhang, A. A. Elzatahry, S. S. Al-Deyab and D. Zhao, *Nano Today*, 2012, **7**, 344-366.
6. P. Innocenzi and L. Malfatti, *Chem. Soc. Rev.*, 2013, **42**, 4198-4216.
7. A. Bertucci, E. A. Prasetyanto, D. Septiadi, A. Manicardi, E. Brognara, R. Gambari, R. Corradini and L. De Cola, *Small*, 2015, **11**, 5687-5695.
8. H. Lülff, A. Bertucci, D. Septiadi, R. Corradini and L. De Cola, *Chem. Eur. J.*, 2014, **20**, 10900-10904.
9. N. S. Kehr, B. Ergün, H. Lülff and L. De Cola, *Adv. Mater.*, 2014, **26**, 3248-3252.
10. Z. A. Ruiz, D. Brühwiler, T. Ban and G. Calzaferri, *Monatsh. Chem.*, 2005, **136**, 77-89.
11. Q. Cai, Z.-S. Luo, W.-Q. Pang, Y.-W. Fan, X.-H. Chen and F.-Z. Cui, *Chem. Mater.*, 2001, **13**, 258-263.
12. W. Dong, Y. Sun, C. W. Lee, W. Hua, X. Lu, Y. Shi, S. Zhang, J. Chen and D. Zhao, *J. Am. Chem. Soc.*, 2007, **129**, 13894-13904.
13. D. Chen, L. Cao, F. Huang, P. Imperia, Y.-B. Cheng and R. A. Caruso, *J. Am. Chem. Soc.*, 2010, **132**, 4438-4444.
14. S. P. Buthelezi, A. O. Olaniran and B. Pillay, *Molecules*, 2012, **17**, 14260-14274.
15. M. Anbia and S. Salehi, *Dyes Pigm.*, 2012, **94**, 1-9.
16. C.-H. Huang, K.-P. Chang, H.-D. Ou, Y.-C. Chiang and C.-F. Wang, *Microporous Mesoporous Mater.*, 2011, **141**, 102-109.
17. K. P. Singh, D. Mohan, S. Sinha, G. Tondon and D. Gosh, *Ind. Eng. Chem. Res.*, 2003, **42**, 1965-1976.
18. S. Sivamani and B. Leena Grace, *IJBST*, 2009, **2**, 47-51.
19. A. R. Nestic, M. J. Kokunesoski, T. D. Volkov-Husovic and S. J. Velickovic, *Environ. Monit. Assess.*, 2016, **188**, 1-12.
20. K. Y. Ho, G. McKay and K. L. Yeung, *Langmuir*, 2003, **19**, 3019-3024.

21. M. Hassellöv, J. W. Readman, J. F. Ranville and K. Tiede, *Ecotoxicology*, 2008, **17**, 344-361.
22. E. Fischer, *Berichte der deutschen chemischen Gesellschaft*, 1894, **27**, 2985-2993.
23. J. Rao, J. Lahiri, L. Isaacs, R. M. Weis and G. M. Whitesides, *Science*, 1998, **280**, 708-711.
24. H.-J. Schneider, P. Agrawal and A. K. Yatsimirsky, *Chem. Soc. Rev.*, 2013, **42**, 6777-6800.
25. P. Snyder, M. Lockett, D. Moustakas and G. Whitesides, *Eur. Phys. J. Spec. Top.*, 2014, **223**, 853-891.
26. E. Persch, O. Dumele and F. Diederich, *Angew. Chem. Int. Ed.*, 2015, **54**, 3290-3327.
27. D. Chandler, *Nature*, 2005, **437**, 640-647.
28. F. Biedermann, W. M. Nau and H.-J. Schneider, *Angew. Chem. Int. Ed.*, 2014, **53**, 11158-11171.
29. H.-J. Schneider, *Angew. Chem. Int. Ed.*, 2009, **48**, 3924-3977.
30. D. A. Dougherty, *Acc. Chem. Res.*, 2012, **46**, 885-893.
31. R. E. Morris and P. S. Wheatley, *Angew. Chem. Int. Ed.*, 2008, **47**, 4966-4981.
32. M. Vallet-Regí, F. Balas and D. Arcos, *Angew. Chem. Int. Ed.*, 2007, **46**, 7548-7558.
33. J. Kärger, T. Binder, C. Chmelik, F. Hibbe, H. Krautscheid, R. Krishna and J. Weitkamp, *Nat Mater*, 2014, **13**, 333-343.
34. N. Yanai, K. Kitayama, Y. Hijikata, H. Sato, R. Matsuda, Y. Kubota, M. Takata, M. Mizuno, T. Uemura and S. Kitagawa, *Nat Mater*, 2011, **10**, 787-793.
35. N. G. Gubernator, H. Zhang, R. G. W. Staal, E. V. Mosharov, D. B. Pereira, M. Yue, V. Balsanek, P. A. Vadola, B. Mukherjee, R. H. Edwards, D. Sulzer and D. Sames, *Science*, 2009, **324**, 1441-1444.
36. E. C. Tyo and S. Vajda, *Nat Nano*, 2015, **10**, 577-588.
37. Y. Lu and W. Chen, *Chem. Soc. Rev.*, 2012, **41**, 3594-3623.
38. W. Wei, Y. Lu, W. Chen and S. Chen, *J. Am. Chem. Soc.*, 2011, **133**, 2060-2063.
39. C. Vázquez-Vázquez, M. Bañobre-López, A. Mitra, M. A. López-Quintela and J. Rivas, *Langmuir*, 2009, **25**, 8208-8216.
40. C. Wang, Y. Yao and Q. Song, *Colloids Surf., B*, 2016, **140**, 373-381.
41. A. Katrib, *J. Electron. Spectrosc. Relat. Phenom.*, 1980, **18**, 275-278.
42. M. Fujiwara, H. Fujii, K. Tainaka, T. Matsushita and S. Ikeda, *Analytical Sciences/Supplements*, 2002, **17icas**, i1065-i1067.

43. E. Coutino-Gonzalez, D. Grandjean, M. Roeffaers, K. Kvashnina, E. Fron, B. Dieu, G. De Cremer, P. Lievens, B. Sels and J. Hofkens, *Chem. Commun.*, 2014, **50**, 1350-1352.
44. I. I. Slowing, B. G. Trewyn, S. Giri and V. S. Y. Lin, *Adv. Funct. Mater.*, 2007, **17**, 1225-1236.
45. K. C. W. Wu, Y. Yamauchi, C.-Y. Hong, Y.-H. Yang, Y.-H. Liang, T. Funatsu and M. Tsunoda, *Chem. Commun.*, 2011, **47**, 5232-5234.
46. Z. Fei Yin, L. Wu, H. Gui Yang and Y. Hua Su, *PCCP*, 2013, **15**, 4844-4858.
47. R. Konaka, E. Kasahara, W. C. Dunlap, Y. Yamamoto, K. C. Chien and M. Inoue, *Free Radical Biol. Med.*, 1999, **27**, 294-300.
48. A. Fujishima, T. N. Rao and D. A. Tryk, *J. Photochem. Photobiol. C.*, 2000, **1**, 1-21.
49. A. Hagfeldt and M. Graetzel, *Chem. Rev.*, 1995, **95**, 49-68.
50. H. Yamashita, Y. Ichihashi, M. Takeuchi, S. Kishiguchi and M. Anpo, *J. Synchrotron Radiat.*, 1999, **6**, 451-452.
51. J.-M. Herrmann, J. Disdier and P. Pichat, *Chem. Phys. Lett.*, 1984, **108**, 618-622.
52. T. Umebayashi, T. Yamaki, H. Itoh and K. Asai, *Appl. Phys. Lett.*, 2002, **81**, 454-456.
53. J. Tauc, *Mater. Res. Bull.*, 1968, **3**, 37-46.

# Acknowledgements

This PhD life of mine is full of adventures. Thanks to all that accompanied me during this period. It was a special experience in Strasbourg.

First of all, I would like to thank my supervisor, Prof. Luisa De Cola for giving me this opportunity to join and work in this amazing group. I've learned a lot of knowledge and skills during these years. Also, I would like to thank European research council (ERC) for the funding.

Among the PhDs/post-docs, the first person I wish to thank here is Eko. I would consider you also as a supervisor (even through it's not recorded in any official document) for everything. You really helped me a lot in the lab with all the projects and all the equipment you know. Without you I don't think it's possible to finish my PhD. Thank you Claire for the help with all the administrative documents and many other French related things. You know how impossible these things can be. For the thesis, I would like to thank Vito for the dye adsorption project, Frank for the zeolite sensing project, Loïc for the Cu(0) project, Dedy for the titania bio project and Veronika for the organotitania project. Without you guys these work cannot be finished.

For the lab crew, I would like to thank Youssef for all the help in the lab and outside the lab, life in France is not that easy since I'm not French speaking. Thanks Ricardo for all your help and entertainment. Thank you Alessandro Bertucci with all the conversations both related and not related to science. Thanks Laura and Leana for the Italian related stuff. Thank you, Ingrid, for bringing the positive atmosphere. Thanks Alessandro Aliprandi for your unique jokes. Thanks Federica for the activities during weekends. Thanks Stephan for your Germanic humor. Thank you, Serena, for the consideration thoughts (e.g. birthdays). Thanks Ines for all your work to keep this lab running. Thanks Nadia and Valentina for your nice Sicilian things. Thanks Amparo for all the awesome Spanish jamón. Thanks Frank for all your help with everything. Thanks Loïc for all the

photophysics knowledge and the French specialties. Thanks Dedy for all the bio stuff and the activities outside the lab. Thank you, Veronika, for all your help and your Czech things. Thanks John for being the native British.

Special thanks to Chien-Wei, as we are both foreigners here, you gave me a lot of help for both the PhD work and everyday life. I really appreciate.

I also would like to thank to all the De Cola group members: Remi, Deanne, Céline, Nina, Beatrice, Leticia, Simone, Matteo, Rebecca, Damiano, Angélique, Valentin, Mike, Alberto, Etienne, Henning and Elena. Thanks for all the time we spend together.

Thanks to the Chinese crew in the building, in the chemistry faculty and from basketball. It's always nice to speak our own languages and share some thoughts.

Thanks you, Prof. Jurriaan Huskens, without you I might never applied to Luisa's group and all the things above would be in another parallel universe.

In the end I would thank my family that gave me full supports for studying abroad. I miss you all.

# Curriculum Vitae

## 1. PERSONAL and CONTACT INFORMATION

Name: Pengkun CHEN      Email: [pengkun.chen@unistra.com](mailto:pengkun.chen@unistra.com)  
Date of Birth: December 2<sup>nd</sup> 1987      Nationality: Chinese      Gender: Male

## 2. EDUCATION

01.09.2013 - now, expecting graduation on 10.02.2017

- Université de Strasbourg, France
- Institut de Science et d'Ingénierie Supramoléculaires
- PhD in Chemistry

01.09.2010 - 31.08.2012

- University of Twente, the Netherlands
- MESA+ Institute for Nanotechnology
- Master of Science in Nanotechnology

01.09.2006 - 30.06.2010

- University of Electronic Science and Technology of China
- Bachelor of Engineering in Applied Chemistry

## 3. AWARDS

UTS scholarship in University of Twente

People's scholarship in UESTC

## 4. PERSONAL SKILLS

*Leadership and social skills*

- In charge of several lab instruments during PhD study.
- Team worker with good communication skills, experienced working in various types of teams such as university research groups, company R&D team, sales team and production team.

*Language skills*

- Mother tongue: **Chinese**.
- **English: C1**, proficient user; **French: A2**, Basic user; **German: A2**, Basic user.  
(Based on common European framework of reference for languages)

*Computer skills*

- Proficient user of Microsoft Office programs and lab instrument programs. Experienced in common data analysis and graphing software such as Excel, ImageJ and Origin.

## 5. PATENT

Highly selective artificial neurotransmitter receptors, Frank Biedermann, Dedy Septiadi, Eko Adi Prasetyanto, [Pengkun Chen](#) and Luisa De Cola, *European patent EP16305278*

## 6. PUBLICATIONS

Modular Graphene-Based 3D Covalent Networks: Functional Architectures for Energy Applications, X. Zhang, A. Ciesielski, F. Richard, [P. Chen](#), E. A. Prasetyanto, L. De Cola and P. Samori, 2016, *Small*, doi:10.1002/sml.201503677

Reactivity Mapping with Electrochemical Gradients for Monitoring Reactivity at Surfaces in Space and Time, S. Krabbenborg, C. Nicosia, [P. Chen](#) and J. Huskens, 2013, *Nature Communications*, doi:10.1038/ncomms2688

Shape-controlled fabrication of micron-scale surface chemical gradients via electrochemically activated copper(I) "click" chemistry, Carlo Nicosia, Sven O. Krabbenborg, [Pengkun Chen](#) and Jurriaan Huskens, 2013, *J. Mater. Chem. B*, doi: 10.1039/C3TB20902D





# Titania and silica based hybrid porous nanomaterials: from synthesis to applications

## Résumé

Mon doctorat se focalise sur la synthèse, la caractérisation et les applications de matériaux poreux à base de silice, dioxyde de titane et zéolite. La silice poreuse, le dioxyde de titane et les zéolites ont été synthétisés en utilisant des méthodologies différentes. Des matériaux de silice fonctionnalisés ont été utilisés pour des applications en adsorption de colorant, ce qui est utile pour le traitement de l'eau. Un nouveau système réticulé et un nouveau dispositif ont été créés pour améliorer la capacité d'adsorption et pour le traitement d'une grande quantité d'eau. En tirant parti des pores, une nouvelle méthode de formation de clusters de Cu (0) a été établie. Les propriétés photophysiques ont été étudiées, en utilisant plusieurs sources de cuivre et différents matériaux poreux. L'utilisation du confinement pour la détection de petites molécules biologiques tels que les neurotransmetteurs a été démontrée. Plusieurs applications ont été développées sur la base de ces récepteurs de neurotransmetteurs artificiels. Un matériau de titane mésoporeux multifonctionnalisé a été utilisé pour les applications en biologie. En comparaison avec la silice, plus couramment utilisée, sa photoactivité pourrait apporter des avantages supplémentaires. Finalement, de nouveaux types de matériaux de type organotitanes hybrides ont été développés, et leurs propriétés photo-catalytiques ont été démontrées.

## Résumé en anglais

My PhD research focus on the synthesis, characterization and applications of silica, titania and zeolite based porous materials. Porous silica, titania and zeolite have been synthesized using different methodologies. Functionalized silica materials have been used for dye adsorption application which is useful for water treatment. A new cross-linked system and device have been created to enhance the adsorption ability and for large quantity of water treatment. By taking advantage of the pores, new method for Cu(0) cluster formation have been established. The photophysics of the Cu(0) clusters reduced from different copper source in different porous materials has been investigated. The use of the confinement for sensing has been demonstrated for small bio molecules, such as neurotransmitters. Several applications have been developed based on this artificial neurotransmitter receptors. Multi-functionalized mesoporous titania material has been used for bio-applications. Compare to the widely used silica material, its photoactivity could bring extra advantages. Finally, new types of hybrid organotitanium materials have been developed and their photocatalytic properties have been investigated.